Electron dynamics in crossed-field discharges

Thibault Dubois

UNIVERSITÉ D'ORLÉANS

Énergie - Matériaux - Sciences de la Terre et de l'Univers (EMSTU)

Centre National de la Recherche Scientifique (CNRS)

Institut de Combustion Aérothermique Réactivité et Environnement (ICARE)

THÈSE présentée par :

Thibault Dubois

soutenue le : **23 novembre 2023**

pour obtenir le grade de : **Docteur de l'Université d'Orléans**

Discipline/ Spécialité : **Physique des plasmas**

Electron dynamics in crossed-field discharges

Dynamique des électrons dans les décharges en champs croisés

THÈSE dirigée par :

Mme TSIKATA Sedina	Associate Professor School of Aerospace Engineering, Georgia Institute of Technology, Georgia, USA

RAPPORTEURS :

M. HARA Kentaro	Assistant Professor Department of Aeronautics and Astronautics, Stanford University, California, USA
M. TACCOGNA Francesco	Senior Researcher Institute for Plasma Science and Technology, National Research Council, Bari, Italy

EXAMINATEURS :

M. PELLERIN Stéphane	Professeur - **Président du jury** GREMI-CNRS, Université d'Orléans, France
M. MINEA Tiberiu	Professeur LPGP-CNRS, Université Paris Saclay, France
M. GARRIGUES Laurent	Directeur de Recherche LAPLACE-CNRS, Université Paul Sabatier, France
M. ESCARGUEL Alexandre	Professeur PIIM-CNRS, Université d'Aix-Marseille, France

Contents

List of Figures

List of Tables

Chapter 1

Introduction

Contents

The plasma state is often described as the "fourth state of matter". Even though it represents 99% of the matter in the universe, it is extremely poorly represented on the surface of the earth. A few environments - fire, lightning and auroras - allow us to see it naturally. The evolution of technology has nevertheless allowed us to exploit this particular state, and it now provides us with many services and represents an important part of our lives, even if it remains invisible for most. We will see in this introduction two particular sources of plasma which are today major constituents of the science and technology of communications and electronics.

1.1 The Hall thruster

At the time of writing, there are about 6500 artificial satellites in service in Earth orbit (UCS Satellite Database [4]), not counting the thousands that are no longer operational. More than 60% of them are used for communications, and 20% for Earth observation, for example to collect data on climate, monitor the weather or resource availability. The remaining is shared mainly between scientific satellites or used for GPS positioning. It should be noted that there has been a drastic increase in the number of satellites dedicated to communications in recent years, mainly due to the appearance of constellations such as OneWeb or Starlink, whose role is to provide Internet access in remote areas.

These new actors are part of what is now called "New Space", that is, a democratization of access to space, no longer through institutional actors as was the case formerly, but through private actors. Several factors can be determined, but one will especially retain the miniaturization of electronics and the democratization of many technologies such as 3D printing, coupled with an inherent decrease in the risks of space launches, as well as a political will to support this movement. The sudden appearance of a new and potentially profitable market has caused a bubble similar to the appearance of the Web, with the daily creation of companies and start-ups trying to take advantage of this new opportunity.

The majority of these satellites have a common need for mobility, for four different reasons:

- Positioning. Conventional launchers rarely offer the possibility of placing the satellite in the required orbit, this option being generally reserved for very large objects. Most small satellites are sent in clusters of several dozen or even hundreds, and therefore need their own means to get where they are needed.

- Maintainance of the satellite on station. The definition of space is generally fixed at the Karman line located at 100 km of altitude, but traces of atmosphere persist well beyond, and thus slow down by friction the objects in orbit. It is thus necessary for them to compensate this drag.

- Avoidance maneuvers to prevent collision. Still inconceivable a few years ago due to the immensity of space, collisions are now a reality with the increasing number of objects in orbit. For example, in early September 2019, an ESA satellite had to perform an avoidance maneuver against a satellite in the Starlink constellation.

- Deorbiting. At the end of its life, a satellite is usually left for its orbit to decay until it falls back into the Earth's atmosphere, where it is destroyed. In practice, this can take up to several years, during which time the satellite becomes an uncontrollable projectile endangering the existence of other satellites or astronauts in orbit. Some actors are already taking this problem into consideration and it is likely that in the future political decisions will be taken to require satellite operators to return them to the atmosphere at the end of their life. The opposite could lead to a chain reaction scenario like the Kessler syndrome, which would make it impossible to use low earth orbit for decades.

1.1.1 Notion of space propulsion

The law of conservation of momentum implies that an isolated system conserves its total momentum. Therefore, if we want to impart a velocity to an object in a given direction, it is necessary to shed something, to eject a mass in the opposite direction.
This is the case, for example, with means of transportation. An airplane absorbs the air at the front and then ejects it backwards with a higher speed. In these cases, the ejected particle has a negligible velocity before, and then a velocity opposite to the motion of the vehicle just after the reaction.
The case of a sailboat or a solar sail is similar, although the particles, respectively air molecules and photons, have a non-zero momentum relative to the sail before the collision. The total momentum of the vehicle and the substance on which the thrust occurred, called the propellant, remains constant before and after the reaction.
The main difficulty of space propulsion comes from the almost total absence of matter on which to push. The spacecraft is thus obliged to carry with it the propellant from the beginning of the

journey. The maximum gain of speed thus obtained, the ΔV, can be calculated with the help of the Tsiolkovsky equation :

$$\Delta V = V_e \times ln\left(1 + \frac{m_p}{m_{dry}}\right) \tag{1.1}$$

This formula links ΔV to the propellant ejection velocity V_e, to the mass of the unrefueled vessel m_{dry} and to the mass of the propellant m_p. The presence of a logarithm, which increases slowly, is easily understood. Indeed, to reach a high ΔV, the spacecraft has to carry with it a lot of propellants to eject. But the presence of this propellant consequently increases the total mass of the spacecraft, and thus decreases the efficiency of the thrust. To reach a high ΔV, it is thus necessary either to have a high ejection speed, or to carry an immense mass of fuel.
Nevertheless, in a chemical propellant, the energy that can be transmitted to the particles to accelerate them comes directly from the propellant itself, from the chemical bonds. The highest ejection velocity ever tested with a chemical propellant dates from the 1970s. It was a combination of lithium, fluorine and hydrogen, allowing ejection speeds of nearly 5.3 km.s^{-1} [5], but it is far too complex to implement for practical use. In practice, the mixture of liquid hydrogen and liquid oxygen (LOX/LH2), used for example in the Ariane 5 rocket or the SLS, is the best possible option, with ejection speeds around 4.3 km.s^{-1}.
Taking this speed limit into account, several orders of magnitude can be established. With the objective of reaching the moon, more than 90% of the mass at lift-off of the SLS is the fuel (the majority of the remaining 10% being the mass of the tanks needed to hold this fuel). We can also look further into the future, and imagine interstellar travel. If we want to reach the nearest star, Proxima Centauri, in less than 1000 years of travel time, we need to achieve a spacecraft speed of 0.5 % of c, the speed of light. Tsiolkovsky's equation tells us that if we use the mixture LOX/LH2, to send a 350 ton spacecraft (the mass of an Airbus A380) we need to use about 10^{154} tons of fuel, which is much more than the mass of the known universe.

1.1.2 Spacecraft electric propulsion

Another solution appears in Equation 1.1. Instead of increasing the on-board mass, we can try to find a solution to increase the ejection velocity. We saw just before that the only solution consisted in injecting an large quantity of energy in a reduced mass. Naturally, this energy cannot come from chemistry, since it would be a mechanism similar to combustion, where the available energy would be proportional to the fuel mass. One of the most evident solutions is the use of solar panels. The energy thus recovered from the outside can be injected into a given mass of fuel. For example, with 10 m^2 of panel area in space, and a transmission efficiency of 20%, we get about P = 2700 W of available power. With the simple kinetic energy formula 1.2, we can determine that if this power is injected into a mass flow of $\dot{m} = 10$ mg/s, we can reach a theoretical ejection speed of more than $V_e = 23$ km.s^{-1} (typical orders of magnitude for electric propulsion).

$$P = \frac{1}{2} \times \dot{m} \times V_e^2 \tag{1.2}$$

This speed is far greater than anything achievable with chemical propulsion. Without going into the details of how this energy is injected into the fuel, which is the core of plasma electric propulsion, we can define a quantity for an thruster called *specific impulse*. Noted I_{SP}, its unit is the second, and it is defined as the time during which one kilogram of propellant is able to provide 9.81 N of thrust. It is also equivalent to the ejection velocity divided by g.

Thruster	**Power (W)**	**Thrust (mN)**	**I_{SP} (s)**	**Technology**
NANO R^3 (*Enpulsion*)	15 - 45	0.01 - 0.33	1500-5000	FEEP
NPT30-I2-1U (*Thrustme*)	35 - 65	0.3 - 1.1	2400+	Gridded ion
NPT300 (*Thrustme*)	200 - 500	8 - 12	1200 - 3000	
Spaceware™ - nano (*Exotrail*)	40 - 60	1.5 - 2.5	800	Hall thruster
Spaceware™ - small (*Exotrail*)	1000-1500	50 - 80	–	
SPD-100B (*OKB Fakel*)	1350	83	1600	
PPS-1350 (*Safran*)	1500	90	1660	
BHT-1500 (*Busek*)	1500	101	1700	
BHT-20K (*Busek*)	20000	1005	2515	

Table 1.1: *Comparison between different types of modern electric thrusters from different companies. It can be seen that the typical I_{SP} of a Hall thruster increases with its power.*

Although the I_{SP} of the electric thruster is much more larger than that of the chemical thrusters, the energy to be consumed is proportional to the square of the ejection velocity. This physical limit today prevents very large thrusts from being obtained, with the most powerful electric thrusters in use today delivering a thrust of the order of 1 N. It is thus impossible to use them to leave the surface of the earth, their use remaining confined to space. In the future, we can hope that the spatialization of powerful energy sources, like nuclear reactors, will be able to overcome this problem.

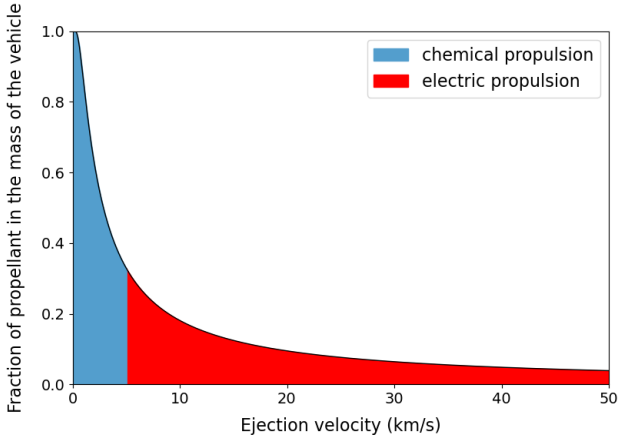

Figure 1.1: *Ratio of propellant mass to initial spacecraft mass as a function of propellant ejection velocity, for a* $\Delta V = 2$ *km.s*$^{-1}$*. The ejection velocity is limited to 5 km.s*$^{-1}$ *with a chemical thruster.*

The interest of this electric technology lies nevertheless in its fuel economy, since it allows a large reduction in the quantity of propellant required compared to chemical propulsion, for a given ΔV. The current price of a launch into orbit still being several thousands of euros per kilogram, the cost reduction made possible by the use of an electric thruster instead of a chemical thruster in orbit is evident.

1.1.3 Hall thruster operation

There are several electric thruster technologies, each with its own advantages and disadvantages. One of the most widely used is the Hall thruster (Hall-effect thruster), also called the Stationary Plasma Thruster (SPT).
They were first developed in the Soviet Union, through the work of Morozov [6] in the 1970s. Its potential was immediately understood and exploited, with the USSR sending a 450 W demonstrator, EOL 1, for the first time in 1971 aboard the METEOR-1 satellite [7, 8]. This first successful test was rapidly followed by the development of several other thrusters, including the well-known SPT-100, still in use today, and whose architecture has served as the basis for many thrusters, including the Safran PPS-1350 and the Busek BHT-1500. After the end of the Cold War and the fall of the USSR, the West became interested in these thrusters, and sent its first demonstrators into space in the early 2000s. One notable mission using a Hall thruster was the European probe SMART-1 in 2003 which was sent from Earth to lunar orbit using only 82 kilos of fuel.
The adoption of this technology is linked to its good performance for an electric thruster: more than 50% of the injected energy is transmitted to the particles, and its typical thrust of 100 mN for 1500 W is among the highest, allowing a reduction in the satellite's time on station. Nevertheless, it has a relatively high I_{SP}, of the order of 1500 - 2000 s.

On Figure 1.2, we can see that a Hall thruster is made of two ceramic cylinders, commonly of boron nitride, nested one inside the other, in order to create an annular channel a few centimeters wide. Inside these cylinders are placed magnets, sometimes coils, in order to create a radial magnetic field of a few hundred Gauss in the exit plane of the channel.
At the rear of this channel is the anode, generally polarized at a few hundred volts with respect

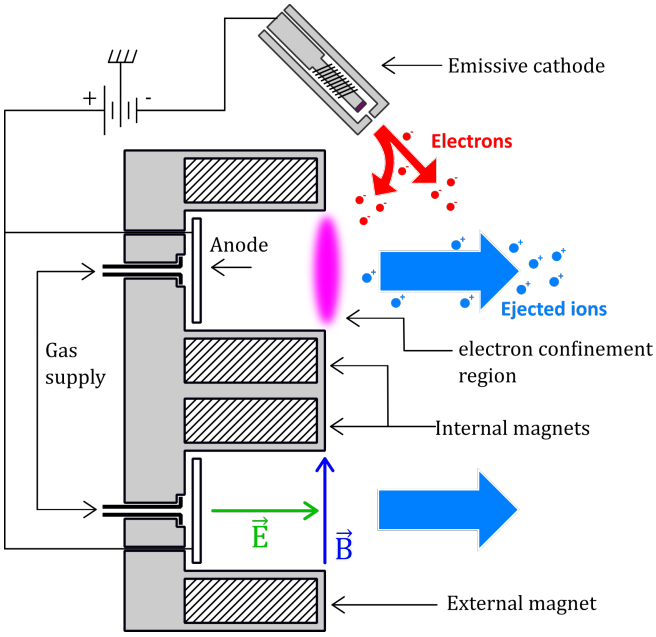

Figure 1.2: *Schematic of a Hall thruster seen from the side. The confinement of the electrons at the exit of the channel, combined with the presence of the anode at the rear of the channel, causes a potential drop that ejects the ions to the right at high speed. The electric field vector* **E** *and magnetic field vector* **B** *are shown in green and blue respectively.*

to an emissive cathode located outside the thruster. The cathode is a source of electrons for maintenance of the electric field and for neutralization of the ion beam. A gas, typically xenon, is injected at the base of the discharge channel, near the anode, at a rate of a few milligrams per second.

At start-up, before the plasma ignites, the electrons emitted by the cathode move towards the anode due to the potential difference. As they cross the exit plane of the channel, these electrons are trapped by the magnetic field lines and start to rotate around them. This increases their residence time, improving the probability of collisions with the xenon atoms from the back of the channel.

As a result of these collisions, some of the xenon atoms become ionized, emitting in turn electrons which are confined by the field lines. The value of the magnetic field has been chosen to magnetize the electrons and not the ions, because of the latter's higher mass. The Larmor radius of the electrons is of the order of a millimeter, while that of the ions is of the order of a meter, well above the size of the channel.

Increasing the number of electrons in this magnetic confinement zone causes a local potential drop. The resulting axial electric field, perpendicular to the radial magnetic field, causes the development of a force in the azimuthal direction, which affects the electrons. The electron current created in the azimuthal direction is called the Hall current, and gives its name to the Hall thruster. Its main interest is to heat the electrons, in order to increase the ionization probability during electron-atom collisions.

Figure 1.2 shows the thruster in steady state. The electrons are confined in a torus-shaped volume at the exit of the channel, and heated by the Hall current. Their high residence time and energy allow them to efficiently ionize the atoms coming from the bottom of the channel, in a zone located just before the exit plane (ionization region). The positive ions newly created by the collisions form in a zone with a strong potential gradient due to the presence of the positive

anode and the electron bulk (acceleration area). They undergo acceleration towards the right of the scheme.
The force applied to the ions is equal to the force transmitted to the electrons, which is transmitted to the magnets through the field lines. Thus, the force applied to the ions is transferred to the body of the electric thruster, which pushes the thruster to the left on the schematic.

1.2 The planar magnetron

1.2.1 Plasma-assisted thin film deposition

Thin film deposition is defined as the deposition of a very thin layer of a material on the surface of a substrate, in order to improve its properties or to give it particular characteristics. The most evident application today is in electronics, for the manufacture of microprocessors, which requires the superposition of a large number of extremely thin layers. It is also possible to create thin layers in optics, to modify the transmission/relief properties of a mirror, a windshield or a pair of glasses, for example. It can be used for coating mechanical objects, to modify the surface properties, such as resistance to wear or corrosion.
The method used for deposition was long limited to gas phase deposition. This involves vaporizing an element in a vacuum for deposition on a substrate and this technique is known as thermal evaporation thin film deposition. Although very simple to implement, it is extremely limited. It requires the use of materials with low evaporation temperatures, and does not allow for very precise control of the thickness of the layer created on the substrate surface.
The improvement of vacuum techniques in the 1960s allowed the implementation of more efficient processes based on plasma sputtering. This technique makes it possible to eliminate previous limitations, by widening the range of usable materials, and allows control of the deposit with greater precision.

In order to understand the mechanism of a DC sputtering source, it is necessary to recall the mechanism of a classical discharge in a gas. A cathodic discharge consists of a very simple system. A conductive plate made of the material to be deposited is placed in front of a second plate acting as anode, and the substrate is placed on the surface of the anode, forming the cathode, and the whole is placed in a vacuum chamber. There is naturally a small amount of free electrons in the gas, for example because of the ionization due to the cosmic rays. Under the influence of the electric field between the plates, an electron is accelerated towards the anode, and collides on its way with the gas atoms. A certain balance must exist between the voltage, the distance between the plates and the atomic density in order to ensure not only that the electron collides with a gas atom, but also that the electron acquires sufficient energy before the collision to ionize the atom. If these conditions are met, we can define a first Townsend coefficient α, which reflects the number of electrons created by this first electron, before it reaches the anode. If this coefficient is greater than one, the two free electrons that remain after the ionization (the one present before the collision, plus the one that has been removed from the atom) will be able to restart the same mechanism. It will cause an exponential increase in the number of free electrons in the discharge, called avalanche. Redefining the α coefficient as the rate of increase in the number of electrons per unit length, we arrive at the equality:

$$\alpha = n_i \sigma e^{-n_i \sigma L \frac{E_i}{qU}} \tag{1.3}$$

where n_i is the atomic density, σ the electron-atom collision cross-section, L the distance between the electrodes, and U the applied voltage. E_i is the ionization energy and depends on the gas.

Symmetrically, for each free electron created, a positive ion is also released in the discharge. This ion goes towards the cathode. If its energy is sufficient at the time of the impact with the cathode, it will extract a certain number of electrons from it, to replace those which were absorbed by the anode. The average number of electrons created at the cathode for each ionic impact is the second Townsend coefficient γ. The condition for maintaining the discharge, in order to preserve the existence of the plasma, is defined as follows:

$$\alpha L \geq \ln\left(1 + \frac{1}{\gamma}\right) \tag{1.4}$$

There is a value U_{min} called Paschen's minimum for the voltage necessary for the appearance of a discharge, depending on the conditions, in particular the pressure. If the voltage is increased beyond this minimum value, then the current follows, and this allows the charges to reorganize in order to obtain the appearance of a sheath in front of the cathode. Almost all the potential drop takes place in this sheath, as well as the ionization.
To achieve a DC sputtering source, it is necessary to ensure that the gas ions have enough energy so that in addition to extracting electrons from the cathode, they can also sputter the atoms from it. These are sprayed directly onto the substrate, where they are deposited to form a thin film layer.
The typical gas pressure in service are a few Pascals, with high constraints on the accessible range. In addition, the voltage required to establish this type of discharge is of the order of a few thousand volts, which makes its energy efficiency rather low. Other defects exist, such as an high heating of the substrate due to the electron current, as well as a lack of flexibility in the choice of the pressure range since the conditions of Paschen's law must be respected. Most importantly, the deposition rate is low, due to weak ionization.

1.2.2 Operating principle of a planar magnetron

There are some improvements that can be made to the plasma discharge configuration, to allow for better ionization and control. In particular, in order to overcome the limitations imposed by the Townsend discharge mechanism, it is necessary to increase as much as possible the number of ionizations per electron. A first step in this direction was made by Penning in 1936 [9]. In a cylindrical configuration, he proposed the addition of a magnetic field in this type of discharge, thus increasing the life span of the electrons by trapping them by means of the field lines.
Different configurations appeared during the following decades, until Chapin [10] proposed in 1974 the configuration known as the "planar magnetron", which is the most widely used today.
The planar magnetron consists of a planar cathode (target) at which the plasma is localized in a crossed-field configuration. The magnetic field is most commonly provided by permanent magnets behind the target.

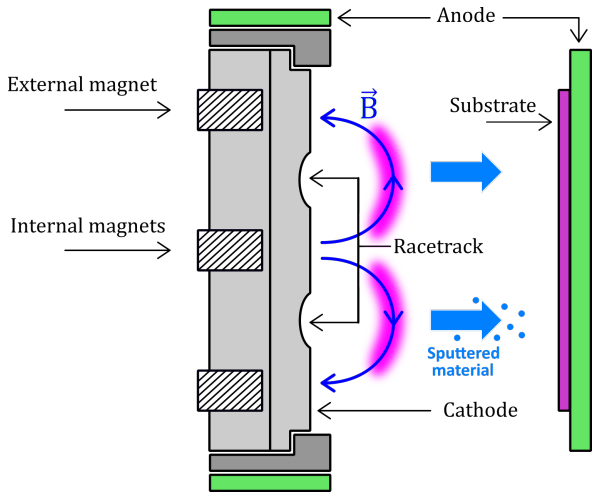

Figure 1.3: *Planar magnetron seen from the side. The anode has been represented here by a plate on which the substrate is deposited, but it is more often the walls of the chamber that have this function.*

Figure 1.3 shows a schematic of a planar magnetron. This figure shows the two most commonly-used anode configurations. The anode is either a plate located directly in front of the target, as in a DC glow discharge, or a guard ring located around it. In both situations, the anode is simply grounded, like the walls of the chamber, and the cathode is subjected to a relative negative potential of a few hundred volts.
In the same way as in a Hall thruster, the magnetic field traps the electrons in a cyclotron motion around the field lines, to which is added an azimuthal motion linked to the Hall current. On the other hand, unlike a Hall thruster, the magnetic field lines are not purely radial, but cross through the cathode. However, the electrons are reflected at the surface of the cathode by the sheath that forms there. This confinement zone delimited by the magnetic arc defines the area where the majority of the ionization occurs. The sputtering on the surface of the target is not uniform, and it is under this zone of ionization that we find the zone of maximum erosion, called the racetrack.
By overcoming the limitations of a Townsend discharge by means of a magnetic field, it is possible to work under more desirable conditions. In addition to requiring lower operating voltages, the pressure in the chamber can be lowered to less than one Pascal, compared to several Pa previously. This means that there are fewer collisions between the gas atoms and the sputtered target atoms, allowing them to conserve their energy. The much higher ionization level also allows acceleration

of the growth of the film on the surface of the substrate, of the order of several tens of nm/s, versus less than 0.1 nm/s with a DC glow discharge.

1.2.3 Continuous mode (DCMS) and pulsed mode (HiPIMS)

A magnetron can operate in different modes, depending on the nature and properties of the coating to be applied. The continuous (DCMS) or unipolar pulsed (HiPIMS) modes are interesting in the case of a metal deposit, and are the ones that are closest to the operation of a Hall-effect thruster. This discussion will voluntarily leave aside the other modes, for example the radiofrequency or bipolar pulsed modes, preferred for electrically insulating thin films. It should be noted that this mode of operation, alternating negative and positive pulses, enables the positive charges accumulated on the film surface during the first phase to be eliminated, through the bombardment of electrons during the second phase.
The direct current magnetron sputtering (DCMS) mode was the first to be developed. As its name suggests, it involves the application of a DC voltage between the cathode and the anode. It allows a high film growth rate. However, although DCMS operation takes place at a lower pressure than a simple DC glow discharge, the majority of the ions that reach the substrate surface come from the gas, reducing the quality of the thin film. It would be possible to correct this problem by increasing the operating voltage and current, but in this case one would be limited by the power the target can receive before melting. The electron density is therefore relatively low, on the order of 10^{15} - 10^{17}m^{-3} [11].

An alternative is the implementation of the HiPIMS mode (high-power impulse magnetron sputtering). Introduced in 1999 by Kouznetsov [12], the principle is to operate at high power for periods of typically a few tens of microseconds, at a frequency ranging from a few Hz to hundreds of Hz. This allows operation at much higher power, up to several thousand watts per cm^2, while limiting the heating of the target. The ionization levels reached are consequently higher, with densities up to 10^{20} m^{-3}. The majority of the atoms reaching the substrate are thus ionized, which allows a better control of the deposition. In addition, HiPIMS operation allows the pressure in the chamber to be lowered. In comparison to the DCMS mode, the majority of the ions that reach the substrate come from the target and not from the gas, which improves the mechanical properties of the thin film and its adhesion. The disadvantage of the HiPIMS regime is its lower duty cycle, about one percent, which consequently decreases the film growth rate compared to DCMS.

1.3 Electron drift in the E×B configuration

The two technologies just described, a Hall thruster and a planar magnetron, are both E×B discharges. This is a configuration where the electrons are not only confined by the magnetic field, but also heated by an electron drift motion.
Consider an idealized situation, with a constant magnetic field. A charged particle with an initial velocity perpendicular to the magnetic field lines rotates around one of these field lines. The direction of the rotation can be determined from Lenz's law, which indicates that the effects are opposed to the cause that creates them. In this case, the direction of rotation depends on the charge of the particle, so that the local magnetic field created by the rotation of the particle opposes that imposed by the external system. By applying the law of dynamics, we can determine the rotation frequency and the radius of the orbit as follows:

$$\omega_c = \frac{|q|B}{m} \qquad \text{and} \qquad r_c = \frac{v_\perp m}{|q|B} \tag{1.5}$$

where m and q are, respectively, the mass and charge of the particle, and B the norm of the magnetic field. $v_\perp$ is the velocity perpendicular to the field lines, that is, the root mean square of the velocities along x and y. ω_c is called the cyclotron frequency, and the radius of the cyclotron orbit r_c is known as the Larmor radius.
In practice, such an orbit is not stable in time since the electric charge radiates by bremsstrahlung. This effect is nevertheless neglected hereafter. If an electric field is introduced perpendicular to the magnetic field, the rotating particles are influenced by it. At any point of the rotation around the orbit, positively charged particles are accelerated in the direction of the electric field, and the opposite for negative charges. The effect of the electric field is therefore a variation of the perpendicular velocity along the orbit. We see in the formula of the radius of Larmor the influence of the perpendicular velocity. The consequence is a compression of the shape of the orbit, from a circle to an oval (Fig. 1.4). It is this modification of the geometry of the rotation which induces a displacement in the direction perpendicular to the electric and magnetic fields. The drift speed of the center of the orbit, called E×B drift of the guide center, is given by :

$$\mathbf{v}_{E\times B} = \frac{\mathbf{E}\times\mathbf{B}}{B^2} = \frac{E_x}{B_y}\mathbf{e_z} \tag{1.6}$$

Note that this drift does not depend on the charge or mass of the particle considered. This can be easily understood by studying the formulas, and by noticing that the different linear effects compensate each other. On the one hand, the gyration frequency of an ion for example is lower than that of an electron, since it is inversely proportional to the mass. On the other hand, the Larmor radius is proportional to the mass. Thus, a heavier particle makes fewer orbits for a given time, but has a larger drift per orbit. The two effects compensate each other perfectly, and the particle drift speeds are identical.
Following the same principle, the acceleration due to the electric field is opposite for a proton and an electron, but the direction of rotation of these two particles is also opposite. The direction of the drift is therefore the same whatever the charge. The result is an identical drift for all types of particles, from the electron to the multi-charged ion. There is therefore no creation of current, only a global movement of the plasma in the E×B direction.
The situation is somewhat different in the plasma sources described above, namely a Hall thruster and a planar magnetron. In the former, the magnetic field in the ionization region is primarily radial, and its magnitude is chosen to magnetize only the electrons, to have a Larmor radius for the ions greater than the size of the system, of the order of several tens of centimeters. The E×B drift applies only to the electrons, causing a Hall current to appear. Such an effect can also

be obtained in a plasma where the ions are also magnetized, if the propagation of these ions is disturbed by collisions.
E×B plasma sources take advantage of this drift by using a radial magnetic field and an axial electric field. The resulting Hall current propagates in the azimuthal direction and loops back on itself. It heats the electrons with high efficiency, increasing the ionization probability in electron-atom collisions. This geometry is therefore preferred in plasma sources requiring a high level of ionization.

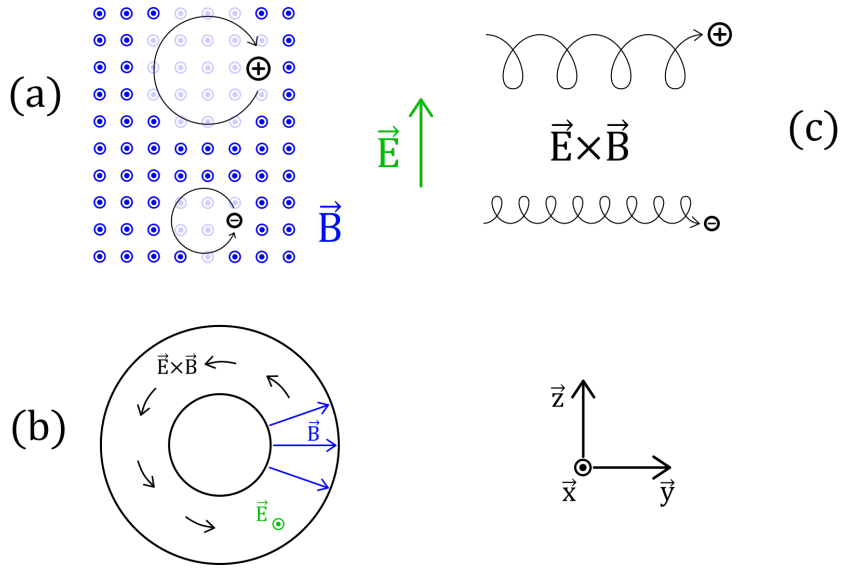

Figure 1.4: *In the presence of a magnetic field B, a charged particle whose initial velocity is perpendicular to the field lines orbits around them (a), in a direction that depends on its charge. The addition of an electric field E perpendicular to B causes a translational motion in the direction perpendicular to B and E (b), at the speed E/B. In the case of a cylindrical geometry (c), with a radial magnetic field and an axial electric field, the E×B drift is in the azimuthal direction, and continues without being stopped by a wall. The direction of this rotation is reversed if the E or B field is reversed.*

1.4 Classical electron transport

We have so far described the E×B sources as idealized electron traps, without taking into account any losses. In practice, a fraction of the electrons cross the field lines to reach the anode. This is why the cathode must not only provide electrons to neutralize the discharge, but also compensate for this loss in the confinement region (Fig 1.2). Several mechanisms can explain this phenomenon as we will see later, but we will start by studying the simplest transport, linked to the geometry of the source and to collisions [13, 14].
Consider the usual equation for the conservation of the momentum :

$$m_p n_p \frac{d\mathbf{v}}{dt} = q n_p \left[\mathbf{E} + \mathbf{V} \times \mathbf{B}\right] - \nabla p - m_p n_p \nu_m \mathbf{V} \tag{1.7}$$

where m_p is the mass of the considered particle, n_p the particle density, q its charge and ν_m the frequency of collision with the species able to modify its trajectory. The case study is the simplest possible configuration, at steady state, and assuming a zero pressure gradient. The equation for an electron can be simplified to the form :

$$\frac{-e}{m_e}\left[\mathbf{E} + \mathbf{v} \times \mathbf{B}\right] = \nu_m \mathbf{V} \tag{1.8}$$

We have set e as the positive elementary charge. According to Fig. 1.4, the electric field is taken to be purely axial in the $\mathbf{e_x}$ direction, the magnetic field purely radial in the $\mathbf{e_y}$ direction, and the azimuthal direction is defined by e_z.

$$\mathbf{E} = E_x \mathbf{e_x} \qquad \text{and} \qquad \mathbf{B} = B_y \mathbf{e_y} \qquad \text{and} \qquad \mathbf{V} = V_x \mathbf{e_x} + V_y \mathbf{e_y} + V_z \mathbf{e_z}$$

Projection in the e_x direction : $\frac{-e}{m_e}\left[E_x + V_z B y\right] = \nu_m V_x$

Projection in the e_z direction : $\frac{e}{m_e}\left[V_x B_y\right] = \nu_m V_z$

$$V_x = \frac{-eE_x}{m_e \nu_m}\left(\frac{1}{1 + \left(\frac{-eBy}{m_e \nu_m}\right)^2}\right) \qquad \text{and} \qquad V_z = \frac{eE_x}{m_e \nu_m}\left(\frac{\frac{-eBy}{m\nu_m}}{1 + \left(\frac{-eBy}{m_e \nu_m}\right)^2}\right) \tag{1.9}$$

These velocities reveal ω_c the cyclotron frequency (Eq. 1.5), compared to the frequency of collision of electrons with massive particles, ν_m. The ratio of these two frequencies is a dimensionless parameter β known as the Hall parameter, and can be interpreted as the number of orbits performed by an electron between two significant collisions. In conductive materials such as metals, the electron gas model gives β generally lower than unity. However, the principle of E×B plasma sources being to increase the residence time of the electrons and to heat them between two collisions in order to allow a high ionization rate, it is evident that the cyclotron frequency must be much higher than the collision frequency.

The collision frequency is written

$$\nu_m = n_n \sigma_{Xe-e} \overline{V} \tag{1.10}$$

with $n_n = 10^{19}$ m^{-3} the density of neutrals in the ionization area, $\sigma_{Xe-e} = \pi \times r_{Xe}^2 = \pi \times (108 \times 10^{12})^2 = 3.66 \times 10^{20}$ m^2, the effective cross section of hard sphere type momentum transfer between electrons and neutrals [15], and $\overline{V} = 1.9 \times 10^5$ m.s^{-1} the average velocity of an electron at 10 eV. Hence

$$\rightarrow \nu_m = 10^{19} \times 3.66 \times 10^{20} \times 1.9 \times 10^5 \approx 7 \times 10^6 \text{ s}^{-1}$$

$\omega_c = \frac{eB_y}{m_e}$ with $e = 1.6 \times 10^{-19}$ C the absolute value of the electron charge, $B_y = 250 \times 10^{-4}$ T a typical magnetic field value for the discharges considered in this work, and $m_e = 9.1 \times 10^{-31}$ kg the electron mass. This gives

$$\rightarrow \omega_c = \frac{1.6 \times 10^{-19} \times 250 \times 10^{-4}}{9.1 \times 10^{-31}} \approx 4 \times 10^9 \text{ s}^{-1}$$

$$\rightarrow \beta = \frac{\omega_c}{\nu_m} \approx 1000 >> 1$$

β is much higher than 1, which means that the drift movements have time to be established between two collisions. We can therefore rewrite the previous velocities :

$$\mathbf{V_x} = \frac{-eE_x}{m_e \nu_m} \left(\frac{1}{1+\beta^2} \right) \mathbf{e_x} \approx -\frac{E_x}{\beta B_y} \mathbf{e_x} \tag{1.11}$$

$$\mathbf{V_z} = \frac{eE_x}{m_e \nu_m} \left(\frac{\beta}{1+\beta^2} \right) \mathbf{e_z} \approx \frac{E_x}{B_y} \mathbf{e_z} \tag{1.12}$$

We find in the azimuthal z direction the guide center drift E×B which was evoked previously, causing the heating of the electrons (Eq. 1.6). It is independent of the collisions in the case where these are negligible compared to the cyclotron frequency. Moreover, in the axial direction x, an axial drift of the electrons appears. This drift results from the collisions, and disappears in the absence of them. It is this type of electron transport through the magnetic field lines that is expected, and therefore qualified as normal.

1.5 Anomalous electron transport

The axial current density J_x caused by collisions is therefore at least three orders of magnitude less than the Hall current density J_z which, in theory, should make the losses nearly negligible under standard Hall thruster or planar magnetron operating conditions:

$$|J_x| = \frac{|J_z|}{\beta} \tag{1.13}$$

However, in practice, the experimental measurement of this transport shows much higher values than expected in both Hall thrusters [16, 17] and planar magnetrons in HiPIMS operation [18, 19], but interestingly is much less common in DCMS mode [20].
Indeed, each electron that escapes from the confinement must be replaced by a cold electron, which decreases the efficiency of the ionization. But above all, this flow of electrons that diffuses through the field lines and reaches the anode causes an artificial and useless increase of the electric current to maintain the same discharge voltage. There are some areas where such a waste of energy has limited consequences, but it is unfortunately a critical point in the sectors we are interested in, namely space propulsion with Hall thrusters and the deposition industry for planar magnetrons.
There is still no complete and satisfactory explanation of this mechanism, although much progress has been made and many points identified over the last twenty years. For a long time, the only mechanism considered, notably by Morozov, was linked to the plasma-wall interaction, via a collision mechanism similar to what has already been mentioned, in which the wall would play the role of a massive particle with respect to the electrons: [21, 22, 23] (these articles are derived from older references, originally published in Russian [24, 25, 26]).
Nevertheless, it was determined that the role of the wall was not sufficient to explain all of the transport, and was not even responsible for most of it. In particular, Meezan [27] found that while the collisional model is sufficient to explain the transport between the anode and the B-field region, the anomalous transport is much larger, by several orders of magnitude at the B max-field region. He assumed that this was related to plasma fluctuations (observed by him and others at this location, [28, 29, 30]). This finding is also supported by the fact that anomalous transport has also been found in planar magnetrons, in spite of the absence of walls in this architecture.
The role of instabilities was further highlighted a few years later, in studies considering instabilities in the wall sheath, in the category of plasma-wall interaction [31, 32], but also by instabilities (generally referred to as turbulence), at the core of the plasma itself.

Among these instabilities, the role of the ECDI (Section 1.6.2) appears to be particularly critical and will receive specific attention in this work.

1.6 Classical instability in E×B sources

A large number of instabilities are present in magnetized plasmas. A brief and non-exhaustive discussion of just a few instabilities relevant to this work is made in this section. A more complete description of the existing set of oscillations and instabilities which might arise in the Hall thruster plasma can be found in Choueiri [33], and for planar magnetrons in Ehiasarian[34] although the two overlap.

1.6.1 Low frequency modes

Low frequency modes in this context will be considered to be those plasma modes whose frequency is of the order of kHz to a few tens of kHz. They do not represent specific wave types, but particular forms of large-scale plasma organization.

- **Breathing mode**

  This is an axial and complete oscillation of the plasma, at a frequency of the tens of kHz. It was thus named by Boeuf and Garrigues [1] because of the movement of the plasma periodically into and out of the discharge channel. Fig. 1.5 illustrates this periodic motion (visible via the plasma emission) in a 100 W Hall thruster.

  The historical hypothesis by Fife [35], and the one most often proposed, is a prey-predator model of an ionization wave, based on the Lotka-Volterra equations. The ionization in the discharge channel occurs at a higher rate than the gas flow can compensate, leading to a rapid depletion of the neutral density. The decrease of the neutral density leads to a displacement of the ionization zone towards the anode, in a zone where the electrons are less hot, and thus a decrease of the ionization rate. This lower ionization rate allows again the amount of neutrals to rise, bringing the ionization zone back to the exit of the channel, leading to a periodic phenomenon. Fig. 1.6 shows a numerical result from Boeuf and Garrigues showing the periodic oscillation in the overall discharge current which arises due to the breathing mode.

  Although historically observed in Hall thrusters, the breathing mode can also be found in planar magnetrons despite a more uniform gas pressure in the absence of walls around the source [36]. It is also interesting to note that there is a significant correlation between the breathing mode and anomalous transport [37, 38, 39] which may presumably be via its interaction with the electron cyclotron drift instability by varying the electric field.

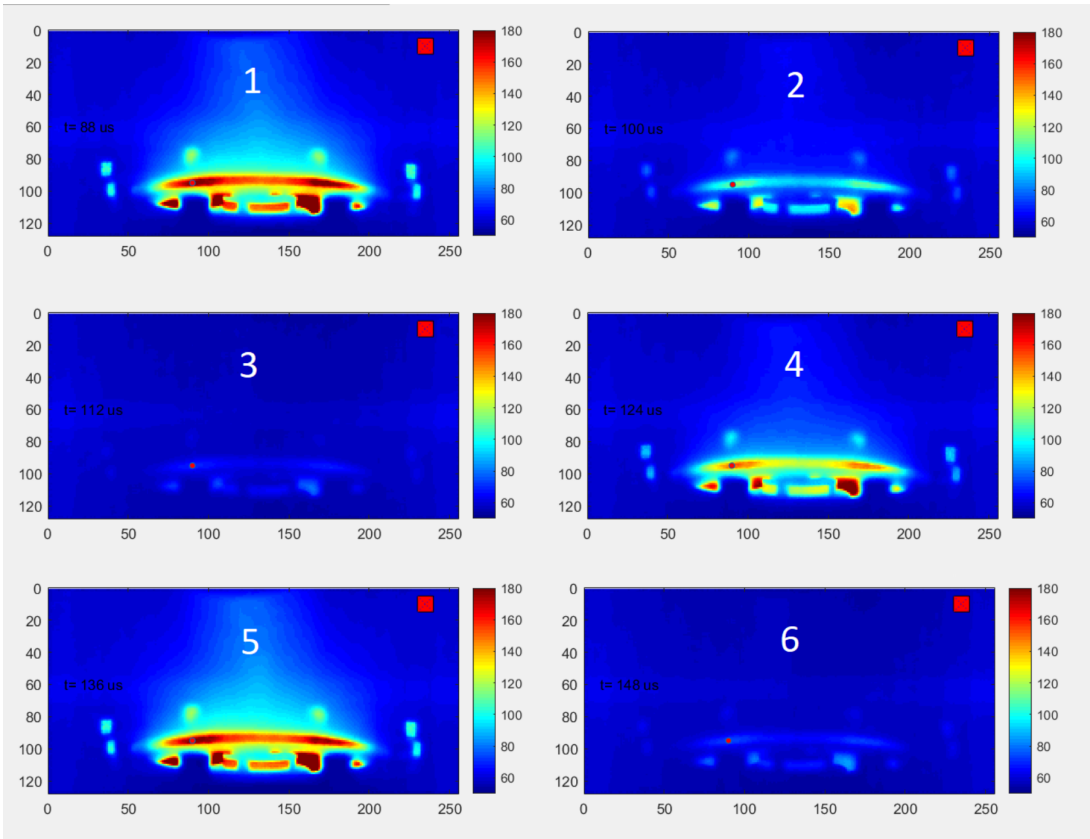

Figure 1.5: *Side view of the plasma emission oscillating with the breathing mode. These images were observed with a Phantom V1210 high-speed camera on a 100 W Hall thruster. With 12 µs between each image, the periodic movement of the plasma in and out of the discharge channel is clearly visible. The horizontal and vertical axes are labelled in pixels.*

- **Spokes**

Rotating spokes are structures characterized by a local increase in the density of the plasma, which moves perpendicular to the field lines, in the azimuthal direction. They are found in all plasma sources of E×B geometry, such as Hall thrusters and planar magnetrons, but also Penning sources and plasma columns[40, 41, 42, 43].
The term "spokes" has generally been applied to describe the appearance of large-scale enhanced ionization regions in these plasmas, grouping under the same name several different mechanisms that share the same visual effect, depending on the source.

Differences between the spokes created across a range of discharges exist. In a planar magnetron, the shape of the spoke depends on the material used for the target. Spokes most commonly appear to rotate in the same direction as the E×B drift, but a reversal in the direction of rotation, seen in planar magnetrons, may occur if the discharge power is reduced ([44, 45]). This direction of rotation appears to depend on the energy injected in the discharge [46, 47].

A number of hypotheses have emerged to broadly account for the appearance of such structures. They could result from the propagation of a uniform ionization front[48] linked to a very intense local electric field, as exists in plasma jets [49], or be linked to the charge

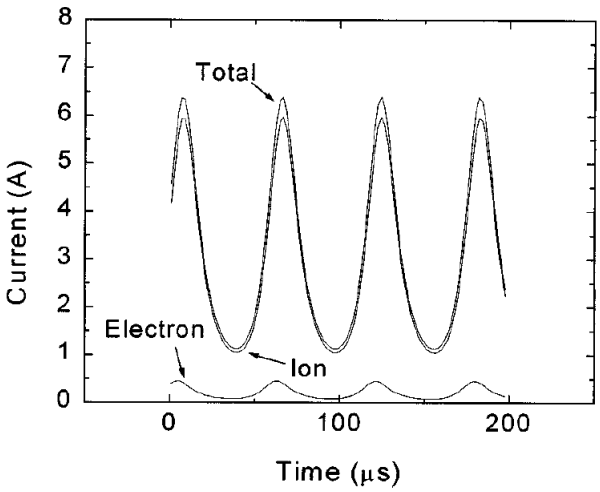

Figure 1.6: *Time evolution of the total current, electron current, and ion current at the exhaust in the SPT-100 Hall thruster for an applied voltage of 240 V and a xenon mass flow rate of 5 mg/s. A periodic oscillation of the discharge current caused by the breathing mode is observed, and reflected in both ion and electron currents. Image from Boeuf and Garrigues [1]*

separation caused by the modified Simon-Hoh instability [50, 51, 52]. Work by Kawashima and colleagues [53] pointed to spokes as being driven by a gradient-driven instability, with other works pointing to the role of the magnetic field gradient in sustaining the spoke [54].

The possible role of spokes in anomalous transport has been highlighted in recent studies[55, 56, 57].

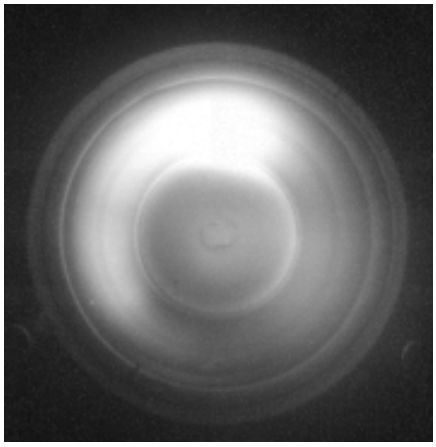

Figure 1.7: *Grayscale image of a spoke rotating in the azimuthal direction in a 200 W Hall thruster, recorded using a fast Phantom V1210 camera.*

The breathing mode and spoke have already been studied experimentally and numerically by other authors, and findings from such work suggest that both play a role in the anomalous transport that is still poorly explained. Theywill not be the main subject of this work, but their relevance is in their influence on the results of the measurements via their "smoothing" of the electron properties, as will be explained later.

1.6.2 High frequency instabilities

High frequency instabilities in this work refer to MHz-frequency instabilities. A range of types has been identified, including the modified two-stream instability and lower hybrid drift instability [58, 59, 60], primarily in numerical and theoretical studies, but this work will focus on two types identified experimentally, notable because their roles in anomalous transport are supported by recent numerical work.

1. **Electron cyclotron drift instability (ECDI)**

   The electron cyclotron instability propagates mainly perpendicular to the magnetic field, in the azimuthal direction in the E×B configuration (although it has been shown that it has components in all directions). It has been historically studied since the 1970s in the case of non-collisional shock waves in the magnetosphere [61, 62].

   The Earth's magnetic field interacts with the electric field created by the charge separation at the entrance of the magnetosphere. The ions are considered as not magnetized, because the characteristic times of evolution of the shock, and thus of the movement of the heavy particles, are fast compared to the ion cyclotron rotation velocity. The mechanism identified by Gary at the origin of this instability is a resonant interaction between an electronic Bernstein wave [63], and the more classical ion acoustic wave [64]. The frequencies of these are normally very different, and therefore unable to create this coupling. However, in a configuration allowing a relative movement of the electron with respect to the ions, the Doppler effect brings the frequency of the Bernstein electron waves towards lower frequencies.
   The first theoretical studies, in the magnetosphere [65, 66, 67, 68], as well the later work by Adam *et.al* [69] and Ducrocq [70] in the context of a Hall thruster, have focused on a one or two-dimensional geometry, in which the wave would have no component in the direction parallel to the magnetic field. The two waves can only be resonant at the same frequency, i.e. :

$$\omega_{n,Be} - \mathbf{k}.\mathbf{V} = \omega_{ia}$$

$$\omega_{n,Be} >> \omega_{ia} \quad \text{and} \quad \omega_{n,Be} \simeq \omega_c \quad \text{and} \quad \mathbf{k} = k_y \mathbf{e_y}$$

$$\rightarrow \; k_{n,y} \;=\; n\frac{\omega_c}{V_{E\times B}} \;=\; n\frac{\omega_c B_y}{E_x} \qquad \text{with } n = 1, 2, 3, .. \tag{1.14}$$

   where $\omega_{n,Be}$ and ω_{ia} represent the Bernstein and ion acoustic wave frequencies, with $\mathbf{k}.\mathbf{V}$ as the frequency shift resulting from the global drift at a velocity $\mathbf{V}$. The electron cyclotron frequency is ω_c.

   In this situation, the coupling of two stable waves gives an unstable solution for discrete values of wavenumber k, in resonance with the harmonics of the electron cyclotron frequency (with each of these resonances associated with a different integer value n).

   Nevertheless, in the case where a non-negligible component according to k_z exists, which implies a form of Landau damping according to Ducrocq and Bernstein [70, 63], the unstable modes are damped, and the dispersion relation tends towards one close to that of an acoustic ion wave.

The first direct evidence for the presence of the ECDI in thrusters, and for the significance of a non-negligible k_z component to the ECDI, emerged in experimental work (coherent Thomson scattering) by Tsikata [2]. This work also developed an updated linear kinetic theory dispersion relation reflecting all three wave vector components, showing that the presence of the k_z component would result smoothing of the unstable lobes (both real and imaginary frequency components). In related experimental studies performed by Tsikata, Honoré, Grésillon and Lemoine, [71, 72, 73], it was shown that a linear and continuous dispersion relation, akin to the ion acoustic wave, was a consistent observation.

This 3D dispersion relation was subsequently analyzed in some detail by Cavalier [3], who established numerical schemes allowing the investigation of various dependencies, such as the magnitude of the k_z component, allowing direct comparisons between the experimental results and theory.

The first direct correlation between the ECDI and anomalous electron transport was established in numerical particle-in-cell simulations in 2004 by Adam, Héron and Laval [69]. This seminal work was the first to tie, unambiguously and self-consistently, a particular instability to the phenomenon of anomalous electron current, and to identify the ECDI as a fundamental mode in thrusters arising from the fast electron azimuthal drift. Since then, the presence and role of this instability in transport have been investigated and highlighted by a large number of simulations, in both 1D and 2D, carried out by numerous groups worldwide [74, 38, 60, 75, 76]. Multiple linear kinetic theory studies have also analyzed the instability in the context of thrusters [77, 70, 78]. Very recently, Villafana *et al.* [79] developed 3D numerical simulations revealing the extent to which the consideration of the mode in 3D modifies growth and saturation of this instability.

2. **Ion–ion two-stream instability (IITSI)**

The term "ion-ion instabilities" encompasses a range of waves excited due to the presence of ion streams which are: (i) of different densities, (ii) formed from different ion species (originating from different atomic species), (iii) of different relative velocities, or, (iii) composed of different charge states of the same atomic species. Several examples have been analyzed theoretically and some experimentally identified, including in Refs. [80, 81, 82].

In thrusters and planar magnetrons, the name "ion-ion two-stream instability", or IITSI, was coined to refer specifically to a MHz-frequency propagating in the direction of the ion beam/stream.

The ion-ion two-stream instability was first detected and characterized during coherent scattering experiments to identify the ECDI [2], and the mode was simply described as an "axial mode", with a frequency on the same order of that of the ECDI plus an additional Doppler frequency shift thought to be due to the fast streaming ion beam.

In later work by Tsikata *et al.* [83], it was shown that the only possible agreement with experimental findings of the mode angular extent, dispersion relation and frequency was the consideration of a linear kinetic theory dispersion relation which included not only magnetized electrons and unmagnetized singly-charged ions, but also doubly-charged (xenon) ions.

Recent numerical results (Hara and Tsikata) demonstrated, for the first time, the excitation of both the ECDI and IITSI [76], confirming the original theoretical and experimental analysis demonstrating the origins of this instability. Perhaps more significantly, this work also showed that the IITSI influences anomalous electron transport via its coupling to the

ECDI, a new feature absent from all previous numerical simulations attempting to show the excitation of the ECDI in the presence of a single ion species plasma.

In the years leading up to the identification of this mode, planar magnetron studies in DCMS [84, 20] and HiPIMS [12] had provided evidence for anomalous electron transport across the magnetic field lines, and as with Hall thrusters, such transport was believed to be linked to the presence of azimuthal electric field fluctuations resulting on an axial force on electrons. The work of Lundin in 2008 was one of the earliest to make the case for instability-driven transport in planar magnetrons [85].

The new role of the IITSI, coupled to the ECDI, shows that the origins of anomalous electron transport are even more complex than originally imagined in both Hall thrusters and planar magnetrons. Additional analysis, considering now the presence of a population of triply-charged ions [86], shows a level of transport which can actually be attenuated in comparison to a plasma containing a combination of singly- and doubly-charged ions. Further studies on mode coupling appear to be necessary in order to understand the full range of phenomena affecting the global electron transport in crossed-field discharges.

The existence of these modes and their link with anomalous transport are well established, but they are particularly difficult to measure and identify experimentally, and even more difficult to simulate, as the coupling between them makes their description necessarily 3D. To establish hypotheses and validate simulations, very precise information on plasma properties and instabilities is required.

Chapter 2

Coherent and incoherent Thomson scattering diagnostics

Contents

2.1 Notion of Thomson scattering

2.1.1 Scattering principles

Scattering in the optical sense of the term is the deflection in one direction of a photon or a light beam by another particle, matter or a wave. It can be without modification of the energy of the photon, in which case we refer to elastic scattering, or on the other hand, be inelastic and cause a change in wavelength of the photon. It is generally necessary to distinguish between the cases where the scattering is made by matter, that is,generally by electrons bound to an atom or a molecule, and those where it is the result of the collision with a free or weakly-bound particle.
In the case of light-matter interaction, this thesis considers in particular Rayleigh scattering, a type of elastic scattering by electrons bound to an atom. From a classical point of view, a photon can be seen as an oscillating electric field, and thus an electron as a charged ball, electrically bound to the nucleus of its atom. When this field interacts with the electron, the latter rises above its orbit, excited by this field, and is then attracted back to the nucleus, re-emitting the same field that excited it, in a potentially different direction. For the plasma sources studied in this manuscript, Rayleigh scattering by the atoms of rare gases - helium, argon, krypton and xenon - are considered. This work also involves consideration of Raman scattering. This is an inelastic scattering mechanism in matter, caused by the interaction with vibrational states. Two shifts are observed, where the photon loses energy, so shifts to the lower-frequency range of the spectrum (called a Stokes shift) and where it gains energy, shifting to the higher-frequency range (anti-Stokes shift). Raman scattering is used for calibration with nitrogen in this work, crucial to determining the absolute electron density.

The other mode of scattering is scattering by free or weakly-bound charged particles (at a minimum, particles which are no longer bound after a collision), in this contex, the free electrons of the plasma. Compton scattering is the general term in this case, including inelastic cases caused by the ionization of an atom (electron stripping), but we will only encounter here and be concerned with the case where an electron is really free before the collision, i.e. a purely elastic scattering, the so-called Thomson scattering. Thomson scattering by ions is also possible, but largely ignored for Doppler reasons that we will discuss later. Broadly, the principle of scattering diagnostics (mainly Thomson scattering in this work) is to analyze the scattered light to find properties of the particles responsible for the scattering.

2.1.2 Observation angle

We have briefly discussed the different types of scattering in terms of energy modification and photon-particle collision mechanisms, but without mentioning the notion of direction until now. The scattered radiation is in fact only the electric field re-emitted by the oscillation of a charged particle, itself set in motion by the action of the coherent radiation emitted by the laser. Light being a transverse wave, and the laser radiation being polarized, this has consequences on the oscillation plane of the particle, and thus on the radiation that it re-emits in turn.
Let's start by writing the field emitted by the laser as simply as possible. We assume a monochromatic plane wave, linearly polarized, the electric field of which is represented by :

$$\mathbf{E_i}(\mathbf{r}, t) = \mathbf{E_{i0}} \exp\left[i\left(\mathbf{k_i} \cdot \mathbf{r} - \omega_i t\right)\right] \tag{2.1}$$

where $\mathbf{r}$ is the position vector of the point considered in space, E_{i0} the wave amplitude, $\mathbf{k_i}$ the wave vector in the propagation direction of the laser beam, and ω_i its angular frequency. We are mainly concerned here with Thomson scattering, and with scattering by free electrons in the plasma.

The individual energy of a photon of the laser is much lower than the mass energy of the electron, and thus the recoil of the electron due to the conservation of the momentum during the collision with the photon is largely negligible. The terms p_e, E_e, m_e, and V correspond to, respectively, the momentum, kinetic energy, mass and velocity of the electron, with p_p, and E_p representing the momentum and energy of the photon. The values h, c, λ, and ν represent, respectively, the Planck constant, the speed of light in a vacuum, and the wavelength and frequency of the photon, the following relations can be written:

$$\underbrace{\mathbf{p_{e,i}}}_{\text{momentum of the electron before the collision}} + \overbrace{\mathbf{p_{p,i}}}^{\text{momentum of the photon before the collision}} = \underbrace{\mathbf{p_{e,f}}}_{\text{momentum of the electron after the collision}} + \overbrace{\mathbf{p_{p,f}}}^{\text{momentum of the photon after the collision}} \tag{2.2}$$

$$|p_e| = |p_p| \tag{2.3}$$

$$\left.\begin{array}{l} p_p = \frac{h}{\lambda} \\ E_p = h\nu \end{array}\right\} \rightarrow p_p = \frac{E_p}{c} \qquad \left.\begin{array}{l} p_e = m_e V \\ E_e = \frac{m_e V^2}{2} \end{array}\right\} \rightarrow p_e = \frac{2E_e}{V} \tag{2.4}$$

$$\rightarrow \frac{E_p}{c} = \frac{2E_e}{V} \qquad \text{and} \qquad Ve = \frac{E_p}{m_e c} \tag{2.5}$$

$$\rightarrow E_e = \frac{E_p^2}{2m_e c^2} = \frac{(2.33 \text{ eV})^2}{9.1 \times 10^{-31} \text{ kg} \times (3 \times 10^8)^2 \text{ m.s}^{-1}} = 5.3 \times 10^{-6} \text{ eV} \tag{2.6}$$

The energy variation of the scattered photon due to the recoil of the electron is only 5×10^{-6} eV, much lower than the initial energy of the incident photon (2.33 eV), and negligible compared to the energy variation due to the Doppler effect due to the motion of the electron, of the order of 1 eV.

This is not always the case. For example, in the case of gamma photons involved in the Mössbauer effect, the individual energy of the photon is sufficient to have an influence on the momentum of the atomic nucleus, which slightly but measurably modifies the wavelength of the scattered photon.

Under the previous assumption, Ref. [87] tells us that the field $\mathbf{E_s}(\mathbf{x}, t)$ generated by an electron which undergoes an acceleration $\mathbf{a}(t)$, with ϵ_0 the vacuum permittivity and e the elementary charge, is of the form :

$$\mathbf{E_s}(\mathbf{x}, t) = \frac{-e}{4\pi\epsilon_0}\left[\frac{\mathbf{n} - \boldsymbol{\beta}}{\gamma^2\left(1 - \boldsymbol{\beta}.\mathbf{n}\right)^3 R(t')^2}\right] + \frac{-e}{4\pi\epsilon_0 c}\left[\frac{\mathbf{n}\times\left(\left(\mathbf{n} - \boldsymbol{\beta}\right) \times \frac{d\boldsymbol{\beta}}{dt}\right)}{\left(1 - \boldsymbol{\beta}.\mathbf{n}\right)^3 R(t')}\right] \tag{2.7}$$

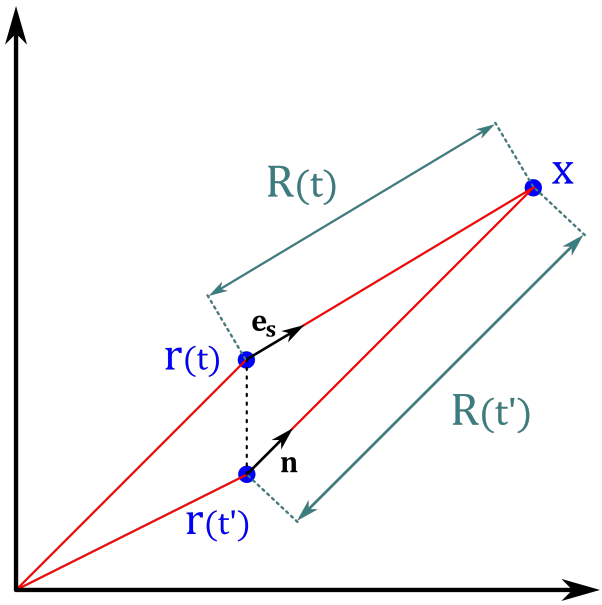

Figure 2.1: *Due to the finite propagation velocity c of an electromagnetic field in a vacuum, the scattered field measured at a point $\mathbf{x}$ at time t was emitted earlier at time t' by the electron at position $\mathbf{r}(t')$. During this time, the electron moves from position $\mathbf{r}(t')$ to position $\mathbf{r}(t)$. From the distance R between the position r of the electron and the position x of the detector, we can define the vectors $\mathbf{R}(t) = R(t)\mathbf{e_s}$ and $\mathbf{R}(t') = R(t')\mathbf{n}$.*

where $\mathbf{n}$ represents the unit vector in the $\mathbf{x}-\mathbf{r}(t')$ direction, as represented in Figure 2.1. Indeed, in a general case, to take into account the propagation of the electric field at the velocity c in vacuum, the field $\mathbf{E_s}(\mathbf{x}, t)$ must be calculated from the position $\mathbf{r}'$ of the electron at the time $t' = t - \dfrac{R(t')}{c}$, with thus $R(t') = |\mathbf{x}| - |\mathbf{r}(t)|$. This equation is relativistic, with the presence of the Lorentz factor γ, and $\boldsymbol{\beta} = \dfrac{\mathbf{v}}{c}$. However, since the electron's own velocity is very low compared to c, this leads to the approximations $\boldsymbol{\beta} \approx 0$, $\gamma \approx 1$, which allows Equation 2.7 to be rewritten as:

$$\mathbf{E_s}(\mathbf{x}, t) = \frac{-e}{4\pi\epsilon_0}\left[\frac{\mathbf{n}}{R(t')^2}\right] + \frac{-e}{4\pi\epsilon_0 c}\left[\frac{\mathbf{n} \times \left(\mathbf{n} \times \dfrac{d\mathbf{v}(t')}{dt}\dfrac{1}{c}\right)}{R(t')}\right] \tag{2.8}$$

A second simplifying hypothesis can be made. The scattered electric field $\mathbf{E_s}(\mathbf{x}, t)$ is collected by a detector placed at a distance $R(t)$ much larger than the motion of the electron $|\mathbf{r}(t)| - |\mathbf{r}(t')|$ during its oscillation. In the far field approximation, we can assume that $\mathbf{r}(t) \simeq \mathbf{r}(t')$, and thus $R(t) \simeq R(t')$. $\mathbf{n}$ is thus replaced by $\mathbf{e_s}$, the unit vector indicating the direction of scattering,

$$\mathbf{E_s}(\mathbf{x}, t) = \frac{-e}{4\pi\epsilon_0}\left[\frac{\mathbf{e_s}}{R(t)^2}\right] + \frac{-e}{4\pi\epsilon_0 c^2}\left[\frac{\mathbf{e_s} \times \left(\mathbf{e_s} \times \mathbf{a}(t)\right)}{R(t)}\right] \tag{2.9}$$

Equation 2.9 can be separated into two parts. The left-hand term can be identified as the electric field created in vacuum by a point particle at constant velocity in an inertial frame of reference. It is known as the electrostatic field, which decreases in R^2. The computation is not developed here, but it may be interesting to note that the difference between the left term of Equation 2.7 and the simplified Equation 2.9 is a magnetic field. We can therefore say that the nature of the magnetic field created by a moving particle is simply the effect of special relativity on its electric field. We are only interested in the term on the right, the one which expresses the acceleration $\mathbf{a}(t)$ undergone by the electron, the real scattered field. This decreases as a function of R, and is thus larger in the far field. We therefore consider

$$\mathbf{E_s}(\mathbf{x},t) = \frac{-e}{4\pi\epsilon_0 c^2}\left[\frac{1}{R\left(t'\right)}\mathbf{e_s}\times\left(\mathbf{e_s}\times\mathbf{a}\left(t\right)\right)\right] \tag{2.10}$$

Via the Lorentz force, the incident electric field creates an acceleration on the electron of the form $\mathbf{a}(t) = -\frac{e}{m_e}\mathbf{E}_i\left(\mathbf{r},t\right)$. The effect of the magnetic field of the incident beam on the electron trajectory is not taken into account, this being a factor c^2 weaker than the electric field. This would not have been the case if the electron velocity was comparable to c, but it has already been established that we are not in this configuration. The scattered field equation is rewritten as follows:

$$\mathbf{E}_\mathrm{s}(\mathbf{x},t) = \frac{-e}{4\pi\epsilon_0 c^2}\left[\mathbf{e_s}\times\left(\mathbf{e_s}\times\mathbf{E}_{\mathrm{i}0}\right)\right]\frac{-e}{R(t)m_e}\exp\left[i\left(\mathbf{k}_\mathrm{i}\cdot\mathbf{R}\left(t\right)-\omega_\mathrm{i}t\right)\right] \tag{2.11}$$

$$\mathbf{E}_\mathrm{s}(\mathbf{x},t) = r_\mathrm{e}\left[\mathbf{e_s}\times\left(\mathbf{e_s}\times\mathbf{E}_{\mathrm{i}0}\right)\right]\frac{1}{R(t)}\exp\left[i\left(\mathbf{k}_\mathrm{i}\cdot\mathbf{R}\left(t\right)-\omega_\mathrm{i}t\right)\right] \tag{2.12}$$

r_e is a physical quantity called the radius of the classical electron, which is 2.81 fm [88]. In reality, an electron is not a physical and compact object, but is regarded as a point without spatial extent, so there is no real meaning in referring to a radius. However, the definition of this quantity r_e is purely classical, and it can be seen as the minimum distance from which an electron starts to interact with an electromagnetic wave.

The power radiated per unit solid angle $\frac{dP_\mathrm{s}}{d\Omega}$ can be linked to the scattered fields as:

$$\frac{dP_\mathrm{s}}{d\Omega} = R^2(t)\epsilon_0 c\left|\mathrm{Re}\big(\mathbf{E_s}(\mathbf{x},t)\big)\right|^2 \tag{2.13}$$

$$\frac{dP_\mathrm{s}}{d\Omega} = R^2(t)\epsilon_0 c\, r_e^2\frac{1}{R(t)^2}\left|\big(\mathbf{e_s}\times\big(\mathbf{e_s}\times\mathbf{E}_{\mathrm{i}0}\big)\big)\right|^2\cos^2\big(i\left(\mathbf{k}_\mathrm{i}\cdot\mathbf{R}\left(t\right)-\omega_\mathrm{i}t\right)\big) \tag{2.14}$$

The power must then be averaged over time, as the detector is unable to measure fluctuations in the electric field whose period is several orders of magnitude shorter than the acquisition time,

$$\frac{dP_\mathrm{s}}{d\Omega} = \frac{1}{2}\epsilon_0 c\, r_\mathrm{e}^2\left|\mathbf{e_s}\times\left(\mathbf{e_s}\times\mathbf{E}_{\mathrm{i}0}\right)\right|^2 \tag{2.15}$$

Since the incident electric field is imposed by the laser, we know that the $\mathbf{E_{io}}$ vector is orthogonal to the beam propagation direction $\mathbf{k_i}$. It is therefore easier to rewrite Equation 2.15 as a function of the angles θ and ϕ defined in Figure 2.2, with $\mathbf{k_s}$ the direction of propagation of the scattered field:

$$\frac{dP_\mathrm{s}}{d\Omega} = \frac{1}{2}\epsilon_0 c\, r_\mathrm{e}^2\big(1-\sin^2\theta\cos^2\phi\big)\left|\mathbf{E}_{\mathrm{i}0}\right|^2 \tag{2.16}$$

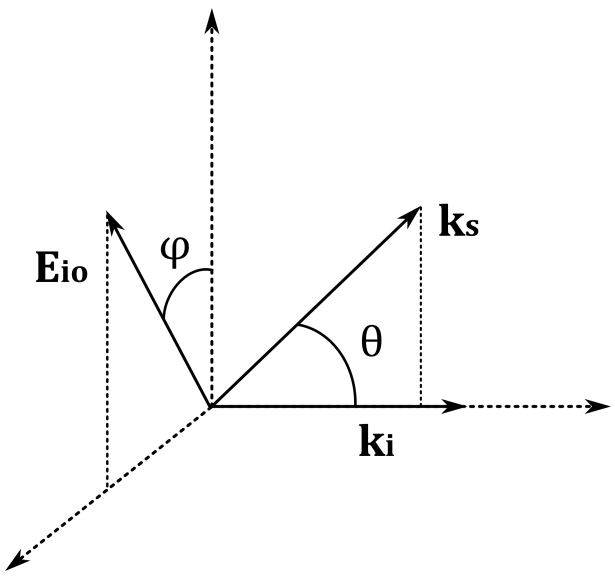

Figure 2.2: *The angle ϕ is defined as the angle between the polarization direction and the scattering plane, while θ is the angle between the laser propagation direction and the scattered direction.* $\mathbf{E_{io}}$ *is orthogonal to* $\mathbf{k_i}$ *(set by the laser).*

The intensity is the power transferred per unit area, and in the case of the diagnostic laser which is considered a monochromatic plane wave propagating in a vacuum, this laser power is written:

$$P_i = \int_S \mathbf{I} d\mathbf{s} = IA \qquad \text{where} \qquad I = \frac{\epsilon_0 c}{2} \left|\mathbf{E}_{\mathrm{i}0}\right|^2 \tag{2.17}$$

where A is the cross-sectional area of the laser beam. To obtain a variable that is easier to manipulate in the equations and independent of the system, we define the Thomson differential scattering cross-section σ_T :

$$P_s = P_i n L \sigma_T = P_i \frac{N}{A} \sigma_T \tag{2.18}$$

where P_s is the scattered power, n is the density of scattering particles, L is the length of the detection volume along the incident light beam, and N is the number of particles in the scattered volume.
Injecting Equation 2.17 into Equation 2.18:

$$P_s = \frac{\epsilon_0 c}{2} \left|\mathbf{E}_{\mathrm{i}0}\right|^2 N \sigma_T \tag{2.19}$$

$$\frac{dP_{\mathrm{s}}}{d\Omega} = \frac{\epsilon_0 c}{2} \left|\mathbf{E}_{\mathrm{i}0}\right|^2 N \frac{d\sigma_T}{d\Omega} \tag{2.20}$$

For a single electron ($N = 1$), we obtain the following result:

$$\frac{d\sigma_T}{d\Omega} = r_{\mathrm{e}}^2 \left(1 - \sin^2\theta \cos^2\phi\right) \tag{2.21}$$

Equation 2.21 gives the angular dependence of the scattered signal on the initial polarization of the laser beam. Figure 2.3 illustrates this angular dependence. As the angle between $\mathbf{E_{io}}$ and $\mathbf{k_i}$ is fixed by the laser (90°), particular care must be taken to maintain an angle of 90° between the electric field (polarization) and the direction of scattering (position of the observation branch). There are two cases that will be encountered later: one where $\mathbf{E_{io}}$, $\mathbf{k_s}$ and $\mathbf{k_i}$ are all positioned

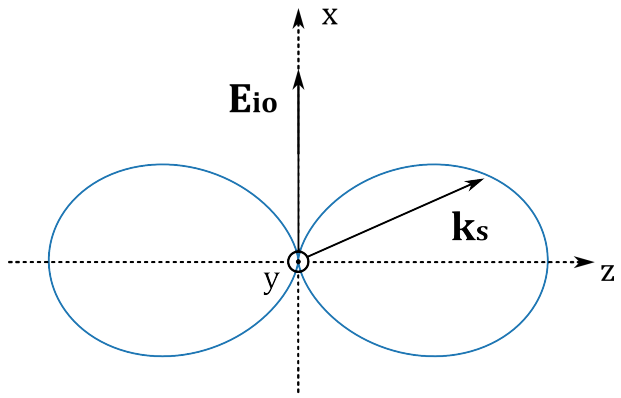

Figure 2.3: *Angular distribution of the differential Thomson scattering cross-section. The angles θ and ϕ have not been indicated on the figure, as it is rotationally symmetrical around* $\mathbf{E_{io}}$*, and* $\mathbf{k_i}$ *can be in any direction in the yz plane.*

at 90° from each other (THETIS), and one where the θ angle is varied while maintaining a ϕ angle of 90° (PRAXIS).
Note also that the Thomson differential scattering cross section can be defined in the same way for an ion. However, as the mass of the particle is present in the denominator of the classical radius definition, we can deduce that the field scattered by an ion is $(r_e/r_i)^2$ weaker, and therefore largely negligible.

2.1.3 Phase and probed wave vector k

The phase of the scattered wave is also relevant, for two reasons: as mentioned above, the photon does not have enough energy to significantly alter the electron's velocity during the collision. However, if the electron already has a non-zero velocity before the collision, this has a Doppler effect on the frequency of the re-emitted photon. The second reason depends on the distribution of electrons in the plasma. The individual scatterings of each photon add up and, provided they are coherent, interfere with each other. Naturally, if the distribution of electrons in the observation volume is random, the individual phases of each scattered photon interact randomly, constructively and destructively, without forming an interference pattern. On the other hand, if the electrons are organized, for example in the presence of a periodic oscillation of electron density, interference patterns may appear in the scattered signal.
First consider the Doppler effect, for an electron velocity $V << c$. The photon propagates in the $\mathbf{k_i}$ direction at velocity c, while the electron has a random velocity $\mathbf{V}$. During the "collision", the electron's own motion causes it to perceive a photon frequency slightly shifted by the Doppler effect, as $\omega_v = \omega_i - \mathbf{k_i}.\mathbf{V}$. So, if the electron velocity V has a component in the same direction as k_i (i.e. away from the photon), the perceived frequency is lower (red shift). On the other hand, if the electron is approaching the photon, the perceived frequency is higher (blue shift).
The same reasoning can be applied to photon re-emission by the electron, where the frequency is written $\omega_s = \omega_v + \mathbf{k_s}.\mathbf{V}$. The two Doppler effects are therefore cumulative, enabling us to define the probe wave vector (observation wave vector) $\mathbf{k} = \mathbf{k_s} - \mathbf{k_i}$. In Thomson scattering measurements (incoherent in this case), the electron properties measured by this Doppler effect, i.e. temperature and electron drift velocity, are therefore only measured along this $\mathbf{k}$ direction. By selecting different orientations for the observation wave vector, it is possible to observe any anisotropies in these properties.

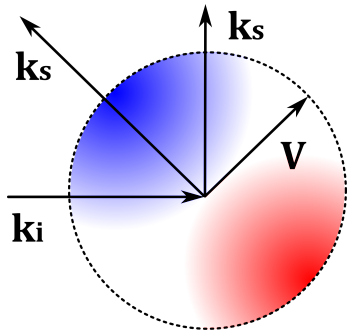

Figure 2.4: *Direction of probed vector (observation wave vector)* $\mathbf{k}$ *as a function of the position of the incident wave vector* $\mathbf{k_i}$ *and scattering wave vector* $\mathbf{k_s}$*. The colors on this figure indicate the effect of the direction of the vector* $\mathbf{V}$ *if it is aligned with* $\mathbf{k}$ *(blue shift) or if, on the contrary, it is opposed to it (red shift).*

Consider all the electrons, neglecting the Doppler effect and assuming for the moment that all the electrons are immobile. The total scattered electric field $E_s(\mathbf{r},t)$ is therefore the sum of the individual fields $E_N(\mathbf{r},t)$ of each of the N electrons, at positions $\mathbf{r_N}$:

$$E_s(\mathbf{r},t) \propto \sum_N E_N(\mathbf{r},t) \tag{2.22}$$

$$E_s(\mathbf{r},t) \propto \sum_N e^{i\left(\mathbf{k_i}.\mathbf{r_N}+\mathbf{k_s}.(\mathbf{X}-\mathbf{r_N})-\omega_i t\right)} \tag{2.23}$$

$$E_s(\mathbf{r},t) \propto \underbrace{e^{i(\mathbf{k_s}.\mathbf{X}-\omega_i t)}}_{\text{shared by all scattered photons}} \sum_N e^{-i\left(\mathbf{k_s}-\mathbf{k_i}\right).\mathbf{r_N}} \tag{2.24}$$

$$E_s(\mathbf{r},t) \propto \sum_N e^{-i\mathbf{k}.\mathbf{r_N}} \tag{2.25}$$

In the exponential, we again see the probed (observation) vector $\mathbf{k} = \mathbf{k_s} - \mathbf{k_i}$. All of the scattered signals interfere with each other. If the electron distribution is random, many of these fields will cancel each other out. On the other hand, if the electrons are distributed in regular planes perpendicular to the direction of $\mathbf{k}$, with a distance between the planes such that the scattered fields are out of phase by a multiple of 2π, then they will interfere constructively and amplify each other. This grating-like, planar arrangement of electron density is typically what is observed in the presence of plasma instability. The distance between two planes required for a constructive phase shift is given by $\lambda_K = \dfrac{2\pi}{k}$. It therefore depends on the angle θ between $\mathbf{k_s}$ and $\mathbf{k_i}$.
These Thomson scattering measurements, known as coherent or collective, can therefore be used to detect the presence of instabilities in the plasma, on several scales by varying the angle θ, and in different directions by varying the position of the plane (k_s,k_i) relative to the plasma source.

2.1.4 Two observation regimes and α arameter

There are certain considerations applicable to signal measurement in the incoherent and the coherent/collective Thomson regimes studied in this work. In order to obtain a laser beam with a high level of coherence, it is preferable to use a continuous laser rather than a pulsed laser. However, using a continuous laser means that the smallest time scale observable during a measurement is limited by the acquisition system, and not by the duration of the laser pulse. In addition, regular density fluctuations can only exist above the Debye length of the plasma λ_{De}, the scale at which charge screening guarantees plasma quasi-neutrality. To achieve coherent scattering, we therefore need a laser wavelength high enough to ensure that the λ_k distance is greater than this scale. This is in the infrared range for the plasma sources observed in this work. On the other hand, if we are interested in the individual properties of electrons without taking into account their distribution in space, a laser wavelength providing a λ_k considerably lower than λ_{De} is required, enabling thermal fluctuations of electrons to be perceived.

In short, the choice is between observing the coherent or incoherent Thomson scattering regime, and separate diagnostics targeting each regime are applied in this work. A parameter $\alpha = \dfrac{1}{k\lambda_{De}}$ is defined in relation to the plasma and laser properties [89], to determine which of these regimes we are in, i.e. coherent if $\alpha > 1$ and incoherent if $\alpha < 1$.

Two previously-developed diagnostics are used this work [2, 90]. For the incoherent regime (THETIS diagnostic), $\alpha = 0.005$, while for the coherent/collective regime (PRAXIS diagnostic), the value of α reaches 20. The next sections of this chapter detail the main features and implementation of the two diagnostics used. In the manuscript, the coherent/collective scattering regime will sometimes be abbreviated as the CTS regime, and the incoherent as the ITS regime.

2.2 PRAXIS

2.2.1 Heterodyne detection

A heterodyne detection scheme is implemented for the coherent scattering measurements using PRAXIS. Two beams are generated. The first, called the primary beam, is at the origin of the Thomson scattering mechanism. It comes directly from the laser and thus defines the direction of the $\mathbf{k_i}$ vector, as shown in Figure 2.5. It is not recovered at the detector and is stopped by a diaphragm after passing through the plasma. The second beam is called the local oscillator (LO) and is aligned in the $\mathbf{k_s}$ observation direction, as shown in figure 2.5. It is generated using an acousto-optical deflector (AOD) applied to part of the original laser beam, such that it has a slightly shifted frequency $\omega_{OL} = \omega_i + \omega_m$. The frequency shift ω_m is very small compared with the original frequency ω_i, to enable the newly produced photons to remain in phase with those scattered by the primary beam.

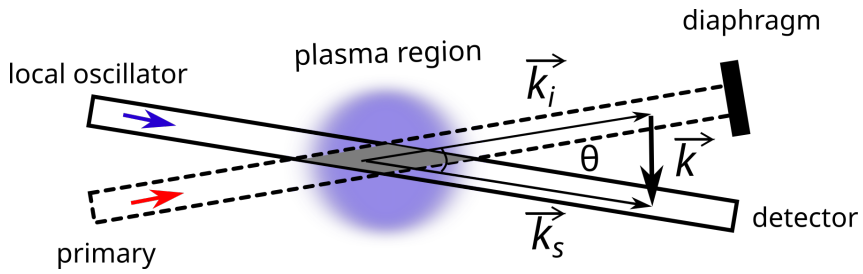

Figure 2.5: *Implementation of the crossing of the local oscillator (blue arrow) and primary beam (red arrow) in front of a plasma source on PRAXIS.* **k** *is the resulting probed (observation) vector.*

The principle of heterodyne detection is to amplify the signal received at the detector. The LO beam propagates in the $\mathbf{k_s}$ direction, and can therefore cause constructive interference with the scattered signal. The total signal propagating in this direction, i.e. the LO beam, the scattered signal plus the interference term, is then brought back to the infrared detector on the bench by a set of mirrors. Electronic processing is used to then filter the total signal received to recover only the interference term. At the end of processing, the interference term is separated into two parts: real $x_f(t)$ and imaginary $y_f(t)$, which are combined as follows:

$$S(\mathbf{k}, t) \propto \big(x_f(t) + iy_f(t)\big) \tag{2.26}$$

Naturally, to guarantee interference, the path length between the primary beam and the LO must be the same before they cross at the plasma.

2.2.2 Implementation of the optical bench

The complete development history of the PRAXIS optical bench, together with a detailed description of its operation and alignment procedures, are explained in Ref. [2]. A few main principles are recalled in this section.
The original laser beam is created using a 42 W CO_2 laser, horizontally polarized (Fig. 2.6). The initial beam is set to a height of 150 mm parallel to the optical table using a periscope (M1 and M2). An L1 lens is used to focus the beam just before the entrance to the CR ceramic tube, whose role is to improve beam quality. A beam splitter (BS) then separates the beam into two parts. The blue part of the beam enters the AOD, to emerge as a local oscillator with a modified frequency, as explained in the previous section. It is then recollimated by the L3 lens, then guided by a set of mirrors to the L5 lens.

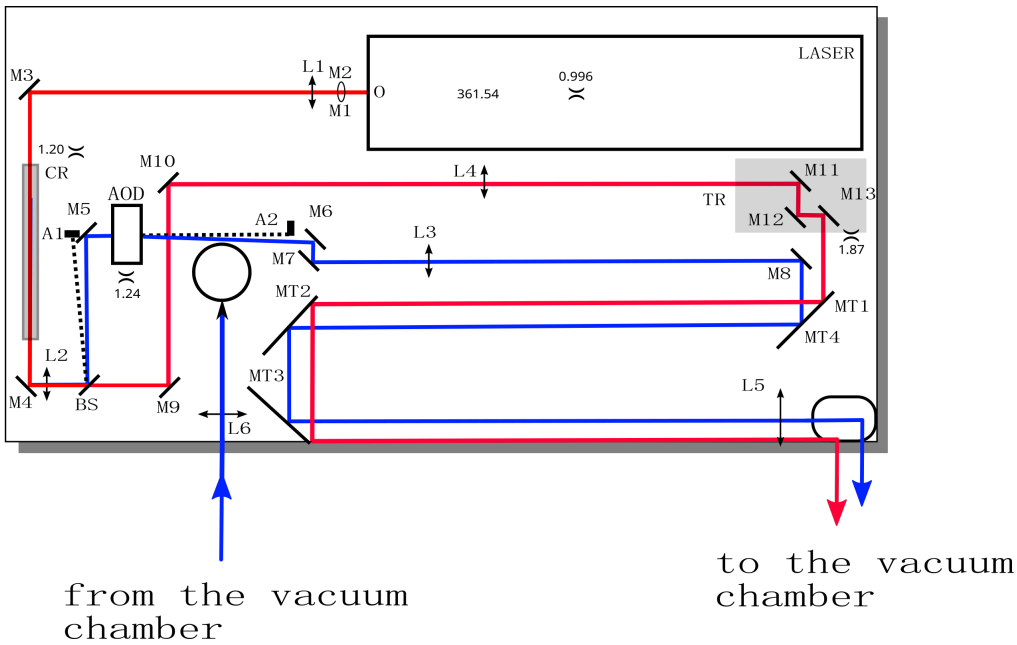

Figure 2.6: *Configuration of optical bench elements on PRAXIS. The OL is in blue and the primary in red.*

The primary beam is shown in red, and is sent to the translator rotator (TR) by a set of mirrors after the BS. This TR has two functions. The first is to allow rotation of the primary beam around the LO, in order to move the position of the (k_s,k_i) plane relative to the plasma source, as explained in section 2.1.3. Its second role is to change the separation between the primary beam and the LO. Varying this separation alters the angle θ between k_s and k_i, and consequently, the observed spatial dimension $\lambda_k = \dfrac{2\pi}{k}$. This operation is performed using a vernier ranging from 3.24 mm to 48 mm, thus enabling a range of exploration from k = 3841 rad.m^{-1} to k = 14226 rad.m^{-1}. The primary beam is then carried to the L5 lens, and sent to the vacuum chamber. This lens, with a focal length of 2 m, allows the beams to intersect at the plasma core, where scattering takes place.
The observation volume V_s, i.e. the volume formed by the intersection of the Gaussian primary and local oscillator beams, each of waist ω_a, is defined by :

$$V_s = \frac{\pi^{3/4}\omega_a}{4\theta} \tag{2.27}$$

Beyond the vacuum chamber, the primary beam is blocked by a diaphragm, and the LO is sent to the IR detector on the optical table using a series of mirrors.

2.2.3 Signal processing

The LO signal is focused at the end of the path onto a HgCdTe detector sensitive to wavelengths from 8 to 12 μm, and cooled by liquid nitrogen to limit thermal noise.
Three values are recorded by this detector, the *cos* (real component of the scattered signal), called XA, the *sin* (imaginary component of the scattered signal), called XB, and the detector current, with I its mean value. Total acquisition time is 65 ms, or 6.5 million samples at an acquisition frequency of 100 MHz. For each measuring point, several types of recordings are made, with *cos*, *sin* and current acquisition channels recording for each measurement. The recordings are made with different combinations of laser beams and plasma present or absent:

- A : LO + Primary + plasma ON + background noise
- B : LO + plasma ON + background noise
- C : LO + Primary + background noise
- D : background noise (detector closed)

A normalization process is performed. First, the average level of signals XA and XB is adjusted to zero by subtraction, to eliminate any vertical offset between the channels. Next, the amplitude of these two signals is normalized by the mean current value. Finally, the standard deviation σ of each of these periodic signals is extracted, and they are adjusted relative to each other, to correct any differences added to the signals by the respective electronic processing.

$$XB = XB \times \frac{\sigma_{XA}}{\sigma_{XB}} \tag{2.28}$$

The spectral density signal from signals A, B, C and D, $\Psi(\mathbf{k}, \omega)$, is determined using a Fourier transform.
The spectral density signal due solely to plasma scattering, $\Psi(\mathbf{k}, \omega)_{plasma}$, is written:

$$\Psi(\mathbf{k}, \omega)_{plasma} = \left(\Psi(\mathbf{k}, \omega)_a \times I_a^2\right) - \left(\Psi(\mathbf{k}, \omega)_c \times I_c^2\right) \tag{2.29}$$

where subscripts a and c denote the acquisition conditions A and C listed above.
The photon noise, originating from the LO and plasma, but without Thomson scattering, is given by:

$$\Psi(\mathbf{k}, \omega)_{photon} = \left(\Psi(\mathbf{k}, \omega)_b \times I_b^2\right) - \left(\Psi(\mathbf{k}, \omega)_d \times I_d^2\right) \tag{2.30}$$

where subscripts b and d denote the acquisition conditions B and D listed above.
The normalized spectrum is obtained from:

$$\Psi(\mathbf{k}, \omega)_{norm} = \frac{\Psi(\mathbf{k}, \omega)_{plasma}}{\Psi(\mathbf{k}, \omega)_{photon}} \tag{2.31}$$

Finally, this spectral density signal is transformed into a physical quantity related to the measurement conditions:

$$S(\mathbf{k}, \omega_a) = \left(\frac{h\nu}{\eta P_p} \frac{\pi w^2}{\lambda^2 r_e^2} \frac{1}{n_0 l_s}\right) \Psi(\mathbf{k}, \omega)_{norm} \tag{2.32}$$

where h the Planck constant, ν the laser beam frequency, and r_e the classical electron radius. In the implementations of this work, η is the measured detector efficiency of 0.7, P_p the primary beam power of 42 W, ω_a the beam waist of 2.5 mm, l_s the scattering length of 50 mm (i.e., the plasma length across which the scattered signal is collected), and n_e is the electron density.

$S(\mathbf{k}, \omega)$ is known as the dynamic form factor, and represents the intensity of density fluctuations over a given frequency range, here -2×10^7 Hz to 2×10^7 Hz, a frequency that can be related to the spatial separation λ_k between the density planes.

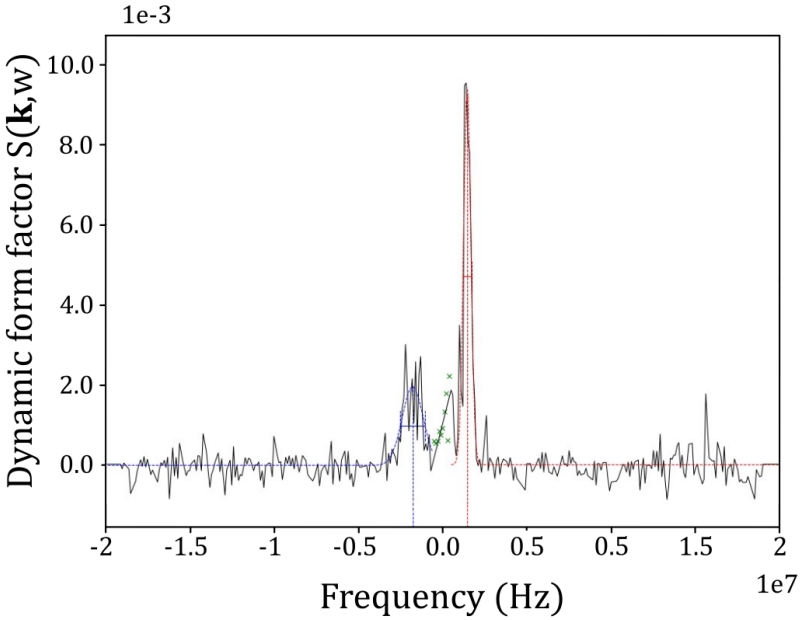

Figure 2.7: *Dynamic form factor $S(\mathbf{k}, \omega)$ with the observation plane aligned in the azimuthal direction. The signal variance is large in the case shown because this acquisition was carried out over a very short plasma pulse (100 μs), in contrast for example to the first spectra studied in Ref. [2]. In spite of this short duration, peaks of the scattering signal are clearly distinguishable from the noise.*

Figure 2.7 shows an example of a plot of the dynamic form factor (units of s) versus frequency. The positive peak represents density fluctuations measured propagating along the positive $\mathbf{k}$ direction, and the negative peak reflects density fluctuations anti-parallel to the $\mathbf{k}$ direction.
The static form factor $S(\mathbf{k})$ and the mean peak frequency are used to study the evolution of the fluctuation intensity. The unitless static form factor is obtained from the integration

$$S(\mathbf{k}) = \int S(\mathbf{k}, \omega) \frac{d\omega}{2\pi} \tag{2.33}$$

2.3 THETIS

2.3.1 Implementation of the optical bench

The background of the THETIS optical bench development, operation and capabilities is explained in Ref. [91]. In this section, only a few main principles are restated.

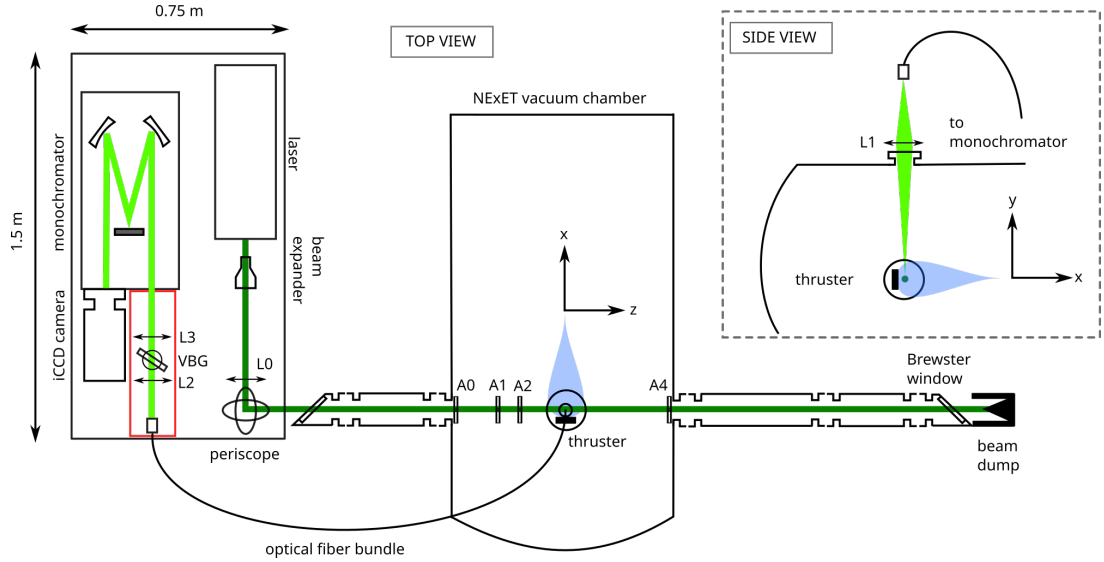

Figure 2.8: *Configuration of the THETIS bench installed on a Hall thruster, seen from above and from the side of the chamber.*

Laser beam path

A single laser beam is created, frequency doubled at 532 nm, with pulse FWHM of 8 ns, and pulse energy of 430 mJ at 10 Hz. Although the average power of this laser is lower than that of the PRAXIS CO_2 laser, the peak power of each pulse is much higher.

As seen in Fig. 2.8, immediately after emission, the beam passes through a beam expander that changes its diameter from 9 mm to 27 mm (reducing the divergence of the beam and improving its focusing). The L0 lens has a focal length of 2 m. A periscope is used to direct the laser into the vacuum chamber. The polarization of the laser must be carefully checked, as there must be a 90° angle between $\mathbf{k_s}$ and $\mathbf{E_{i0}}$. For example, in Figure 2.8, the laser is first emitted with a vertical polarization, and the polarization then is shifted horizontally before the laser enters the chamber. In this configuration, the observation branch must be positioned vertically above the plasma. On the other hand, if no periscope had been used, or if the table had been oriented at a 90° angle to its current position, the polarization would have been vertical and the observation branch would have had to be placed on the same horizontal plane as the laser beam.

After the periscope, the laser beam enters the chamber through a correctly polarization-aligned Brewster window, passes through the plasma in front of the source, then exits the chamber through a second Brewster window before being stopped by a beam dump. To minimize stray light collection inside the chamber, the windows are placed at the ends of tubes and apertures (A0, A1, A2, A4) are placed between these tubes and the chamber.

Observation branch

Incoherent Thomson scattering occurs at the intersection between the plasma and the laser beam. The beam is pre-focused using the L0 lens to achieve a minimum waist at this intersection. The observation branch is placed above the plasma and consists of a plano-convex lens and an optical fiber. The distance between the source, the lens and the entrance to the optical fiber is given by Descartes's conjugate relation :

$$\frac{1}{OA'} = \frac{1}{OA} + \frac{1}{f} \tag{2.34}$$

where OA' is the distance between the lens and the image, OA the distance between the lens and the object, and f the focal length of the lens.
The closer the lens is to the plasma, the greater the solid angle (which is preferred), but this is in some cases limited by the size of the chamber. The magnification effect must also be taken into account, so that the image width of the observation volume is less than the entry width into the fiber.
The collected light is sent to the bench using the optical fiber. The collected light has several components, namely the incoherent Thomson scattering signal, but also Rayleigh scattering and stray light, both at the same wavelength as the laser. In some cases, we also obtain fluorescence, but this particular case will be discussed in Chapter 4. These additional signals tend to overwhelm the weaker Thomson signal and it is necessary to remove or attenuate them.
To do this, we employ a filter (a volume Bragg grating, identified as VBG in the figure) [92], which attenuates a particular wavelength by as much as a factor of 10^4 if oriented at the correct angle with respect to the beam. The use of this element was the key innovation in the THETIS original design, enabling: (i) attenuation of stray light around the laser wavelength, (ii) the construction of a highly-compact diagnostic adapted to diverse implementations, and (iii) a minimization of photon losses compared to conventional systems using triple grating spectrometers. The use of this element has since been adopted by several teams worldwide for the development of new incoherent Thomson scattering diagnostics. The use of the lens L2 in front of the VBG is intended to produce a collimated beam required for correct filtering.

Scattered light processing

The remaining light after passage through the filter is sent to the lens L3 which focuses it onto the slit of a spectrometer equipped with three different gratings, of 300, 600 and 2400 lines/mm. The choice of grating used for each experiment depends on the temperature of the electrons studied. The higher the number of grating lines, the greater the spectral resolution, while the lower the number of grating lines, the broader the spectrum. Thus, 2400 lines/mm is preferred for low electron temperatures of a few eV, and 300 lines/mm for higher temperatures, up to several tens of eV. The dispersed spectrum is recorded using an iCCD camera triggered by the laser Q-switch to provide a very short acquisition window centered on the laser pulse, about 15 ns wide. Both spectrometer and camera are piloted with a computer used for selecting the spectrometer and camera acquisition settings. A typical Thomson spectrum is obtained over 6000 acquisitions (10 min at 10 Hz), from which is subtracted the plasma emission spectrum, also obtained over 6000 pulses in the absence of the laser.

2.3.2 Measurable electron properties

A typical Thomson spectrum is shown in Figure 2.9. It is a Gaussian broadening caused by the Doppler effect linked to the velocity of free electrons in the plasma. The effect of the Bragg

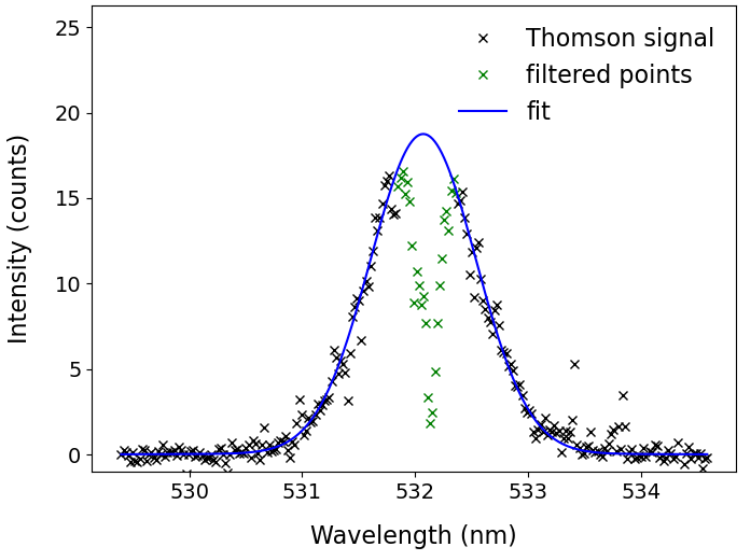

Figure 2.9: *Typical Thomson spectrum obtained with the 2400 lines/mm grating in this work. The Bragg filtered part of the spectrum is shown in the center of the spectrum (green crosses).*

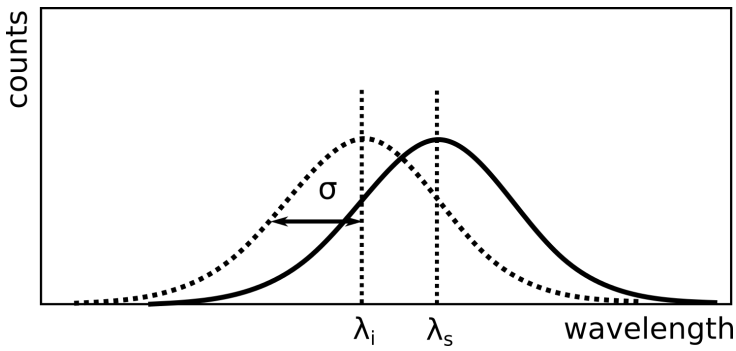

Figure 2.10: *Illustration of the scattered spectrum shift occurring in the presence of a global electron drift. The initial spectrum (dotted line, width σ) is centered at the incident wavelength λ_i and shifts to a new center at λ_s.*

filter at the center of the Gaussian spectrum, where all wavelengths immediately around the laser wavelength (532 nm) have been attenuated, is clearly visible. A fit is performed on this Gaussian spectrum, from which three properties can be extracted: electron velocity drift, electron temperature and electron density.

Electron velocity drift

A distinction is made between the notion of electron temperature along a vector, given by the amplitude of electron movement in any direction, and the notion of global electron drift, which indicates a preferential movement of electrons in one direction over another. The E×B drift described in the previous chapter is a good example, where we would expect to observe a global movement of electrons in the azimuthal direction. This movement is visible as a Doppler effect on the resulting spectrum. This causes a frequency shift in the same direction on all photons, and therefore a shift of the center of the Gaussian with respect to the laser wavelength. This phenomenon is illustrated in Figure 2.10, where the wavelength λ_i is that of the laser, 532 nm, and λ_s the position of the center of the Gaussian. The velocity drift can be calculated using the

formula :

$$\delta v = \frac{c(\lambda_s - \lambda_i)}{2\lambda_i \sin(\theta/2)} \tag{2.35}$$

Electron temperature

Through the Doppler effect, the random motion of the electrons causes the spectral broadening of the scattered light in the form of a Gaussian. So, with σ the standard deviation of the Gaussian, we can find the electron temperature:

$$T_e = \frac{m_e c^2}{4k_B}\Big(\frac{\sigma}{\lambda_i sin(\theta/2)}\Big)^2 \tag{2.36}$$

where k_B is the Boltzmann constant.
There is, however, a subtlety to be taken into account. Under the effect of the instruments, in particular the spectrometer and the slit width at its entrance, an additional spectral broadening effect will appear. The contribution of the optical components to this spectral broadening leads to the definition of an "instrument function" characterizing the setup. In order to quantify it, this instrumental function is recorded each time the acquisition branch is modified, for example, with re-positioned optics, changed spectrometer slit width, or even camera binning. The Bragg filter is aligned to allow stray light through, and a spectrum in the absence of any plasma or scattering is recorded. The spectrum, which in theory should be a Dirac delta function centered at 532 nm, has a broadening equal to the instrument function. Thus, for each electron temperature calculation, the Gaussian fit must first be deconvoluted by this normalized instrument function, otherwise analysis of the spectrum would give a slightly overestimated electron temperature, of the order of a fraction of an eV.

Electron density

The total scattered signal is made up of all the individual signals scattered by each electron in the observation volume. It is thus possible to calculate the electron density from the Gaussian integral (also deconvoluted by the instrument function). However, a number of factors related to experimental conditions are involved in this calculation, such as the size of the observation volume, the solid angle, the transmission quality of the optical fiber or that of the spectrometer. It is therefore necessary to carry out a calibration procedure to quantify all these elements in a single proportional factor called C1. Vibrational Raman scattering is used for this purpose. A known pressure of ultra-pure nitrogen is maintained in the chamber, typically 1000 Pa in this work, and a complete acquisition is then performed for the same duration as for Thomson scattering measurement, i.e. over 6000 pulses.

This Raman spectrum can be compared with a theoretical spectrum, calculated from the work of Penney [93]. The theoretical spectrum depends only on laser wavelength and temperature. By fitting the theoretical spectrum to the experimental spectrum, as shown in figure 2.11, it is possible to calculate the calibration factor C1 by proportionality. This C1 factor is then injected into the Thomson spectrum formula, enabling the determination of the electron density.

Error bar determination

The error bars on the electron properties are calculated from the combined uncertainties of a number of parameters. The overall uncertainty u_T on the electron temperature, density and drift velocity is given by

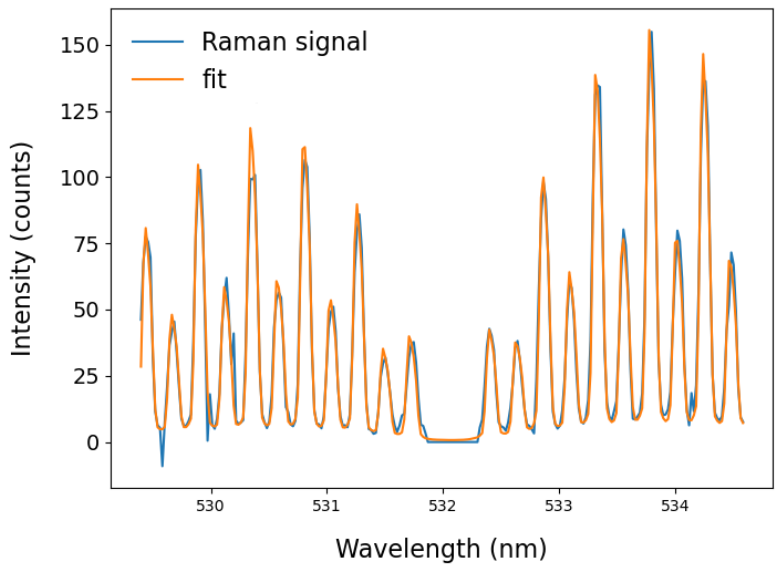

Figure 2.11: *Typical Raman spectrum obtained with a 2400 lines/mm grating in this work. The Bragg-filtered part of the spectrum is shown in the center. The fit gives a gas temperature of 298 Kelvin and an incident wavelength of 532.055 nm. The Raman scattering peaks do not appear as narrow lines due to the broadening caused by the instrument function.*

$$u_T = \sqrt{\sum_{n=1}^{n} [u_i(x_i)]^2} \tag{2.37}$$

where $u_i(x_i)$ represents the uncertainty on a parameter x_i on which the electron temperature, density and drift velocity depend in the measurement. The term $u_i(x_i)$ is calculated as the ratio between the absolute error on the parameter (Δx_i) and the determined value of the parameter x_i. For the electron temperature and drift velocity, two error sources can be identified on: (i) the standard deviation (the Gaussian width of the spectrum), and (ii) the center frequency of the spectrum. A fit of a Gaussian profile to the spectrum produces the optimized value of each parameter (x_i) and a covariance matrix specifying the absolute error Δx_i on both the standard deviation and the center frequency.
For the electron density, four sources of error can be identified, arising from:

(i) the manufacturer-specified precision of the pressure gauge, used during Raman calibration measurements at fixed chamber pressure, equal to 2%

(ii) the laser power variations during measurement, 8%

(iii) the area under the Gaussian fit profile, with absolute error determined from the covariance matrix generated by the fit to the data

(iv) the multiplicative (scaling) value used, following a fit to the Raman spectrum, to calibrate the spectrum area and transform it into an absolute number density of electrons. As with the Thomson spectrum fitting, the fit to the Raman spectrum generates a covariance matrix specifying the error on the scaling value.

Based on these combined uncertainties, the total uncertainties u_T on the electron temperature, density and drift velocity have been calculated. The error bars shown in the figures throughout this manuscript have lengths equal to twice the calculated total uncertainty.

Chapter 3

Investigation of electron dynamics and properties in HiPIMS

Contents

The most commonly used diagnostic for measuring electron properties in plasma sources is the Langmuir probe [94]. However, in recent years, the growing need for highly accurate electron measurements has led to the adoption of new measurement methods, in order to refine and guide simulation models [95]. Langmuir probes are unsuitable for this purpose, as they tend to interfere with measurement results, particularly in sources with strong magnetic fields. These new technologies include THz-domain spectroscopy, for example applied to HiPIMS electron density measurements by Meier *et al.* [96]. However, this new technique, although nonperturbative, has poor spatial resolution, averaging results over the magnetron width. Incoherent Thomson scattering is also of interest, offering both high spatial and temporal resolution. It has recently been applied to the study of the HiPIMS regime, the first measurements of this type having been published by Tsikata *et al.* [97].

Incoherent Thomson scattering measurements in HiPIMS have also been compared to Langmuir probe measurements in work by Ryan *et al.* in Ref. [98], where differences in the electron density measured by the two diagnostics were noted. In recent work by Law *et al.*, incoherent Thomson scattering has been applied to perform detailed characterizations of the bipolar HiPIMS regime in combination with optical emission spectroscopy [99]. These studies confirm the value of the incoherent Thomson scattering diagnostic for the non-invasive characterization of electron properties in the transient HiPIMS regime.

Another point concerns, as explained in the previous chapter, the directionality of incoherent Thomson scattering measurements. The ability to orient the observation wave vector in different directions permits probing of electron properties along the radial (along B) or azimuthal directions. This point in particular allows understanding of electron motion (global drift) parallel and perpendicular to the magnetic field, and the identification of possible anisotropies, which are expected to be a feature of the partially-magnetized plasma. The high spatial resolution of the diagnostic and its non-invasiveness also makes it possible to characterize the region inside the magnetic trap, a few millimeters from the cathode in the pre-sheath, a region for which few measurements exist. Results from this work will be used in subsequent chapters to enrich the linear kinetic theory models describing instabilities in this region.

The new experiments described in these analyses aim to provide a more complete understanding of the electron dynamics in different conditions. Results from different pulse conditions are examined, involving different gas types, peak discharge currents, and pulse durations. The evolution of the electron densities, temperatures, and net drift velocities are studied.

3.1 Implementation

3.1.1 Plasma source configuration

In this study, the DIVA chamber (*Dispositif d'Ionisation de la VApeur*) of the Laboratoire de Physique des Gaz et des Plasmas (LPGP) of the University Paris-Saclay is used. The use of this chamber is within the framework of an ongoing collaboration with the LPGP (T. Minea, C. Ballage). This chamber has been used in previous works and publications of our team [90, 100], including the first use of a Thomson diagnostic on a planar magnetron in HiPIMS configuration [97] and the first detection of the ECDI and IITSI in such a plasma [101].
DIVA is a cylindrical chamber, 430 mm high and 630 mm wide. During experiments with THETIS, tubes of 1000 mm long and 100 mm in diameter are attached to chamber, permitting (Chapter 2) a reduction in reflections from the windows propagating into the chamber and potentially to the region of light collection. In order to improve this attenuation, Brewster windows aligned with the laser polarization are installed at the end of the arms, and anodized aluminum apertures are inserted at the interface between the arms and the chamber, leaving only a hole a few millimeters in diameter for the laser beam to pass through and exit the chamber. The single probing laser beam traverses the chamber across the face of the planar magnetron, with collection of scattered light achieved with a detection branch positioned at 90° with respect to the initial beam line (Figure 3.1).
A vacuum is created in the chamber by means of a primary pump coupled to a turbomolecular pump, with this latter pump protected from the strong gas flow in the chamber by a butterfly valve. In the absence of gas, and with the valve fully open, the residual pressure in the chamber can be as low as 3×10^{-4} Pa.

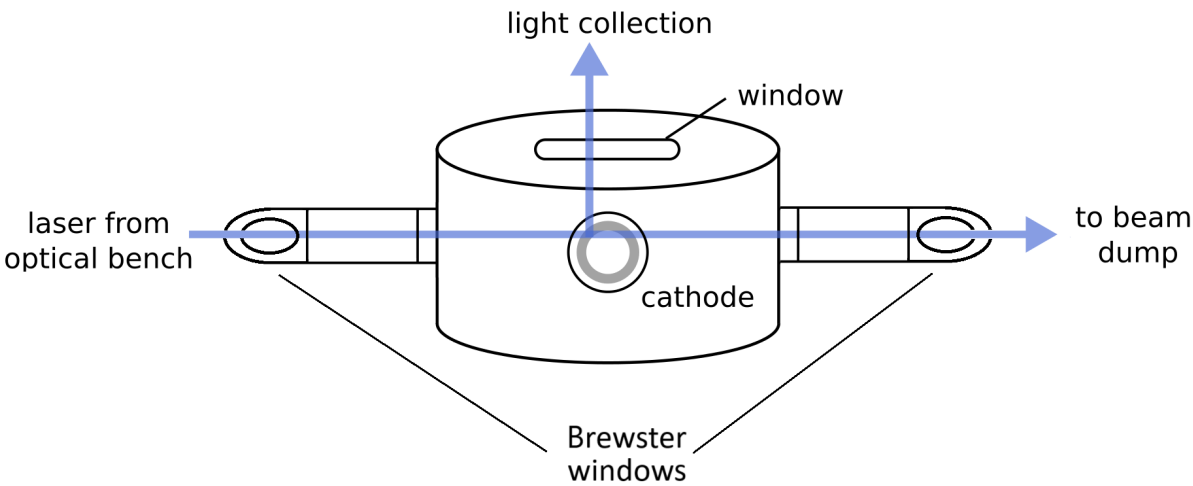

Figure 3.1: *Views (not to scale) of the basic configuration of the laser beam, cathode and chamber*

Two noble gases are used to create the plasmas investigated in this work. The first, argon, is most commonly used for experimental research and in industry for sputtering applications, due to its wide availability and low cost. The second gas, helium, is not conventionally used for thin-film deposition, as its mass is too low to cause sputtering in large quantities. However, the large mass difference between helium and argon allows an investigation of key differences in dynamics between the two gases.

The planar magnetron source used is a circular device equipped with a titanium target (purity 99.9%) of 100 mm diameter, and replaced for some of the high current measurements by a molybdenum target (purity 99.9%) of the same diameter. The cathode is positioned within a guard ring and maintained in place with a retainer plate. Compared to the previous publications [97], the thickness of this guard ring has been reduced to allow a closer approach between the laser beam and the target, to a distance of 3 mm versus 8 mm previously. Hereafter, and in order to avoid any confusion, the minimum distance to which we can approach is $z = 0$, defined as shown in Figure 3.2.

.

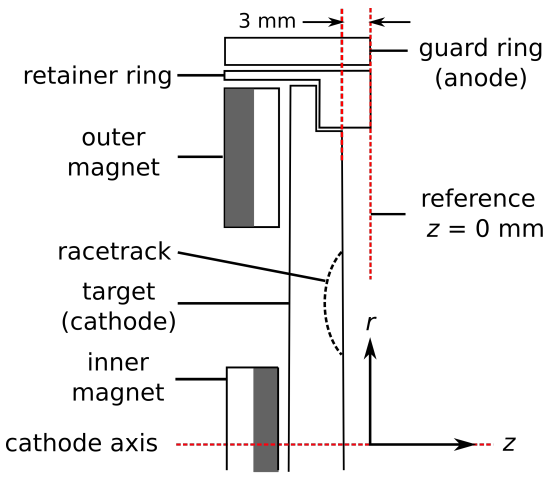

Figure 3.2: *Section view (not to scale) of the planar magnetron assembly used in experiments of this work. The arc-shaped area corresponds to the racetrack, the part of the target eroded by the plasma. The separation between the uneroded cathode surface and guard ring surface is 3 mm. The reference position $z = 0$ mm is taken to be the guard ring surface. The radial position r is measured with respect to the cathode axis.*

The source is equipped with several sets of permanent magnets whose position behind the target can be changed in order to modify the shape and balance of the magnetic field. Two balanced configurations are be exploited here, called C0E0 and C5E5, whose magnetic topology will be presented in the next section. Other configurations are possible on DIVA, a more exhaustive list of which is presented on page 69 of Ref. [91], but have not been used in this manuscript.
The source is powered by a custom DC power supply and a pulser. An applied voltage value is set such as to achieve a desired peak current value I_d when the plasma is on (these current values are shown in the tables of the experimental conditions considered in the following sections). For experiments performed, the laser pulse flashlamp is used as a trigger from which both the plasma initiation and the camera acquisition are timed. A digital delay generator (DG645, Stanford Research Systems) is used to vary the time at which the camera acquisition is initiated relative to the start of plasma pulsing, thereby allowing scattered photons to be collected at distinct temporal instants within the pulse envelope. Discharge current and voltage traces are recorded with a Teledyne Lecroy WaveRunner 625Zi oscilloscope, and using a LeCroy CP150 current probe.

3.1.2 Diagnostic configuration

A more extensive description of the THETIS diagnostic used was made in Section 2.3, and a complete description has already been published by [91]. This section is focused on the implementation of the diagnostic specifically for the planar magnetron study. Figure 3.3 shows the implementation of the light collection from the probe beam which traverses the plasma.

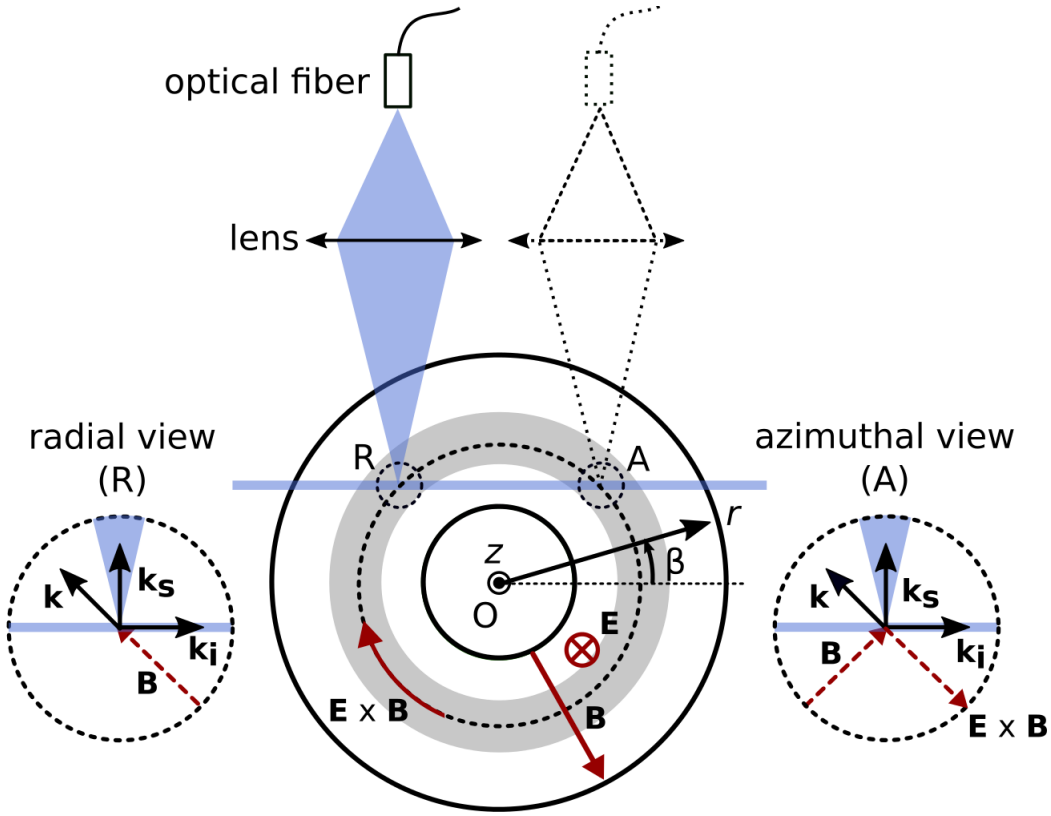

Figure 3.3: *Facing view of the cathode, illustrating how radial and azimuthal observations of the plasma, along the observation wave vector* $\mathbf{k}$*, are obtained. Here,* $\mathbf{k_i}$ *and* $\mathbf{k_s}$ *represent the incident and scattering wave vectors, respectively. The electric field (*$\mathbf{E}$*), magnetic field (*$\mathbf{B}$*), and* $\mathbf{E} \times \mathbf{B}$ *drift directions are indicated. The circles with dashed contours, labeled radial view (R) and azimuthal view (A), show the nature of the observation wave vector orientations at the different positions of the light collection and the corresponding magnetic field and the azimuthal drift directions. The lens and optical fiber are positioned directly above the positions R or A, as shown, for respective radial and azimuthal measurements. The racetrack region where the plasma is localized in depicted in gray. An (r, β, z) coordinate system is defined as shown.*

Looking at the target from the front in Fig. 3.3, the laser beam arrives from the left, and follows a path parallel to the target surface (z = constant) and parallel to the horizontal plane. The configuration of the periscope allows a rotation of the laser polarization, which is along the horizontal plane when entering the chamber, (evolving along the z direction). The detection branch is therefore placed on top of the chamber, in order to maximize the recovery of the scattered signal, as explained in Section 2.1.2. The $\mathbf{k_i}$ vector is directed in the direction of laser propagation,

while the $\mathbf{k_s}$ vector is perpendicular to it, and vertical, directed upwards. We choose a position of the detection branch with a magnification factor of 1. The observation volume is therefore a cylinder 1.5 mm long (imposed by the optical fiber) for a radius of 0.15 mm, (radius of the beam at the waist, limited by the quality factor of the laser), as in previous work on the same source.

In this implementation, a significant difference can be identified with respect to previous publications. We recall that the electron properties are measured in the direction of the observation wave vector $\mathbf{k} = \mathbf{k_s} - \mathbf{k_i}$. The measurements performed in previous work on HiPIMS placed the laser along the horizontal diameter of the target. In doing so, the probed vector $\mathbf{k}$ was aligned at an angle of 45° to the magnetic field lines in the observation volume, not allowing differentiation of the either purely radial or purely azimuthal directions.

In contrast, in the work presented here, the observation volume is aligned with the racetrack, but with the probing laser beam passing across the upper part of the target. Thus, the electron properties can be probed along the purely radial direction, or along the purely azimuthal direction, by moving the light collection assembly (lens and optical fiber) along the cathode face. This is depicted in Figure 3.3. In this figure, the laser beam and light collection are shown in blue and the racetrack region of the cathode is shown in gray.

Two positions on the racetrack, labelled R and A, show the points above which the collection optics (lens and optical fiber) are positioned to make radial and azimuthal measurements, respectively. The circles labeled "radial view" and "azimuthal view" are magnifications of the region showing the resulting direction of the observation wave vector $\mathbf{k}$. The electric field, magnetic field and E×B drift directions are indicated. At position R, the observation wave vector $\mathbf{k}$ points along the same direction as the magnetic field line. At position A, the observation wave vector points antiparallel to the E×B drift direction. In the (r, β, z) coordinate system shown, Oz points out of the plane and $z = 0$ mm corresponds to the guard ring surface. The radial position is indicated by r and the azimuthal angle β is measured with respect to the lateral axis. At positions A (azimuthal measurement) and R (radial measurement), β is 45° and 135°, respectively.

3.2 Spatial exploration

While this work will focus primarily on the variation of electron features as a function of time, the variation of electron properties with axial distance from the target is also of interest.
The spatial profile of the electron density during pulsed operation has a complex structure. This has been observed, for example, in temporal maps from Bohlmark *et al.* [102], which show the plasma, on initiation, forming an expanding torus which moves axially. The temporal behavior, at a fixed axial position, will be discussed in subsequent sections. Here, we show (Fig. 3.4), at a fixed time within the pulse, the axial variation in electron density. Plasma conditions correspond to those listed in Table. 3.1 and spectra are measured at a fixed instant ($t = 5$ μs before the end of the applied pulse). The observation wave vector is aligned with the azimuthal direction. The distance of closest approach of the laser beam center to the guard ring surface in these experiments is 2 mm (i.e., a distance of 5 mm between the laser beam and the uneroded cathode surface, according to Fig. 3.2).
A bi-exponential fit of the form

$$Y = A_1\, e^{-\frac{z}{l_1}} + A_2\, e^{-\frac{z}{l_2}} + A_3 \tag{3.1}$$

is applied to fit the data, where Y represents the electron density, and l_1 and l_2 the characteristic decrement lengths from the fit; A_1, A_2 and A_3 are values produced from the fit. The form shown

Ar - Axial variation				
PW (μs)	I_d (A)	U_d (V)	P (Pa)	z (mm)
70	40	-775 ± 1.9%	1	3 - 80

Table 3.1: *Conditions for argon axial investigations. PW and P represent the pulse width and chamber pressure, respectively. I_d and U_d represent the peak discharge current and peak discharge voltage, respectively.*

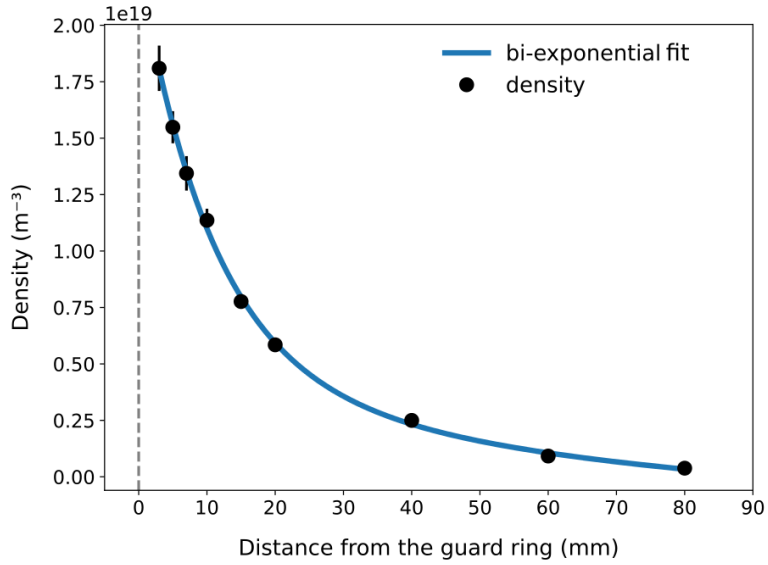

Figure 3.4: *Electron density variation with axial distance from the cathode guard ring. Measurements are carried out with the observation volume positioned for azimuthal observation (position A in Fig. 3.3). A bi-exponential fit (in blue) is applied to the data. The operating parameters used are 70 μs pulse width, 1 Pa Ar pressure, and peak pulse current of 40 A.*

in Eq. 3.1 captures the initial fast drop of the density in the region closer to the cathode, and the slower decrease observed at further axial locations. The values obtained for the l_1 and l_2 decrement lengths are 11 mm (for $z < 20$ mm) and 69 mm (for $z > 20$ mm). This evolution would be influenced by the plasma confinement (dependent on the magnetic field), and would be consistent with the existence of a region of high electron density and gradients close to the target (hence the steeper variation) at $z < 20$ mm, corresponding to the ionization region, and a less confined region (still within the magnetic trap) where the density variation is more gradual, for $z > 20$ mm.

The corresponding axial electron temperature variation is shown in Fig. 3.5. In contrast to the observations made for the electron density in Fig. 3.4, here a single exponential fit (in red) matches the variation in temperature, with a decrement length of 45 mm. **The combination of these observations in density and temperature suggests that, while the magnetic field configuration can produce different degrees of plasma confinement spatially (leading to different density decrement values with z), the underlying processes of energy exchange (which would influence the electron temperature) are similar over the full axial distance explored.**

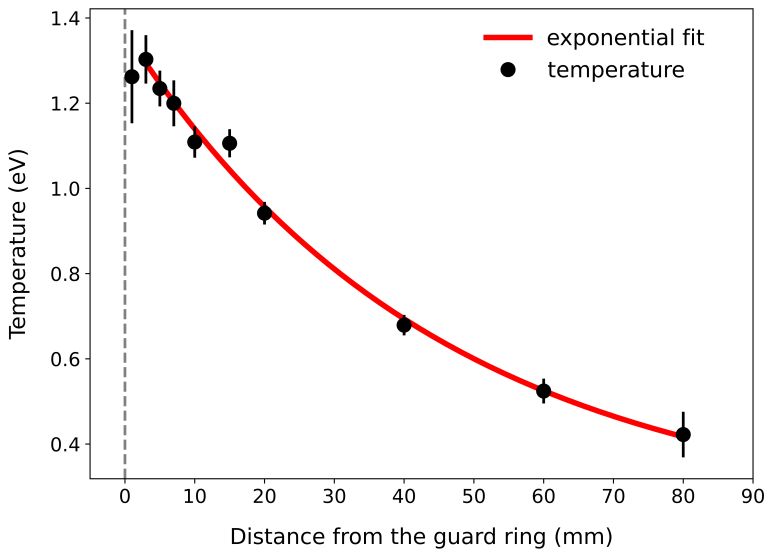

Figure 3.5: *Electron temperature variation with axial distance from the cathode guard ring. Measurements are carried out with the observation volume positioned for azimuthal observation (position A in Fig. 3.3). An exponential fit (in red) is applied to the data. The operating parameters used are 70 μs pulse width, 1 Pa Ar pressure, and peak pulse current of 40 A.*

3.3 Temporal exploration

In this work, a key focus is the measurement of the temporal evolution of the electron properties. A number of operating conditions have been selected to illustrate different temporal evolutions within the magnetic trap.

3.3.1 Temporal variation of electron properties: Ar - Condition 1 (peak discharge current 40 A)

Thomson scattering measurements are made for the conditions shown in Table 3.2, in the radial and azimuthal observation positions. The corresponding measured magnetic field map, determined with a magnetic probe, is shown in Fig. 3.6. The magnetic null point is shown with a green cross and is at the position $(r, z) = (5, 57)$ mm. The laser measurement position above the racetrack is shown with a green circle and is at the position $(r, z) = (28, 8)$ mm. The reference position $z = 0$ mm is, as before, the guard ring surface.

Ar - Condition 1					
PW (μs)	I_d (A)	U_d (V)	P (Pa)	z (mm)	B_r (mT)
70	40	-775 ± 1.9%	1	8	16.1

Table 3.2: *Conditions for argon temporal investigations (Condition 1). PW and P represent the pulse width and chamber pressure, respectively. I_d and U_d represent the peak discharge current and peak discharge voltage, respectively. B_r is the radial magnetic field measured at the center of the racetrack at $z = 8$ mm.*

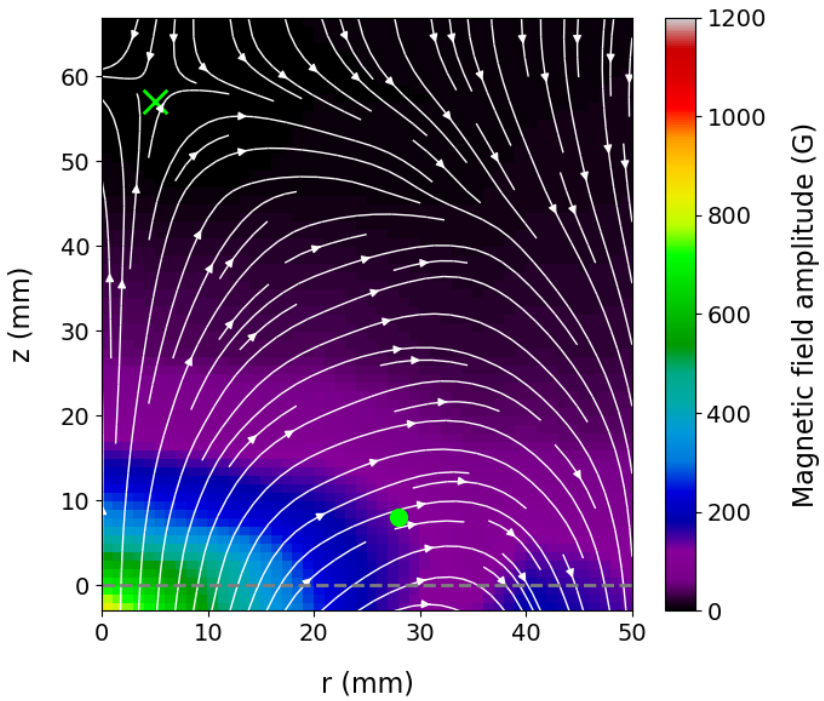

Figure 3.6: *Measured magnetic field map corresponding to Condition 1 (Table 3.2), as a function of axial (z) and radial (r) positions relative to the cathode. The magnetic null point is shown with a green cross and the laser measurement position above the racetrack is shown with a green circle. The reference position z = 0 mm is the guard ring surface.*

Figure 3.7 shows the current and voltage waveforms for these measurement conditions. After an initial oscillation at the start of the pulse, the discharge voltage reaches a peak value of -775 V and decreases to a plateau value near -500 V.

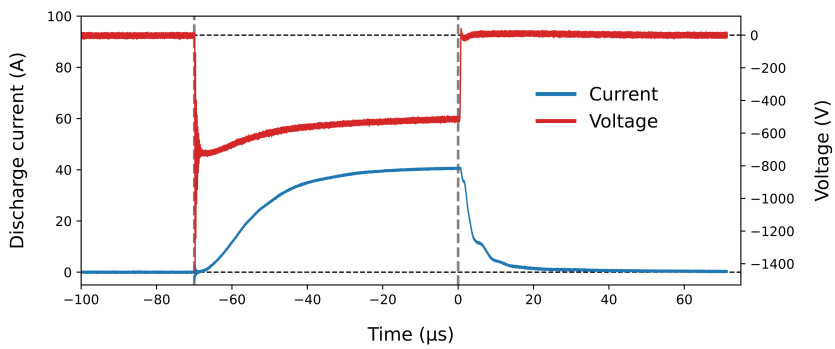

Figure 3.7: *Waveforms of the discharge current (in blue) and discharge voltage (in red) for Ar temporal investigations in Condition 1 (Table 3.2). The applied pulse duration of 70 μs is indicated by the gray dashed vertical lines.*

The density variation of Condition 1 is shown in Fig. 3.8, with radial and azimuthal points shown in black and red, respectively, and the current waveform in blue. As illustrated by Fig. 3.3, the "radial view" leads to electron properties measured along the radial magnetic field direction, achieved by positioning the lens and optical fiber to collect scattered photons from point R. The "azimuthal view" leads to electron properties measured anti-parallel to the E×B drift direction,

achieved by positioning the lens and optical fiber to collect scattered photons from point A.

In Fig. 3.8, near-identical values of the radial and azimuthal density are observed during the application of the pulse ($t \in [-70, 0]$ μs) and into the afterglow phase ($t \in [0, 100]$ μs). **This observation is consistent with the expectation that the electron density in the measurement volume be mostly uniform at the scales of the diagnostic volumetric resolution ($\sim$ 1 mm^3 in this implementation), regardless of the direction (radial or azimuthal) of the observation.**

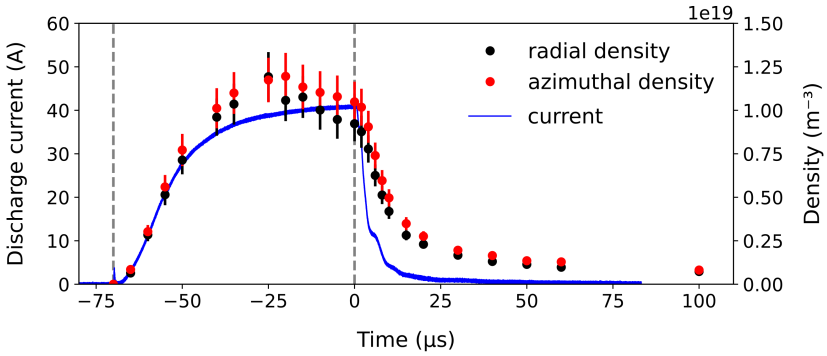

Figure 3.8: *Ar discharge, Condition 1: time evolution of the electron density, in radial (black points) and azimuthal (red points) observation directions. The current pulse waveform is shown in blue. Operating parameters correspond to Condition 1, summarized in Table 3.2. The vertical dashed lines indicate the instants of discharge initiation (-70 μs) and voltage cut-off (0 μs).*

It is also worth mentioning that while features such as spokes [103] may contribute to a potentially non-uniform electron density between the radial and azimuthal directions, the plasma would appear to be uniform at timescales on the order of the time resolution of Thomson scattering technique used (μs scale) and spoke-driven spatial variations would not be perceived.

In order to be able to link the measured electron properties with spokes, it would be necessary for the spokes to be generated in a reproducible way over the 6000 pulses from which a Thomson spectrum is derived. We have no evidence that spokes appear in this way, in spite of the excellent reproducibility of pulses. Variations in the localization of spokes from pulse to pulse, along the racetrack, would make it difficult to directly relate the measurements of these electron properties to the dynamics of electrons within the spokes.

The electron density can be measured from the moment of the discharge initiation (indicated by the vertical dashed line at -70 μs) to the applied voltage cut-off (indicated by the vertical dashed line at 0 μs), and far into the afterglow, where a Thomson scattering signal remains discernible 100 μs after the cut-off. **The presence of a significant electron density far into the afterglow phase indicates electron trapping within the magnetic field at the measurement position close to the target.**

The electron density profile also closely matches the shape of the discharge current profile. The ramp in current is associated with an increase in the electron energy, and an increase in the overall ionization of argon. For the parameters of Condition 1, the peak electron density is observed about 50 μs after discharge initiation, i.e., at $t \sim$ -25 μs in Fig. 3.8, before declining slightly as the current profile (in blue) tends towards a plateau. The observation of an electron density profile which closely matches the current profile is expected from predictions of the ionization

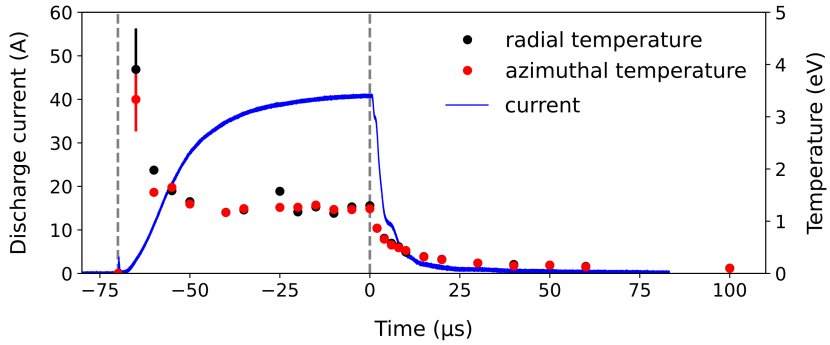

Figure 3.9: *Ar discharge, Condition 1: time evolution of the electron temperature for radial (black) and azimuthal (red) observation directions. The current pulse waveform is shown in blue. Operating parameters correspond to Condition 1, summarized in Table 3.2. The vertical dashed lines indicate the instants of discharge initiation (-70 µs) and voltage cut-off (0 µs)*

.

region model of Raadu and colleagues [104] and is similar to findings from experimental characterizations of electron properties in the HiPIMS regime made using experimental tools such as THz-domain spectroscopy [96] and Langmuir probes [105].

The electron temperature variation accompanying Fig. 3.8 is shown in Fig. 3.9. The radial (black) and azimuthal (red) values superpose, indicating an isothermal plasma for the conditions studied. There is an initial peak of temperature of 3 - 4 eV at the discharge initiation, followed by a plateau of $\sim$ 1.5 eV within the applied pulse and a gradual decline in the afterglow.

The evolution in electron energy has been studied by several authors using probes, typically several centimeters from the cathode (and thus, outside the magnetic trap and ionization region, unlike the present work). Such studies have found the generation of distinct electron populations during pulsing. According to Poolcharuansin and Bradley [106], there may be an initial generation of sheath-heated superthermal electrons (in the 100 eV range) on discharge initiation. Though we have the capacity to measure such high temperatures, and can obtain much closer proximity to the sheath with THETIS than is achievable with probes, the superthermal electrons are unlikely to be detected directly using incoherent Thomson scattering, due to their very low densities (in the range of 10^{13} - 10^{14} m^{-3} according to Ref. [106], whereas the lower limit of our detection capability was previously found to be 10^{16} m^{-3} (seen in Ref. [90])).

Generally, early on in the pulsing, electron populations reaching energies in the range of 5 eV have been observed (hot electrons were found in the range of 10 eV in Ref. [106]), with energies in the 1 - 10 eV range in the pulse, and a cooling of electrons to 1 eV and below in the afterglow region [105]. **In Fig. 3.9, the transition from the observation of warmer electrons at discharge initiation to electron cooling below 1 eV in the afterglow appears compatible with previous probe measurements.**

Probe studies have also shown the presence of bi-Maxwellian distributions for electron energies [107]. For all spectra used to plot the data of Fig. 3.8 and Fig. 3.9, only Maxwellian velocity distributions have been observed, but this does not rule out the presence of a secondary (lower-density) population of higher-energy electrons below the detection threshold.

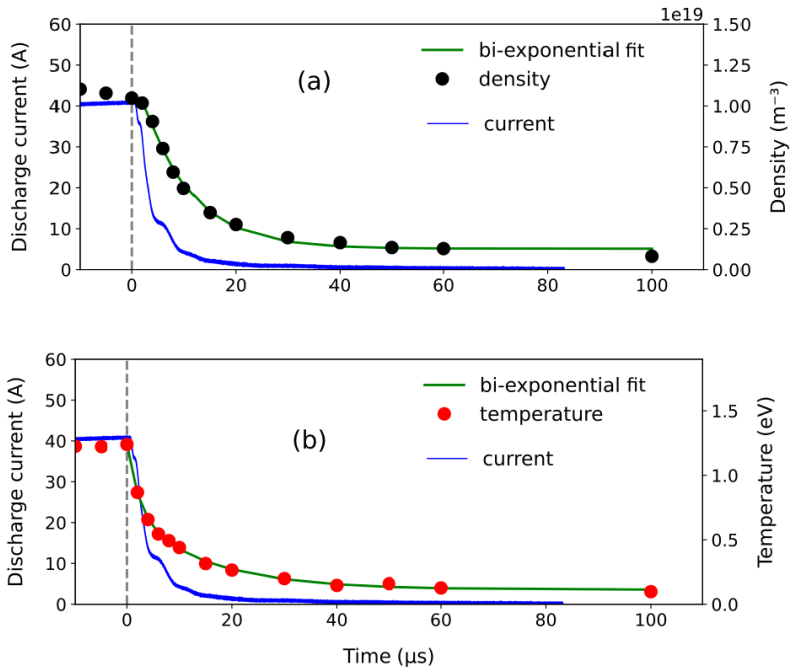

Figure 3.10: *Temporal variation of the electron density and temperature in the afterglow. (a) shows the electron density data (in black) for Fig. 3.8 for $t > 0$. The bi-exponential fit to the data (in green) gives characteristic decrement times τ of 1 and 9 μs. (b) shows the electron temperature data (in red) for Fig. 3.9 for $t > 0$. The bi-exponential fit to the data (in green) gives characteristic decrement times τ of 2 and 15 μs. The discharge current profile is shown in blue for (a) and (b).*

A higher electron temperature at the beginning of the pulse has also been identified in 2D particle-in-cell modeling of the HiPIMS regime [108], followed by electron relaxation and thermalization. In Ref. [108], where HiPIMS pulses of a few μs were analyzed, the current ramp-up on discharge initiation was associated with the presence of three electron populations, with the highest temperature population in the 50 eV range ($< 1\%$ of the total population). Note that the absolute electron temperature values from the model are not directly comparable to those obtained in these experiments, because of differences in the target size, cathode material, pulse length and the configuration of the magnetic field trap.

The density and temperature features of the afterglow can be studied in more detail and reveal information on the electron dynamics when the voltage has been switched off. Fig. 3.10 shows a view of the data during the afterglow ($t > 0$).

A bi-exponential fit of the form

$$Y = A_1\, e^{-\frac{t}{\tau_1}} + A_2\, e^{-\frac{t}{\tau_2}} + A_3 \tag{3.2}$$

is applied to the data, where Y represents the electron density or temperature, and τ_1 and τ_2 the characteristic decrement times from the fit; A_1, A_2 and A_3 are values produced from the fit. This follows the approach of Seo and colleagues for analyzing electron properties in the afterglow obtained using time-resolved probe measurements [109]. In that study, measurements were made on a pulsed planar magnetron at an axial position 80 mm from the cathode (in contrast to the

near-cathode measurements which are the focus of the present work).

As can be seen in Fig. 3.10, in the afterglow, a bi-exponential fit captures the initial rapid rate of decrease of the electron density and temperature, and the slower decrease at longer times. For electron density, the fast and slow decrement times are 1 and 9 μs, respectively. For the electron temperature, the fast and slow decrement times are 2 and 15 μs, respectively. **The existence of the two decrement times is due to an initial fast depletion of the higher-energy electrons formed by the end of the pulse (temperatures slightly above 1 eV for the conditions studied), followed by the slower diffusion of the lower-energy electrons (temperatures below 1 eV).** As expected, the characteristic density decay times for the fast and slow recombination processes are faster for electrons than for excited species previously measured (using tunable diode-laser absorption spectroscopy) and calculated (using the ionization region model) in Ref. [110]. In Ref. [110], fast and slow decay times for Ar metastables in the afterglow were found to be $\sim$ 5 - 20 μs and $\sim$ 110 μs, respectively.

The determination of the radial and azimuthal electron drift velocities close to the target is a novel aspect of this work and one which permits physical interpretations of the electron dynamics in a region which is difficult to analyze using probe techniques. The measured drift velocities for the same spectra used for Fig. 3.8 and Fig. 3.9 are shown in Fig. 3.11.

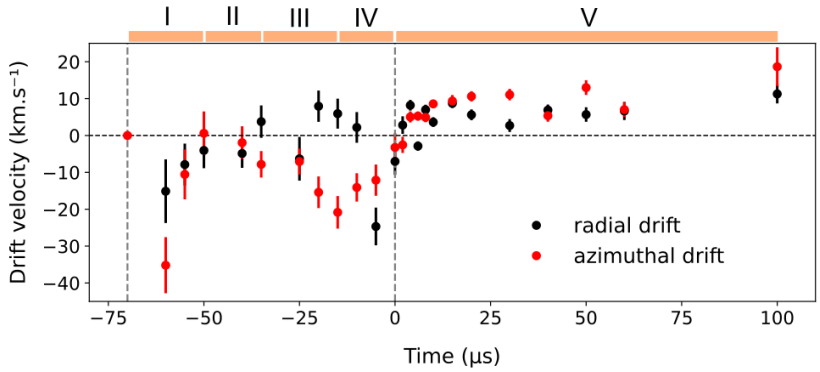

Figure 3.11: *Ar discharge, Condition 1: Electron drift velocity variation with pulse duration, for radial (black) and azimuthal (red) observation positions. The current pulse waveform is shown in blue. Operating parameters correspond to Condition 1, summarized in Table 3.2. The vertical dashed lines indicate the instants of discharge initiation (-70 μs) and voltage cut-off (0 μs). Different segments of time of the plasma pulse have been identified as regions I - V.*

Fig. 3.11 shows, for these conditions, clear evidence for anisotropy of the electron drift in the radial and azimuthal directions. A detailed analysis of the values seen in different temporal regions, identified as I - V, will be conducted shortly. We first consider the broad significance of the measured electron drifts.

Chapurin and Smolyakov [111] showed that the full expression for the fluid (averaged) drift can be written as the sum of the E×B drift, diamagnetic drift, and pressure anisotropy drift. We shall refer to this velocity as $\mathbf{v}_{net}$.

The electron E×B drift is written:

$$\mathbf{v}_{E\times B} = \frac{\mathbf{E}\times\mathbf{B}}{B^2} \tag{3.3}$$

The diamagnetic drift $v_{\nabla P}$ is written:

$$\mathbf{v}_{\nabla P} = -\frac{\nabla P_\perp \times \mathbf{B}}{qn_e B^2} \tag{3.4}$$

where $P_\perp$ is the pressure perpendicular to the magnetic field, q the elementary charge, and n_e the electron density. The pressure term can be expressed in terms of the electron density gradient,

$$\nabla P_\perp = \gamma k_B T_e \frac{\partial n_e}{\partial z}$$

where k_B is the Boltzmann constant and T_e the electron temperature; γ, the adiabatic index, is taken to be 1. The combination of the density gradient (pointing axially towards the cathode) and the radial magnetic field (pointing outwards) gives rise to a diamagnetic drift for electrons which is anticlockwise. This is depicted in Fig. 3.12. The full fluid drift is written

$$\mathbf{v}_{net} = \frac{\mathbf{E}\times\mathbf{B}}{B^2} - \frac{\nabla P_\perp \times \mathbf{B}}{qn_e B^2} - \frac{\nabla_\perp lnB \times (P_{||} - P_\perp)\mathbf{B}}{qn_e B^2} \tag{3.5}$$

where $P_{||}$ is the electron pressure parallel to the magnetic field. We assume that we can, as a first approximation, consider $P_{||} \sim P_\perp$ and drop the pressure anisotropy from consideration (an assumption supported by the results reported in Fig. 3.8). With this done, **the evolution in azimuthal velocities can be considered as the balance of two contributing drifts: the electron E×B drift ($\mathbf{v}_{E\times B}$) and the electron diamagnetic drift ($\mathbf{v}_{\nabla P}$).**
The consideration of the average fluid velocity is indeed appropriate for the experimental measurements, which will derive from the global drift of the electrons measured in the observation volume. As pointed out in Ref. [111], such an analysis differs from that which would be relevant for single particles, where the contribution of curvature and ∇B drifts would be taken into account to determine the net drift velocity.

The variation in the E×B drift is due to the change of the electric field at the measurement position during the pulse. Based on the experimentally-determined values for the electron temperature and density, and local value of the magnetic field, it is possible to account for the variations seen in Fig. 3.11. The diamagnetic drift varies according to changes in the electron temperature, density gradient, and mean electron density during a pulse.

The electron drift for Condition I is shown as a function of time in Fig. 3.11, subdivided into 5 domains (I, II, III, IV and V) which exhibit different evolutions in drift velocity.

- Interval I ($t \in [-70, -50]$ μs): large negative azimuthal drift velocities are seen in this interval, progressively decreasing in amplitude. The peak negative voltage is applied to the cathode and the maximum electric field at the measurement position is observed during the ramp-up phase of the current pulse in Interval I. An estimate of this electric field value is made using the spatial gradient of the potential from particle-in-cell simulations from Revel *et al.* [108] at a position 10 mm from the cathode for conditions of a peak negative potential of -1200 V and a steady-state discharge current of 35 A. This gives an electric field value of 3.5×10^3 V/m. For a local value of 16.1 mT at the measurement position, the expected $\mathbf{v}_{E\times B}$ value is 2×10^5 m/s.

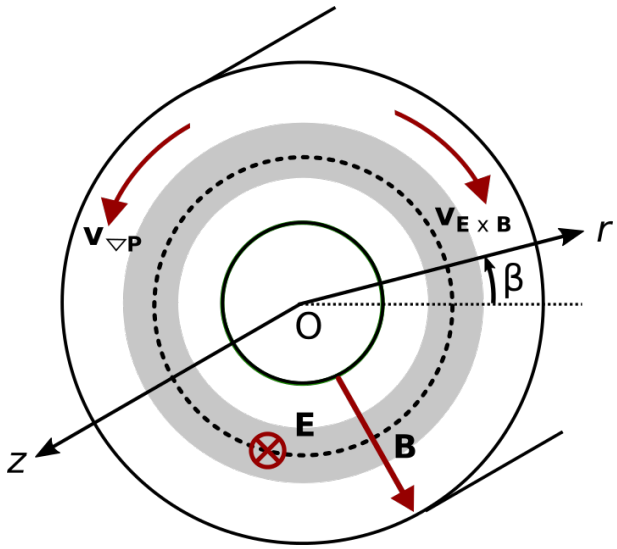

Figure 3.12: *Configuration of the azimuthal diamagnetic drift velocity ($v_{\nabla P}$) and* $\mathbf{E} \times \mathbf{B}$ *drift velocity ($v_{\mathbf{E}\times\mathbf{B}}$) at the cathode. Experimentally-measured net azimuthal velocities which are positively signed are in the same direction as the diamagnetic drift, whereas negatively-signed net azimuthal velocities are in the same direction as the* $\mathbf{E} \times \mathbf{B}$ *drift.*

The axial density gradient from the cathode surface to the measurement position is estimated from a linear slope to the points of Fig. 3.4 between 5 and 10 mm. This gives a value of 1.2×10^{21} e-/m^4. Using an electron temperature of about 1 eV, an estimate for the diamagnetic drift velocity of $\approx 4 \times 10^3$ m/s is obtained in this region.

As seen in Fig. 3.3, the observation wave vector points in the opposite direction to the $\mathbf{v}_{E\times B}$ drift. When the E×B velocity is dominant over the diamagnetic drift, the perceived velocity is negative. This is the case in Interval I. The decrease of the absolute value of the velocity towards zero is likely due to the rapid drop in electric field value.

It is interesting to note that the radial velocity in this region is on the same order as the azimuthal velocity, and decreases at the same rate. The negative radial velocity in Interval I corresponds to a drift of electrons radially inwards. A possible physical interpretation for this motion may be the contraction of the plasma, such as that described in the work of Bohlmark [102].

- Interval II ($t \in [-50, -35]$ μs): this region shows azimuthal and radial drifts close to zero (within the precision of the measurement). For the azimuthal drifts, the value of the $\mathbf{v}_{E\times B}$ drift (which has decreased due to the decrease in the first potential spike of Interval I) appears to be roughly matched by the value of the diamagnetic drift in the opposite direction, which has also decreased. The rate of increase of the plasma density flattens, likely also accompanied with a decrease in the value of $\partial n_e/\partial z$. In the radial direction, the rapid plasma expansion that occurs in Interval I is expected to have slowed or even stopped.

- Interval III ($t \in [-35, -15]$ μs): there is a second increase in the absolute value of the azimuthal drift velocity in Interval III. In this region a low-amplitude electric field at the measurement position can still create the $\mathbf{v}_{E\times B}$ drift, whereas the spatial gradient of the electron density appears to have flattened (hence, the diamagnetic contribution no longer partly cancels out the E×B drift. Indeed, in this interval, the electron density also varies

only marginally in time (Fig. 3.8). Two positive radial drift velocity values in this region are observed, again, potentially consistent with plasma expansion outwards.

- Interval IV ($t \in [-15, 0]$ μs): in Interval IV, there is a new decrease in the azimuthal velocity, expected as the electric field continues to decrease. The radial velocity has a large negative value at -5 μs which would potentially be consistent with a switch to radial contraction of the plasma. Such contraction of the plasma could originate from a reduction of the ionization near the time of the voltage cut-off (an effect visible in the density decrease in Fig. 3.8). It could also be due to the power limitation of the pulser (the ionization cannot increase indefinitely). At the end of Interval IV, both azimuthal and radial velocities approach zero, signifying the continued decrease of the electric field (causing the E×B drift to approach zero) and stabilized motion of the plasma radially (possibly due to the reduction in the expansion and the contraction that characterized the early moments in the discharge). The initial fast decrement time of the electron density in the afterglow phase (Fig. 3.10) is only 1 μs, showing that the space charge which creates the electric field is sustained only for short time scales in the afterglow.

- Interval V ($t \in [0, 100]$ μs): during the afterglow, the applied voltage drops to zero and so does the electric field, such that the strong azimuthal drift also falls to zero. The only remaining azimuthal drift contribution would be the diamagnetic drift, which accounts for the positive azimuthal velocities which can be observed in the afterglow phase. In Fig. 3.10, the electron density in this interval drops by a factor of 10 from 0 to 100 μs in the afterglow, while the electron temperature also decreases by a similar factor. Even without considering a changing density gradient, the simultaneous decrease in electron density and temperature are sufficient to account for a diamagnetic drift velocity which appears mostly flat in the afterglow. The radial velocities are again positive in the afterglow region, suggesting radial outward flow of the electrons. This motion may be expected with the removal of the electric field and the confining drift; electrons may now diffuse outwards along the magnetic field as the discharge dissipates.

3.3.2 Temporal variation of electron properties: Ar - Condition 2 (peak discharge current 80 A)

The sensitivity of the electron properties and the plasma anisotropy to the discharge parameters can be illustrated by the results observed for another operating point in argon. The new parameters are summarized in Table 3.3.

Ar - Condition 2					
PW (μs)	I_d (A)	U_d (V)	P (Pa)	z (mm)	B_r (mT)
60	80	-950	10	8	23.8

Table 3.3: *Conditions for argon temporal investigations (Condition 2). PW and P represent the pulse width and chamber pressure, respectively. I_d and U_d represent the peak discharge current and peak discharge voltage, respectively. B_r is the radial magnetic field measured at the center of the racetrack at z = 8 mm.*

Fig. 3.14 shows the discharge current and voltage waveforms corresponding to the conditions of Table 3.3, or Condition 2. For these conditions, the magnetic field strength and pressure have

been increased with respect to Condition 1, while the pulse width is shorter. The measurement position, $z = 8$ mm, is unchanged from Condition 1.
The corresponding measured magnetic field map is shown in Fig. 3.13. The magnetic null point is at the position $(r, z) = (5, 62)$ mm, where the radial position r is measured from the cathode axis. The laser measurement position above the center of the racetrack is at $(r, z) = (28, 8)$ mm. In contrast to Condition 1, a plateau of the current waveform appears established prior to the voltage cut-off at $t = 0$, and the peak current is now 80 A. The discharge voltage attains a peak close to -950 V and decreases to a plateau value of -550 V. This condition has been selected as an example of another shape of current waveform and we shall analyze the electron property evolution under these conditions.

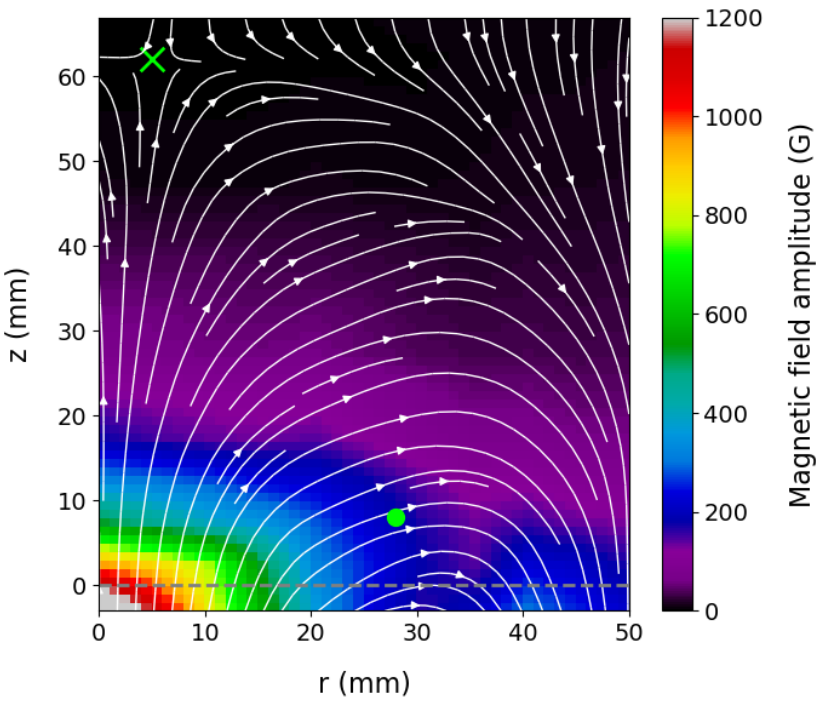

Figure 3.13: *Measured magnetic field map corresponding to Condition 2 (Table 3.3), as a function of axial (z) and radial (r) positions relative to the cathode. The magnetic null point is shown with a green cross and the laser measurement position above the racetrack is shown with a green circle. The reference position z = 0 mm is the guard ring surface.*

The electron density profile corresponding to Condition 2 is shown in Fig. 3.16. Fig. 3.16 shows higher densities than those of Condition 1 (consistent with the higher peak current in Condition 2). A new feature of time-dependent drift current anisotropy is also apparent, with electron densities found to be larger in the radial direction than in the azimuthal direction during the pulse, most noticeably for $t \in [-50, -20]$ μs. The azimuthal density variation follows the current waveform shape, whereas the radial density increases more steeply during the pulse and peaks at -40 μs. This observation points to possible non-uniform ionization in the radial and azimuthal directions as the discharge develops, for these discharge parameters.

The electron temperature variation accompanying Fig. 3.16 is shown in Fig. 3.15. The radial (black) and azimuthal (red) values show a similar trend to the Condition 1 investigation: an initial peak of the electron temperature (associated with the production of warm electrons on discharge initiation) followed by a drop and a plateau between 1 and 2 eV. A decrease to temperatures below 1 eV is observed in the afterglow.
The electron drift for Condition 2 as a function of time is plotted in Fig. 3.17. Interesting differences compared to Condition 1 are evident. Here, three main time intervals (I, II, III) will be used to discuss the evolution of the drift velocity values.

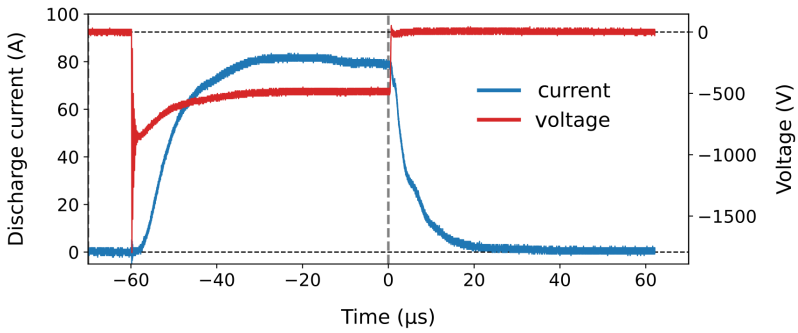

Figure 3.14: *Waveforms of the discharge current (in blue) and discharge voltage (in red) for Ar temporal investigations in Condition 2 (Table 3.3). Condition 2 features higher pressure and applied magnetic field than Condition 1, and an identical measurement position of $z = 8$ mm. The applied pulse duration of 60 μs is indicated by the gray dashed vertical lines.*

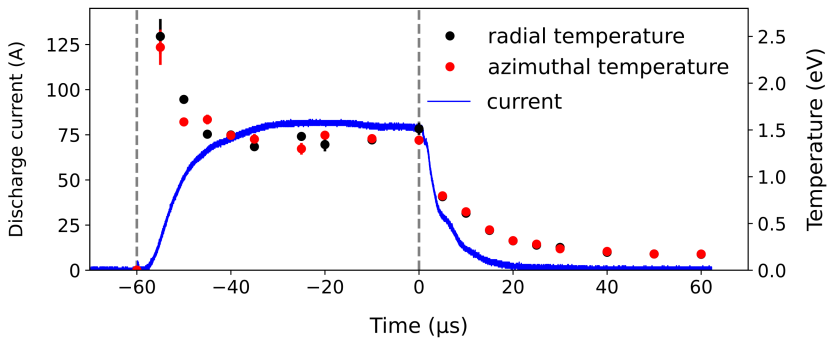

Figure 3.15: *Ar discharge, Condition 2: time evolution of the electron temperature, in radial (black) and azimuthal (red) observation positions. The current pulse waveform is shown in blue. Operating parameters correspond to Condition 2, summarized in Table 3.3. The vertical dashed lines indicate the instants of discharge initiation (-60 μs) and voltage cut-off (0 μs).*

As observed before, soon after the discharge initiation (-60 μs), large values of (negative) drift velocity in the azimuthal and radial directions are observed. This is associated with the establishment of the electric field, which peaks soon after discharge initiation before stabilizing later on in the pulse (Fig. 3.14). As before, we may consider the features of each interval individually:

- Interval I ($t \in [-60, -35]$ μs): after a peak at -55 μs, the azimuthal velocity declines and then increases again in this interval. As the electric field is expected to be declining in Region I, the only contributor to the observation of larger azimuthal velocities would be a reduction in the opposing diamagnetic drift. Although we lack precise information on the behavior of the density gradient, we have evidence of a decrease in the electron temperature in Interval I (Fig. 3.15) which would contribute to lower electron plasma pressure. In Interval I, the radial drift velocity is noticeably flat and slightly negative. The absence of a large evolution in this velocity is a sign of more stabilized radial motion of the electrons than was previously observed for Condition 1 drift velocities (in Fig. 3.11, where the radial drift changed signs during the pulse).

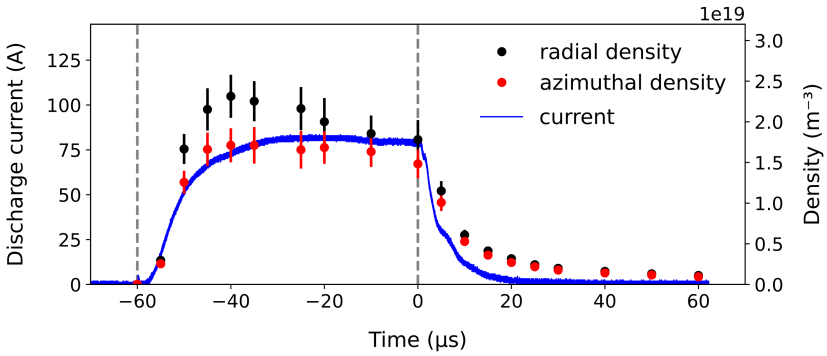

Figure 3.16: *Ar discharge, Condition 2: time evolution of the electron density, in radial (black) and azimuthal (red) observation directions. The current pulse waveform is shown in blue. Operating parameters correspond to Condition 2, summarized in Table 3.3. The vertical dashed lines indicate the instants of discharge initiation (-60 µs) and voltage cut-off (0 µs).*

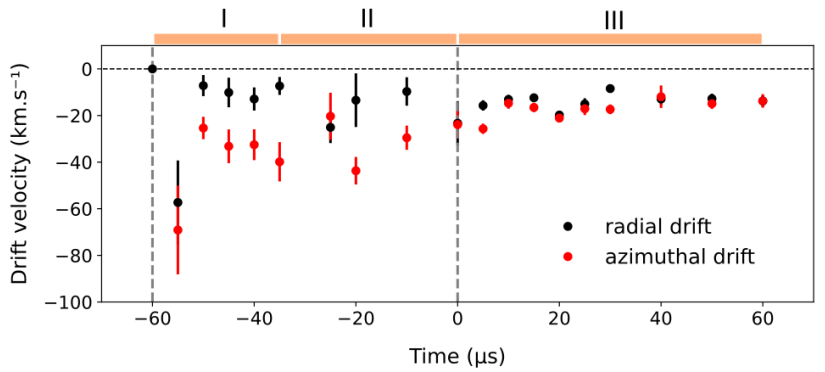

Figure 3.17: *Ar discharge, Condition 2: time evolution of the electron drift velocity, in radial (black) and azimuthal (red) observation positions. The current pulse waveform is shown in blue. Operating parameters correspond to Condition 2, summarized in Table 3.3. The vertical dashed lines indicate the instants of discharge initiation (-60 µs) and voltage cut-off (0 µs). Different segments of time of the plasma pulse have been identified as Intervals I - III.*

- Interval II ($t \in [-35, 0]$ μs): only a slight variation in both the azimuthal and radial velocities occurs in the second half of the pulse. This region coincides with times for which the density and temperature values tend to evolve towards a plateau, as does the electric field.

- Interval III ($t \in [0, 60]$ μs): In contrast to the observations made for Condition 1, the velocity values in the afterglow phase, even after the decrease of the applied voltage to zero, remain negative in sign. The most likely contributor to this observation is an inversion in the gradient of the electron density (originally taken to be directed outwards from the target). The different conditions encountered in Condition 2 could be conducive to such an inversion, due to the higher operating pressure in comparison to Condition 1 (10 Pa versus 1 Pa), as well as the more restricted electron diffusion due to the larger radial magnetic field at the measurement position (23.8 versus 16.1 mT).

3.3.3 Temporal variation of electron properties: He - effect of pulse width

A study of the effect of the pulse width on the electron properties has been conducted using a helium discharge. In this case, we opt to measure the electron dynamics and properties for pulses of three durations: 40, 70 and 100 μs. Table 3.4 summarizes the conditions used, in which the peak discharge current is 75 A, pressure 10 Pa, and the axial position for the measurement (i.e., the separation between the guard ring surface and laser beam) is 2 mm, corresponding to a separation between the laser beam and uneroded cathode surface of 5 mm.

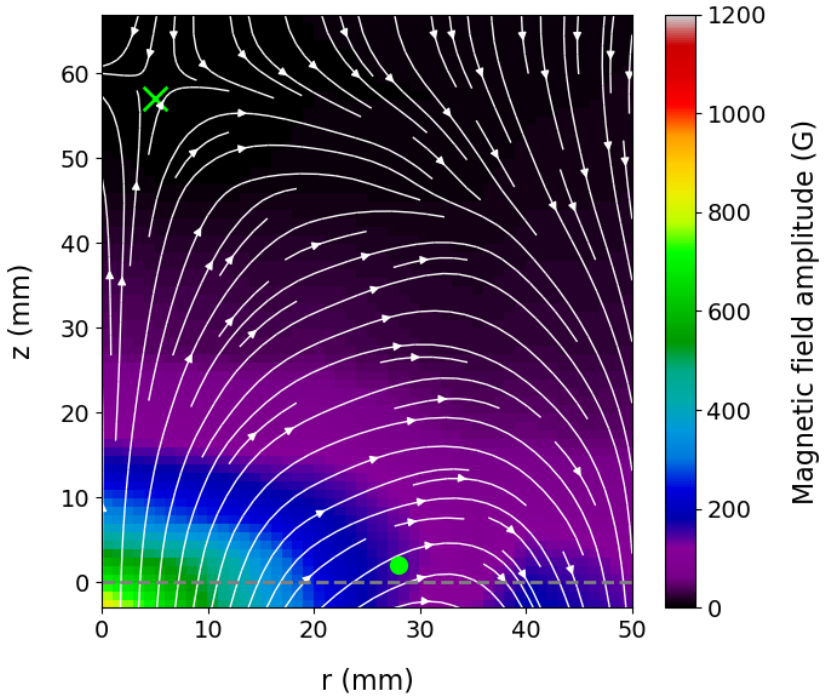

Figure 3.18: *Measured magnetic field map corresponding to He experiments (Table 3.4), as a function of axial (z) and radial (r) positions relative to the cathode. The magnetic null point is shown with a green cross and the laser measurement position above the racetrack is shown with a green circle. The reference position z = 0 mm is the guard ring surface.*

At this measurement position, the radial magnetic field magnitude will exceed the value of 23.8 mT given in Table 3.3, however, it was not possible to determine its value with high precision, due to dimensions of the magnetic probe and the limited access at this axial position.

The corresponding measured magnetic field map and observation volume position are shown in Fig. 3.18. The magnetic null point is at the position $(r, z) = (5, 57)$ mm, where the radial position r is measured from the cathode axis. The laser measurement position above the racetrack is shown with a green circle and is at the position $(r, z) = (28, 2)$ mm.

Figure 3.20 shows the variation of the electron density over the three pulse durations (40, 70, 100 μs), with the accompanying current and voltage waveforms shown in Fig. 3.19. Compared to the investigations with argon, there is an increased time delay for the ramp-up of the discharge current when the discharge voltage is applied. This delay ($\sim 15\mu$s) is a function of the working gas, target material, discharge voltage and operating pressure [112]. **For the 40 μs case, the densities measured in the radial and azimuthal directions differ significantly in the**

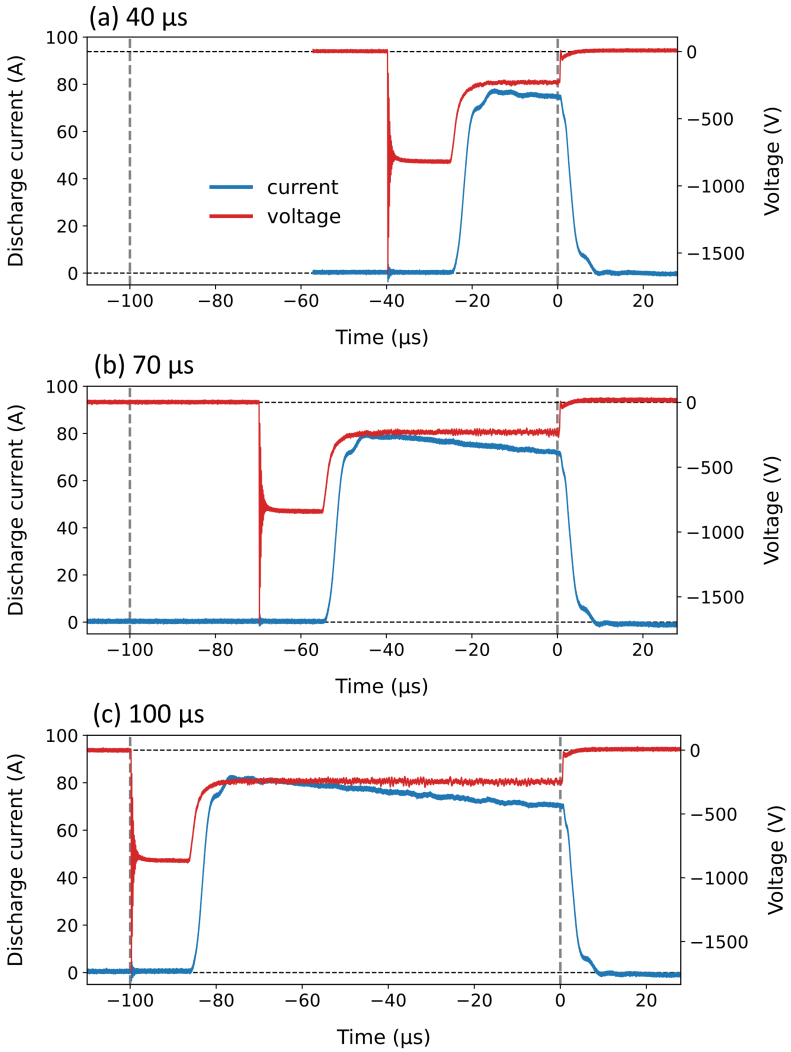

Figure 3.19: *Waveforms of the discharge current (in blue) and discharge voltage (in red) for He temporal investigations (Table 3.4) for applied pulse durations of (a) 40 µs, (b) 70 µs, and (c) 100 µs. The pulse limits are indicated by the gray dashed vertical lines.*

interval $t \in [-20, 0]$ μs, which suggests that the plasma created is not fully spatially uniform in density over this short pulse duration. The longer pulses of 70 and 100 μs, in contrast, show similar magnitudes for the electron density measured in the radial and azimuthal directions, suggesting more spatially uniform ionization. Unlike the argon examples (Condition 1 and Condition 2), where the electron density temporal evolution generally matched the current pulse waveform, for helium there is an initial peak in density as the current ramps up, followed by a decline in density. The higher first ionization energy of He (24.6 eV versus 15.8 eV for Ar) requires higher electron energies for discharge initiation and maintenance. This population decreases after the initial current ramp and thus the ionization (and electron density) also progressively decreases. Note that the absence of azimuthal points in the afterglow region was due to a truncation of the measurement duration and not due to the lack of measurable data in this region.

He				
PW (μs)	I_d (A)	U_d (V)	P (Pa)	z (mm)
40	75	-820	10	2
70	75	-830	10	2
100	75	-840	10	2

Table 3.4: *Conditions for helium temporal investigations. PW and P represent the pulse width and chamber pressure, respectively. I_d and U_d represent the peak discharge current and peak discharge voltage, respectively. Measurements are performed at $z = 2$ mm. The values of current, pressure and measurement position are the same for all pulse widths.*

The trends in electron temperature are shown in Fig. 3.22. The radial and azimuthal temperature magnitudes are similar for the different pulse durations. As the pulse duration increases, the final temperature attained by the bulk electrons at the voltage cut-off increases, from about 5.5 eV in the 40 μs case to about 8 eV in the 100 μs case. **This is another key difference with respect to argon (Condition 1 and Condition 2), in which a temperature plateau tended to develop within the pulse, suggesting that the bulk electron energy gains and losses had balanced each other.** For the helium conditions considered in this manuscript, extending the duration of the pulse extends the duration over which the electrons in the pre-sheath plasma can gain energy. It is worth noting that a first peak of the electron temperature expected at the beginning of the pulse during the current ramp-up could not be measured, as was the case for argon (this is likely due to the low number density of this energetic population). However, the presence of such energetic electrons is absolutely necessary to account for the initial peak of the electron density observed in Fig. 3.20.

We may now consider the effect of the pulse duration on the features of the measured net drift velocity, shown in Fig. 3.21. **For all three pulse durations, the radial drift is positively-signed, indicative of a global movement of electrons in the radial direction away from the center of the target.** This radial drift exceeds the net azimuthal drift during the entire pulse duration and afterglow phase. This is not unexpected: at the measurement location ($z = 2$ mm), it has been noted that the radial magnetic field is be larger than that of Condition 1 and Condition 2 in argon. The values of the average discharge voltage are also lower in the He case, as seen in Table 3.4, compared to Table 3.2 and Table 3.3. The combination of these effects will contribute to smaller magnitudes for the azimuthal drift velocity terms, and hence the net measured radial drift can be dominant in comparison.

The radial drift velocities shown in Fig. 3.21 are large and relatively flat over the pulse durations considered, once the discharge has been established. While we have considered the possibility that the dynamic plasma expansion and contraction may play a role in determining the sign of the radial drift, the evidence of very large values of the radial drift for the helium investigations (100 km.s^{-1} range), coupled with their relatively flat evolution over the pulse duration, suggests other possible origins of the radial drift.

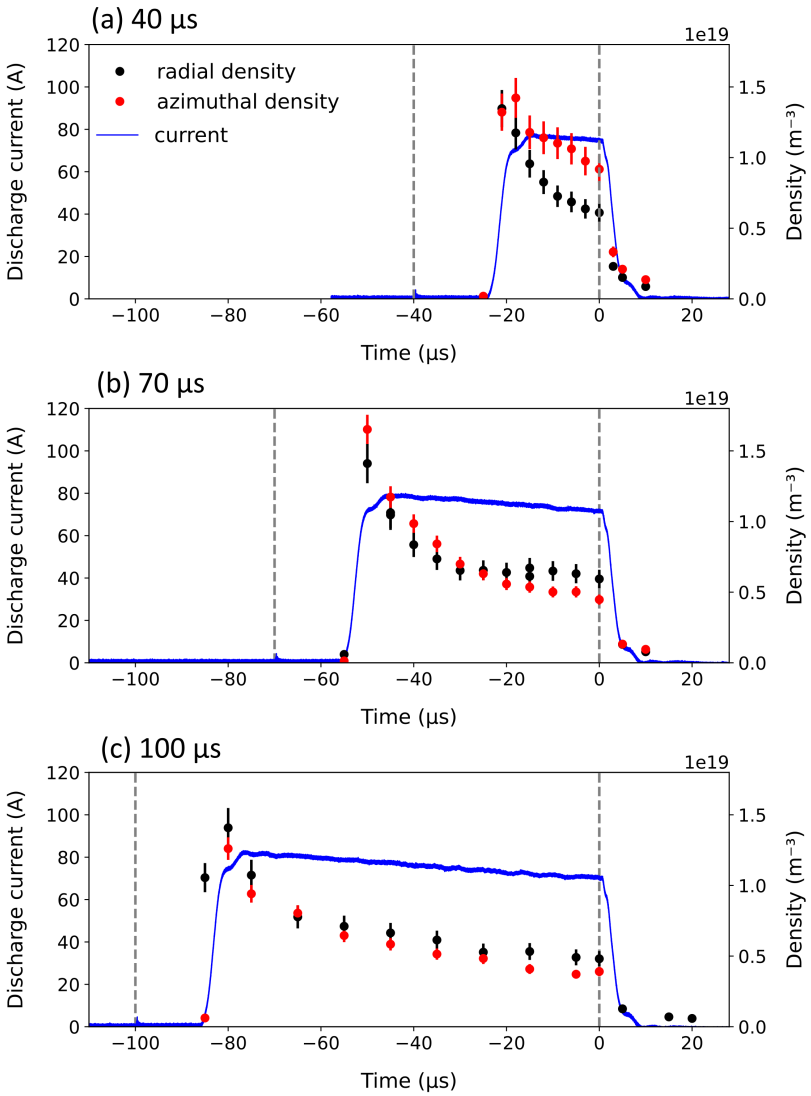

Figure 3.20: *He discharge: time evolution of the electron density, in radial (black) and azimuthal (red) observation positions, for different pulse durations: (a) 40 µs, (b) 70 µs, and (c) 100 µs. The current pulse waveform is shown in blue. Operating parameters are summarized in Table 3.4. The vertical dashed lines indicate the instants of discharge initiation and voltage cut-off (0 µs).*

Before considering these origins, we note that prior measurements of a large radial electron saturation current have been reported by Hecimovic *et al.* [113] in a planar magnetron discharge with a Ti target for a current density of 5 A cm^{-2}, close to our conditions. In Ref. [113], a planar probe was placed about 1 cm from the target, close to the guard-ring. Negative peaks on the local floating potential were recorded in phase with the electron saturation current, consistent with a radial increase in the electron flux, i.e., an increase in electron density and electron velocity. The drop in the floating potential was taken as an indication of increased electron flux and such an observation would be compatible with the radial electron drifts we measure directly in the present work.

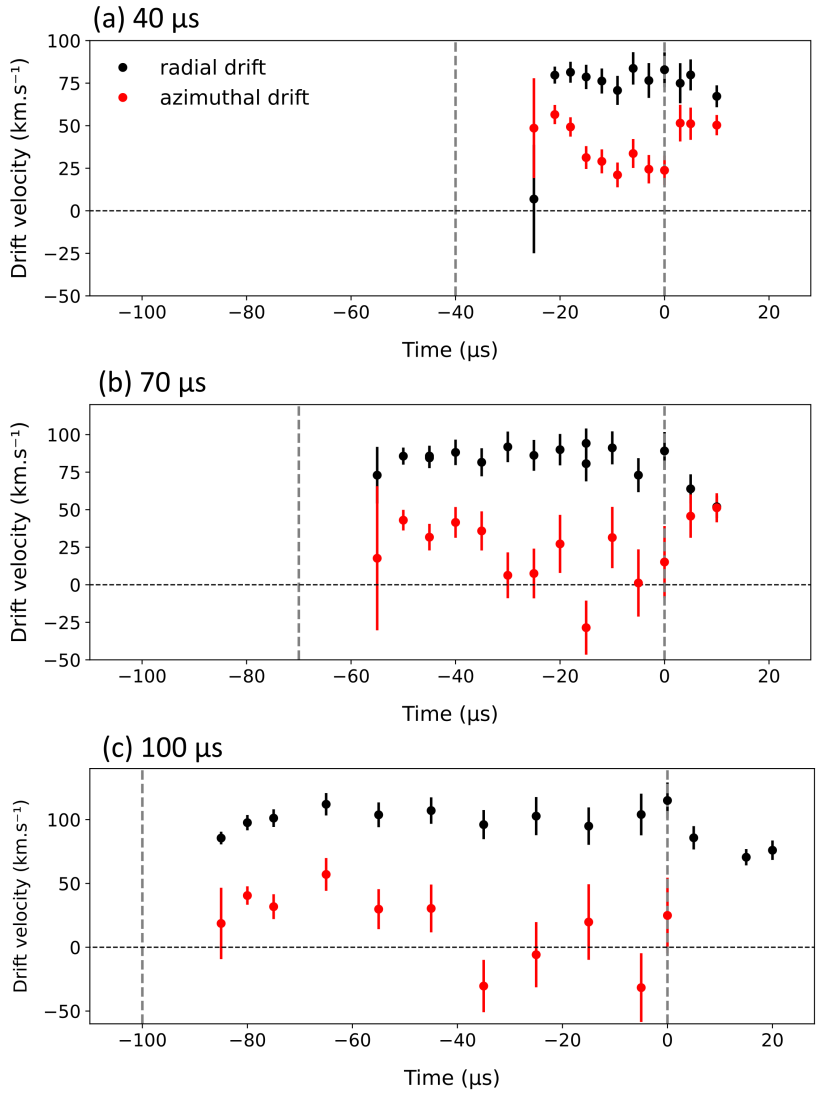

Figure 3.21: *He discharge: time evolution of the electron drift velocity, in radial (black) and azimuthal (red) observation positions, for different pulse durations: (a) 40 µs, (b) 70 µs, and (c) 100 µs. The current pulse waveform is shown in blue. Operating parameters are summarized in Table 3.4. The vertical dashed lines indicate the instants of discharge initiation and voltage cut-off (0 µs).*

Pursuing the fluid treatment of the plasma, we consider whether the centrifugal force F_c on the electrons in a fluid element may be compatible with the measured radial velocities directed outward. Using the azimuthal electron velocity in the fluid element, measured directly as $\mathbf{v}_{net}$, the radial velocity arising from this force is written

$$v_{\parallel} = \frac{\mathbf{v}_{net}^2}{r} t \tag{3.6}$$

where the time t may be considered to be the time taken for the electrons to execute their trajectory along a given magnetic field line over the racetrack (and thus, approximately, as a buildup time for the plasma to become established). This time is on the order of 10 μs, according to Ref. [110].

Using an average value of $\mathbf{v}_{net}$ in Fig. 3.21 of ≈ 25 km.s^{-1}, a time $t/2$ of 5 μs (since the measurement volume is in the center of the racetrack, halfway in the electron trajectory along a radial field line), and r of 28 mm, we find a value $v_{\parallel}$ of 112 km.s^{-1}. **This value is close to the average radial velocity values observed in Fig. 3.21, suggesting that the centrifugal force may indeed be a good candidate to explain the radial velocities. In Ref. [113], this radial electron flux has been explained as an effect of spoke rotation.**

The net azimuthal drift ($\mathbf{v}_{net}$) is positive for the 40 μs case, indicating that the diamagnetic drift exceeds the E×B drift. Indeed, at the axial location used for this measurement ($z = 2$ mm), very close to the cathode, the electron density gradient $\frac{\partial n_e}{\partial z}$ is expected to be large and this would favor a diamagnetic drift velocity on the same order as, or exceeding, the E×B drift. For the 70 and 100 μs cases of Fig. 3.21, there are instants showing a $\mathbf{v}_{net}$ close to zero or even negative; this would suggest that as the discharge evolves for these longer pulses, the electron density gradient $\frac{\partial n_e}{\partial z}$ at the measurement position also changes and could contribute to the diamagnetic drift velocity matching or falling slightly below the E×B drift.

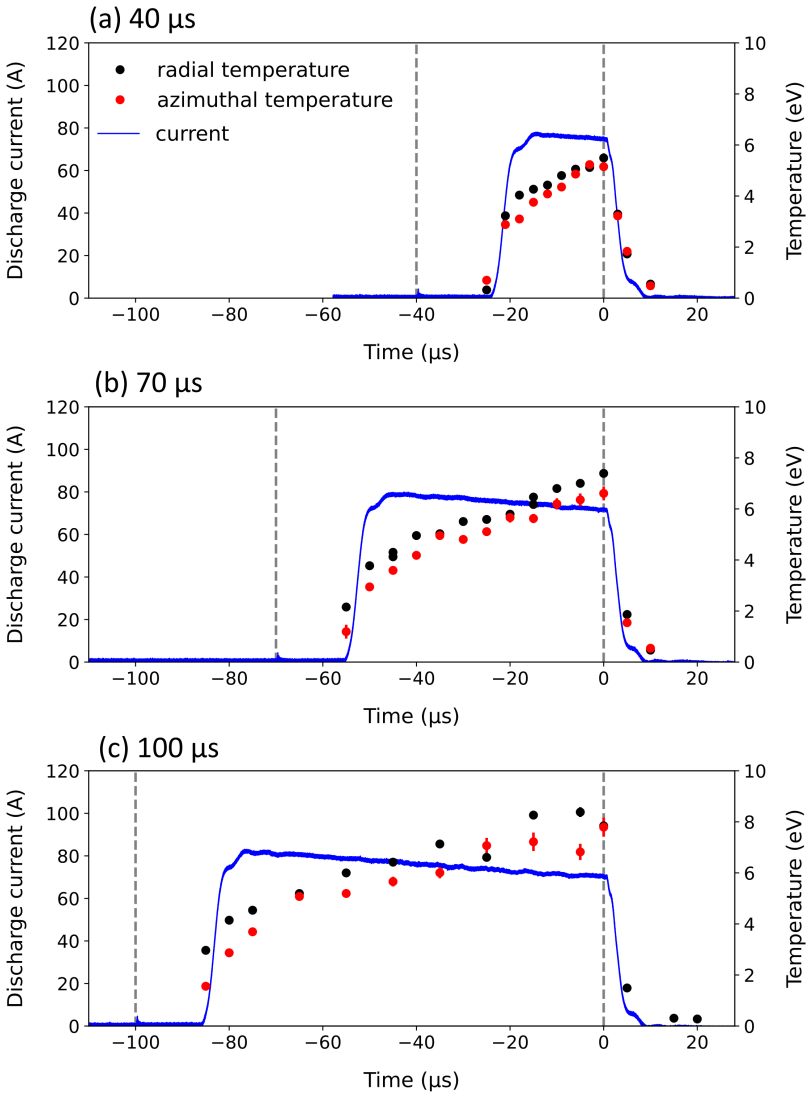

Figure 3.22: *He discharge: time evolution of the electron temperature, in radial (black) and azimuthal (red) observation positions, for different pulse durations: (a) 40 µs, (b) 70 µs, and (c) 100 µs. The current pulse waveform is shown in blue. Operating parameters are summarized in Table 3.4. The vertical dashed lines indicate the instants of discharge initiation and voltage cut-off (0 µs).*

3.4 Discussion

Prior planar magnetron studies on drift velocity

This work is the first to provide a detailed study of anisotropies in the electron properties and dynamics in the HiPIMS regime using laser scattering. We note that in prior work by Mishra, Kelly and Bradley [114], the electron drift velocities were analyzed indirectly, via electric field measurements in HiPIMS using an emissive probe, situated outside the pre-sheath. The measured electric and magnetic fields in that work were used to infer the values of electron drift speed. Here, we investigate the pre-sheath region within a few millimeters of the cathode surface, and determine the drifts directly, from incoherent Thomson scattering spectra. The orientation of the observation wave vector in these experiments provides unambiguous access to the radial and azimuthal drifts, as well as to any anisotropies in the electron properties according to the radial and azimuthal directions.

The methods for determining uncertainties were described in Chapter 2. The favorable experimental conditions in HiPIMS, in particular, the combination of: (i) the large electron densities, reaching up to three orders of magnitude larger than the minimum density measurable with the diagnostic of $10^{16}/\mathrm{m}^3$), and (ii) low electron temperatures, in the range of a few eV, producing less broad scattered spectra, results in small error bars, smaller than the size of the plotted marker point.

The calculation of these error bars allows a determination of whether the differences observed between the radial and azimuthal directions, and the trends in the electron properties as a function of time, can be considered significant. Clear differences can be observed in a number of cases (such as in Fig. 3.20(a)) in the electron properties according to the direction of measurement. **The drift velocity shows the most marked differences between the radial and azimuthal directions, and in these analyses, we have sought to account for these differences by considering the time-dependent features of the discharge.** As the discussions suggest, the drift features (and the electron properties) will be strongly dependent on the operating conditions used. The direct measurement of the drift velocity provides information on the plasma expansion or contraction, the possible contribution of the centrifugal force to the large and sustained radial electron drift, and information on relative contributions of the azimutally-directed E×B and diamagnetic drift components, via the net velocity ($\mathbf{v}_{net}$) measured.

Role of simulations

In these discussions, the origins of the evolving net azimuthal electron velocities and the radial electron velocities have been considered. For the measurement positions considered, these laser scattering measurements provide this information in a way not accessible to other diagnostics. In developing a full understanding of the electron dynamics in the HiPIMS regime, it is worth considering to what extent insights from these experiments and suitable numerical simulations can be combined.

Raadu *et al.* [104] and Brenning *et al.* [115] produced an ionization region model (IRM) and bulk plasma model (BPM) which have proven extremely valuable in allowing a deeper understanding of planar magnetron physics. These global models show, for example, the profiles which are expected to develop for the electron properties (density, temperature) over a typical HiPIMS pulse. They also show spatial variations of electron properties and the potential structure within the plasma. Comparisons of experimental results to such global models would be potentially useful,

although not all of the complexities of the HiPIMS discharge (the development of instabilities affecting electron transport, for example) are reflected in such models.

Revel performed 2D particle-in-cell modeling of the HiPIMS regime for short pulse durations (a few μs) [108], and this work showed spatiotemporal features of the discharge and evidence of features such as oscillations in the electron density. Direct comparisons of such codes to the experimental data would possibly require the simulation of longer pulses (in the range of a least a few tens of μs), computationally expensive for the HiPIMS regime.

An important complement to these measurements would be full 3D particle-in-cell simulations close to the target in the HiPIMS regime. These could provide a means to study the progressive evolution of the particle drifts in a precise manner, and would allow comparison to experiments across a wide range of conditions and locations. However, such codes remain beyond reach at present. Newer simulation approaches, such as sparse particle-in-cell methods described in Ref. [116], could potentially be applied in the future. Garrigues *et al.* [117] successfully adapted such codes to studies of an E×B geometry (Hall thruster), and application to planar magnetron plasmas could be a promising area of research. The interest of such codes is primarily the potential reduction of the computational time in comparison to conventional 3D particle-in-cell codes by orders of magnitude.

3.5 Concluding remarks on the measurements discussed

These investigations, performed in close proximity to the cathode, provide information on electron properties and drifts within the magnetic trap which are not normally accessible to probe measurements. In this implementation, the investigation of anisotropies has been achieved through the positioning of the observation volume such that radial (parallel to the magnetic field line) and azimuthal (perpendicular to the magnetic field line) electron property information can be directly measured. The timed triggering of the acquisition enables a detailed temporal map of electron properties to be determined from the time of discharge initiation far into the afterglow.
These experimental investigations reveal, for the conditions considered, that:

- in argon, while the electron density profile tends to be similar in shape to that of the discharge current profile in time, differences in the radial and azimuthal densities can be perceived at different moments within the pulse, suggesting the non-uniform development of the ionization during pulsing,
- in argon, exponential decreases of electron temperature and density seen in the afterglow are consistent with the existence of two characteristic times: a fast initial decrement on voltage cut-off, followed by a slower decrease. The diagnostic used in this study is sufficiently sensitive for the characterization of such afterglow features, as illustrated in these analyses,
- operation in the HiPIMS regime is associated with the creation of highly-dynamic radial drifts (likely involving plasma expansion and contraction as the pulse evolves) and azimuthal drifts (the result of a balance between E×B drifts and diamagnetic drifts),
- in helium, an electron temperature exhibiting a progressive increase can be seen for longer pulse widths, consistent with the heating of the bulk pre-sheath electrons up to the voltage cut-off. This contrasts with observations made for argon, where a plateau in the electron temperature is rapidly established during the pulses,
- in helium, in close proximity to the cathode surface, the radial electron drift can be seen to significantly exceed the net azimuthal drift, with values on the order of 100 km/s maintained over the pulse duration and drifts directed outwards. The centrifugal force could be responsible for the creation of this large and sustained radial drift of electrons.

In addition to improving the physical understanding of features of the discharge, these evolutions provide important information which can be used in conjunction with numerical codes for the HiPIMS regime, still under development, such as in Ref. [108]. Access to electron property dynamics resolved along a particular wave vector direction (parallel and perpendicular to the magnetic field) can provide clarity regarding the existence of anisotropies in the plasma and how such anisotropies may evolve in time. The relative magnitudes of the radial and azimuthal drifts can provide information on the nature of the electron confinement for different operating conditions and as a function of time.

3.6 Additional observations: high current

A series of exploratory measurements were performed using another power supply (Technix SR1kV-300W) which allowed much higher currents to be reached, exceeding by a factor of 10 the peak current values used in the previous sections of this chapter. Such measurements provide clues on how electron dynamics evolve during very high current pulsing.

The increase in current is accompanied by an increase in the energy deposited in the plasma and, consequently, in the thermal effects on the magnetron. As a result, plasma stability over time tends to decrease and the reproducibility of the current profile (pulse-to-pulse) over the course of several hours also tends to decrease. However, the diagnostic sensitivity makes it possible to obtain a spectrum much faster what was previously achievable in the literature (averaging ten minutes for a single point). It is therefore possible to study such regimes without significant divergence in the plasma conditions.

Three different cases are studied, for which plasma conditions have been chosen to: (i) allow some degree of comparison to the measurements at lower current discussed earlier in the chapter, and (ii) maximize the plasma stability. These discharges are referred to as cases A, B and C, with their associated conditions shown in Table 3.5. While every effort was made to ensure sustained reproducible operation, it was still necessary to limit the number of spectra acquired and the choice was also made to perform only investigations of the radial (and not azimuthal) direction. In Table 3.5, it can be observed that the same chamber gas is used in all of these exploratory cases, however, different current levels are set (along with the incorporation of a different target material (molybdenum), whereas all prior measurements in this work were performed with a titanium target.

High current - conditions							
	gas	target	PW (μs)	I_d (A)	U_d (V)	P (Pa)	z (mm)
A	He	Ti	15	400	-660	10	8
B	He	Mo	80	560	-750	10	5
C	He	Mo	80	660	-630	10	5

Table 3.5: *Conditions for high current temporal investigations. PW and P represent the pulse width and chamber pressure, respectively. I_d and U_d represent the peak discharge current and peak discharge voltage, respectively. Measurements are performed in the magnetic configuration C5E5.*

Figure 3.23 shows the evolution of the electron properties for case A. The voltage is applied from $t \in [-35, 0]$, and the discharge current starts to rise from $t = -5\ \mu s$. The electron density closely follows the discharge current trend, a feature which has already been observed in the lower current cases investigated in this work. It is interesting to observe that the end of the voltage application at $t = 0$ does not mark the end of the current and density increase, since the latter reaches a peak of almost 2 μs later. The density shows an exponential decrease in the afterglow. The electron temperature is observed to decrease near-linearly as soon as the voltage is no longer applied, however, this rate of decrease is far more gradual than the rate of decrease of the current, suggesting that significant electron energization was achieved during application of

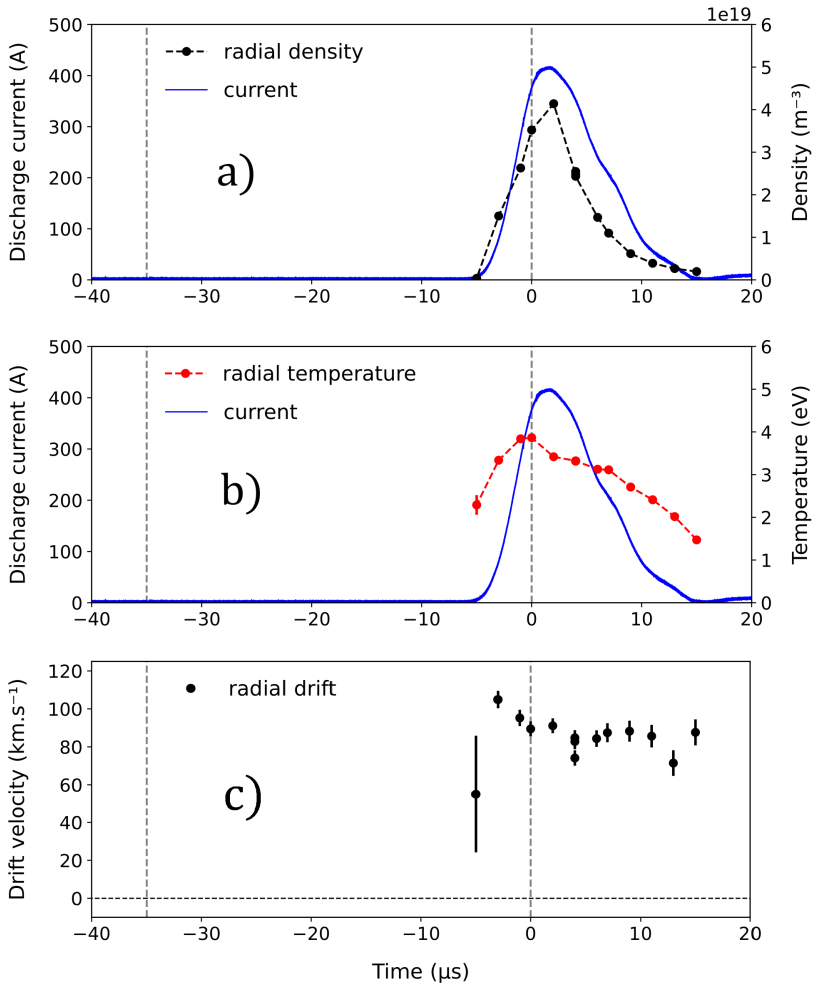

Figure 3.23: *Discharge A (He with Ti): time evolution of the electron density (a), electron temperature (b), and electron drift velocity (c) along the radial direction. The current pulse waveform is shown in blue. Operating parameters are summarized in Table 3.5. The vertical dashed lines indicate the instants of discharge initiation and voltage cut-off (0 µs).*

the high-current pulse. Lastly, it is notable that in spite the the large variation of both electron density and temperature in this high-current regime, the magnitude of the radial drift velocity is constant over the pulse duration - this feature echoes the previous findings with helium at lower currents (Fig. 3.21).

Figures 3.25 and 3.26 correspond to cases B and C in Table 3.5. The helium/molybdenum configuration allows higher current densities to be achieved [118, 119]. During measurements corresponding to case B, it was found that plasma conditions drifted over time, which is why only a few points are shown in Figure 3.25. Case C conditions, obtained for the same gas and target, were chosen for their greater stability.

In Cases B and C, a rapid increase of the discharge current is observed at the beginning of the pulse, about 5 μs after the application of the voltage, followed by a decay (Figure 3.26). There, the electron density again closely follows the shape of the discharge current temporal evolution.

However, in contrast to what was observed in helium at lower current, the measured bulk elec-

tron temperature is high at the beginning of the pulse, before decaying linearly. As explained in Section 3.3 at lower current, the detection of the presence of superthermal electrons at the pulse onset using incoherent Thomson scattering is limited by their density. For these higher-current, higher-density conditions, it is possible that larger numbers of these superthermal electrons are created and now become detectable at the pulse onset, thereby contributing to the higher apparent electron temperatures (broader spectra) observed 3.24.

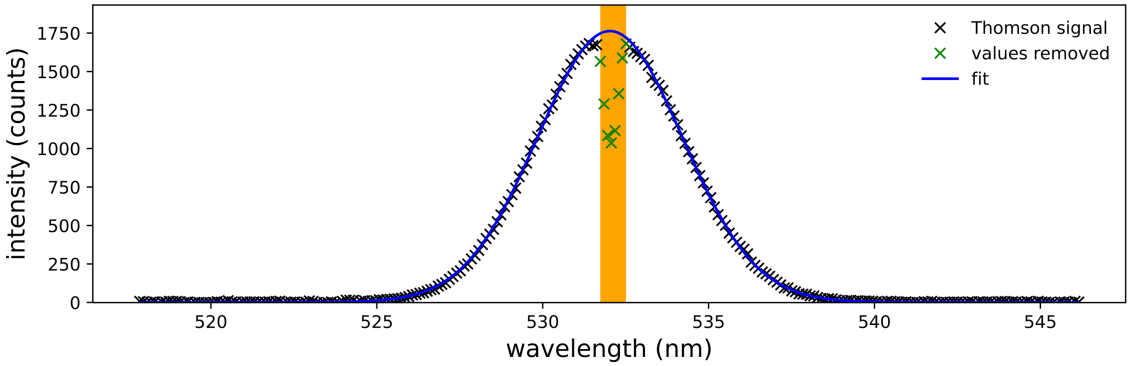

Figure 3.24: *Example of a Thomson spectrum acquired at high current, here under B conditions (560 A). The Gaussian shape is clearly visible.*

Several points of discussion can be identified. A notable difference between the argon and helium studies was the delay between the application of the voltage and the beginning of the current increase. This was almost zero in the argon case, and $\simeq 15\ \mu s$ for helium under the conditions studied (see Fig. 3.19). This was expected, since it has already been mentioned that the model developed by Yushkov and Anders [112] attributes this delay only to the working gas, the target material, the operating pressure and the discharge voltage. However, several of these parameters were changed at the same time when switching from argon to helium. For the high current measurement, in case A, the only one of them to have been modified compared to the previous condition is the discharge voltage, which decreased from 830 V (Table 3.4) to 660 V (Table 3.5).

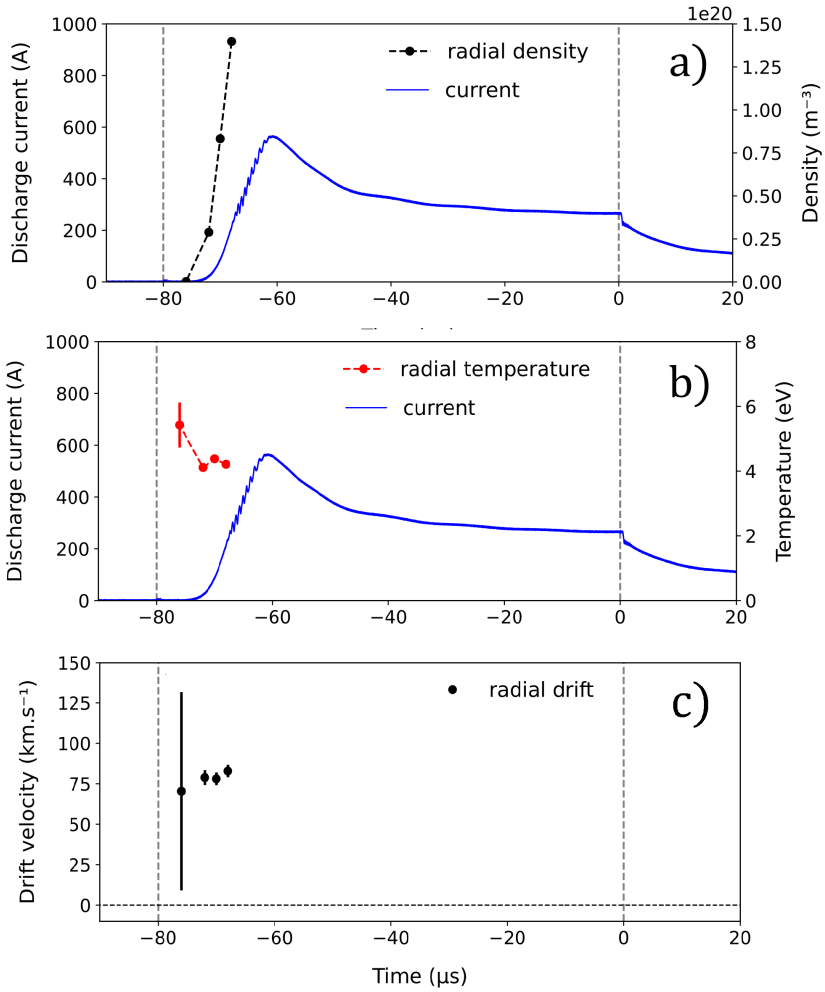

Figure 3.25: *Discharge B (He with Mo at 560 A): time evolution of the electron density (a), electron temperature (b), and electron drift velocity (c) along the radial direction. The current pulse waveform is shown in blue. Operating parameters are summarized in Table 3.5. The vertical dashed lines indicate the instants of discharge initiation and voltage cut-off (0 µs). Only a few acquisitions are plotted, due to the tendency of this particular operating point to drift over time.*

Yushkov and Anders provide a formula to calculate the delay t_f between the voltage application and the current rise:

$$t_f = \frac{a}{V - V_0} \exp\left(\frac{b}{V}\right) \simeq t_f \propto \frac{1}{V - V_0} \tag{3.7}$$

where a and b are constants that depend on the gas and the target material. The approximation made in the above equation is valid when the applied voltage is well above the threshold voltage V_0. In our configuration, this value V_0 is about 400 V, so:

$$t_{f(high\ current)} \propto \frac{1}{660 - 400} \qquad \text{and} \qquad t_{f(low\ current)} \propto \frac{1}{830 - 400} \tag{3.8}$$

$$t_{f(high\ current)} \simeq 2\ t_{f(low\ current)} \tag{3.9}$$

Figure 3.23 clearly shows that this delay is equal to $\simeq 30\ \mu s$ for the high current case, versus $\simeq 15\ \mu s$ for the low current case, thus allowing a verification of Yushkov and Anders' model.

Moreover, we can show that when we change another parameter (target material), while keeping the rest of the parameters constant, there is a significant change to the delay ($\simeq 5s$), visible in Fig 3.25, which remains constant for both molybdenum measurements, as expected from the model.

A second point of discussion for measurements with a titanium target concerns the evolution of electron properties during the pulse. In the case of the lower current measurements (75 A), a linear increase of the temperature is observed during the entire pulse duration, and the temperature never reaches a plateau (Fig. 3.22). The maximum is thus reached for the longest pulse, 10 eV for 100 μs. In contrast, the electron density saturates very quickly (Fig. 3.20) at 1.3×10^{19} m^{-3}, in 5 μs, then slowly decreases until 4×10^{18} m^{-3}, still for the 100 μs case.

For the high current case (400 A), the trend seems to be the same, namely a sudden increase in density, up to 4×10^{19} m^{-3} in 5 μs. Plasma stability issues prevented operation with longer pulses. However, it is reasonable to expect that if longer pulses had been achieved, it could have been possible to reach a peak density proportional to the ratio of peak currents, i.e., 6.9×10^{19} m^{-3} (400 A/75 A $\simeq 5.3$). On the other hand, the temperature increases at the same rate regardless of the peak current, suggesting that the electron heating mechanism, at least in the radial direction, is independent of the electron density or the power injected into the plasma. Only the number of free electrons is changed, but the individual properties of the electrons remain essentially the same.

No low-current molybdenum points could be studied during the time available for these exploratory measurements, however, one last interesting aspect can be identified by comparing the high-current cases. In cases B and C, the pulse lasts several tens of μs, allowing the density peak to be reached, at the beginning of the pulse. Its value is of the order of 1×10^{20} m^{-3} for a maximum discharge current between 560 A and 660 A, i.e. about 50% more than the case A. According to the previous hypothesis, the peak density (for longer pulses) attained in case A would have been 6.9×10^{19} m^{-3}, so there is no significant difference between the materials. Thus, the maximum electron density seems to depend only on the current injected into the magnetron, and depends little on the choice of material used for the target (at least, when comparing Ti and Mo).

However, a notable difference arises when comparing the electron temperatures. While case A (as well as the low current titanium cases) showed a linear increase, the temperature in cases B and C reached almost immediate saturation at the beginning of the pulse around 5 eV, before slowly decreasing and reaching a plateau at 4 eV. The energization mechanism of the electrons, and the peak temperature they attain, seem to be closely related to the target material. Significantly higher temperatures (10 eV) are attained in the titanium cases. This result is not surprising, since it is known [120, 121] that in the HiPIMS configuration, at the start of the discharge, the majority of ions originate from the gas, but the plasma quickly evolves into one largely dominated by ions from the target.

Finally, as observed in case A, the radial drift velocities are about 100 $km.s^{-1}$ and remain at a plateau throughout,identical to what was observed in the previous cases with helium. The maintenance of the velocity of several several tens of $km.s^{-1}$ in the afterglow is also observed for these high-current measurements.

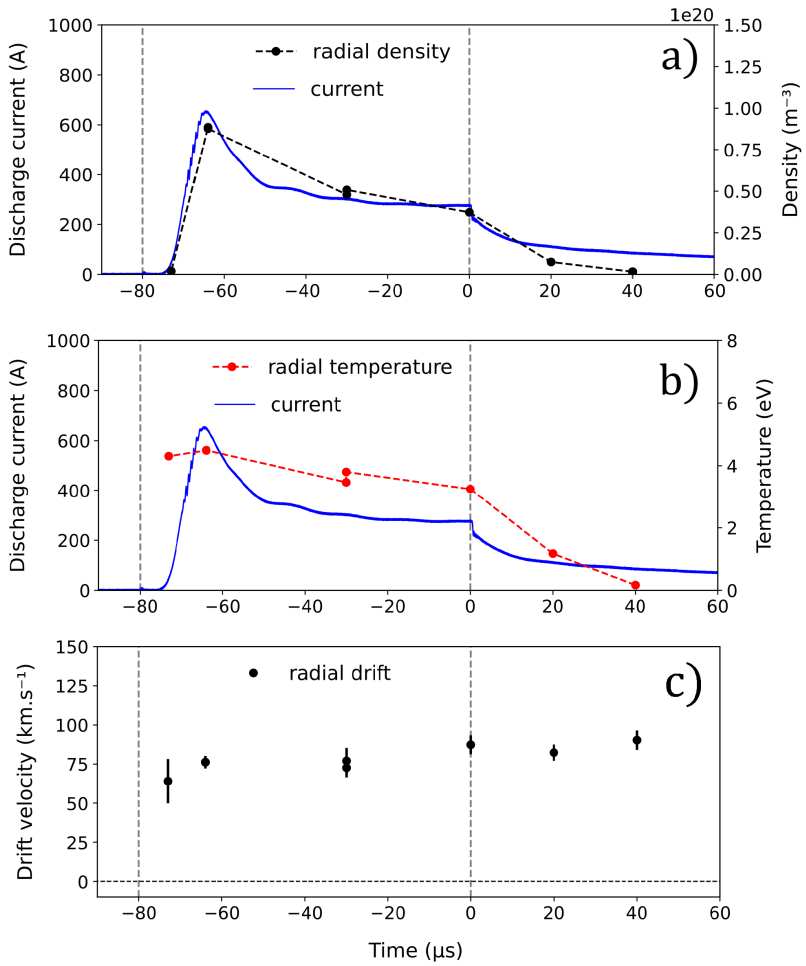

Figure 3.26: *Discharge C (He with Mo at 660 A): time evolution of the electron density (a), electron temperature (b), and drift velocity (c) along the radial direction. The current pulse waveform is shown in blue. Operating parameters are summarized in Table 3.5. The vertical dashed lines indicate the instants of discharge initiation and voltage cut-off (0 µs).*

3.6.1 Concluding remarks on the high-current measurements

By comparing the high-current conditions A (helium/titanium), B and C (helium/molybdenum) with each other, and with the lower-current conditions studied previously, a number of conclusions could be identified:

(i) the delay between the application of the current and the actual start of the discharge is is well described by Yushkov and Anders' model and seems to depend mainly on the nature of the target.

(ii) the value of the maximum electron density reached during the pulse depends solely on the value of the discharge current, whereas its variations over time depend on the nature of the target.

(iii) the electron heating mechanism seems to be linked solely to the nature of the target and does not depend on the power injected into the plasma.

3.6.2 Conclusion (Français)

Ces recherches, réalisées à proximité immédiate de la cathode d'un magnétron planaire, fournissent des informations sur les propriétés des électrons et leurs dérives à l'intérieur du piège magnétique qui ne sont généralement pas accessibles aux mesures par sondes. Dans cette implémentation, l'étude des anisotropies a été réalisée en positionnant le volume d'observation de sorte que les informations sur les propriétés des électrons dans la direction radiale (parallèles à la ligne de champ magnétique) et azimutale (perpendiculaires à la ligne de champ magnétique) puissent être directement mesurées. Le déclenchement temporel de l'acquisition permet d'établir une carte temporelle détaillée des propriétés des électrons depuis le moment de l'initiation de la décharge jusqu'à la phase de post-décharge.
Ces investigations expérimentales révèlent, pour les conditions considérées, que :

- Dans l'argon, bien que le profil de densité électronique tende à être similaire en forme à celui du profil de courant de décharge dans le temps, des différences dans les densités mesurées dans les directions radiales et azimutales peuvent être perçues à différents moments au cours de l'impulsion, suggérant un développement non uniforme de l'ionisation pendant l'impulsion,
- Dans l'argon, les décroissances exponentielles de la température et de la densité électroniques observées dans l'after glow sont cohérentes avec l'existence de deux temps caractéristiques : une décroissance initiale rapide au moment de la coupure de la tension, suivie d'une décroissance plus lente. Le diagnostic optique utilisé dans cette étude est suffisamment sensible pour caractériser de telles caractéristiques de post-décharge, comme illustré dans ces analyses,
- Le fonctionnement dans le régime HiPIMS est associé à la création de dérives radiales hautement dynamiques (impliquant probablement une expansion et une contraction du plasma à mesure que l'impulsion évolue) et de dérives azimutales (résultant d'un équilibre entre les dérives E×B et les dérives diamagnétiques),
- Dans l'hélium, une augmentation progressive de la température électronique peut être observée pour des durées d'impulsion plus longues, ce qui est cohérent avec le chauffage des électrons, du pré-glow jusqu'à la coupure de tension. Cela contraste avec les observations faites pour l'argon, où un plateau dans la température électronique est rapidement établi pendant les impulsions,
- Dans l'hélium, à proximité immédiate de la surface de la cathode, la dérive électronique radiale peut être observée dépassant significativement la dérive azimutale nette, avec des valeurs de l'ordre de 100 km/s maintenues pendant la durée de l'impulsion et des dérives dirigées vers l'extérieur. La force centrifuge pourrait être responsable de la création de cette dérive radiale importante et soutenue des électrons.

En plus d'améliorer la compréhension physique des caractéristiques de la décharge, ces évolutions fournissent des informations importantes qui peuvent être utilisées en conjonction avec des codes numériques pour le régime HiPIMS, encore en développement, comme dans Ref. [108]. L'accès à la dynamique des propriétés des électrons résolue le long d'une direction de vecteur d'onde particulière (parallèle et perpendiculaire au champ magnétique) peut fournir une clarté concernant l'existence d'anisotropies dans le plasma et comment de telles anisotropies peuvent évoluer dans le temps. Les magnitudes relatives des dérives radiales et azimutales peuvent fournir des informations sur la nature du confinement des électrons pour différentes conditions de fonctionnement et en fonction du temps.

En comparant les conditions de haute intensité de courant A (hélium/titane), B et C (hélium/molybdène) les unes avec les autres, et avec les conditions de courant plus faible étudiées précédemment, un certain nombre de conclusions ont pu être identifiées :

(i) le délai entre l'application du courant et le début réel de la décharge est bien décrit par le modèle de Yushkov et Anders et semble dépendre principalement de la nature de la cible.

(ii) la valeur de la densité électronique maximale atteinte pendant l'impulsion dépend uniquement de la valeur du courant de décharge, tandis que ses variations dans le temps dépendent de la nature de la cible.

(iii) le mécanisme de chauffage des électrons semble être lié uniquement à la nature de la cible et ne dépend pas de la puissance injectée dans le plasma.

Chapter 4

Electron properties in a Hall thruster: measurements and exploitation in linear kinetic theory

Contents

4.1 Influence of channel walls and the importance of radial exploration

The previous chapter focused on describing the temporal and spatial (axial) evolution of electron properties in a pulsed E×B source, with the information resolved along the azimuthal and radial directions. In Hall thrusters, the operation is considered steady state (i.e., standard operating conditions use a constant discharge current I_d with low standard deviation, often only a few percent of the mean I_d). It should be noted that even during what is considered steady state operation, large-scale global oscillations (such as the kHz-scale breathing mode [1]) could well lead to variations in the electron properties.

In addition to temporal fluctuations inherent to the discharge of the Hall thruster, spatial variations are expected. For example, the magnetization of the electrons at the exit plane will create

an ionization region with high electron temperatures and densities, superior to electron temperatures and densities encountered within the channel and far outside the exit plane. It is also expected that the plasma conditions will vary along the radial direction of the channel [122], [123]. Although rotational symmetry is found in a Hall thruster, the difference in radius between the inner and outer edge of the channel imposes a magnetic field that is necessarily larger on the inner edge [21]. The guiding center drift being inversely proportional to the value of the radial magnetic field, this has a direct influence on the drift velocity, as well as other electron properties.

As discussed earlier in this manuscript, studies on the electron cyclotron instability have identified it as a likely contributor to anomalous electron transport. Since the work of Adam, Héron and Laval [69] showing evidence for this link, the presence of this instability has been demonstrated in numerous simulations 1D and 2D [124, 125, 60, 75, 76]. Linear kinetic theory analysis has also been used to study the dispersion relation characteristics for the instability in different contexts [77, 70, 126, 127].
As discussed earlier, it was found from laser scattering experiments that a radial component of the instability exists, parallel to the magnetic field, and inclusion of this component in linear kinetic theory [2, 3] smoothes the discrete resonances (in real frequency and growth rate) to some degree, showing that excitation of this wave occurs not only at discrete wavenumbers, but over a broad and continuous range. This was an early indication of the importance of the radial direction in understanding the features of the instability and transport. It will be shown here that an additional effect can be attributed to the gradient of electron properties.

Subsequent numerical simulations by Héron and Adam [128] were performed accounting for the radial direction (2D radial-azimuthal particle-in-cell (PIC)) and revealed coupling of the instability to wall-emitted electrons, and a resulting influence on transport. These newly-observed effects studies were an indication of importance of the radial direction (overlooked in the vast majority of Hall thruster simulations which focused on an azimuthal-axial geometry), and the value of studying the evolution of the electron properties and dynamics in the radial direction.

In order to assert that the anomalous electron transport can be related to the different components of this instability, it is therefore necessary to use a PIC code that is not only 3D, but that also takes into account a sufficient number of particles to satisfy the statistical needs and results in an equilibrium state. Unfortunately, since the minimum size of a cell is limited by the Debye length, and the time step by the plasma frequency, a condition imposed by the electron properties, the time required to run 3D simulations is prohibitively long, particularly for the needs of thruster design and qualification. Progress towards a full 3D PIC code has recently been achieved in the work of Villafana *et al.* [79]. A 3D sparse-grid PIC method recently implemented at LAPLACE by Garrigues aims at reducing the computational time of the simulation by reducing the number of macroparticles in the model [129]. In order to qualify such codes with experimental data, it is important to measure, with high accuracy, properties of electrons in the acceleration and ionization region, where the anomalous transport takes place.

Several types of probes exist to measure these plasma conditions, of which the best known and most widely used is the Langmuir probe. Nevertheless, these probes must be used under very specific conditions, at the risk of obtaining results that are far from reality [130]. The acceleration and ionization region of a Hall thruster, where the anomalous transport of electrons takes place, does not usually correspond to these conditions, since there is a high magnetic field, and the mere presence of the probe in the plasma modifies its properties. For example, in the presence of a B field, the collection of electrons depends on the angle at which the probe is positioned relative

to the field lines, which can significantly influence the electron temperature measurement. As mentioned before, damage is caused to the probe itself in this zone of high power density, an issue amplified in a continuous discharge, since the thermal effects on the probes are amplified. The simplicity of probes (both in design and in implementation) means that they remain by far the most widely-used diagnostic (and indeed, recent work by Brown and Jorns uses Langmuir probe measurements to identify ECDI-like fluctuations in the ion current, albeit at different scales to those predicted in simulations [131]).

The use of non-intrusive optical diagnostics has advantages, as discussed in Chapters 2 and 3. Notably, incoherent Thomson scattering would allow for a highly spatially-resolved and accurate measurement of the radial electron properties, in the absence of plasma perturbation. This investigation on a Hall thruster is the subject of the current chapter.

4.2 Implementation

4.2.1 Diagnostic and installation procedure

Experiments are conducted on PPS-1350ML Hall thruster in the PIVOINE-2G installation at the ICARE laboratory of CNRS Orléans, within the framework of a measurement campaign funded by the CNES R&T program.

The thruster is a laboratory version of Safran Aircraft Engines (SAE) 1.5 kW PPS®1350 thruster, the same model used on ESA's SMART-1 probe in 2003. A description of the chamber can be found in Ref. [132], but this national testing facility has since been upgraded. Today, this chamber has a volume of 24.2 m^3, and maintains a pressure of 2×10^{-5} mbar at a gas flow rate of 21 mg/s of Xe.

The measurements performed in this chapter involve the use of the THETIS incoherent Thomson scattering diagnostic, applied in Chapter 3 to planar magnetron investigations, but with some important differences and adaptations. The goal of these investigations is to perform a radial exploration of the discharge channel, which implies a relative displacement of the observation volume in the plane parallel to the thruster exit plane, both horizontally and vertically. The PIVOINE-2G measurement installation only allows the thruster to be moved axially, so these new measurements require the displacement of the observation volume. A schematic showing the implementation is provided in Fig. 4.1.

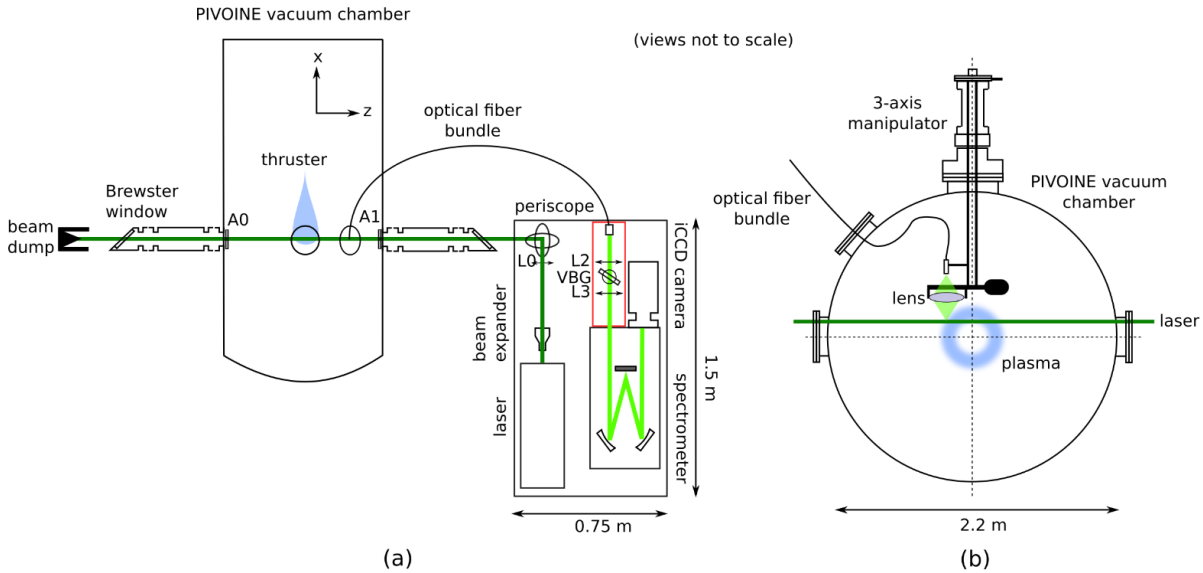

Figure 4.1: *(a) View of THETIS optical bench implementation on PIVOINE, and (b) configuration of light collection within the chamber*

Fig. 4.1 shows the full optical configuration. The main laser beam is directed across the plasma region, through tubes equipped with Brewster windows and apertures for the reduction of stray light. As is customary, the scattered radiation is recovered at an angle of 90° with respect to the laser line, and transmitted using an upgraded optical fiber bundle to the bench. In this implementation, two ports on the vessel are reserved for the initial laser beam. A third port at 45° is now used to connect the optical fiber to the exterior. The optical fiber and collection lens are mounted on an assembly of optical posts which connect to a 3-axis manipulator, allowing high-resolution positioning of the optics relative to the plasma volume.

In the recent past, our team successfully carried out the first comprehensive measurements with incoherent Thomson scattering on a Hall thruster [133]. However, this was a different configuration, with a 200 W thruster and a reduced chamber size. The observation branch was situated outside the vacuum chamber 2.8 (as was also done for planar magnetron investigations), which presented advantages, notably in the simplification of alignment procedures and the protection of the optics. Modifications to this setup are required for implementation on PIVOINE-2G, mainly due to the large diameter of the PIVOINE vessel (2.2 m) and therefore the necessity for placing the observation branch directly inside the chamber.

Key modifications to the experiment, made to achieve the first comprehensive incoherent Thomson scattering investigations of a large plasma thruster in this work, include:

- **New optical fiber bundle**: in the standard design of THETIS, an optical fiber bundle is used to conduct light from the plasma volume to the detector (iCCD camera). This bundle was installed outside the vacuum chamber in previous implementations. However, the dimensions of PIVOINE required that a new bundle be designed for installation within the vessel with a connection to the exterior. A new custom design was proposed and later fabricated by CeramOptec, using an assembly of 19 fused silica fibers of 300 μm-diameter. The numerical aperture of the new fibers was 0.29 (as opposed to the previous 0.22 [91]), improving light collection. The new bundle was constructed with flange allowing adaptation to the PIVOINE chamber.

- **New vacuum manipulator**: a 3-axis manipulator was used to allow the light collection optics inside the chamber (lens and optical fiber) to be precisely positioned from outside the vessel (Fig. 4.1), with an accuracy of 0.005 mm. This key functionality was needed for radial investigations of the thruster plasma.

- **Upgraded detection branch**: the new detection branch inside the vessel is composed of a lens of diameter 100 cm (to maximize light collection) with a focal length of 20 cm. The lens is located 40 cm above the object position (the laser line) and 40 cm below the end of the fiber bundle. The positioning of the lens relative to the thruster is a compromise: maximum light collection is facilitated by increasing the solid angle when the lens is brought a close as possible to the desired detection volume. However, positioning the lens close to the plasma increases the opportunity for damage from the ion beam and deposition.

The final configuration used is shown in Fig. 4.2. This figure shows, at left, the incoming probing beam (in green) traversing an aperture attached to the vessel wall and an alignment laser beam (in red) which was used when establishing the position of the thruster relative to the detection optics. At right, this figure shows various components of the detection branch mounted inside the vacuum chamber. The final configuration features a stabilizing spring (not visible) in order to damp oscillations of the post to which the optics are attached.

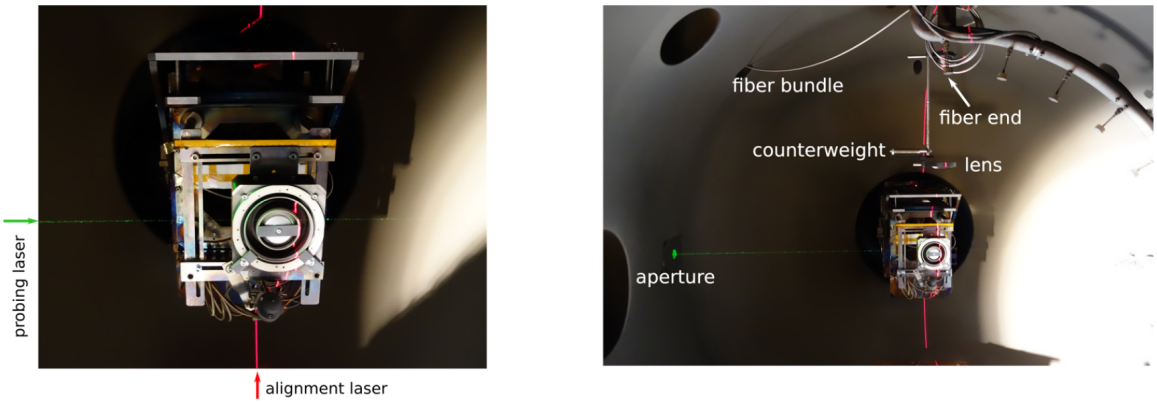

Figure 4.2: *Laser beam and optical configuration inside the vacuum vessel. At left, the inital laser beam (in green) crosses the thruster face laterally and an alignment laser beam (in red) is visible. At right, various components of the mounted detection branch, inside the vacuum chamber, are shown.*

4.2.2 Experimental challenges encountered

The complexity of the required new implementation, the device to be studied, and the environment, posed challenges, some of which are described below.

- **Presence of graphite dust**: Due to the presence of the collection lens directly inside the chamber, a surface deposition of the lens developed during the observation campaign. Two types of deposition on the lens were observed:

  (i) graphite dust, due to sputtering of the graphite tiles at the end of the vacuum chamber from bombardment by the ion beam, and

  (ii) apparent metallic particles, likely due to progressive sputtering of metal surfaces within the chamber. This coating required periodic polishing of the lens with diamond paste in order to avoid a gradual reduction in light transmitted through the lens.

  To account for this effect, the Raman calibration, performed for each radial position along the discharge channel, was repeated several times during the measurement campaign. It was observed that the signal intensity decreased with time, in linear relation with the time elapsed since the start of the thruster at the beginning of the campaign. A corrective factor taking into account the date on which each measurement was carried out was therefore added.

- **Fluorescence**: Measurements in the vicinity of the thruster exit plane, in contrast to measurements previously discussed on the planar magnetron in Chapter 3, posed an additional challenge: fluorescence from the $BNSiO_2$ ceramic walls of the thruster. To mitigate this effect, the Thomson spectra were processed by successive subtraction of the form A-B-C+D, where :

  A = Plasma emission + Thomson scattering + fluorescence + camera noise

  B = Plasma emission + camera noise

  C = Fluorescence + camera noise

  D = Camera noise

The radial evolution of the plasma properties was observed by successively placing the probed wave vector $\mathbf{k} = \mathbf{k_s} - \mathbf{k_i}$ along the radial direction, then along the azimuthal direction. The fluorescence is larger in amplitude on the side where the laser enters the chamber, which in this configuration corresponds to measurements in the radial direction, as shown in Fig. 4.3a. This leads to a higher background noise and uncertainties for these radial measurements. For this reason, the results presented in this chapter are limited to measurements in the azimuthal direction. Fig. 4.3b illustrates this: measurements are made at multiple radial positions (red squares) across the channel, with the observation wave vector at each point aligned with the azimuthal direction.

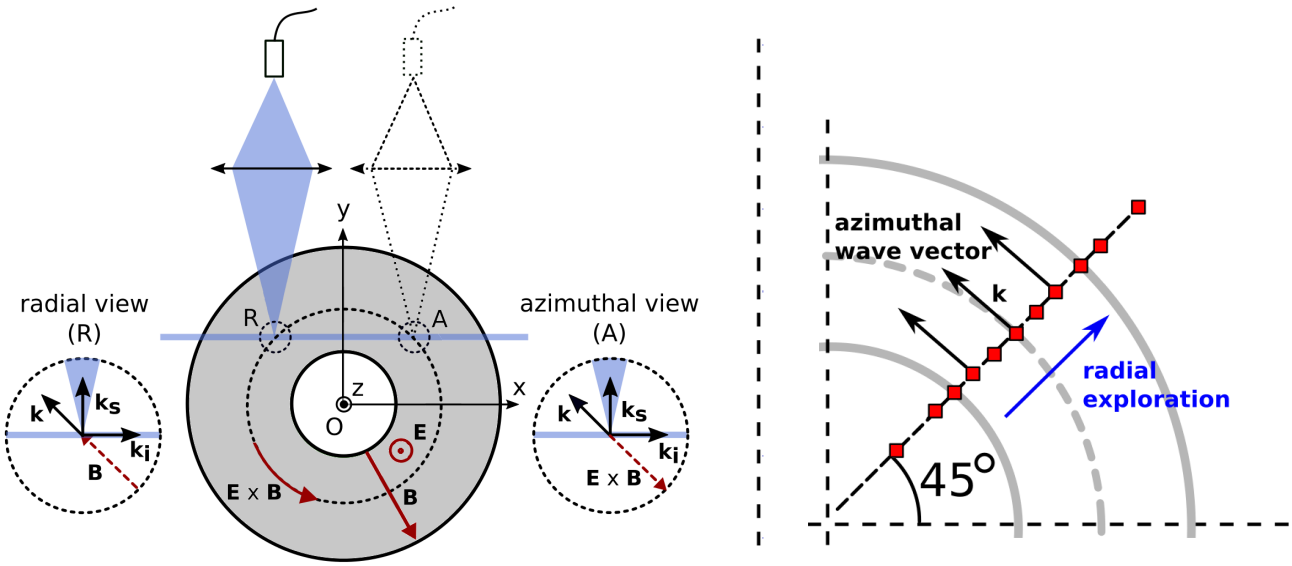

(a)

Front view of the Hall thruster, with the position of the observation branch to observe the electron properties along the radial (R) and azimuthal (A) directions. In the azimuthal position, the properties are therefore collinear to the E×B drift and perpendicular to the magnetics field lines B

(b)

Radial exploration of the discharge channel. Each of the red squares represents a different radial position where the electron properties are measured.

Figure 4.3

- **High stray light levels**: The choice was made to prioritize measurements at the thruster exit plane, in order to obtain information which could most closely reflect electron property variations from the inner to the outer thruster walls. The closest observation position achievable was 1 mm from the exit plane and this was used throughout. At this position, stray light was observed at high amplitudes even after filtering by the VBG. It was found that the dimensions of the thruster, compared to the 200 W version used in a prior study, allowed for laser light reflection over a much larger area. Adjustments were made to minimize the stray light, including repositioning of the retaining pieces of the ceramic, however, high levels of stray light would be expected for any configuration which places the laser beam near material surfaces. In a future investigation, a second VBG filter could be used in combination with the existing filter, to further attenuate stray light. However, for the research presented here, in the absence of this second filter, it was decided to manually exclude the central peak due to stray light on the Thomson spectra.//

- **Presence of Xe emission**: Xenon shows several characteristic emission lines which fall

within the spectral range of interest for the measurement of the electron temperatures (tens of eV). This is unavoidable and renders obtaining a good signal-noise ratio difficult, particularly when the electron temperatures are high (broad spectra) and/or the density is low (small spectral area). The level of the emission varies with the thruster operation regime. In these experiments, emission lines remained a problem even after the spectrum subtraction procedures. It was necessary to analyze Xe measurements using additional procedures specifically adapted to remove emission lines. This is addressed shortly. The choice was also made to complete the measurements using krypton, which shows far fewer emission lines within the spectral region of interest. This gave the opportunity to perform as study with better-resolved spectra. However, since xenon is the standard working gas for thrusters, obtaining more high quality measurements with xenon are a priority for the future. This can best be addressed by improving the signal-noise ratio as much as possible.

- **Apparent location of the electric field maximum**: Low signal levels were observed throughout most nominal regimes of the PPS-1350ML which were tested, despite the location of the observation volume only 1 mm from the exit plane. This contrasts with observations made on the 200 W thruster [133], where signals were readily detectable even a few millimeters from the exit plane. This observation on the PPS-1350ML is consistent with an electric field maximum (where the peak in electron density is expected) situated inside the thruster channel and less accessible to measurement. The solution adopted was the testing of various combinations of voltage, flow rate and coil current in order to find plasma configurations which shifted the plasma further outside the exit plane. These configurations were identified by monitoring the amplitude of the plasma emission as a guide. The inaccessibility of the electric field maximum proved to be an important restriction for the measurements in this experimental campaign.

4.2.3 Data processing

Chapter 2 of the manuscript explains how to extract electron density, temperature, and drift velocity from a Thomson spectrum. However, due to the issues detailed in the previous section, an additional step in the procedure is required. One of these issues is the presence of light emission from the plasma, which is theoretically eliminated by performing a background subtraction when obtaining the Thomson spectrum. However, in cases where this light emission is significant compared to the Thomson scattering, the remainder of this subtraction is not negligible and is superimposed on the Thomson spectrum. It is therefore necessary to measure the position of these emission peaks, then manually remove the points acquired at these spectral positions. This essential procedure nevertheless reduces the accuracy of the Gaussian fit, and increases the uncertainty in each of the electron properties.
The second difficulty is due to the very large stray light level, which extends over a range of a few nm due to the width of the instrument function. The part of the Thomson spectrum centered on 532 nm is therefore largely masked by this stray light, and has to be manually suppressed for each point as for the emission. This is illustrated in Fig. 4.4, where the exclusion zone (orange rectangle) for the Thomson spectrum is much wider than that for the Raman spectrum. This large exclusion zone has a significant effect on the accuracy of the drift velocity, defined by the position of the center of the Gaussian.

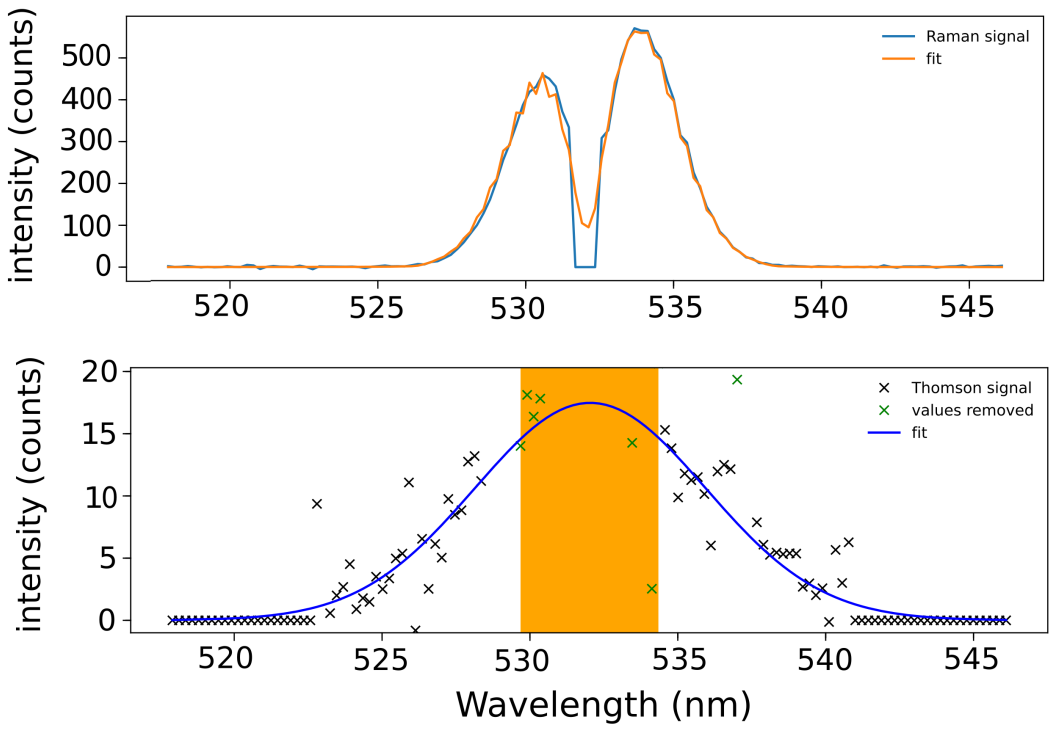

Figure 4.4: *Example of a Raman spectrum (top) and Thomson spectrum (bottom) acquired in the thruster experiments using a 600 lines/mm grating. The orange rectangle represents the center of the spectrum which is not taken into account for Gaussian fitting due to large stray light levels, redistributed over relatively a wide spectral range.*

4.3 Experimental measurements: conditions and results

Two noble gases were used in these investigations, xenon and krypton, corresponding to the most commonly used gases in Hall-effect thrusters. For each gas, the temperature, density and azimuthal drift velocity of the electrons was measured. The conditions used in these investigations of thruster radial properties are summarized in Table 4.1. This table shows the anode and cathode mass flow rates (respectively, $\dot{m}_a$ and $\dot{m}_c$) in mg/s, the discharge current I_d in A, discharge voltage U_d in V and the magnitudes of the radial magnetic field measured at the inner ceramic channel rim ($B_{r,\,inner}$), center of the channel ($B_{r,\,center}$), and the outer ceramic rim ($B_{r,\,outer}$).

Measurements were performed in a radial sweep across the entire width of the 1.5 cm-wide channel, in 1.875 mm increments, as shown in Figure 4.3b. Four additional measurement points were added on either side of the channel, two going radially towards the thruster axis, and two radially outward beyond the outer channel rim, in order to allow investigation of the plasma evolution over a greater radial distance. 13 distinct measurement points overall were made, each of which was made in the plane parallel to the exit plane, at a distance $z = 1$ mm. For the xenon measurements, only 8 points out of the 13 were kept, because of the absence of a sufficiently distinct Thomson signal in the eliminated cases (i.e., the signal to noise ratio was too poor to allow the Thomson signal to be separated from the background noise).

	$\dot{m}_a$ (mg/s)	$\dot{m}_c$ (mg/s)	I_d (A)	U_d (V)	$B_{r,\,inner}$ (G)	$B_{r,\,center}$ (G)	$B_{r,\,outer}$ (G)
Kr	6.5	0.7	9.6	125	265	175	155
Xe	8	0.7	8.8	130	250	160	140

Table 4.1: *Operating conditions for incoherent Thomson scattering experiments with krypton and xenon.* $\dot{m}_a$ *and* $\dot{m}_c$ *are the gas flow rates to the anode and cathode, respectively.* B_r *is the radial magnetic field measured 1 mm outside the exit plane of the thruster at three radial locations: the inner ceramic edge, the center of the ceramic channel, and the outer ceramic edge.*

Radial variation of electron temperature

Measurements obtained for the radial variation of the electron temperature in Kr and Xe are shown in Fig.4.5.
With Kr, two clear trends can be seen. There is a first linear growth in temperature between 0 - 12 mm from the inner channel wall, followed by a second linear growth with a larger slope in the vicinity of the outer channel. The electron temperature varies from 14 eV at the inner wall to a maximum of 63 eV beyond the outer wall. This observation provides clues regarding the nature of the electron confinement, showing that the region of electron magnetization extends radially past the edge of the outer ceramic.

The temperature values obtained with Xe are much noisier, due to the higher emission lines in the spectral range of interest, as mentioned previously. We can nevertheless see that the tendency towards higher electron temperatures towards the outer channel, clear in the Kr case, appears to be mirrored here.

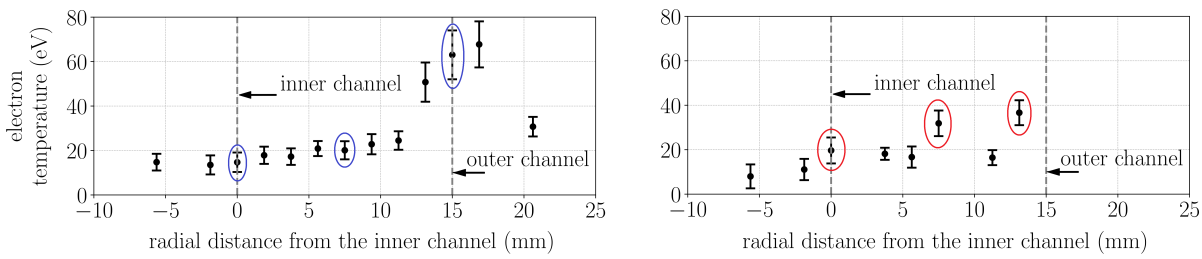

Figure 4.5: *Evolution of electron temperature in the radial direction, measured by incoherent Thomson scattering, for (left) krypton, and (right) xenon. The experimental conditions corresponding to these results are listed in Table 4.1. The points circled in blue and red are highlighted for the purpose of a later discussion in this chapter.*

Radial variation of electron density

Measurements obtained for the radial variation of the electron density in Kr and Xe are shown in Fig.4.6.
For Kr, an increase in the electron density towards the outer wall is observed, from 4.7×10^{17} m^{-3}, to 1.38×10^{18} m^{-3}. There is also a local maximum observable near 5 mm from the inner wall, followed by a second maximum beyond the outer wall. The first density maximum inside

the channel may be linked to the particular potential structure created at the chosen operating point. The second maximum in density, located beyond the edge of the outer channel (between 15 and 20 mm), mirrors the finding for the electron temperature, where the hottest electrons were localized in this region. These electrons are expected to contribute to increased ionization (and thus higher electron densities) in this region. For Xe, the measurement uncertainty is larger, but an increase in the electron density moving towards the outer channel remains visible.

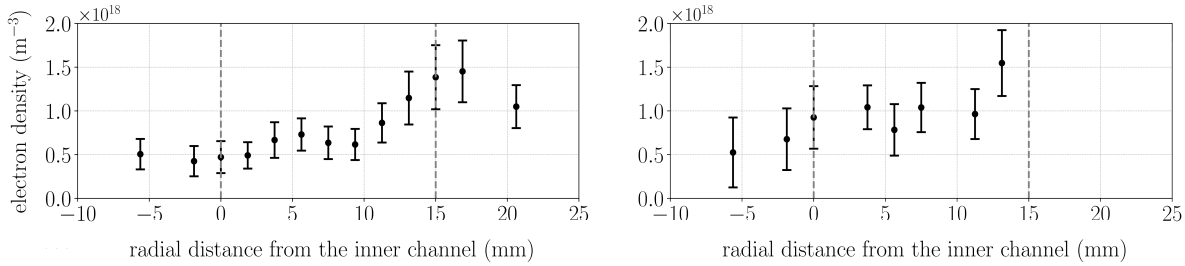

Figure 4.6: *Evolution of electron density in the radial direction, measured by incoherent Thomson scattering, for (left) krypton, and (right) xenon. The experimental conditions corresponding to these results are listed in Table 4.1.*

Radial variation of electron drift velocity

For Kr, the electron drift velocity increases from the inner to the outer wall, as seen in Fig. 4.7. This is consistent with the non-uniformity of the radial magnetic field (arising from the differing diameters of the inner and the outer channels). The electric field value at the axial location for the measurements is unknown, but a typical value on the order of 10^4 V/m [134], with the values of magnetic field measured at the walls, would give an E×B drift velocity in the range of 10^5 - 10^6 m/s, similar to the range of values seen in Fig. 4.7.
In Xe, the drift velocities are substantially lower, and no clear trend of increasing velocities towards the outer channel is apparent. This may be due in part to the noisier data, but it might also be due to the particular operating regime and the resulting potential structure at the measurement location.
Overall, we have noted the increase in the electron temperature, density and drift velocity as we move towards (and beyond) the outer channel wall. It is interesting to note that, in contrast, a plateau in the properties exists near the inner wall (radial distances < 0 mm). It is an indication that there is a uniform plasma extending radially for a few millimeters around the inner wall location, while near the outer wall, the plasma properties reach their maximum a few millimeters outside the channel (possibly related to the beam divergence). The radial maps of electron properties provide some insight into such features and suggest non-uniform ionization and electron energization in the radial direction.

4.3.1 Discussion

This is the first measurement of radial variations of electron properties in a Hall thruster using incoherent Thomson scattering.

This measurement indicates that the plasma is strongly inhomogeneous along the radial direction, but more importantly that the electron density, temperature, and the velocity drift are generally increasing towards the outer channel wall. This is different from what has previously

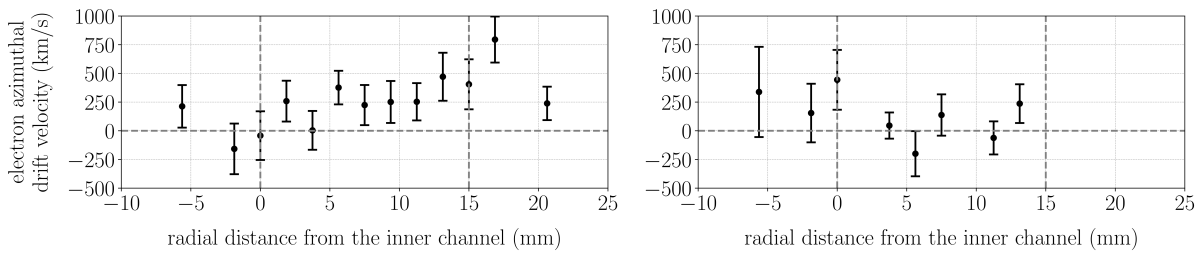

Figure 4.7: *Evolution of electron drift velocity in the radial direction, measured by incoherent Thomson scattering for (left) krypton, and (right) xenon. The experimental conditions corresponding to these results are listed in Table 4.1.*

been observed with Langmuir probe measurements, which instead show an isothermal temperature along a field line, or a higher temperature near the inner channel [135]. The effects observed in this work seem to be much more pronounced in krypton, whereas most of the prior measurements or radial simulations have been performed with xenon.

Nevertheless, recent PIC simulations reveal, under certain conditions, a similar behavior, with an overall increase of the electron temperature towards the outer edge of the channel. In particular, Ref. [136] finds both an anisotropy of electron properties, and different features of the inner and outer wall sheaths. The temperature perpendicular to the field lines increases very strongly near the outer wall, and decreases near the outer wall. The difference in sheath behavior at the two edges is attributed to the magnetic mirror effect, as well as to the centrifugal force due to the E×B drift. Prior work by Héron and Adam [128] also revealed clear differences in the sheaths established at the inner and outer channel walls.

The evolution of the density gradient clearly indicates that there is a non-uniform radial ionization, which would indicate an (axial) electric field value which is not the same across the entire channel width, for the conditions considered.
The main difference between the two gases is found in the drift velocity. Previous Thomson scattering measurements on a smaller thruster had also found drift velocities compatible with what is observed here in the case of krypton [133]. The diamagnetic drift is opposite in direction to the E×B drift (and weaker than the E×B drift, since the measured electron drift velocity remains positive).
The observed drift velocity is much lower for xenon, but this is not necessarily significant. There is always the possibility that the axial locations for the peak drift velocities, for the conditions shown, are not identical. Thus, by setting the axial observation position at 1 mm outside the thruster exit plane, this position may be close to the peak drift location for krypton, but miss the peak drift location for xenon (situated potentially further inside the channel). Previous measurements have already qualitatively demonstrated the existence of regions in which electron drift velocity varies significantly, sometimes even reversing the direction of rotation [137].

The experimental results provide interesting clues on the degree to which the electron properties (and thus, linked features such as the ionization and potential) vary radially. It is difficult to make overarching conclusions, given the limited set of experimental conditions tested, and the experimental constraints encountered.

However, in the next stage of this study, work is planned to compare the experimental results obtained to those from a sparse PIC numerical simulation, currently under development by

Garrigues and Chung To Sang [138]. This simulation work seeks to study the evolution of the potential and electric field in three dimensions, including the radial direction, and will model the experimental conditions used in this work. This complementary analysis should prove valuable for interpreting the experimental trends in electron properties.

4.3.2 Discussion (Français)

Il s'agit de la première mesure des variations radiales des propriétés électroniques dans un propulseur à effet Hall utilisant la diffusion Thomson incohérente.
Cette mesure indique que le plasma est fortement inhomogène le long de la direction radiale, mais plus important encore, que la densité électronique, la température et la dérive de vitesse augmentent généralement vers la paroi externe du canal. Cela diffère de ce qui a été observé précédemment avec les mesures par sonde de Langmuir, qui montrent plutôt une température isotherme le long d'une ligne de champ, ou une température plus élevée près du canal interne [135]. Les effets observés dans ce travail semblent être beaucoup plus prononcés dans le krypton, tandis que la plupart des mesures ou simulations radiales antérieures ont été effectuées avec du xénon.

Cependant, des simulations PIC récentes révèlent, dans certaines conditions, un comportement similaire, avec une augmentation globale de la température électronique vers le bord externe du canal. En particulier, la référence [136] trouve à la fois une anisotropie des propriétés électroniques et différentes caractéristiques des gaines de paroi interne et externe. La température perpendiculaire aux lignes de champ augmente très fortement près de la paroi externe et diminue près de la paroi externe. La différence de comportement de la gaine aux deux bords est attribuée à l'effet de miroir magnétique, ainsi qu'à la force centrifuge due à la dérive E×B. Des travaux antérieurs de Héron et Adam [128] ont également révélé des différences claires dans les gaines établies aux parois des canaux interne et externe.
L'évolution du gradient de densité indique clairement qu'il y a une ionisation radiale non uniforme, ce qui indiquerait une valeur de champ électrique (axial) qui n'est pas la même sur toute la largeur du canal, pour les conditions considérées.
La principale différence entre les deux gaz se trouve dans la vitesse de dérive. Des mesures précédentes par diffusion Thomson sur un propulseur plus petit avaient également trouvé des vitesses de dérive compatibles avec ce qui est observé ici dans le cas du krypton [133]. La dérive diamagnétique est opposée à la dérive E×B (et plus faible que la dérive E×B, puisque la vitesse de dérive électronique mesurée reste positive).
La vitesse de dérive observée est beaucoup plus faible pour le xénon, mais cela n'est pas nécessairement significatif. Il existe toujours la possibilité que les emplacements axiaux pour les vitesses de dérive maximales, pour les conditions présentées, ne soient pas identiques. Ainsi, en fixant la position d'observation axiale à 1 mm à l'extérieur du plan de sortie du propulseur, cette position peut être proche de l'emplacement de la dérive maximale pour le krypton, mais manquer l'emplacement de la dérive maximale pour le xénon (potentiellement situé plus à l'intérieur du canal). Des mesures antérieures ont déjà qualitativement démontré l'existence de régions dans lesquelles la vitesse de dérive électronique varie considérablement, parfois même en inversant la direction de rotation [137].
Les résultats expérimentaux fournissent des indices intéressants sur le degré de variation radiale des propriétés électroniques (et donc, des caractéristiques liées telles que l'ionisation et le potentiel). Il est difficile de tirer des conclusions générales, compte tenu de l'ensemble limité de conditions expérimentales testées et des contraintes expérimentales rencontrées.
Cependant, dans la prochaine étape de cette étude, il est prévu de comparer les résultats expérimentaux obtenus à ceux d'une simulation numérique PIC sparse, actuellement en cours de

développement par Garrigues et Chung To Sang [138]. Ce travail de simulation vise à étudier l'évolution du potentiel et du champ électrique en trois dimensions, y compris dans la direction radiale, et modélisera les conditions expérimentales utilisées dans ce travail. Cette analyse complémentaire devrait s'avérer précieuse pour interpréter les tendances expérimentales des propriétés électroniques.

4.4 Comparison of experimental results with linear kinetic theory

4.4.1 3D model to describe azimuthal instability

The connection between anomalous electron transport and the electron cyclotron drift instability (ECDI) was briefly addressed in Section 1.6.2. In order to describe the connection between the ECDI and the plasma properties, it is convenient to employ linear kinetic theory. The 3D dispersion relation of this azimuthal mode was established by Tsikata [2] following experimental results showing 3D propagation for the instability. This dispersion relation was subject to assumptions relevant to a Hall thruster. This same approach applies to both Hall thruster and HiPIMS discharges. The assumptions made are as follows:

(i) the high degree of ionization in Hall thrusters and HiPIMS magnetrons ensures that the neutral density is low enough to consider the plasma as collisionless.

(ii) the vectors $\mathbf{E}$ and $\mathbf{B}$ are idealized and considered as purely axial and radial respectively. The drift velocity of the electrons is therefore equal to $\mathbf{V_d} = -\left(\frac{E}{B}\right)\mathbf{e_y}$. This hypothesis will be discussed in the particular case of the planar magnetron, since a non-negligible drift in the radial direction has been observed experimentally for several conditions in this work.

(iii) no spatial gradient is considered for E and B. Similarly, the plasma is also considered to be uniform, and thus the electron properties unchanged in all directions. This hypothesis will also be discussed later.

(iv) the ions are not affected by the magnetic field, and move at constant velocity in the axial direction, contrary to the electrons, which are magnetized. The latter follow a Maxwellian and isotropic velocity distribution.

(v) the electrostatic perturbation of the potential is of the form $e^{i(\mathbf{k}.\mathbf{r}-(\omega+i\gamma)t)}$), with γ the instability damping frequency, and the Fourier transforms are derived assuming a monochromatic plane wave.

(vi) Only one type of atomic species (Xe or Kr) is considered at a time. This assumption is more natural in the case of the thruster (though not accurate, because multiply-charged species are present in most regimes), but more difficult to defend in the case of the HiPIMS discharge, where the ions can come from both the target and the working gas. This will be examined in detail.

Under the given assumptions, the linear kinetic theory gives the following dispersion relation:

$$1 + \frac{1}{k^2\lambda_{De}^2}\left[1 + \mathrm{g}\left(\frac{\omega - k_y V_d}{\omega_c}, k_\perp^2 r_c^2, k_z^2 r_c^2\right)\right] - \frac{1}{2k^2\lambda_{Di}^2}\mathrm{Z}'\left(\frac{\omega - k_x v_p}{\sqrt{2}kv_{thi}}\right) = 0 \tag{4.1}$$

where λ_{De}, ω_c, r_c are respectively the Debye length, the electron cyclotron frequency and the Larmor radius for electrons. The wave number k can be separated into 3 components, k_x, k_y and k_z, and by convention $k_\perp$ is in the plane perpendicular to the magnetic field lines such that $k_\perp = \sqrt{(k_x^2 + k_y^2)}$. The constants λ_{Di}, v_p and v_{thi} concern the ions and represent, respectively the Debye length, the ion axial velocity and the ion thermal velocity. The Gordeev function g is defined as [139] :

$$\mathrm{g}(A, B, C) = \frac{A}{\sqrt{2C}}\mathrm{e}^{-B}\sum_{m=-\infty}^{+\infty}\mathrm{Z}\left(\frac{A-m}{\sqrt{2C}}\right)\mathrm{I}_m(B) \tag{4.2}$$

with I_m representing the modified Bessel functions of first kind,

$$I_m(x) = \sum_{p=0}^{\infty}\frac{1}{p!(p+m)!}\left(\frac{x}{2}\right)^{2+m} \tag{4.3}$$

Z and Z' are, respectively, the plasma dispersion function and its derivative. These are defined as

$$\mathrm{Z}(x) = i\sqrt{\pi}e^{-x^2}\,\mathrm{erfc}(-ix) \tag{4.4}$$

$$\mathrm{Z}'(x) = -2[1 + x\mathrm{Z}(x)] \tag{4.5}$$

where $erfc$ is the complementary error function.

Several parameters of this equation, such as the Debye length, are directly derived from the electron properties, which are assumed to be discrete in the model. The numerical resolution of this dispersion relation was enabled by the iterative method developed by Cavalier in 2013 [77]. It allows the influence of the inclusion of a component in the k_z direction (parallel to the magnetic field lines) to be checked. It also allows the evaluation of the effect of a modification or a variation of the plasma properties on the dispersion relation.

In Ref. [77], Equation 4.1 was written, in the cold ion limit, as:

$$1 + \frac{1}{k^2\lambda_{De}^2}\left[1 + \mathrm{g}\left(\frac{\omega - k_y V_d}{\omega_{ce}}, k_\perp^2 r_c^2, k_z^2 r_c^2\right)\right] - \frac{1}{(\omega - k_x v_p)^2} = 0 \tag{4.6}$$

This assumption was based on experimental measurements showing a temperature of the ions in the azimuthal direction that is about two orders of magnitude lower than that of the electrons, based on spectroscopic (laser-induced fluorescence) measurements [140]. We initially adopted this choice, including for HiPIMS discharges, although it is more questionable, especially in cases

where a light gas such as helium is used. To better reflect reality, the model was then modified to take into account a non-zero ion temperature of 0.3 eV, still according to Cavalier's method [3].

This low temperature value has only a limited influence on the instability of the mode. This is no longer true if the ion temperature is higher. The effect of increasing the ion temperature is to damp the ECDI, and it is well known that the ion temperature is strongly anisotropic in a Hall thruster, with much higher values in the axial direction, as measured with LIF [141]. The ECDI is therefore extremely damped in the axial direction. The study is limited to the purely azimuthal direction, for which a low ion temperature is a valid assumption.

The method adopted seeks to obtain, by iteration, a value of the real frequency ω for each value of k respecting Equation4.6. Assuming that $k_y V_d >> \omega$, we take an initial value of $\omega = 0$, which is injected in the Gordeev function to obtain a new value of ω and so on to converge to the result. The iterative scheme in its non-normalized form, and taking only the positive root, is of the form :

$$\hat{\omega}_{n+1} = \hat{k}_x \hat{v}_p + \hat{\omega}_{r,n+1} + i\epsilon\hat{\gamma}_{n+1} \tag{4.7}$$

with $\hat{\omega}_{r,n+1}$, $\hat{\gamma}_{n+1}$, h_n defined by :

$$\begin{aligned}
\hat{\omega}_{r,n+1} &= \frac{\hat{k}}{\sqrt{2}}\sqrt{\frac{h_n + \sqrt{h_n^2 + g_{i,n}^2}}{h_n^2 + g_{i,n}^2}} \\
\hat{\gamma}_{n+1} &= \frac{\hat{k}}{\sqrt{2}}\sqrt{\frac{-h_n + \sqrt{h_n^2 + g_{i,n}^2}}{h_n^2 + g_{i,n}^2}} \\
h_n &= 1 + k^2 + g_{r,n}
\end{aligned} \tag{4.8}$$

where $g_{r,n}$ and $g_{i,n}$ are the real and imaginary parts of the Gordeev function at step n, and ϵ is the sign of $-g_{i,n}$.

For the numerical solution of the Gordeev function (Eq. 4.2) and the modified Bessel functions of the first kind (Eq. 4.3), n is taken in the interval $[-20, 20]$ and p in the interval $[0, 200]$. A larger number p of functions must be considered in the case of high wave number, but the limit here is to values of k_y up to 13000 rad.m^{-1}, for comparison with experimental values. Too small an interval n in the Gordeev function attenuates the amplitudes of the resonances, but it has been observed empirically that an increase beyond the chosen interval has no effect on the amplitude. The complementary error function in the plasma dispersion function is developed asymptotically in $+\infty$ and iterated up to 25. The total number of iterations on ω depends on the comparison between ω_n and ω_{n-1}, until the difference between the two (normalized) is less than 10^{-10}.

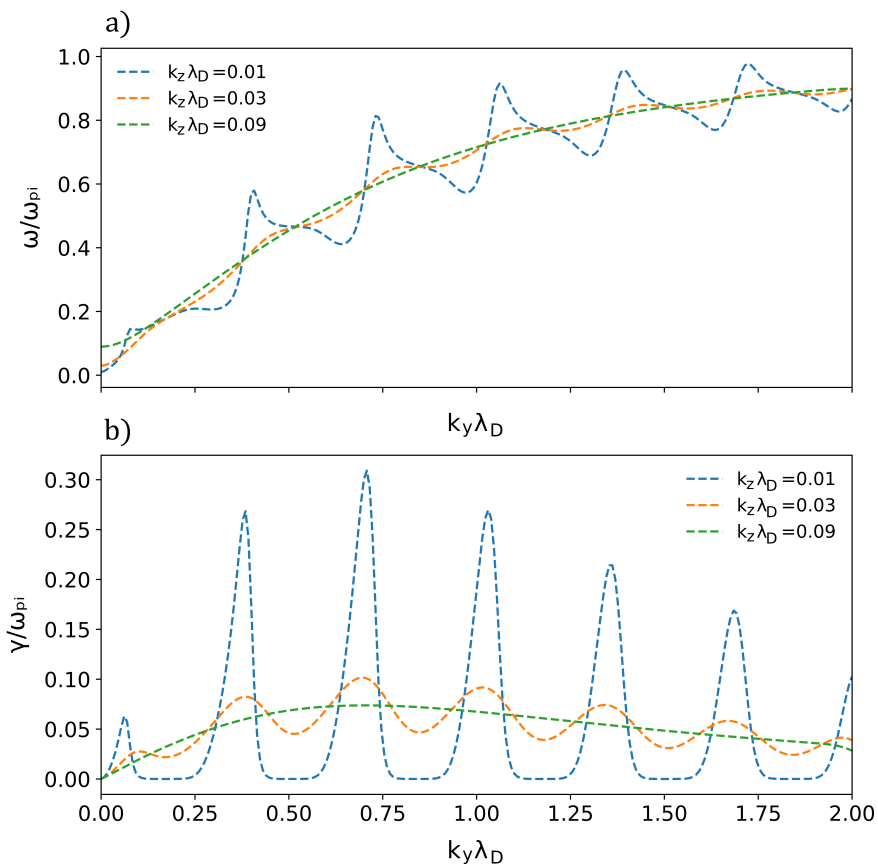

Figure 4.8: *Influence of k_z on the dispersion relations and the growth rate (normalized real frequency ω/ω_{pi}, normalized imaginary frequency γ/ω_{pi}), under typical conditions of a 5 kW Hall thruster PPS-X000 from Safran. Normalizations are made by λ_{De}, the ion plasma frequency $\omega_{pi} = \sqrt{e^2 n_i/\epsilon_0 M_{ion}}$ and the speed of sound $c_s = \lambda_{De}/\omega_{pi}$. This is an exact reproduction of a curve from Cavalier's thesis [3] (p. 36), with identical parameters, and has been made to validate the iterative code used in this thesis.*

Figure 4.8 illustrates the typical form of the dispersion relation. It shows both the real frequency (a) and the growth rate (b) as a function of k_y, for different values of k_z, and arbitrary fixed plasma conditions representative of a Hall effect thruster. For low values of k_z, we clearly observe peaks in the growth rates at the positions of the resonance harmonics between $k_y V_d$ and the electron cyclotron frequency, as explained in Section 1.6.2. In contrast, for higher values of k_z, the growth rate is strongly attenuated and both real and imaginary frequencies become less discrete. Regardless of the value of k_z, the maximum value of the real frequency tends towards the ion plasma frequency, as with an ion acoustic wave.

It should also be mentioned that Figure 4.8 shows that the value of k_z has no influence on the value of wavenumber at which the wave is excited, but only on amplitude of the growth rate γ and to some extent, if discrete lobes remain present, the real frequency ω.

4.4.2 Injection of a unique set of values into the discrete model

The Cavalier model that we have just presented was developed under conditions corresponding to a Hall effect thruster almost identical to the one used in our experiment. We can therefore, by taking similar assumptions, adapt his method to our conditions. At the time, he used the group velocity obtained from experimental dispersion relations to recover electron properties with his model, notably electron temperature. In this manuscript, we have the opportunity, for the first time, to apply accurate measurements of these electron properties using incoherent Thomson scattering measurements, and we can therefore perform the reverse process. By injecting our experimental results on true electron properties into the code, we can obtain a theoretical dispersion relation, which may then be compared directly to previous results obtained by Tsikata [2].

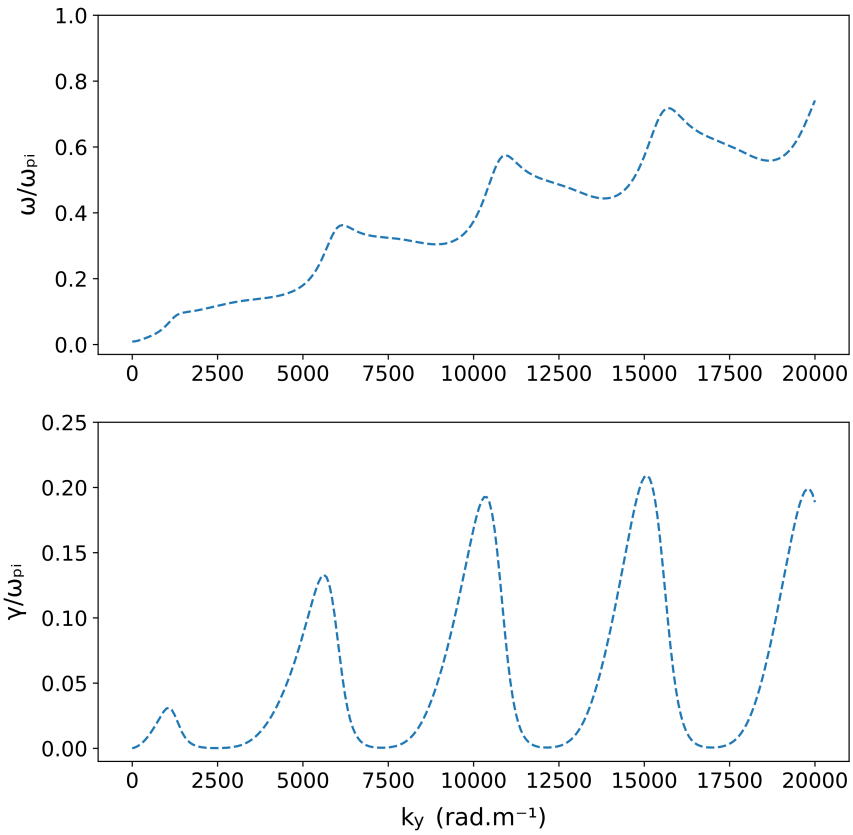

Figure 4.9: *Dispersion relations and growth rate normalized by ω_{pi}, corresponding to the 5th point from the left, for krypton (i.e. channel center), in Figure 4.5.*
Corresponding measured conditions: T_e = 22.82 eV, n_e = 6.16× 10^{17} m^{-3}, B = 165.4 G

The experimental conditions are as follows: the ejection velocity of the ions is taken to be v_p = 1.6× 10^4 m.s^{-1}, and we assume a single degree of ionization. In the absence of reliable electric field measurements, and despite the observed radial variation of ionization, the electric field is fixed constant at E = 10^4 V.m^{-1}. In the future, 3D PIC simulations may provide clarity on the precise value of this parameter. The values of drift velocity, electron temperature and electron density are determined through the incoherent Thomson scattering measurements carried

out using the THETIS diagnostic. The magnetic field B varies radially in the channel. It was measured at three points, at the center of the discharge channel and at the walls. It was then interpolated for the rest of the positions, assuming an intensity variation proportional to the inverse of the square of the radius, due to the circular geometry. Therefore, only the dispersion relation for the positions between the two walls, $r \in [0, 15]$ mm are plotted, in the absence of a reliable measurement of the magnetic field outside the channel. The value of k_z is taken to equal to 540 rad.m^{-1}, the value measured experimentally by Tsikata [2] in experiments showing the existence of all three wavenumber components for the ECDI.

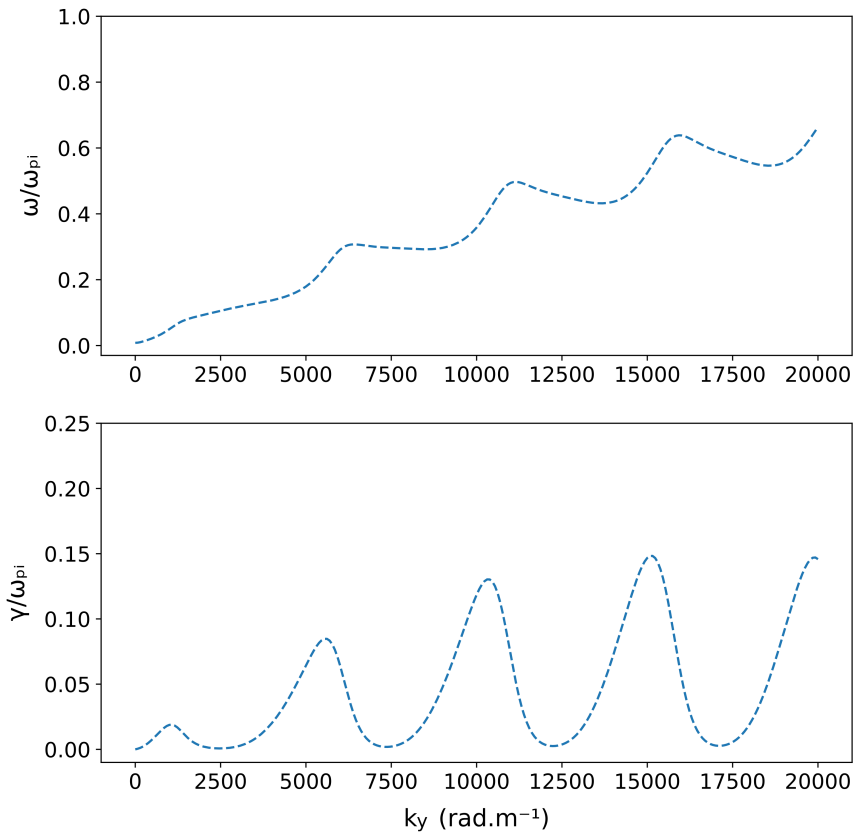

Figure 4.10: *Dispersion relations and growth rate normalized by ω_{pi}, corresponding to the 8th point from the left, for xenon (i.e. channel center), in Figure 4.5.*
Corresponding measured conditions: T_e = 31.86 eV, n_e = 1.04×10^{18} m^{-3}, B = 146.6 G

Figure 4.9 shows both the real frequency and growth rate obtained, using the directly measured electron and magnetic field properties at the center of the discharge channel, for krypton. Figure 4.10 shows the same for xenon. Here, the drift velocity was simplified and taken equal to E/B, and the value of real frequency and growth rate were normalized by ω_{pi}. The chosen value of k_z corresponds here to a value of $k_z\lambda_d = 0.45$, allowing comparison with what was obtained for Figure 4.8. We find the same lobes caused by the resonances in the growth rate, which are superposed on a simple ion acoustic wave (frequency).

4.4.3 Smoothing by injecting several sets of values into the discrete model

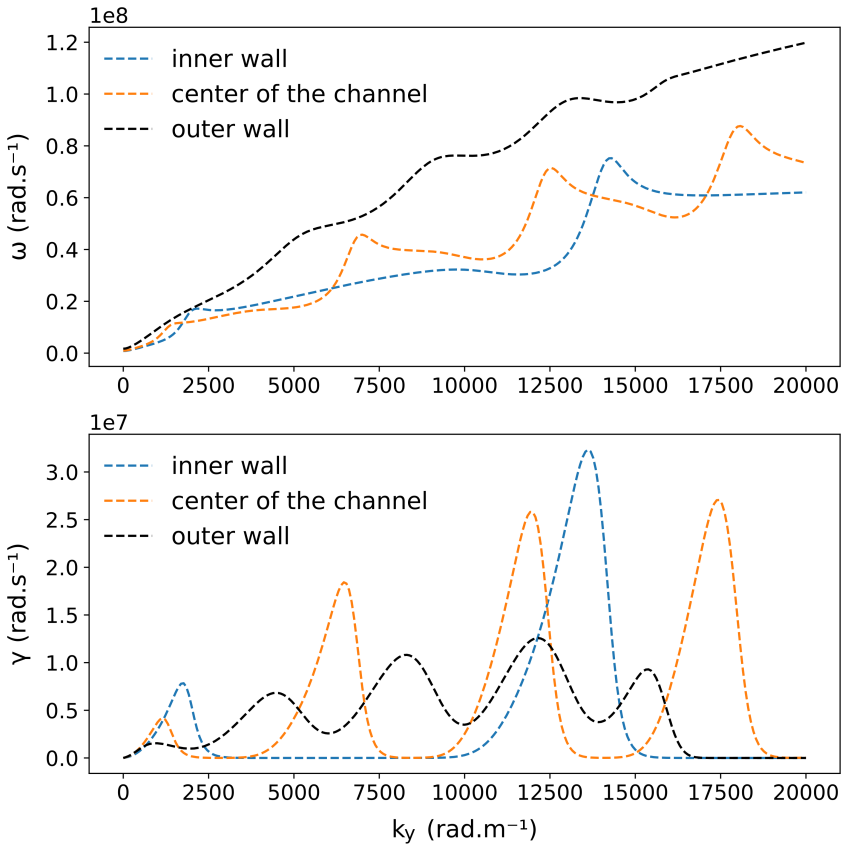

Figure 4.11: *Dispersion relations and growth rate for the three circled points of Figure 4.5, for krypton. These points correspond to three different radial locations in the channel.*
inner wall : $T_e = 14.71$ *eV,* $n_e = 4.72 \times 10^{17}$ m^{-3}, $B = 266$ *G*
center : $T_e = 20.09$ *eV,* $n_e = 6.35 \times 10^{17}$ m^{-3}, $B = 178$ *G*
outer wall : $T_e = 63.03$ *eV,* $n_e = 1.39 \times 10^{18}$ m^{-3}, $B = 153.4$ *G*

In order to verify the influence of the different measured experimental parameters on the dispersion relation for the ECDI, we overlay on Figures 4.11 and 4.12 the dispersion relations obtained for three distinct radial positions of the observation volume, namely at the level inner wall, the center of the channel, and the outer wall. Since the electron drift velocity has significant uncertainties, of the order of the value of the measured point, the decision is made to fix the value of $V_d = E/B$ in order to be independent of these error limits. The resulting values, of the order of 400 km.s^{-1} at the inner wall, to 600 km.s^{-1} at the outer wall, are quite compatible with the experimental values. The electron temperature values used at each location correspond to the points circled (in blue for krypton, in red for xenon) from Fig.4.5, and the corresponding electron densities determined for these radial locations are also used.

Some key observations can be made for the linear kinetic theory dispersion relation, common to both gases:

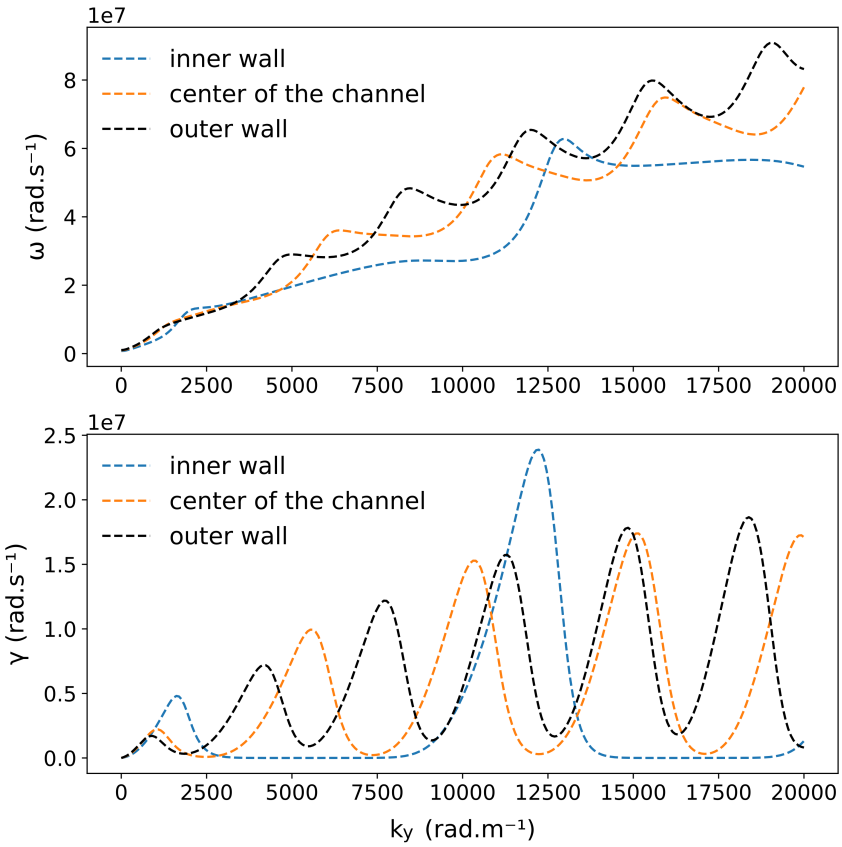

Figure 4.12: *Dispersion relations and growth rate for the three circled points of Figure 4.5, for xenon. These points correspond to three different radial locations in the channel.*
inner wall : $T_e = 19.66$ *eV,* $n_e = 9.25 \times 10^{17}$ m^{-3}, $B = 250$ *G*
center : $T_e = 31.86$ *eV,* $n_e = 1.04 \times 10^{18}$ m^{-3}, $B = 166$ *G*
outer wall (-1.875 mm) : $T_e = 36.64$ *eV,* $n_e = 1.55 \times 10^{18}$ m^{-3}, $B = 141.8$ *G*

(i) the number of unstable lobes in the k_y range increases as one approaches the outer wall. This effect can of course be attributed to the increase in azimuthal drift velocity related to the magnetic field gradient.

(ii) there is a smoothing effect on the lobes as electron temperature increases, moving radially towards the outer wall. This feature is more pronounced in krypton (where higher electron temperatures are measured) than in the case of xenon.

The important concept here is the variation of electron properties along the discharge channel. The slope, the position and the number of lobes of the dispersion relation all change significantly depending on the radial position in the channel. The coherent Thomson scattering diagnostic PRAXIS, with which the first experimental observations of the ECDI dispersion relations were made, has an observation volume that is greater than the channel dimensions. Thus, the signals observed with PRAXIS under similar conditions represent an average over the full width of the channel, taking into account the gradient of electron properties. Indeed, it was speculated early on [2] that this might contribute to the appearance of continuous, non-discrete experimental

dispersion relations. The linear kinetic theory dispersion relations shown in Fig. 4.11 and Fig. 4.12 show how this can be the case.
The transverse length of the PRAXIS observation volume, with ω_a as the laser beam waist and θ as the angle between the primary and local oscillator beams forming the observation volume, is at minimum:

$$l_l = \frac{\sqrt{\pi}\omega_a}{\theta} = 185\ mm \tag{4.9}$$

As such, a range of local electron parameters are traversed by the measurement volume. It should be emphasized, however, that the experimental dispersion relation measurement from PRAXIS is weighted in favor of the regions with the highest plasma density, i.e., the channel regions. Thus, while the observation volume covers several centimeters in the transverse direction, the primary source of the signal (and the variations in plasma properties contributing to it) remains localized at the channel regions.

4.4.4 Comparison of model results with previous measurements

In order to obtain a dispersion relation representative of what can be observed with a diagnostic such as PRAXIS, it is therefore necessary to average the dispersion relations over the channel width.
Figures 4.13a and 4.14a show the set of dispersion relations from the linear kinetic theory which are obtained for each radial position for the two gases. Each curve is solved using the experimentally-measured electron properties from the implementation of the THETIS diagnostic, described earlier.

Figures 4.13b and 4.14b show the average of these dispersion relation solutions for each gas, reflecting the fact that the PRAXIS experimental dispersion relation measurement naturally encompasses all of these individual dispersion relations.

As seen in Figures 4.13a and 4.14a, there is a strong smoothing effect on the dispersion relation by addition of the individual signals, with the position k of the lobes for each curve slightly offset from the previous one. Thus the average tends towards a much more linear curve than that obtained by considering only discrete and spatially unvarying electron properties over the whole channel width.

This point in particular is fundamental. As discussed previously, the inclusion of k_z serves to partially smooth the lobes seen in the 3D linear kinetic theory analysis, rendering those solutions closer to the measured continuous (non-discrete) experimental dispersion relations. Here, it is now shown that to a large extent, the discrepancy between linear kinetic theory (which shows the presence of residual resonances) can be resolved by taking into account the variations of plasma properties which are inherent in the coherent Thomson scattering measurement. In summary, the coherent Thomson scattering measurement is continuous because it captures the ensemble of these variations and the resulting modes present.

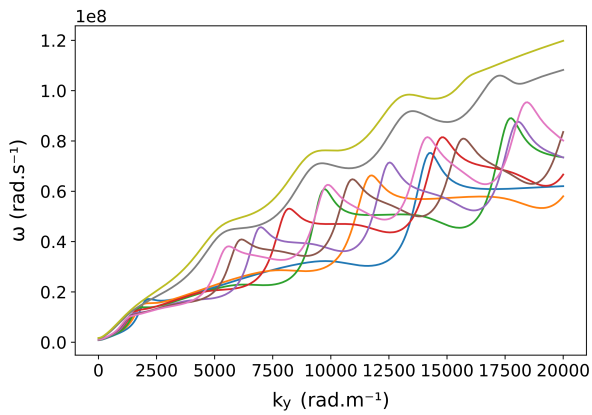

(a) *Dispersion relations (linear kinetic theory) for all radial positions within the channel of Figure 4.5, for krypton.*

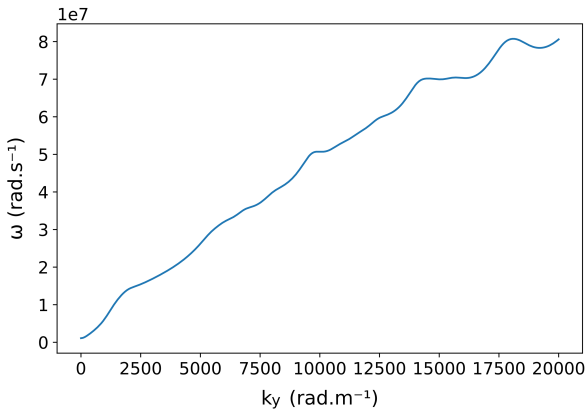

(b) *Averaged dispersion relation (linear kinetic theory) over the entire channel width, for krypton.*

Figure 4.13

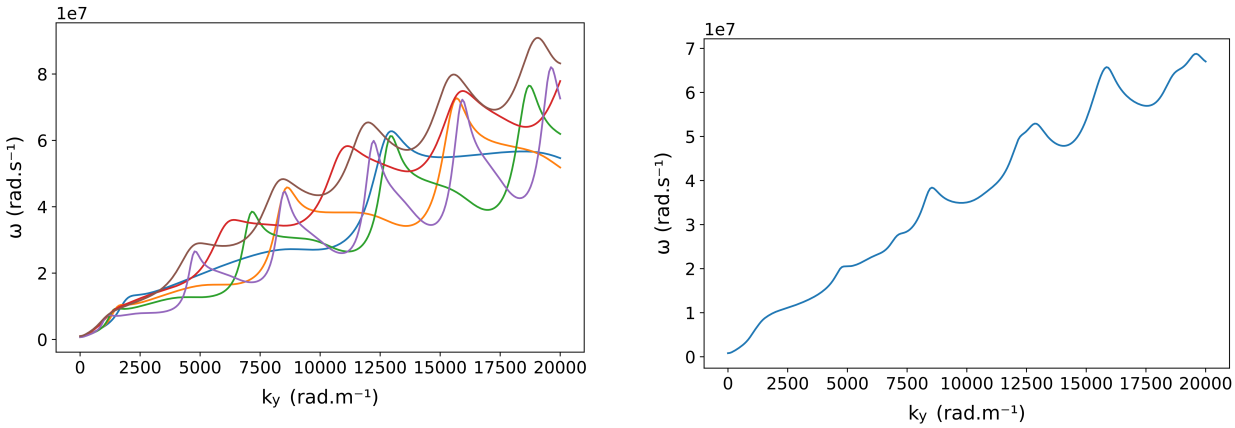

(a) *Dispersion relations (linear kinetic theory) for all radial positions within the channel of Figure 4.5, for xenon.*

(b) *Averaged dispersion relation (linear kinetic theory) over the entire channel width, for xenon.*

Figure 4.14

The smoothed curve of Figure 4.14b obtained for xenon can be compared with previous results of coherent Thomson scattering measurements, obtained on another kW-scale thruster (300 V, 20 mg.s^{-1}, 7.5 mm from the exit plane, in Ref. [2]). Although it was not possible to perform coherent Thomson scattering measurements on this kW-scale thruster during this thesis, it is instructive to consider how experimental results obtained in that work would compare to the new linear kinetic theory analysis which accounts for a range of electron properties inherent in the measurement.

The result of this comparison is shown in Figure 4.15. The mean dispersion relation for xenon in Fig. 4.14b is reproduced (gray dashed line - note that the lobed feature persists because only 5 radial positions were used to determine the averaged dispersion relation). Two straight lines are shown (in gray) as envelopes around the lobed mean dispersion relation. These lines have corresponding slopes of 4472 and 3174 m/s (group velocities). A line in red, identified as the average of the ion acoustic waves, is shown. This line is determined in the following way. The ion acoustic wave dispersion relation is written in the form

$$\frac{\delta\omega}{\delta k} = \sqrt{\frac{k_B T_e}{m_i}} \tag{4.10}$$

where, as in previous sections, k_B is the Boltzmann constant, T_e the electron temperature, and m_i the ion mass. $\frac{\delta\omega}{\delta k}$ is the group velocity of the dispersion relation, calculable directly using the measured electron temperatures. The line in red represents the average of the ion acoustic wave dispersion relations determined for every available radial position. Lastly, the previously-measured experimental dispersion relation (blue line, group velocity 4559 m/s, [2]) is shown to fall well within the range given by the mean linear kinetic theory (bounded by the gray lines) and close, but not identical, to the average ion acoustic wave solution.

To summarize this result, two points are worth noting.

(i) the difference between the linear experimental dispersion relation, and those from linear kinetic theory, which show strongly amplified lobes, can probably be explained by the variation of the electron properties along the radial direction.

(ii) the smoothed ECDI is not identical to a simple ion acoustic wave. The presence of lobes has a local amplification effect on the frequency (which is higher than that of an ion acoustic mode). As a result, the averaged ECDI over the whole channel is at slightly higher frequencies than a simple ion acoustic wave. The averaged dispersion relation for the ECDI, while it can appear linear and continuous, is not that of an ion acoustic wave.

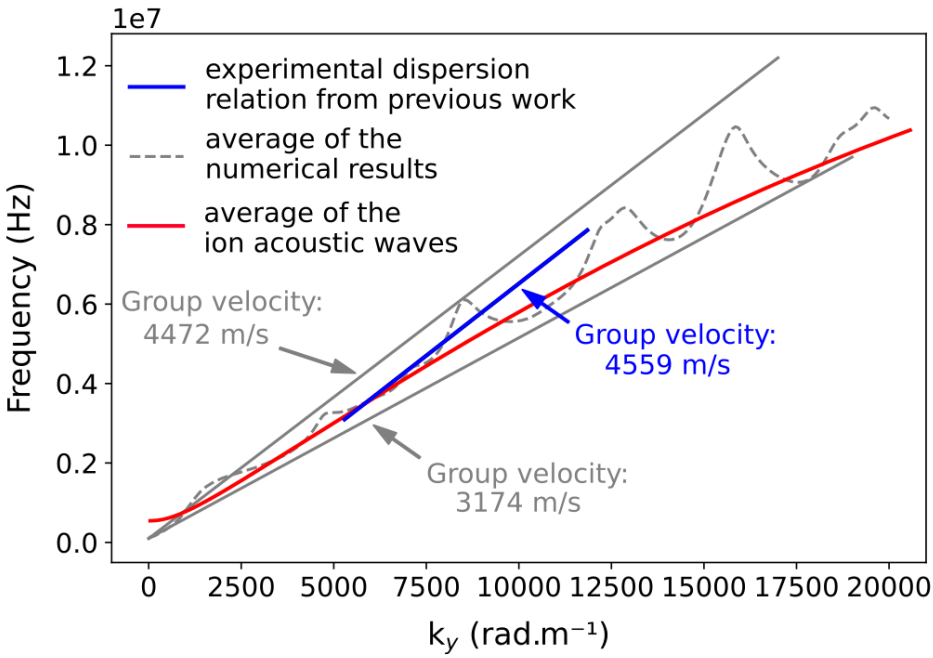

Figure 4.15: *Comparison between the average dispersion relation from linear kinetic theory, obtained over the full channel width for xenon (gray dashed line), and the experimental results by collective scattering on a Hall effect thruster under similar conditions (blue line). For comparison, the averaged ion acoustic wave dispersion relation expected over the channel width is shown (red line). The two gray lines depict an envelope surrounding the averaged linear kinetic theory solution.*

Chapter 5

Application of the linear kinetic model to the HiPIMS case

Contents

In the previous chapter, comparisons between the ECDI dispersion relation in the Hall thruster were made using: (i) linear kinetic theory, with electron properties substituted from direct measurements made using THETIS, and (ii) prior experimental dispersion relations, measured directly using PRAXIS. These analyses were only partial, as PRAXIS was not implemented during this thesis for new thruster measurements.

We can, however, reproduce the same method with more complete data, this time using temporally-resolved electron property measurements made in the HiPIMS discharge (Chapter 3), adapting the model slightly to take into account the specific features of the planar magnetron plasma. In this case, we have access to more extensive incoherent Thomson scattering measurements under different conditions (via THETIS). More importantly, as will be shown later, it was possible to measure the experimental dispersion relation directly (via PRAXIS) under the same plasma conditions.

5.1 Procedure and methods for exploiting THETIS results

Two cases are studied here, corresponding to: (i) Condition 1 for argon (Table 5.1), and (ii) helium investigations with a pulse width of 100 μs (Table 5.2). The results are the same as those presented previously, but are reproduced here for convenience.

The purpose of this chapter is to describe an analytical method and not to present experimental results. For convenience, all example curves from the linear kinetic theory analysis use the cold ion approximation, as described previously. By normalizing the wave frequency ω with the ion plasma frequency ω_{pi}, we can ignore the nature of the ion during iteration. This choice increases

Ar - Condition 1					
PW (μs)	I_d (A)	U_d (V)	P (Pa)	z (mm)	B_r (mT)
70	40	-775 ± 1.9%	1	8	16.1

Table 5.1: *Conditions for argon temporal investigations (Condition 1). Reproduction of table 3.2 for convenience. PW and P represent the pulse width and chamber pressure, respectively. I_d and U_d represent the peak discharge current and peak discharge voltage, respectively. B_r is the radial magnetic field measured at the center of the racetrack at z = 8 mm.*

He				
PW (μs)	I_d (A)	U_d (V)	P (Pa)	z (mm)
100	75	-840	10	2

Table 5.2: *Conditions for helium temporal investigations. Reproduction of table 3.4 for convenience. PW and P represent the pulse width and chamber pressure, respectively. I_d and U_d represent the peak discharge current and peak discharge voltage, respectively. Measurements are performed at z = 2 mm.*

the readability of the results shown and ensures that variations in the shape of the curves are correctly attributed to the intrinsic mass of the ion (or ions) under consideration. In the following chapter, where comparisons between this method will be made to real results, a non-zero ion temperature will be considered.

In the discussion of the models in this chapter, for simplicity, it is assumed that: (i) k_x, the axial wavenumber component of the ECDI, is zero; this simplifies the dispersion relation and is justified by the weak dependence of the mode features on the magnitude of k_x, shown in past studies, e.g. Ref. [2], and (ii) $k_z = 540$ rad.m^{-1}, again, a value based on prior experimental work showing 3D propagation of the ECDI [2].

5.1.1 Impact of ion mass on linear kinetic theory solution

One important difference between planar magnetron operation in HiPIMS and the Hall thruster is the diversity of ion species. In the Hall thruster, xenon (or krypton) ions are expected to be as singly-, doubly-, and triply-charged species [142]. In the planar magnetron, the working gas (argon or helium in this work) can be present at multiple charge states, but ions are also produced from the metallic target (titanium, in most of the experiments studied in this manuscript).

As a result, it is possible to consider the effect on the ECDI linear kinetic theory dispersion relation when different ion atomic species (in this example, singly-charged light helium and singly-charged heavy titanium) are present in HiPIMS. The real frequencies ω and growth rates γ produced in such a case are illustrated in Figure 5.1.

Figure 5.1 shows the real and imaginary frequency solutions for the ECDI for the different ion species. The unstable resonances are located at similar values of wavenumber for both helium and titanium, despite the difference in the masses of the nuclei. The main difference is in the

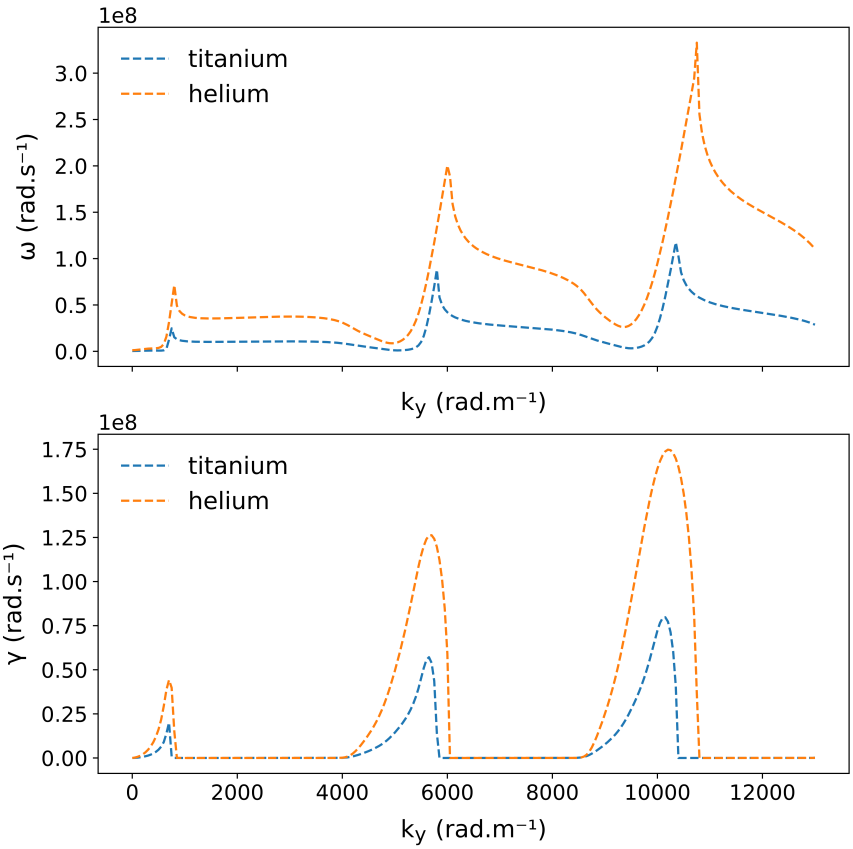

Figure 5.1: *Comparison between the non-normalized dispersion relation solutions obtained by considering singly-charged ions (100 % titanium and 100 % helium), for the conditions shown in Table 5.2, where pulse-averaged* $n_e = 10^{19}$ m^{-3} *and pulse-averaged* $T_e = 6$ *eV.*

real frequency of the excited modes: the lighter helium ion mass, in comparison to titanium, increases the excited mode frequency, proportional to the inverse of the square root of the ratio of the masses of the nuclei, here $\left(\sqrt{\frac{4}{48}}\right)^{-1} \simeq 3$.

In the development of the models described in this chapter, we begin with a somewhat artificial case. Experiments with argon and with helium produce, at a given time t within a pulse, a set of values of electron properties: electron temperature, density and drift velocity (T_e, n_e, V_d) uniquely defining that time t. Before considering the effect of the argon or helium ion mass on the dispersion relation, we take an ion species as a baseline (singly-charged titanium, which is the same target material for both gases in these experiments) and consider how the dispersion relation, using just this baseline ion, is modified when the (T_e, n_e, V_d) conditions measured are accounted for. The idea of this analysis is to observe the impact of the combination of electron properties on an artificial baseline case before then arriving at the more representative combined experimental and theoretical analyses in the next chapter.

5.1.2 Evolution of pulse parameters: electron density and temperature

Although we have information on the drift velocity of electrons from incoherent Thomson scattering measurements, for simplicity, we first assume a constant drift velocity $V_d = \frac{E}{B}$ in order to discuss the analysis method. The fixed value imposed for now is 6×10^5 m.s^{-1}, on the order of what would be expected a few millimeters from the target. It should be noted that there are no direct experimental measurements of the electric field within a few millimeters of the target; the value given is based on rough extrapolations of the electric field value from HiPIMS PIC numerical simulations [108] and from the magnetic field map a few millimeters from the target (Fig. 3.6).
The electron density and temperature undergo large variations during the pulses. However, since no significant anisotropy was observed in these two parameters (between the radial and azimuthal observations), we choose to use only the properties measured in the azimuthal direction. This choice is arbitrary, and we could have chosen to consider the properties along the radial direction, or an average of the two directions. This is, however, not the case for the electron drift velocity, whose anisotropy has been demonstrated in this work. We will consider the linear kinetic theory dispersion relation under the combination of (T_e, n_e, V_d) found in the experiments and study how the dispersion relations evolve over time due to the varying electron properties during plasma pulsing. As stated above, this analysis will rely, to start, on the use of a baseline ion species (singly-charged titanium).

Argon conditions

For the conditions of Table 5.1, the electron density varies from 10^{16} m^{-3} at the beginning of the pulse to 10^{19} m^{-3} at the maximum, before falling back to about 10^{17} m^{-3} near the end of the afterglow (Fig. 5.2). The electron temperature, on the other hand, reaches its maximum at the beginning of the pulse, at nearly 4 eV, before falling back to a plateau around 1.5 eV during the duration of the pulse, and reaches less than 0.1 eV after 100 μs in the afterglow.

This succession of electron property evolutions allows us to define three different temporal stages. At the beginning of the discharge, a low density is observed for a high electron temperature temperature (stage 1), then when the equilibrium is established, a high electron density coexists with a medium temperature (stage 2), and finally, after the end of the voltage application, a low electron temperature coincides with a low electron density (stage 3).

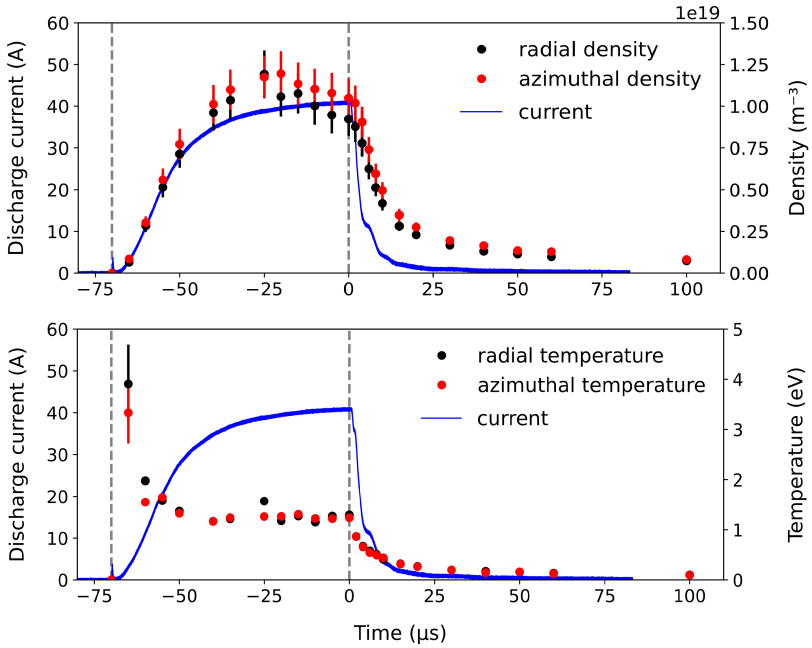

Figure 5.2: *Ar discharge, Condition 1: time evolution of the electron properties, in radial (black points) and azimuthal (red points) observation directions. The current pulse waveform is shown in blue. Operating parameters correspond to Condition 1, summarized in Table 5.1. The vertical dashed lines indicate the instants of discharge initiation (-70 µs) and voltage cut-off (0 µs). Reproduction of figures 3.8 and 3.9 for convenience.*

Fig. 5.3 shows the normalized linear kinetic theory result for the real and imaginary frequencies for the three different stages of the discharge. The measured electron temperatures and densities applied to the dispersion relations are shown in the figure caption. It is clear that as the electron properties of the discharge change over time, the dispersion relations of the ECDI also evolve. Initially, the dispersion relation appears continuous, before evolving towards discrete frequency peaks. The growth rates evolve in parallel.
When spectrum averaging is used in coherent Thomson scattering experiments, in order to allow the ECDI fluctuations to be clearly distinguished from the noise (e.g. Tsikata [2]), the duration of the full spectrum acquisition is typically 65 ms. This is much longer than the total duration of the discharge, which is at most a few hundred μs including the afterglow. Spectrum averaging in these conditions will reflect the ensemble of the electron density and temperature values found over the pulse duration. The instants of highest electron density will contribute most significantly to the averaged spectrum.

We may plot what the averaged dispersion relation would look like, accounting for the variation of electron properties. This is done in Figure 5.4 for the real frequency, assuming a purely azimuthal and constant drift velocity $V_d = \dfrac{E}{B}$. We find the presence of the lobes already mentioned, for every different condition, in (a), and in (b), the averaged result, weighted by the electron density.

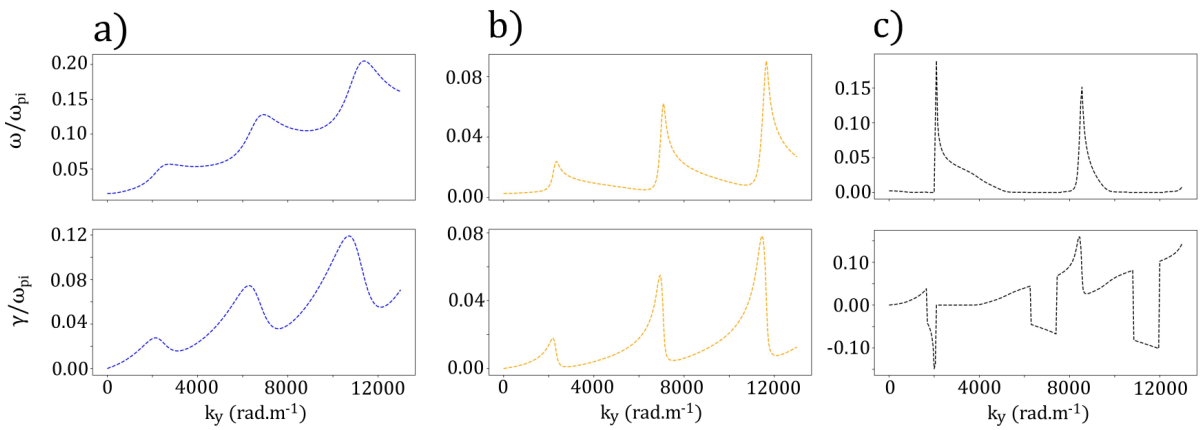

Figure 5.3: *Real frequency and growth rate normalized by ω_{pi} for different plasma conditions, corresponding to the points identified in Figure 5.2. The ion mass considered here is taken to be that of the target (Ti) ions. This will remain the case until otherwise stated (Section 5.1.4).*
a) T_e = 3.33 eV and n_e = 8.48 × 10^{17} m^{-3}, $t = -75$ μs;
b) T_e = 1.31 eV and n_e = 1.13 × 10^{19} m^{-3}, $t = -15$ μs;
c) T_e = 1.13 eV and n_e = 1.29 × 10^{18} m^{-3}, $t = 60$ μs

Helium conditions

For helium conditions, the electron properties evolve almost linearly throughout the discharge (Fig. 5.5). The same reasoning as before with argon is used, averaging the pulses and weighting their contribution to the overall frequency by their electron density.
The result of this analysis is shown in Figure 5.6. In (a), the curve with the most pronounced (discrete) real frequency lobes is measured at $t = -85$ μs, when the electron density is still very low, $n_e = 3.75 \times 10^{17}$ m^{-3}. The other curves are smoother as the electron density increases and the temperature decreases. The smoothing effect shown in Figure 5.6(b) when the solutions are averaged is much more pronounced than in the argon case, but this averaged solution in (b) is still not a true linear curve. Higher electron temperatures would contribute to the appearance of a non-discrete dispersion relation in linear kinetic theory.

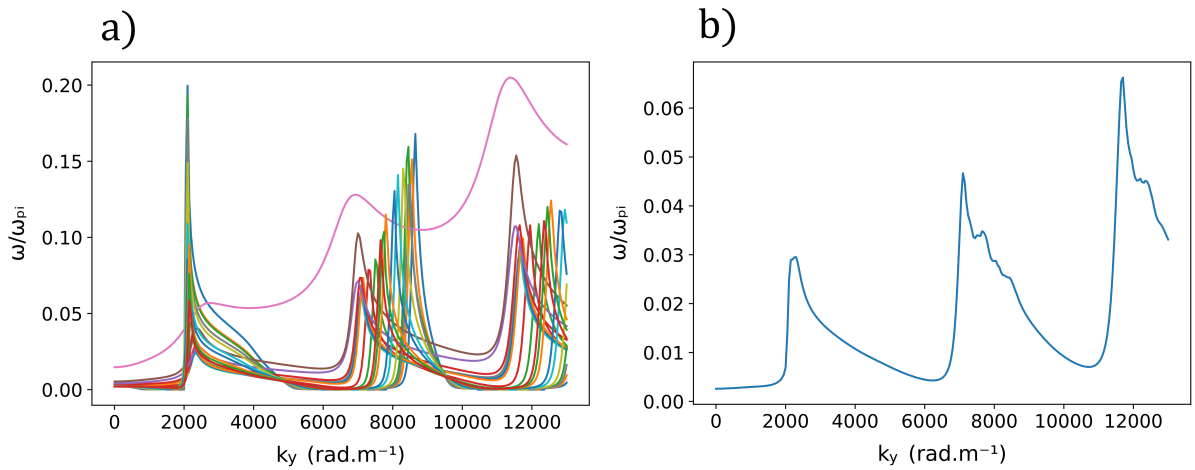

Figure 5.4: *(a) Superposition of normalized frequencies as a function of k_y obtained by injecting the measured electron properties for each of the points in Figure 5.2 into the linear kinetic theory dispersion relation. (b) Average of the pulses weighted by the respective electron density of each point.*

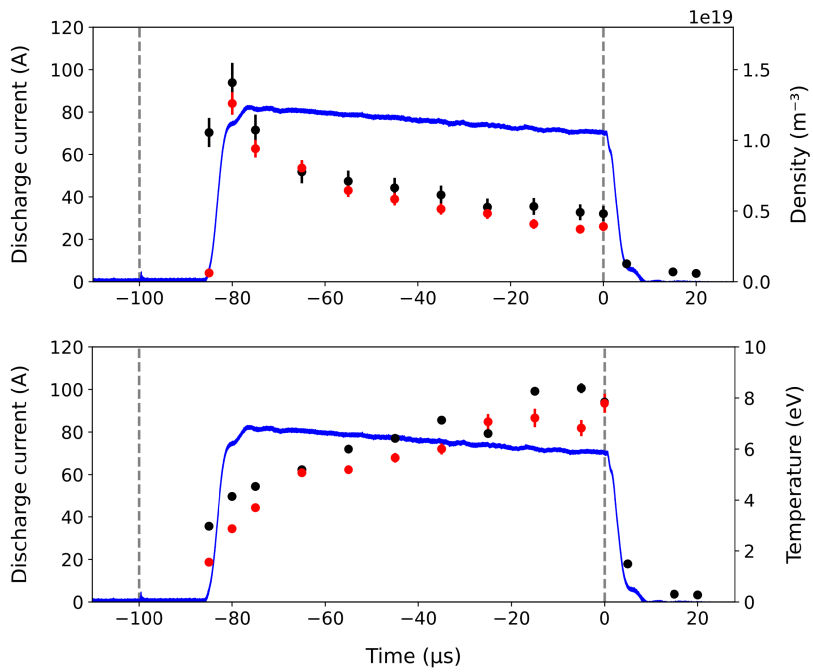

Figure 5.5: *He discharge: time evolution of the electron properties, in radial (black) and azimuthal (red) observation positions. The current pulse waveform is shown in blue (a). Operating parameters are summarized in Table 5.2. The vertical dashed lines indicate the instants of discharge initiation (-100 μs) and voltage cut-off (0 μs). Reproduction of figures 3.20 and 3.22 for convenience.*

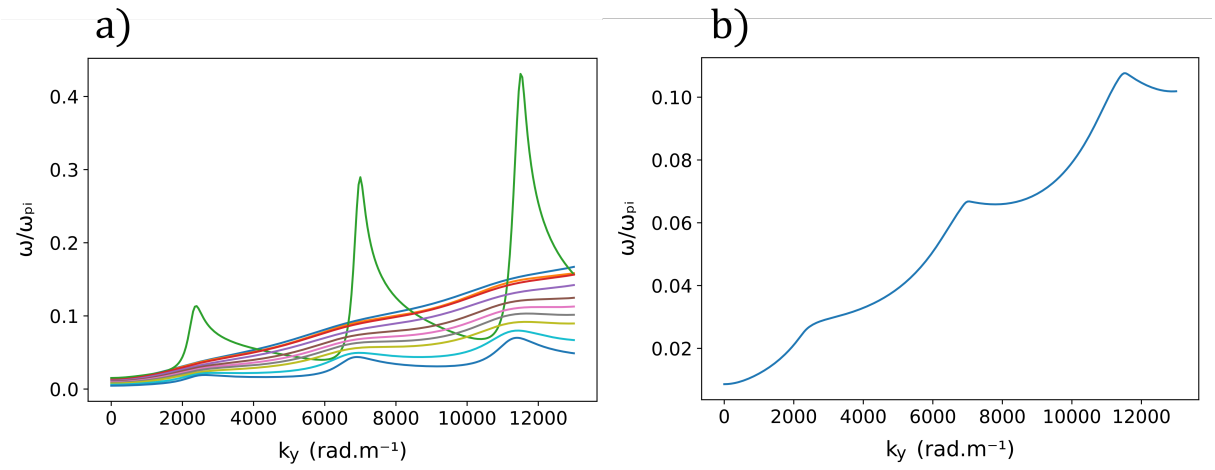

Figure 5.6: *(a) Superposition of normalized frequencies as a function of k_y obtained by injecting the measured electron properties for each of the points in Figure 5.5 into the linear kinetic theory dispersion relation. (b) Average of the pulses weighted by the respective electron density of each point.*

5.1.3 Evolution of pulse parameters: drift velocity variation

In this section, we now address the dispersion relation solutions which correspond to the experimentally-measured values of the electron drift velocity for the argon and helium conditions. For reference, these results are reproduced in Fig. 5.7, showing the nature of the variation in the net electron drift which was determined previously during the plasma pulsing.

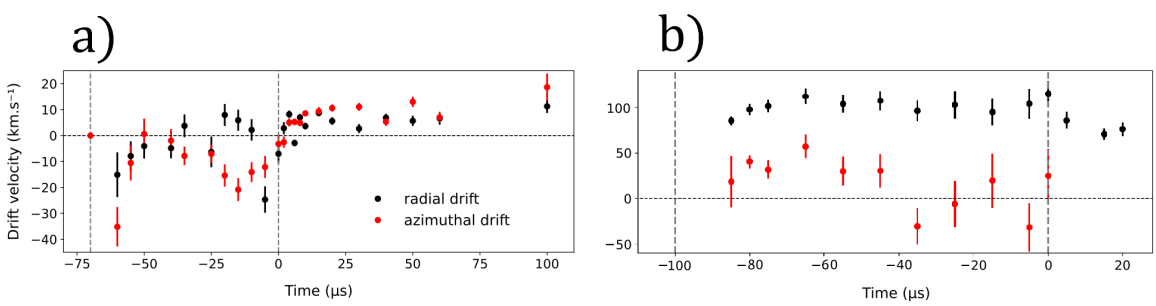

Figure 5.7: *Time evolution of the electron drift velocity, for (a) argon and (b) helium. Radial (black) and azimuthal (red) observation drift velocities are shown. Operating parameters are summarized in Table 5.2 and Table 5.1. The vertical dashed lines indicate the instants of discharge initiation (-100 µs) and voltage cut-off (0 µs). Reproduction of Figures 3.11 and 3.21 for convenience.*

We have up to this point neglected to take into account the real drift velocity measured with the THETIS diagnostic, assuming for simplicity a constant drift velocity $V_d = \dfrac{E}{B}$ of 6×10^5 m.s^{-1}. Values of the same order of magnitude can be observed, for example, the first point measured for argon at $t = -75$ μs at a drift velocity in the $E \times B$ direction of 2×10^5 m.s^{-1}. However, this point is exceptional because it is located at the beginning of the pulse, before the increase of the density and the internal reorganization of the plasma.

It has been shown in Chapter 3 that in fact, during the whole duration of the pulse, there is a

competition between the $E \times B$ drift and the diamagnetic drift of the electrons. In some points, it has even been observed that the electrons drift in the direction opposite the $E \times B$ drift, in particular during the afterglow, when the voltage is no longer applied. In all cases, the net drift velocity, for argon and helium at the measurement positions for the experiments, is only of the order of a few tens of km.s^{-1}.

It is obvious that any modification of the drift velocity would have a major impact on the shape of the dispersion relation, contributing more significantly than even the electron temperature or electron density. Indeed, the very reason for the existence of the ECDI is due to a resonant interaction between a Bernstein wave and an ion acoustic wave which is only made possible by the Doppler effect caused by the drift velocity V_d.
This is illustrated in Figures 5.8 and 5.9. These figures now show the dispersion relation using the same weighted average model presented in the previous section, for the argon and helium conditions, but now taking into account the net measured drift velocity. The frequency lobes observed earlier have been smoothed, leading to the appearance of continuous dispersion relations more similar to what has been observed with PRAXIS measurements in the past on the planar magnetron ([101]).

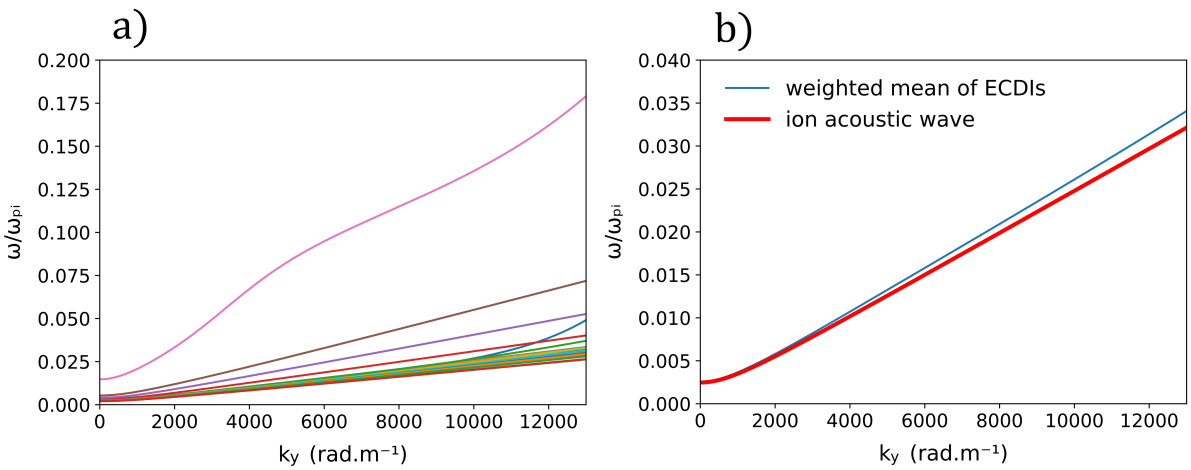

Figure 5.8: *(a) Superposition of normalized real frequencies from the linear kinetic theory dispersion relation, as a function of k_y. Frequencies are obtained by injecting the measured electron properties, including the drift velocity, measured for the argon conditions (Table 5.1). (b) Average of the pulses weighted by the respective electron density of each point (blue), compared to an ion acoustic wave solution which would be obtained under the same experimental conditions (red).*

Figure 5.8 uses the (T_e, n_e, V_d) combinations found for the argon experiment to plot a series of dispersion relations for each combination (Figure 5.8(a)). In Figure 5.8(b), the average dispersion relation solution, density-weighted, is shown in blue. To this line is added the dispersion relation for an ion acoustic mode under the same conditions. The two solutions are observed to be similar. This approach, now applied to the electron property data in helium, leads to the results of Figure 5.9. Again, the inclusion of the real drift values and other measured electron properties leads to linear, continous dispersion relation solutions in (a). On averaging these solutions, with electron density weighting in (b), the resulting dispersion relation (blue) is now significantly different from an ion acoustic wave dispersion relation (red).

We can therefore affirm the following point. The dispersion relation of the ECDI can be con-

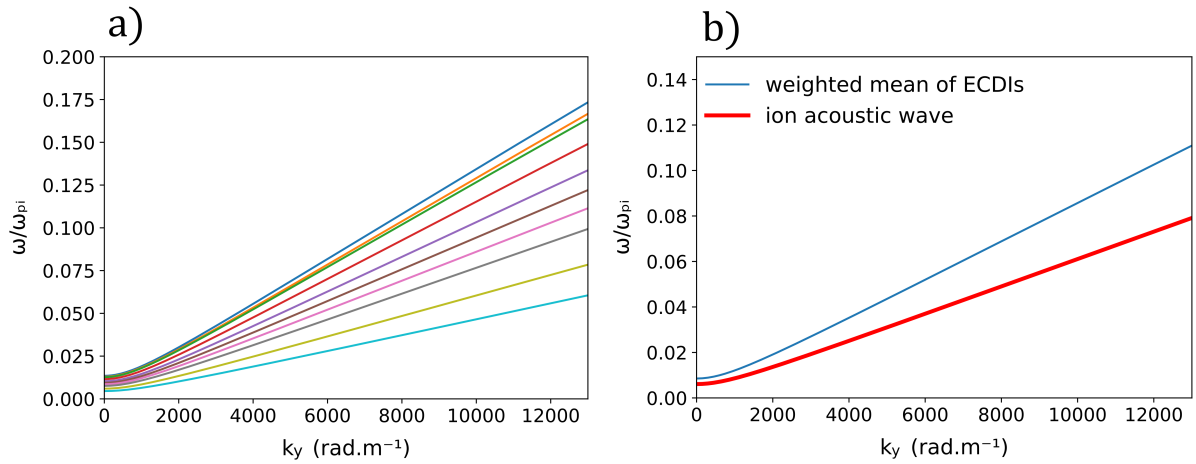

Figure 5.9: *(a) Superposition of normalized real frequencies from the linear kinetic theory dispersion relation, as a function of k_y. Frequencies are obtained by injecting the measured electron properties, including the drift velocity, measured for the helium conditions (Table 5.2). (b) Average of the pulses weighted by the respective electron density of each point (blue), compared to an ion acoustic wave solution which would be obtained under the same experimental conditions (red).*

sidered as that of an ion acoustic wave enriched with peaks due to resonances. Averaging the real frequencies over time (i.e., averaging over multiple unique combinations of (T_e, n_e, V_d)) does not equate to removing the peaks to recover an ion acoustic wave - instead, it results in a new solution with a steeper slope (caused by the presence of the resonances, i.e., the Bernstein mode contributions). This necessarily results in a higher group velocity for the ECDI than would be expected for a simple ion acoustic wave under the same plasma conditions. Recovering a pure ion acoustic wave solution would require consideration of the ECDI with a zero drift velocity (a condition which could not excite the ECDI to begin with).

5.1.4 Consideration of two types of ion

In the previous cases, only one type of ion was considered. As explained at the beginning of this chapter, the analysis was first undertaken using a baseline ion species (Ti+, atomic mass 48) and the dispersion relation considered under the various combinations of (T_e, n_e, V_d), determined from argon and helium investigations.

In order to more accurately match the reality of the HiPIMS experiment, it is now necessary to consider both the target and working gas ions. We do not have direct measurements that allow us to track the respective proportions of one or other of these species during the discharge pulsing. Nevertheless, work by authors such as Ehiasarian *et al.* [143] shows that in a discharge of this type, the proportion of the respective ions evolves during the pulse. The plasma is initially dominated by the ions produced from the working gas, to evolve towards a discharge dominated by the metal target ions.

HiPIMS discharges are known to have a high level of ionization, which provides the advantage of significant control of the thin film deposition. The ionized flux fraction of metals is usually measured using a polarized quartz crystal microbalance, as in Ref. [144], or by optical emission, as in Ref. [145]. The values usually found in this type of HiPIMS discharge are between

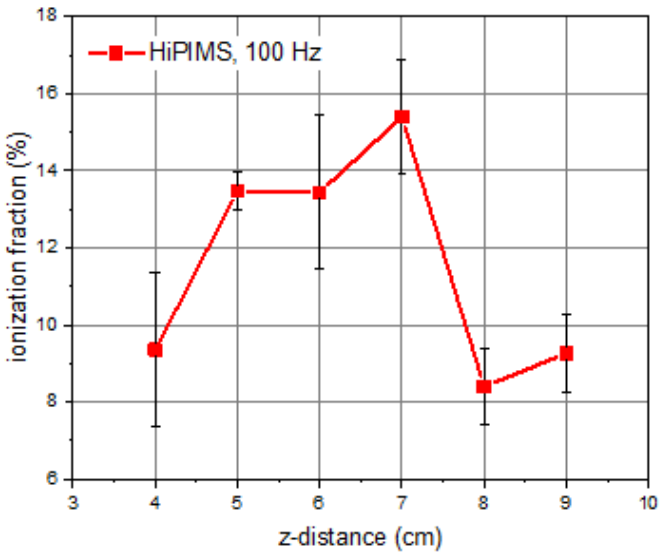

Figure 5.10: *Ionized fraction of titanium for a HiPIMS discharge for conditions corresponding to Table 5.1. Data from A. Kapran (private communication).*

30% and 50% for a titanium target. Within the framework of this study, we had access to precise measurements made using a quartz crystal microbalance from Kapran et al. [146], under the same experimental conditions as the argon discharge 5.1. Fig. 5.11 shows an example of the data from Kapran (private communication) indicating an ionized Ti^+ fraction of around 12% for the conditions corresponding to those of Table 5.1, within a few centimeters of the target.

In order to take into account both ion species, the procedure adopted is as follows:

(i) first, we calculate separately the two dispersion relations for each of the metal and gas ions with their respective masses. For example, for the first pulse corresponding to the argon condition (Table 5.1), we calculate the dispersion relation for each of the 25 points now setting the ion mass $M = 18$ (representing the argon ion), and recalculate the dispersion relation for these 25 curves by then setting $M = 48$ (for the titanium ion).

(ii) next, each of the 50 dispersion relations is normalized by its own value of ω_{pi}, by setting $n_i = n_e$ and, respectively, $M = 18$ or $M = 48$

(iii) each of the normalized dispersion relations is multiplied by a new value of ω_{pi}, where $n_i = n_e \times F_i$, F_i being the respective fraction of each ion, defined according the relation

$$F_i = \frac{\text{number of ions of species i}}{\text{number of ions from gas + number of ion from target}}$$

This provides a complete scan of the possible dispersion relations between [$F_{Ar} = 0$; $F_{Ti} = 1$] to [$F_{Ar} = 1$; $F_{Ti} = 0$]. This procedure, more complex than a simple average between two curves, is necessary because of the presence of n_i and M inside a square root in the formula of the dispersion relation. The evolution is not linear with respect to the proportion of either species. The same procedure above, described for a combination of Ar/Ti, is applied to He/Ti ions.

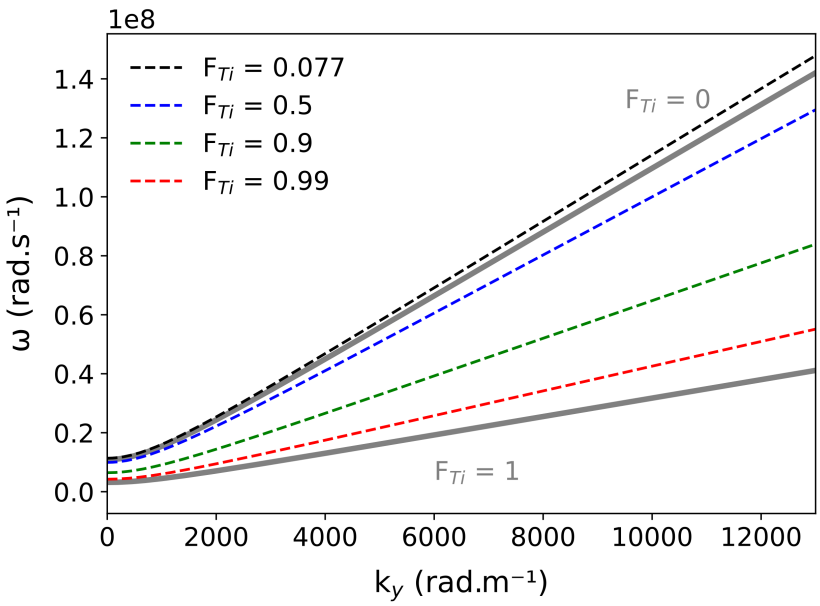

Figure 5.11: *Theoretical dispersion relation, obtained for different ion populations, considering a combination of helium and titanium ions. The grey curves represent the limit cases, with 100% titanium ions ($F_{Ti} = 1$) or 100% helium ions ($F_{Ti} = 0$). The colored curves represent different fractions of titanium ions. The fraction that gives the highest mode frequency is in black.*

The results of this dispersion relation analysis applied to a combination of He/Ti ions is shown in Figure 5.11. This figure clearly illustrates the non-linearity of the evolution with respect to the proportion of the ion species. The curve corresponding to $F_{Ti} = 0.9$ is located midway between the two limit curves. Similarly, the curve corresponding to $F_{Ti} = 0.5$ is closer to $F_{Ti} = 0$ than $F_{Ti} = 0.99$ is to $F_{Ti} = 1$. There is however, another interesting feature, where the black curve corresponding to $F_{Ti} = 0.077$, thus a titanium ion fraction very close to 0, gives the highest mode frequencies.

This effect is replicated in Figure 5.12, for a combination of Ar/Ti ions, although the smaller mass difference ($M = 4$ for helium, versus $M = 40$ for argon, with $M = 48$ for titanium) makes the readability more challenging. Only the curve corresponding to a fraction of titanium ions of 0.999 is in the interval between the two gray curves, and the curve with the steepest slope is obtained for an almost equal proportion of the two ions, with $F_{Ti} = 0.455$ and thus $F_{Ar} = 0.545$.

These results have a straightforward explanation. During the normalization/multiplication process explained above, both the ion density and the mass of the ion appear in the ω_{pi} formula. The complete calculation of the weighted frequency accounting for the presence of both species, $\omega_{F_{Ti}}(k)$, is therefore of the form:

$$\omega_{F_{Ti}}(k) = \omega_{Ti}(k) F_{Ti} \sqrt{\frac{M_{gas}}{M_{Ti}}} + \omega_{gas}(k)(1 - F_{Ti}) \tag{5.1}$$

where $\omega_{Ti}(k)$ is the dispersion relation frequency produced from considering only Ti ions, and $\omega_{gas}(k)$ is the dispersion relation frequency produced from considering only gaseous ions (helium or argon).

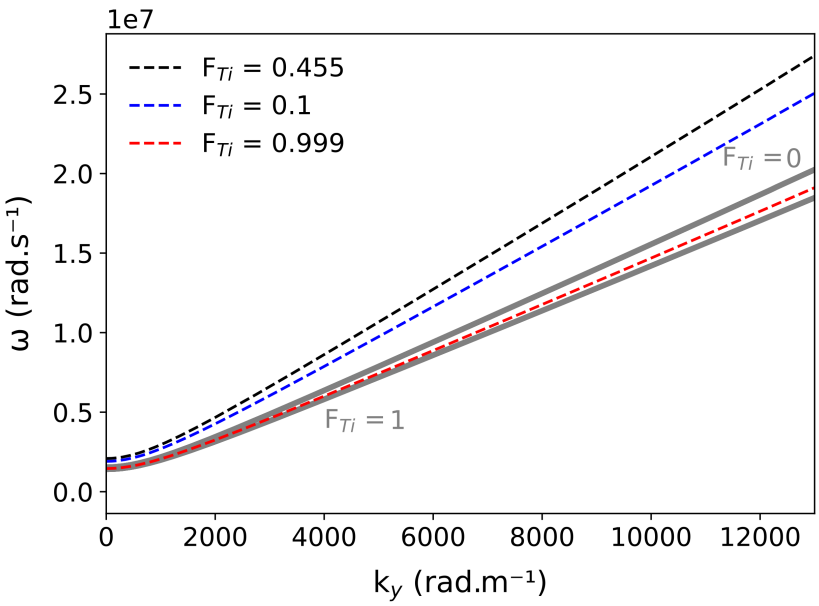

Figure 5.12: *Theoretical dispersion relation, obtained for different ion populations, considering a combination of argon and titanium ions. The grey curves represent the limit cases, with 100% titanium ions ($F_{Ti} = 1$) or 100% argon ions ($F_{Ti} = 0$). The colored curves represent different fractions of titanium ions. The fraction that gives the highest mode frequency is in black.*

The weighted frequency $\omega_{F_{Ti}}(k)$, normalized by $\omega_{Ti}(k)$, produced in this analysis is shown in Figure 5.13, for both argon and helium. As this figure illustrates, the normalized mode frequency does not have a linear dependence on the titanium ion fraction, and the two gases show very different dependencies of the mode frequency on this titanium ion fraction. For the heavier argon species, almost the entire set of normalized frequencies are greater than 1, with the exception of the points furthest to the right of the curve, close to $F_{Ti} = 1$. For the lighter gas, helium, the majority of normalized mode frequency values are below unity, with the exception of the values closest to zero.

The model explained here allows calculation of the dispersion relation which could be measured with a dedicated coherent Thomson scattering diagnostic like PRAXIS. The exact form of this dispersion relation depends on the electron properties, which are known from previous measurements made with THETIS. It also depends very strongly, in particular in the case of helium, on the respective proportion of each of the two main ion populations (originating from the process gas and the target).

An obvious criticism could be levelled at the model used. We have considered the signal from a discharge of process gas ions discharge, then that of a discharge with target ions, without taking into account the interaction between them. In a complex plasma like that of a planar magnetron, the individual effects of the different species are often complicated by interactions between them. One example is the appearance of the ion-ion two stream instability (IITSI) in Hall thrusters and planar magnetrons, driven by the existence of ion populations of multiple charge states.

The simplifying hypotheses applied to this analysis can, however, be defended by a simple point, briefly mentioned in Ref. [144]. During discharge pulsing, the two ion species do not coexist

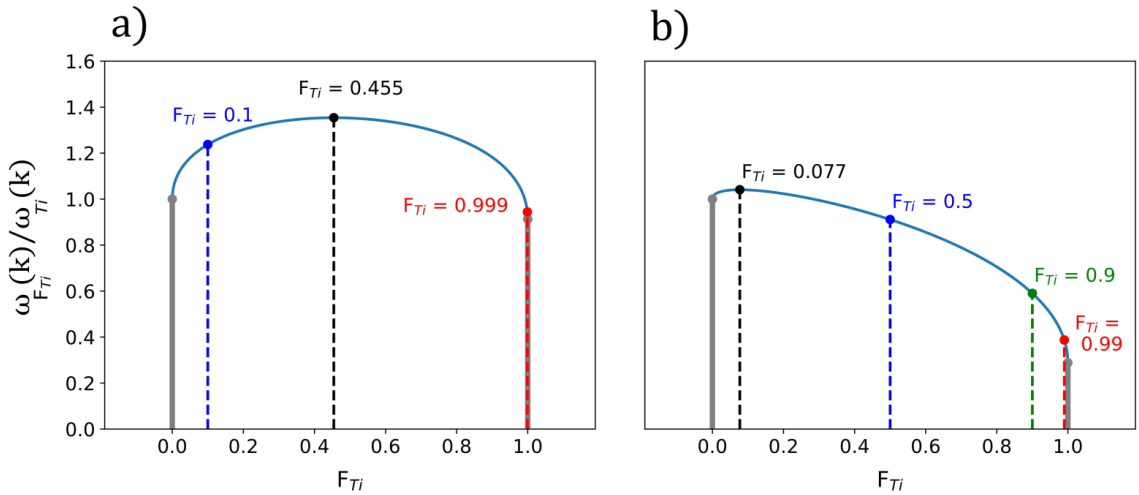

Figure 5.13: *Maximum amplitude of the ECDI frequency as a function of the fraction of titanium ions present in a mixture of species. (a) corresponds to the argon/titanium discharge, and (b) to the helium/titanium discharge. The frequencies are normalized to the ECDI mode frequency obtained with titanium ions only.*

in constant quantities from the beginning to the end of the discharge. Bohlmark *et al.* [147] showed quantitatively in a HiPIMS argon discharge the variation of the proportions of working gas and target ion species. That work considered a titanium target, cathode voltage of 800 V and a pulse energy of 9 J, and showed that during the initial period of pulsing (0 - 20 μs), the plasma is largely dominated by Ar^+ ions, and that during the remainder of the pulse (40 - 100 μ s) is largely dominated by Ti^+ ions. Thus, the period of co-existence between the two ion populations can be relatively short in comparison to the total duration of the discharge.

The idealized discharge in the model can therefore be considered as the immediate succession of two discharges containing only gaseous ions (of the working gas), followed by metal ions (of the target). In taking this analysis further, it would be interesting adapt the model to account for periods during which multiple ion populations are present, and to take into account the interactions and modes driven in the presence of multi-charged ions. In practice, in equation 4.1 on page 91, an additional term will have to be added to the left-hand side of the equation for each species considered, each with its own real frequency (assuming their temperature is not zero), and its own vpa velocity. Taking into account different species with different velocities has made it possible, for example, to attribute the axial mode to an Ion-ion two-stream instability between Xe+ and Xe2+ ions for Hall thrusters.

Chapter 6

Detection of high-frequency instabilities by coherent Thomson scattering in the HiPIMS configuration

Contents

6.1 Context of study

The previous chapters were devoted to the use of THETIS diagnostics for *in situ* measurement of electron properties. The difficulties involved in obtaining accurate and precise measurements using probes were discussed. When measuring plasma properties with a probe, the measurement volume is limited by the size of the probe or sheath [148]. Consequently, the measurements obtained are the result of the average over this same volume. This limitation also applies to instability measurements.

Instabilities in the MHz-frequency range and of sub-millimeter length scales, such as the ECDI and IITSI, are challenging to detect with probes. This is due not only to their frequencies and length scales, but also due to their localization in the E×B plasma (in the ionization region of and in regions of high magnetic field). The application of the PRAXIS diagnostic is intended to overcome such limitations. The development and application of this diagnostic [2] was initially geared towards the study of high-frequency modes in a Hall-effect thruster, and confirmed the existence of the instabilities described in the introduction to this manuscript. This work served as the basis for theoretical analysis and simulation, for example, motivating the development and use of the three-dimensional ECDI dispersion relation, and discovery of the coupling between the ECDI and the IITSI, later found in numerical simulations [76].

In planar magnetrons, in both HiPIMS and DC, experimental studies with this coherent Thomson scattering diagnostic were conducted in Ref. [101]. The ECDI was found in that context with characteristics similar to those in thrusters (angular propagation). The IITSI was also identified, showing more collimated propagation than in thrusters.

This work seeks to extend investigations of the HIPIMS regime, which poses particular challenges because of: (i) the transient and rapidly-evolving nature of the discharge, which means that instabilities develop within a plasma where the electron properties evolve constantly, and (ii) the short discharge duration (tens of μs), which means that techniques which could be used to reduce signal variance (e.g. spectrum averaging in a steady-state discharge [2]) are not directly applicable. The signal-to-noise ratios are therefore poorer. We propose here to make a detailed study of high-frequency instabilities in the HiPIMS planar magnetron (dispersion relations and angular propagation), and better understand the features of such instabilities in this context.

Very recently, the clever use of multiple probes on an E×B plasma (Hall-effect thruster) was implemented to study modes like the ECDI. There, measurement of the ion saturation current was used as a proxy for identifying instabilities and proposing mechanisms for their growth and saturation, in the work of Brown and Jorns in a large Hall thruster [149]. However, as mentioned in the same reference, and also discussed in Ref. [131], it is conceivable that insertion of the probe into the channel could interfere with the measurement. Furthermore, these probe studies resolve larger length scales than those at which the instability is predicted to contribute to transport. Because we have at our disposal a non-intrusive optical diagnostic system, we devote the final section of this chapter to a short study of how the behavior of instabilities is altered when a probe is inserted into the plasma.

6.1.1 Diagnostic implementation for planar magnetron investigations

A more complete description of the PRAXIS optical diagnostic can be referred to in Section 2.2. In the configuration studied here, the chamber (DIVA) is identical to that used for incoherent Thomson scattering investigations with THETIS and the conditions of the plasma discharge are similar to those of Chapter 3, where we measured the electron properties. This choice was made to enable the combination of the measurements and results from the two diagnostics.

In particular, we examine two discharge conditions, corresponding to the argon discharge condition (Table 5.1) and helium discharge condition (Table 5.2) studied in the previous chapter. For convenience, these discharges are hereafter referred to as the "argon" and "helium" discharges, and their conditions are shown in Table 6.1.

Condition Ar			
PW (μs)	I_d (A)	U_d (V)	P (Pa)
90*	40	-600*	1

Condition He			
PW (μs)	I_d (A)	U_d (V)	P (Pa)
100	75	-810*	10

Table 6.1: *Conditions for argon and helium temporal investigations of this chapter. Reproduction of tables 3.2 and 3.4 for convenience. PW and P represent the pulse width and chamber pressure, respectively. I_d and U_d represent the peak discharge current and peak discharge voltage, respectively. The values marked with an asterisk* are those that have been modified from the conditions of the measurements in Chapter 3 to maintain the same current profile.*

In Table 6.1, slight modifications have been made to the previous plasma conditions. The argon pulse width has been increased from 70 μs to 90 μs, and the discharge voltage has been decreased from -775 V to -600 V for argon, and from -840 V to -810 V for helium. This choice was necessary to obtain discharge current profiles of the same amplitude and shape as during the previous chapters, and to ensure that the measurements here thus occur in a comparable plasma. The slight divergence in the voltage and pulse duration values can most likely be attributed to an slight increase in the depth of the racetrack (due to plasma erosion), as the target was used several times during the interval between the two sets of measurements. The waveforms corresponding to the conditions of Table 6.1 are shown in Figures 6.1 and 6.2.

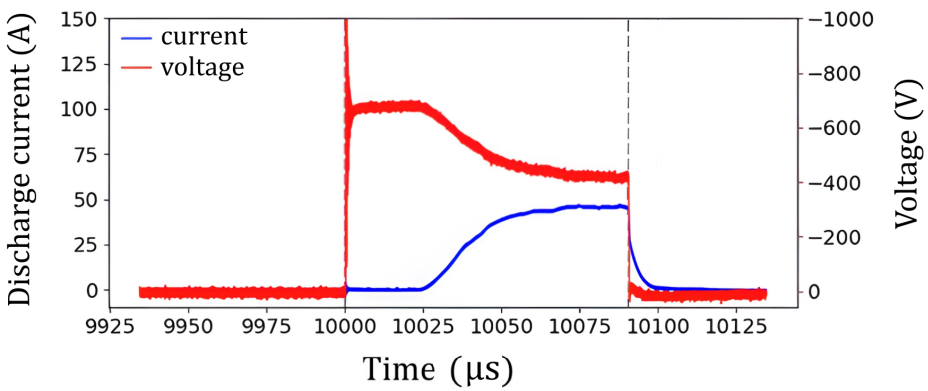

Figure 6.1: *Waveforms of the discharge current (in blue) and discharge voltage (in red) for Ar conditions (Table 6.1). The pulse limits are indicated by the gray dashed vertical lines.*

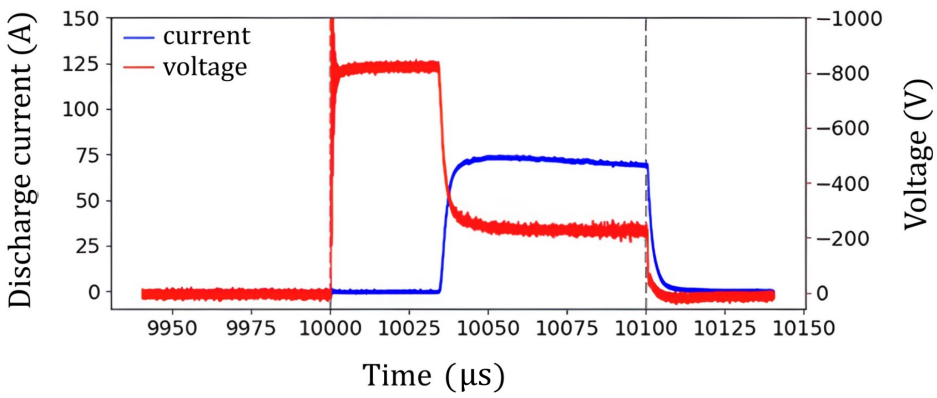

Figure 6.2: *Waveforms of the discharge current (in blue) and discharge voltage (in red) for He conditions (Table 6.1). The pulse limits are indicated by the gray dashed vertical lines.*

The PRAXIS optical bench is positioned with respect to the planar magnetron (cathode) as shown in Figure 6.3. Mirrors in the schematic are denoted by M and MT. The primary (red) and local oscillator (blue) beams enter the chamber through the left-hand window, and leave through the right-hand window after intersecting in the plasma. The local oscillator (mixed with the plasma scattered radiation) is to sent detector (D) using the arrangement of mirrors and periscopes. A photo of the optical bench setup installed on the DIVA chamber is shown in Fig. 6.4.

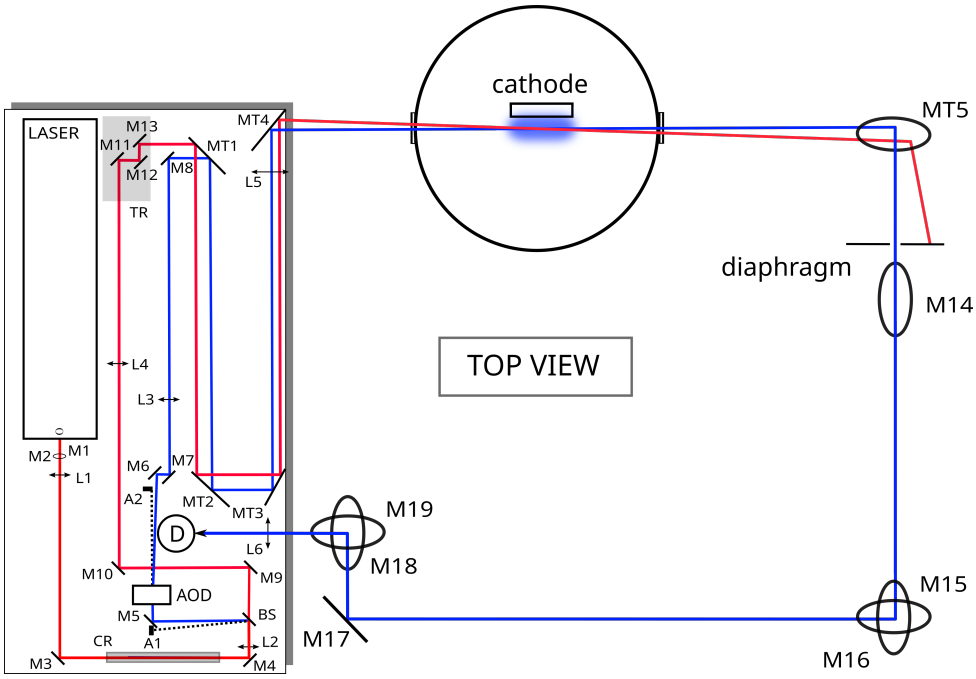

Figure 6.3: *Configuration of the PRAXIS optical bench elements for planar magnetron investigations on the DIVA vacuum chamber. The trajectories of the diagnostic local oscillator (blue) and primary beams (red) are shown.*

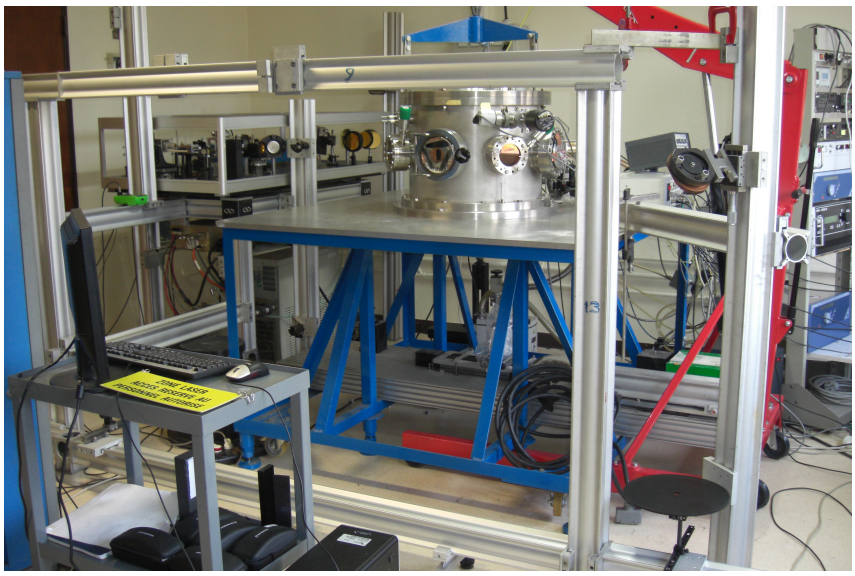

Figure 6.4: *PRAXIS coherent Thomson scattering (CTS) diagnostic installed for investigations on the DIVA plasma chamber at the LPGP laboratory (Orsay).*

The observation plane, defined by the beam crossing, is located at an axial distance $z = 10$ mm or $z = 20$ mm in experiments. We recall here that the angle between the beams allows the observation vector $\mathbf{k}$ magnitude to be defined, as described in Figure 2.5. The wavenumber k is varied over a range of 4150 - 12745 rad.m^{-1}.

6.1.2 Synchronization considerations and implementation

During incoherent Thomson scattering measurements with THETIS, the pulsed discharge was left on for long periods before the starting measurements. This allowed the effects of heating over time to stabilize and the magnetron to operate at a constant temperature and steady state. Acquisitions made with the pulsed laser were triggered so as to produce time-resolved collection of photons at particular times during a given pulse.

For PRAXIS, the laser is continuous, but the acquisition window is typically 65 ms (6.5×10^6 points, at a 100 MHz acquisition frequency) and must be triggered to match the HiPIMS discharge pulsing. The triggering must also be done on a stabilized, reproducible discharge (i.e. stabilized target temperature).

The following procedure is therefore adopted:

(i) The discharge voltage and current are monitored in real time using a Teledyne Lecroy WaveRunner 625Zi oscilloscope and a LeCroy - CP150 probe, with plasma pulses run continuously and without acquisition. The shape of the discharge voltage and current profiles is known from previous steady-state measurements, already shown in Chapter 3 (Figs. 3.7 and 3.19).

(ii) Once the current and voltage profiles match those observed previously, the repetition of the discharge is stopped, and a single train of pulses over a duration of 1 sec is launched, on which the acquisitions are made.

(iii) After the acquisition, the current and voltage profiles profiles are re-checked to ensure that they match the target profiles. If not, the operation is restarted.

It has been observed that as long as the delay between the cut-off of the continuously-pulsed discharge and the single pulse train is less than 5 seconds, the shape of the current and voltage match in both cases.

A second point must be considered. In addition to the thermal effects which could lead to a slight change to the plasma features, a plasma pre-ionization effect may exist between the pulses (in which the residual plasma/electrons from a preceding pulse assist in the creation of the succeeding pulse). Since the full coherent Thomson scattering acquisition lasts 65 ms, a Stanford Research Systems digital delay generator (model DG645) is used to delay the start of the plasma pulse relative to the acquisition trigger.

For the argon discharge, synchronization of the acquisition and plasma pulsing is achieved as follows:

(i) A train of 100 Hz plasma pulses with a total duration of 1 second is launched at $t = 0$ on the planar magnetron. Each pulse has an individual duration of 90 μs, and is separated from the previous one by 10 ms.

(ii) The CTS (coherent Thomson scattering) acquisition lasts 65 ms. It is synchronized to start exactly at $t = 0$, and overlaps plasma pulses at $t = 0$ ms, $t = 10$ ms, $t = 20$ ms, up to $t = 60$ ms. The first recorded pulse, $t = 0$ ms, is never included in the analyses, in order to avoid a possible error linked to an acquisition time delay, as well as the previously-mentioned cold-start effect.

For the helium discharge, the procedure is slightly different:

(i) A train of 10 Hz pulses, with a total duration of 1 second, is launched at t = -90 ms on the planar magnetron. Each pulse has a duration of 100 μs, and is separated from the previous one by 100 ms.

(ii) The CTS acquisition, with a total duration of 65 ms, is started at $t = 0$. A single pulse is recorded at $t = 10$ ms. Once again, this offset is designed to avoid cold-start effects and computer reaction times.

For both discharges, the measured current and voltage shown in Figures 6.1 and 6.2 correspond to the discharge at $t = 10$ ms, i.e., the second discharge of each pulse train.

6.1.3 Data analysis and signal slicing

In the HiPIMS configuration, the plasma is switched on intermittently, so that a signal can only be measured during a fraction of the total acquisition time. To optimize signal detection, the following procedure is applied:

(i) The CTS acquisition, lasting 65 ms, is performed on 6.5×10^6 samples, i.e. a frequency of 100 MHz. When processing and analyzing this signal, it is divided into 65 units, each lasting 1 ms, i.e. 10^5 samples per unit. Each unit is designated by its u number, between 0 and 64. Thus, unit $u = 0$ represents the period between the start of acquisition and the first millisecond, unit $u = 10$ the period between the 10th and the 11th millisecond, and so on.

(ii) Plasma pulses have an individual duration of 100 μs, ten times shorter than the duration of a u unit. This makes it possible to have a single pulse and its afterglow within a single unit. For an argon discharge, we expect to obtain a signal on $u = 0$, $u = 10$, $u = 20$, $u = 30$, $u = 40$, $u = 50$ and $u = 60$. For helium, a signal can only be found on the unit $u = 10$. For the reasons mentioned above, the unit $u = 0$ for argon is never considered.

(iii) To perform Fourier transforms to obtain the dynamic form factor, each of these u units is again divided into 100 sub-units of 1000 points, and an FFT is performed for each of these 100 sub-units, then averaged between them. This empirical choice was made to reduce the signal variance sufficiently for the wave peaks to be distinguishable from the noise.

A Gaussian fit is performed on the negative and positive part of each spectrum, between -20 MHz and +20 MHz, as seen in Fig. 6.5. These fits are checked individually. Due to a very large number of points, especially for argon due to the multiple repetition of the signal in a pulse train, it is possible to exclude all incorrect fits, typically, from spectra with a very low signal level compared to the others.
Figure 6.5 shows the dynamic form factors for three units, $u = 9$, $u = 10$ and $u = 11$, to visualize the results of this processing. In this figure, the dashed blue and red lines indicate the position of the negative and positive peak frequencies, respectively, as a result of the Gaussian fit. The presence of a signal is clearly visible on the $u = 10$ unit, unlike the other two, which are discarded due to low signal levels.

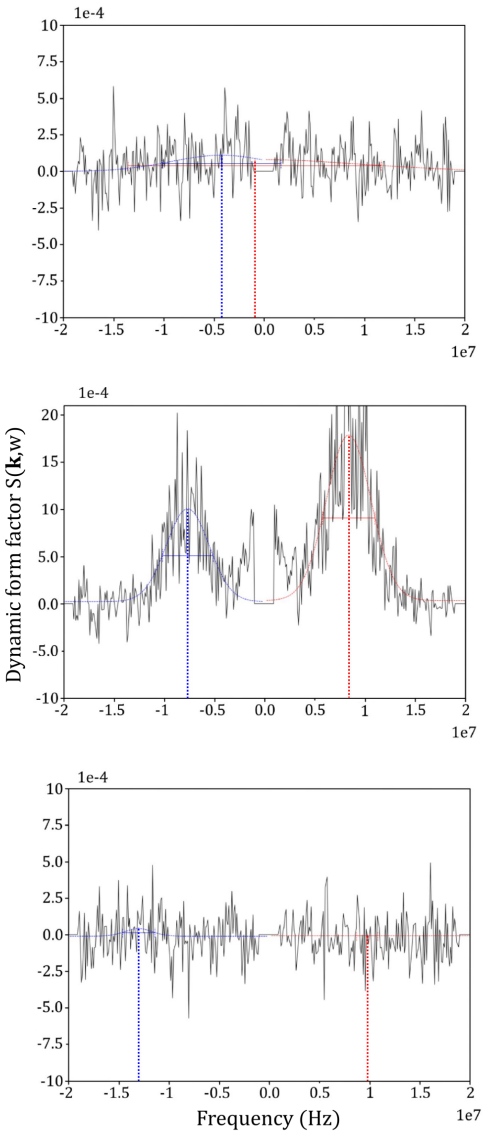

Figure 6.5: *The dynamic form factor $S(\mathbf{k}, \omega)$ as a function of frequency (Hz) for successive "units" of the CTS acquisition spectrum in 1 ms steps. Units 9, 10, and 11 are shown from top to bottom for the helium discharge. The dotted blue and red axes represent the center of the Gaussian fits on the negative and positive parts of the spectrum, respectively. Only the unit 10 is retained in the subsequent analysis.*

6.2 Angular exploration

In these experiments, angular exploration involves a rotation of the primary beam with respect to the oscillator, such that the resulting observation wave vector defined by these two beams rotates in the $(\mathbf{E}, \mathbf{E} \times \mathbf{B})$ plane. This is achieved using the translator-rotator element on the optical bench. It allows the directivity of the density fluctuations to be studied with a high level of detail, and this was used to precisely map out the propagation of the ECDI and IITSI previously, such as in Ref. [2].

While this rotation can occur through the full 360° in the $(\mathbf{E}, \mathbf{E} \times \mathbf{B})$ plane, there are particular features which limit the angular range from which the signals can be collected. These are primarily: (i) the positioning of a low-profile mirror which would block or diffract the primary beam path after rotation, and (ii) imperfections such as impact damage on the primary beam mirrors, which would result in diffraction susceptible to damage the detector. In part because of this limitation, in this study the angles explored mainly target the upper right quadrant seen in Figure 6.6. This figure shows, via the direction of the arrows indicated, the direction of the observation wave vector as it crosses the plasma.

In Fig. 6.6, the angle parallel to the vertical, with $\mathbf{k}$ pointing upward and thus along the electron azimuthal drift direction, is 305°. Facing the planar magnetron, this direction of $\mathbf{k}$ is parallel to the electron $\mathbf{E} \times \mathbf{B}$ drift at the 09h00 clock position, but antiparallel to the drift at the 03h00 clock position (e.g. see Fig. 3.12 for reference to the drift and applied field directions). This is the origin of the positive and negative frequency peaks which can be observed at this angular position, for example, in Fig. 6.5 for unit 10. The horizontal observation angle, with $\mathbf{k}$ pointing outwards and thus antiparallel to the cathode applied electric field, is 215°.

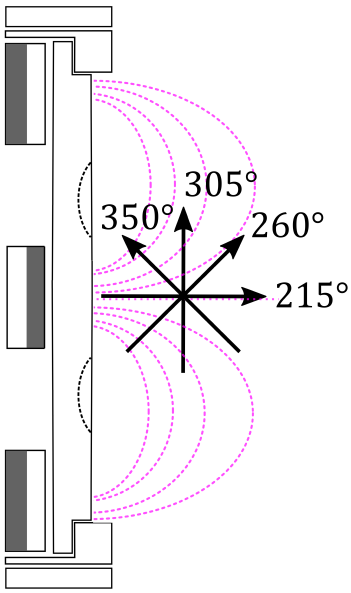

Figure 6.6: *Orientation of the observation wave vector* $\mathbf{k}$ *(black arrows) relative to the planar magnetron target surface, seen from the side, at different angular positions of the translator-rotator on the optical bench. The density fluctuations are measured in different directions in order to map out the presence of instabilities in the* $(\mathbf{E}, \mathbf{E} \times \mathbf{B})$ *plane. The magnetic field lines are shown in dotted lines.*

Signals are identified in cases where the intensity of an FFT peak is not negligible compared to the noise, such as in Figure 6.5, where a signal in unit 10 is present at -7.5 MHz and 8 MHz, but not in unit 9, nor in unit 11.

6.2.1 Angular features in the argon discharge

We first study the argon discharge. Due to the repetition of several acquisition times during the discharge (here unit 20, 30,...60), the spectra have been averaged to reduce the signal variance. The superimposed raw spectra are shown in the appendix A for illustrative purposes.
The figures presented in this section show only the frequency-integrated signal intensity ($S(k)$), static form factor) as a function of the angle in the $(\mathbf{E}, \mathbf{E}\times\mathbf{B})$ plane. The evolution of $(S(k))$ has been measured for the positive and negative part of the spectrum, when both peaks are present and can be clearly identified. The results of such an angular exploration for the argon conditions are shown in Fig. 6.7.

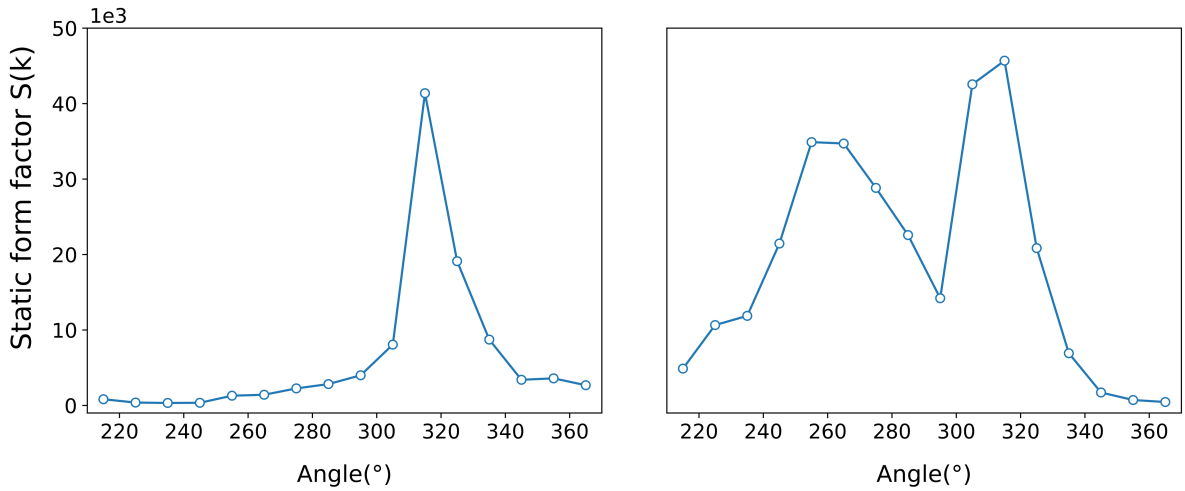

Figure 6.7: *Results of an angular exploration in the argon discharge, at an axial distance 12 mm from the target. The corresponding observation wave vector k is 5630 rad.m^{-1}. The static form factor (integrated signal intensity) is shown as a function of angle in the $(\mathbf{E}, \mathbf{E}\times\mathbf{B})$ plane. The figure on the left corresponds to the identified negative frequency peak; the figure on the right corresponds to the identified positive frequency peak. The same convention is used for the following figures.*

In Figure 6.7, the angular range explored is between 210° and 360°. This is the widest range that was used. The observation volume is placed 12 mm from the target, a distance close enough to probe the ionization region without significant diffraction of the laser beams. Some key observations can be made from this exploration:

(i) The left figure (negative frequency peak) shows a sharp peak around 315°. No other peak can be observed. The right figure (positive frequency peak), shows one peak at 315° and a second more flared peak around 260°. The signal level is about the same for the two peaks at 315° around 45×10^3, and slightly lower for the peak at 260°, around 35×10^3. **The observation of fluctuations around 315° on both figures is due to the presence of fluctuations parallel and antiparallel to the observation wave vector (due to the observation volume traversing the target diameter)**. This is very characteristic of an azimuthally-propagating mode. The slight offset from the pure azimuthal direction

(305°) in an indication that the mode propagates with an inclination from the vertical, i.e., with a component aligned with the horizontal electric field.

(ii) A second positive-frequency mode exists at 260°, at an angle of 45° with respect to the target surface. This mode seems to propagate in a single direction.

(iii) A small signal is visible in the figure on the right, around 220°, which could correspond to the detection of axially-propagating fluctuations, propagating in the same direction as the **k** vector (i.e. pointing away from the target).

In order to study these features further, two other investigations are carried out in argon at different axial positions (10 mm and 20 mm, albeit at a slightly different wavenumber of 4150 rad.m^{-1}). The results of the angular exploration at 10 mm are shown in Fig. 6.8 over an angular range between 200° and 300°.

On the negative frequency side of the spectrum, a peak is observed around $270 - 280°$, and a similar peak is found on the right (positive frequency side), but at a higher intensity, 800×10^3 versus 250×10^3. The angular range does not allow us observation of the azimuthal mode previously identified at 310°. However, in this case, the higher signal associated with an investigation at a closer target distance allows the (positive frequency) mode previously identified near 260° to be identified. Another low-amplitude mode (negative frequency) near 260° can now be identified.

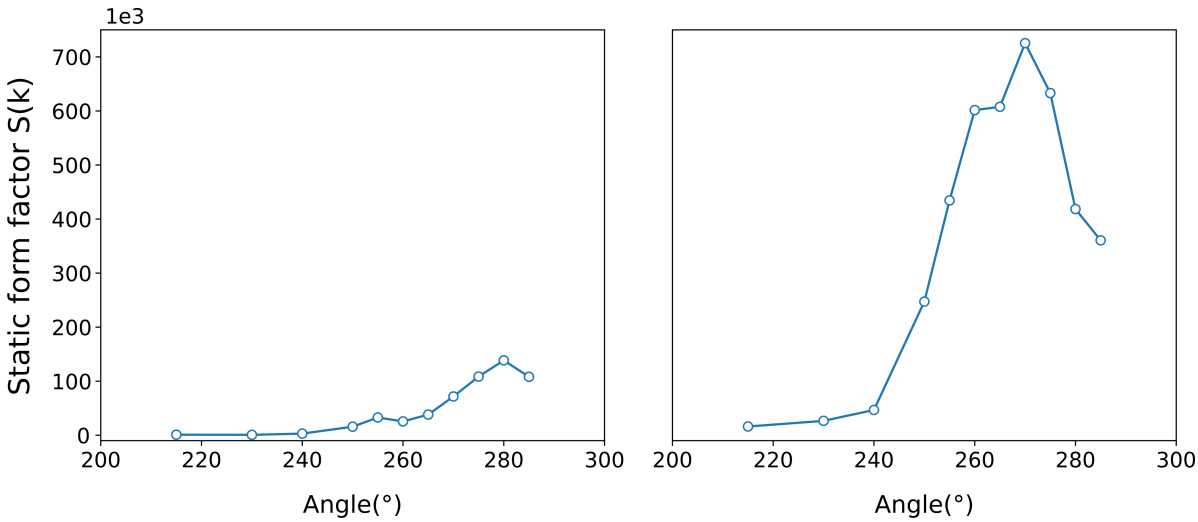

Figure 6.8: *Results of an angular exploration in the argon discharge, at an axial distance 10 mm from the target. The corresponding observation wave vector k is 4150 rad.m^{-1}. The static form factor (integrated signal intensity) is shown as a function of angle in the* $(\mathbf{E}, \mathbf{E} \times \mathbf{B})$ *plane. The figure on the left corresponds to the identified negative frequency peak; the figure on the right corresponds to the identified positive frequency peak.*

The last angular exploration measurement for argon in this section is carried out at a 20 mm axial distance. The corresponding results are shown in Fig. 6.9.
Fig. 6.9, corresponding to measurements at a further axial location, shows weaker signals (weaker density fluctuations are observed further away from the target). As a result, it is difficult to make conclusions regarding the negative frequency peaks (left). However, , we for the positive frequency peaks, fluctuations are once again identifiable around 260° reaching levels close to 100×10^3.

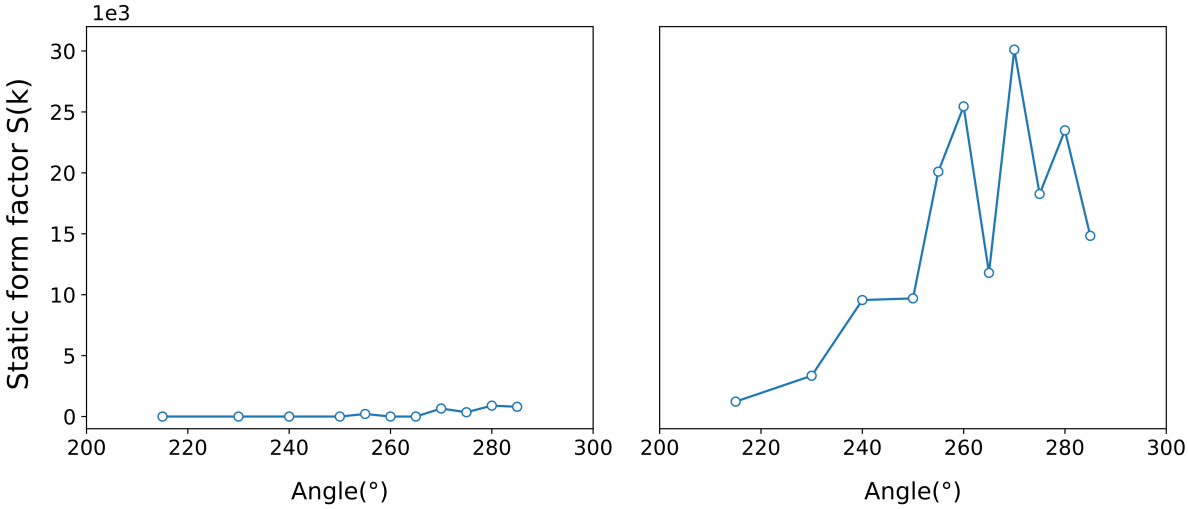

Figure 6.9: *Results of an angular exploration in the argon discharge, at an axial distance 20 mm from the target. The corresponding observation wave vector k is 4150 rad.m*$^{-1}$*. The static form factor (integrated signal intensity) is shown as a function of angle in the* $(\mathbf{E}, \mathbf{E} \times \mathbf{B})$ *plane. The figure on the left corresponds to the identified negative frequency peak; the figure on the right corresponds to the identified positive frequency peak.*

The measurements shown in Fig. 6.7, Fig. 6.8, and Fig. 6.9, performed under identical plasma conditions, show compatible information. A mode is always identified around 260°, propagating at 45° with respect to the target and primarily in one single direction, which we will call for the time being a "tilted mode". A component of this mode seems to exist in the opposite direction, but at a much reduced amplitude. A second mode is detected in the primarily azimuthal direction (near 315°). It is present at similar amplitudes on either side of the racetrack, which supports the idea that it is an azimuthally-propagating mode observed at positive and negative frequencies.

6.2.2 Angular features in the helium discharge

The same analysis is made for the helium discharge. Here, only one pulse is present during the CTS acquisition, in unit 10, so there is no question of averaging. The results of these angular studies are shown in Figures 6.10, 6.11 and 6.12. On the figures, some points are represented in orange, corresponding to points where the measurement was made, but where no significant signal could be detected.

In Figure 6.10, measurements are carried out (as for Fig. 6.7) 12 mm from the target. The angular range is 210° - 365°. On the right figure, a sharp signal peak can be seen near 260 °, similar to the tilted mode seen for argon. There is also a smaller peak near 220°, suggestive of an axial mode moving away from the target. It is interesting to notice the comparatively low level of the azimuthal fluctuations in the vicinity of 315° at this axial position; the dominant signal is for the tilted mode.

On the left figure (negative frequency data), a broad, low-level peak, around 30×10^3, exists for a position centered on 340°. This same peak is not found on the right, where instead a much larger peak is found near 260° and at a level of 120×10^3. The symmetry of this large peak at 260° is visible on a single point, on the left figure.

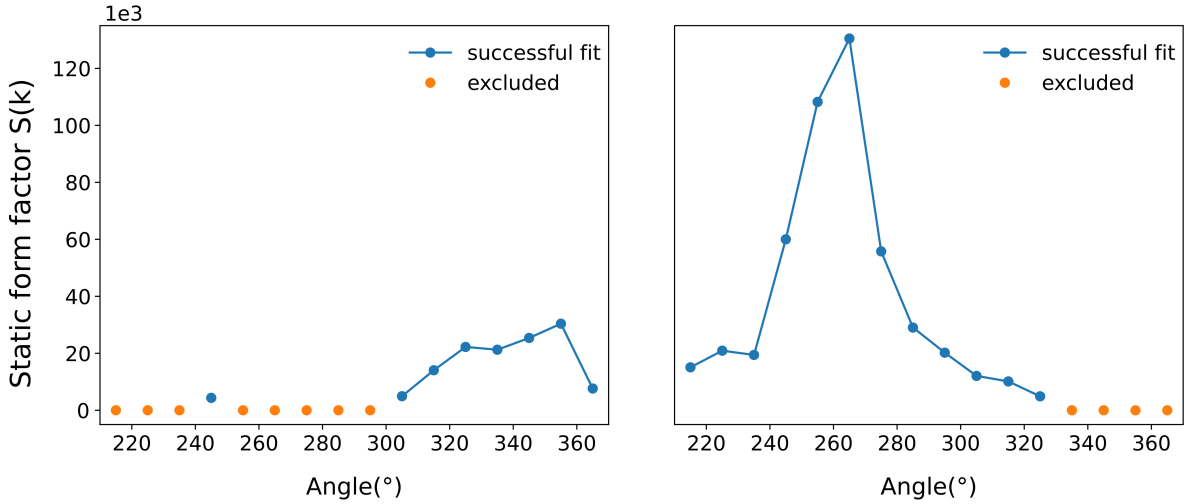

Figure 6.10: *Results of an angular exploration in the helium discharge, at an axial distance 12 mm from the target. The corresponding observation wave vector k is 5630 rad.m^{-1}. The static form factor (integrated signal intensity) is shown as a function of angle in the* $(\mathbf{E}, \mathbf{E} \times \mathbf{B})$ *plane. The figure on the left corresponds to the identified negative frequency peak; the figure on the right corresponds to the identified positive frequency peak.The orange dots are the positions where no signal was detected.*

In Fig. 6.11, angular measurements are performed at the axial distance of 10 mm, as was done for Fig. 6.8. The angular range is smaller, going only up to 300°. On the left figure, the level of density fluctuations increases around 280°, but these fluctuations are much more significant on the right (positive frequency data) where the signal amplitude is 400×10^3, versus 25×10^3 at the left. The mode seen in this angular range is again evidence of tilted propagation away from the target. On the left as on the right, we also find a large signal distinct from those seen at neighboring angles, at 255°, indicative of tilted propagation at an angle close to 45° with respect to the target surface.

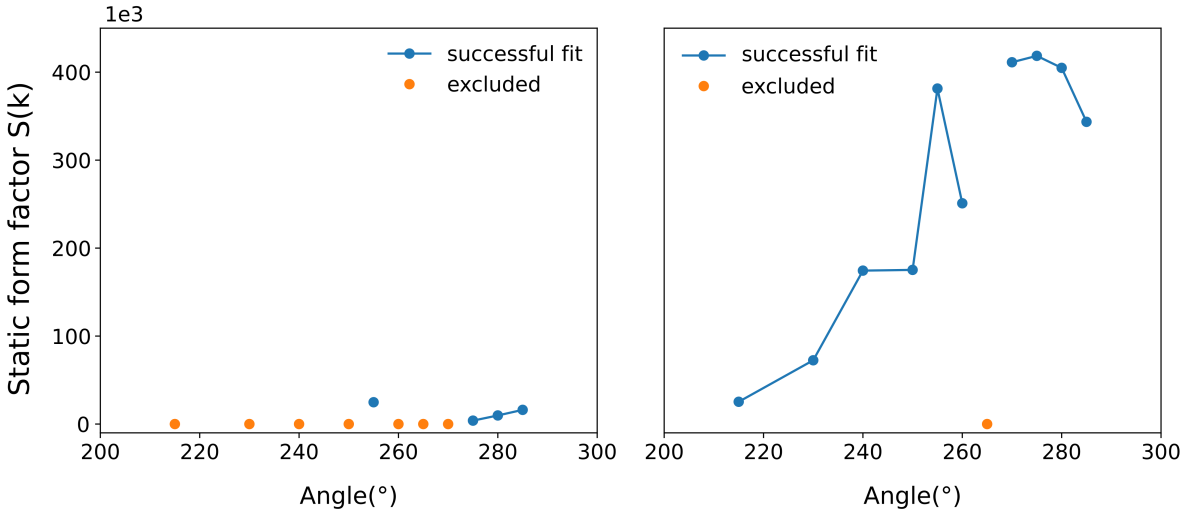

Figure 6.11: *Results of an angular exploration in the helium discharge, at an axial distance 10 mm from the target. The corresponding observation wave vector k is 4150 rad.m*$^{-1}$*. The static form factor (integrated signal intensity) is shown as a function of angle in the (*$\mathbf{E}, \mathbf{E} \times \mathbf{B}$*) plane. The figure on the left corresponds to the identified negative frequency peak; the figure on the right corresponds to the identified positive frequency peak.The orange dots are the positions where no signal was detected.*

Fig. 6.12 shows the angular exploration results for the last axial position for helium, at 20 mm. The left hand figure (only orange points indicated) shows that only low-level signals (not interpretable) were observed. In contrast, the positive frequency data is present at sufficient levels, showing a large-amplitude signal, centered around 260°. Once again, this observation corresponds to mode propagation away from the target at 45° with respect to the target surface. The three figures - Figs. 6.10, 6.11 and 6.12 - thus show complementary results, which can be interpreted quite simply. We find here again tilted mode propagation, much more intense for the positive frequency data, indicating a preferred direction of propagation (away from the target). The azimuthal mode also exists, but is much lower in amplitude than the tilted mode.

The mode frequency generally does not show a strong dependence on the angle. The frequency-angle plots are therefore reserved for the appendices (Appendix B) and are not analyzed here. The notable finding is a difference between the mode frequencies observed for the two gases, with an average frequency around 9 MHz observed for helium, versus 2 MHz for argon. This increase in frequency with a lighter gas is in agreement with what was expected, already observed both in linear kinetic theory and using PIC simulations, e.g. in Croes *et al*. [150].

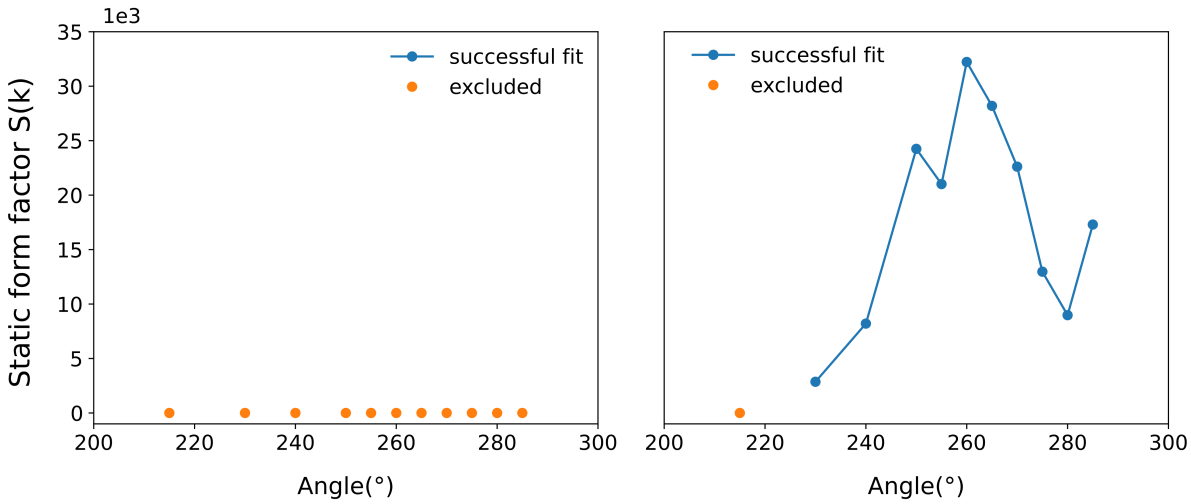

Figure 6.12: *Results of an angular exploration in the helium discharge, at an axial distance 20 mm from the target. The corresponding observation wave vector k is 4150 rad.m^{-1}. The static form factor (integrated signal intensity) is shown as a function of angle in the* $(\mathbf{E}, \mathbf{E} \times \mathbf{B})$ *plane. The figure on the left corresponds to the identified negative frequency peak; the figure on the right corresponds to the identified positive frequency peak. The orange dots are the positions where no signal was detected.*

6.3 Angular exploration: further discussion

6.3.1 Azimuthal mode

This discussion focuses first on the peak around 315°. Only Figures 6.7 and 6.10 show this angular range, for argon and helium, with the others not exceeding 290°. In the case of argon, a narrow peak is present in both the negative and positive parts of the spectrum, at a similar amplitude. As explained earlier, this is due to the observation of two sides of the racetrack, at the 03h00 and 09h00 positions.

We therefore observe a high-frequency mode propagating azimuthally around the planar magnetron racetrack; these are the expected characteristics of an ECDI. There is, however, a slight tilt of around 10° with respect to the pure azimuthal direction, visible on both sides of the spectrum. It would have been interesting to measure whether the same inclination was observable on other axial planes slightly offset from the distance z of the observation plane. However, subsequent measurements were inconclusive on this point, as the primary beam diffraction was too intense beyond 300° for smaller values of z. It should be noted, however, that the same angle of 10° to the vertical was observed in Tsikata's thesis [2], and thus the observed mode was found to possess a component in the direction antiparallel to the electric field.

The case of helium is more difficult to analyze at first glance, due to the presence of other extremely intense peaks, seen for example in Fig. 6.10. However, if these peaks are disregarded for moment, and the angular positions are restricted around 315°, a trend emerges, with the presence of signals on both sides of the spectrum, atamplitudes of a few 10^3, i.e., the same amplitude as that previously observed with argon.

6.3.2 Tilted mode

Previous measurements on the planar magnetron revealed the presence of an axially-propagating mode, at further axial distances, which we expected to observe here, in addition to the azimuthal mode. In reality, the peak observed, and present in all three argon figures, is at 260°. It has been temporarily named the tilted mode, because of its 45° angle with respect to the axial direction. To understand this phenomenon, we need to consider the planar magnetron geometry and the shape of the observation volume.

The latter is a rhombus centered on the middle of the target (Fig. 2.5), at a point where the magnetic field lines are *not* parallel to the cathode surface (Fig. 6.6). The preferred hypothesis for the observation of the tilted mode is that we perceive a mode propagating perpendicular to the field lines (as with the axially-propagating IITSI). In the case of argon in this work, when the **k** vector is aligned at 260°, it is precisely aligned so as to be perpendicular to the field lines corresponding to the lower part of the target. If this angular position had been accessible, we would also have observed a peak in the positive part of the spectrum when the wave vector is oriented at 170°.

Analyses of the figures corresponding to the helium discharge reinforce this hypothesis, due to the prominence of these fluctuations. Indeed, the signal observed on the positive part of Fig. 6.10 at 260° is extremely large, unquestionably confirming the existence of this tilted mode. The same signal is found on the following figures, very precisely around 260°.

In prior measurements on the planar magnetron plasma, evidence of axial fluctuations (propagating both parallel and antiparallel to the electric field) was found. The fluctuations propagating towards the cathode were observed to be lower in amplitude. It is logical, given the planar magnetron rotational symmetry, to assume that the tilted mode observed at 260° in Fig. 6.7 is accompanied by the same mode at 170°. This particular angle was not accessible in the measurement. However, the opposite direction, i.e. 170 + 180 = 350°, was. In theory, we should therefore have had a strong peak at this position on the left-hand side of the spectrum (since the direction of the observation vector is inverse to that of the main mode), and a weaker signal at this same position on the right-hand side of the spectrum. However, the signal level observed at 350° on the left, although non-zero, is very low in amplitude.

The case with helium shows these characteristics more clearly. If the hypothesis is correct, with the existence of a tilted mode perpendicular to the B field lines at 260° and 170°, we should also be able to observe this mode in the opposite direction (i.e., at 80° (inaccessible) and 350°). The plot in Fig.6.10 shows a clear signal at 350°. The fact that a signal is found at this position, even more intense than the peak at 305°, supports the idea that it reflects the presence of the tilted mode. To explain the existence of this mode, it is important to understand the fundamental operation of the planar magnetron, where we recall that some of the ions return to the target in order to sputter it. There is therefore a reverse ion flow, and electron density fluctuations which can be perceived propagating both towards and away from the racetrack.

A second point deserves mention. In the measurements observing the tilted mode at 260°, (with the exception of Fig. 6.10, carried out with a k value of 5630 rad.m^{-1}), the signal is particularly broad, and seems to show two distinct peaks, at 250° and 270°. It is possible that the broad peak consists of two superposed peaks, however, resolving this feature could require significantly increasing the number of points per spectrum and the acquisition frequency.

6.3.3 Some concluding remarks on the angular measurements

Regarding the amplitudes of the fluctuations in helium and argon, it is difficult to make direct comparisons at present (for example, by considering the relative static form factor $S(k)$ values). The mean discharge energy per pulse differs for the experiments with the two gases. It might be expected that lighter ions would respond more quickly to perturbations in the electron density (and thus, damp the oscillations, possibly leading to lower saturated mode amplitudes for the ECDI, for example). However, studying such effects would require more controlled experimental conditions (such as comparable plasma pulse energies for both gases). It should be noted that the linear kinetic theory analyzed for the different gases would provide information on the real mode frequencies and growth rates, but would not give an indication of the *saturated* mode amplitudes; it is these saturated mode amplitude levels which would dictate what is perceived directly in experiments. Numerical simulations would permit more detailed study of such effects.

As mentioned earlier in this manuscript, the presence and nature of the ion-ion two stream instability was confirmed in such plasmas [83, 86, 76], where different ion species (differing in charge state and/or atomic species type) coexist with magnetized electrons. In this work, we did not extensively analyze this mode using linear kinetic theory. It would be interesting for future work to use the complete dispersion relations developed for such plasmas to determine whether the respective densities and velocities of each of the ion flows could explain the experimental results observed using PRAXIS in this chapter. It would also be interesting to carry out a systematic spectroscopy campaign to accurately determine the evolution of each of these populations under the exact conditions of the discharge used in this manuscript. This is particularly true for the helium pulse, given that this gas is much less frequently used than argon in planar magnetron studies, and the available literature on the subject is less extensive.

Key aspects of these angular observations can be summarized as follows:

(i) an azimuthal mode is found, around 315°, on all spectra where this angle is accessed. This mode is of equal intensity in both lateral positions on the racetrack (antiparallel and parallel to the observation wave vector), and of similar levels for both gases. It has an angular deviation with respect to the vertical, towards the target, of 10° (in the $(\mathbf{E}, \mathbf{E} \times \mathbf{B})$ plane). This has previously been observed in DC planar magnetron studies and in the Hall thruster, and is now shown to be a feature of planar magnetron HiPIMS operation.

(ii) A tilted mode is clearly observed at 260°, in both argon and helium. It appears to decrease in intensity with distance from the target, and is significantly stronger in helium than in argon. There is an inverse mode, propagating in the opposite direction, but attenuated by at least an order of magnitude. It is possible that this 260° mode is, in fact, made up of two sub-modes at 250° and 270°, but the level of signals measured does not allow us to make definitive conclusions on this point.

(iii) The tilted mode cannot be explained as a manifestation of the ECDI. In the axial direction, ion temperatures are larger than in the azimuthal direction and this effect would contribute to mode damping axially. It is more likely that the mechanism behind this instability is similar to that of the IITSI. If this is the case, the directivity of the tilted mode may be connected to an ion flow which is not purely axial (i.e., this flow may show a significant radial component). This would be compatible with the strong radial drift directly measured for the electrons in Chapter 3.

6.4 Experimental dispersion relations

It was found that at least two different modes exist in these HiPIMS discharges, a tilted mode and an azimuthal mode, with the latter showing features of the electron cyclotron drift instability, ECDI. The presence of these modes was established by angular exploration at a fixed wavenumber value.

In order to study the mode features more closely, the orientation of the observation wave vector is set to match the main directions in which the modes have been observed to propagate, and the dispersion relation is directly measured (over a k range of 4000 - 13000 rad.m^{-1} for all figures). Dispersion relation investigations in the azimuthal direction (of the ECDI) are performed at 305°. Dispersion relation measurements of the tilted mode are conducted at a fixed angle of 260°. One dispersion relation measurement, performed at 215°, allows the investigation of purely axial fluctuations. Such analyses, particularly of the ECDI, which has been studied in this manuscript analytically, allow direct comparisons between the linear kinetic theory and the experimental dispersion relations.

In this section, the convention used for the angular exploration measurements is adopted, in which:

- figures on the left correspond to values measured for the negative frequency peak and thus mode propagation **antiparallel** to the observation wave vector (absolute frequencies values are shown throughout), and,
- figures on the right correspond to values measured for the positive frequency peak and thus mode propagation **parallel** to the observation wave vector.

6.4.1 Dispersion relations in the argon discharge

Figure 6.13 shows the dispersion relation at 305° direction, corresponding to the azimuthal mode, for the observation volume placed 12 mm from the target.

The evolution of the static form factor, and therefore the amplitude of the mode, is visible in the lower part of the figure. Below an amplitude of 1000, the signal level is too low to be distinguished from the noise, and makes it impossible to conclude that the mode is present. The signal level decreases exponentially with increasing k values. For this reason, the only wavenumber range observed here is between 5000 and 8000 rad.m^{-1}. The factor of 2 difference in the amplitudes between the two directions is not significant, having been observed regularly on the same pulse under identical conditions.

The upper part of the figure shows the frequency (in Hz) at which the mode is detected for each value of k, for each of the 6 pulses present during the entire CTS acquisition. As explained at the beginning of the chapter, the first pulse at $u = 10$ is not taken into account in the analysis of the results, in order to avoid a "cold start" effect. It is not taken into account in the linear fit used to calculate the mode group velocity v_g. It is, however, included in the figures where possible, for the purposes of illustration.

The mode dispersion relations shown in Fig. 6.13 are linear over the observed wavenumber range, as observed during previous studies. The group velocity is around 2 km.s^{-1}, with a difference of around 300 m/s between the two directions. This is within the expected margin of error.

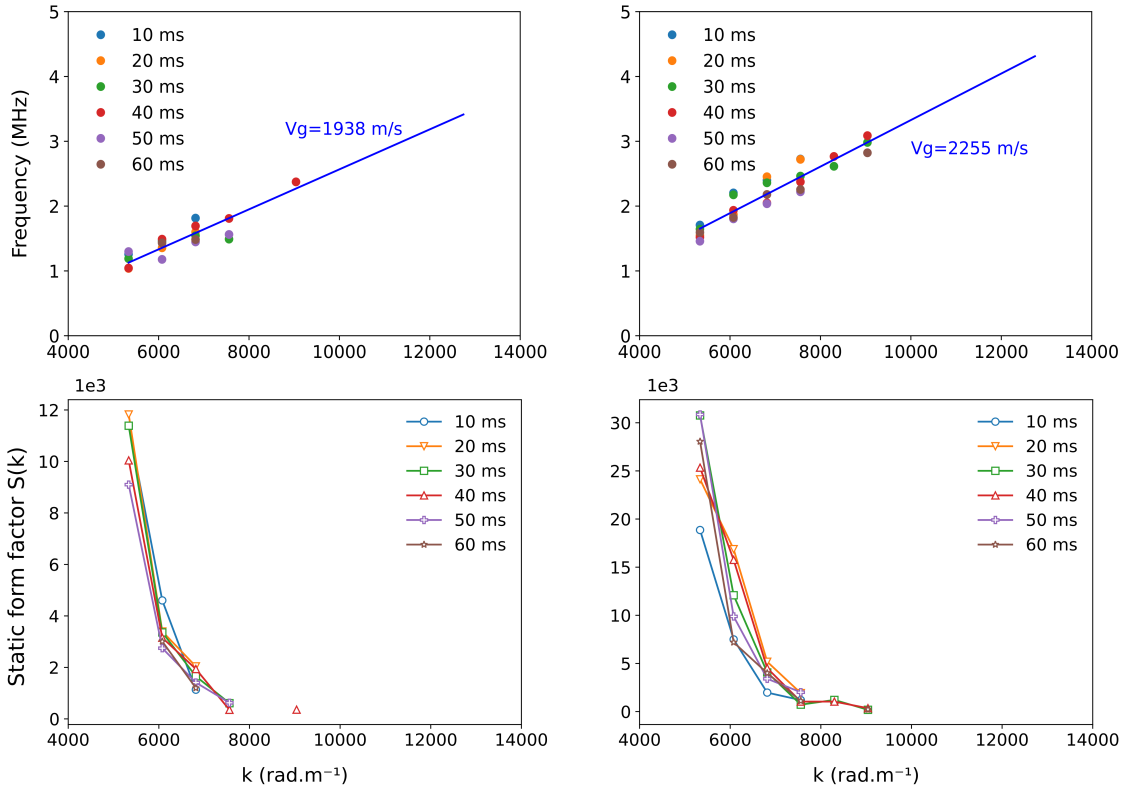

Figure 6.13: *Experimental dispersion relations in the argon discharge, at an axial distance 12 mm from the target and angle* 305°. *Figures on the right correspond to fluctuations parallel to the wave vector; figure on the left to fluctuations antiparallel to the wave vector. The group velocity* v_g *is determined by a linear fit and is shown in blue. The static form factor (integrated signal intensity) is shown as a function of* k *for the respective dispersion relations.*

The dispersion relations and variation in mode amplitude are now examined in the axial direction, with k aligned with at the angle 215°, at the same axial position of 12 mm. The results are shown in Fig. 6.14.

Fig. 6.14 shows a clear difference in the $+\mathbf{k}$ and $-\mathbf{k}$ directions of mode propagation. The amplitude on the right is significantly larger in amplitude than that on the left, by a factor of more than 4. No significant analysis can be done on the data at the left due to the low amplitudes measured. The data at right (corresponding to fluctuations propagating axially outward from the target) can be analyzed. The group velocity is close to 3 km.s^{-1}. It should be remembered, however, that no significant signal peak was observed in this axial direction during the angular explorations, carried out at a k value of 5630 rad.m^{-1}, whereas a small signal was observed when k was at 4150 rad.m^{-1}. The exponential drop in the form factor with k seen for many modes in past work means that in some cases, low-amplitude modes only become clearly detectable at the smallest wavenumber values. This appears to the case with the axial fluctuations in this work.

Dispersion relations measured at 10 mm are next considered, at 260° (to observe the tilted mode). These experiments are repeated, two days apart, and shown in Fig. 6.15 and Fig. 6.16, in order to check the repeatability of the measurements.

The results from Fig. 6.15 and Fig. 6.16 are identical, indicating the experiments are repro-

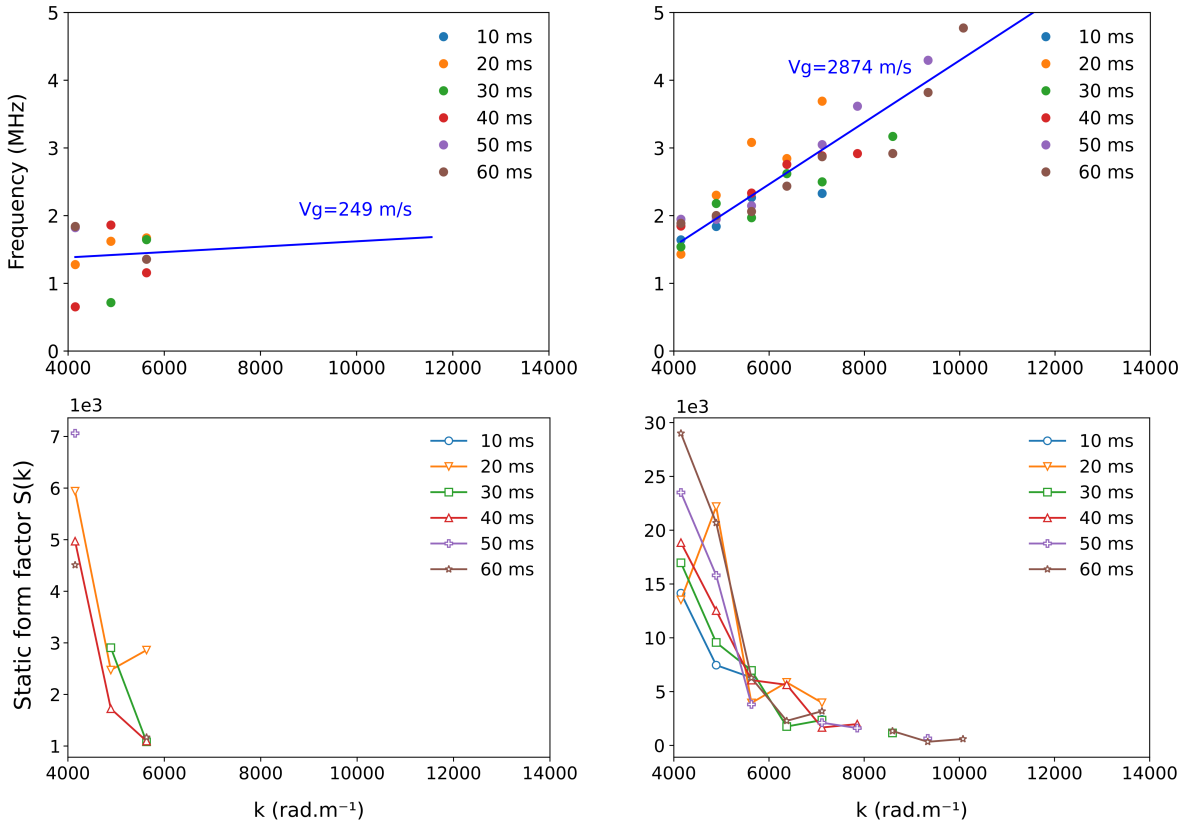

Figure 6.14: *Experimental dispersion relations in the argon discharge, at an axial distance 12 mm from the target and angle* 215°. *Figures on the right correspond to fluctuations parallel to the wave vector; figure on the left to fluctuations antiparallel to the wave vector. The group velocity* v_g *is determined by a linear fit and is shown in blue. The static form factor (integrated signal intensity) is shown as a function of* k *for the respective dispersion relations.*

ducible. As was found earlier, the tilted mode propagates with larger amplitudes away from the target (right) than towards the target (left).

Summary

The results obtained with argon are therefore consistent with those previously found. The frequencies observed for the azimuthal mode are identical in both directions, compatible with those of an ECDI in this type of discharge, and the dispersion relation is linear. The tilted mode, on the other hand, propagates predominantly away from the target, with a weaker inverse component. In the purely axial direction (215°), although difficult to detect by angular scanning, there is a weak mode, at a higher frequency than the azimuthal mode, propagating axially away from the target.

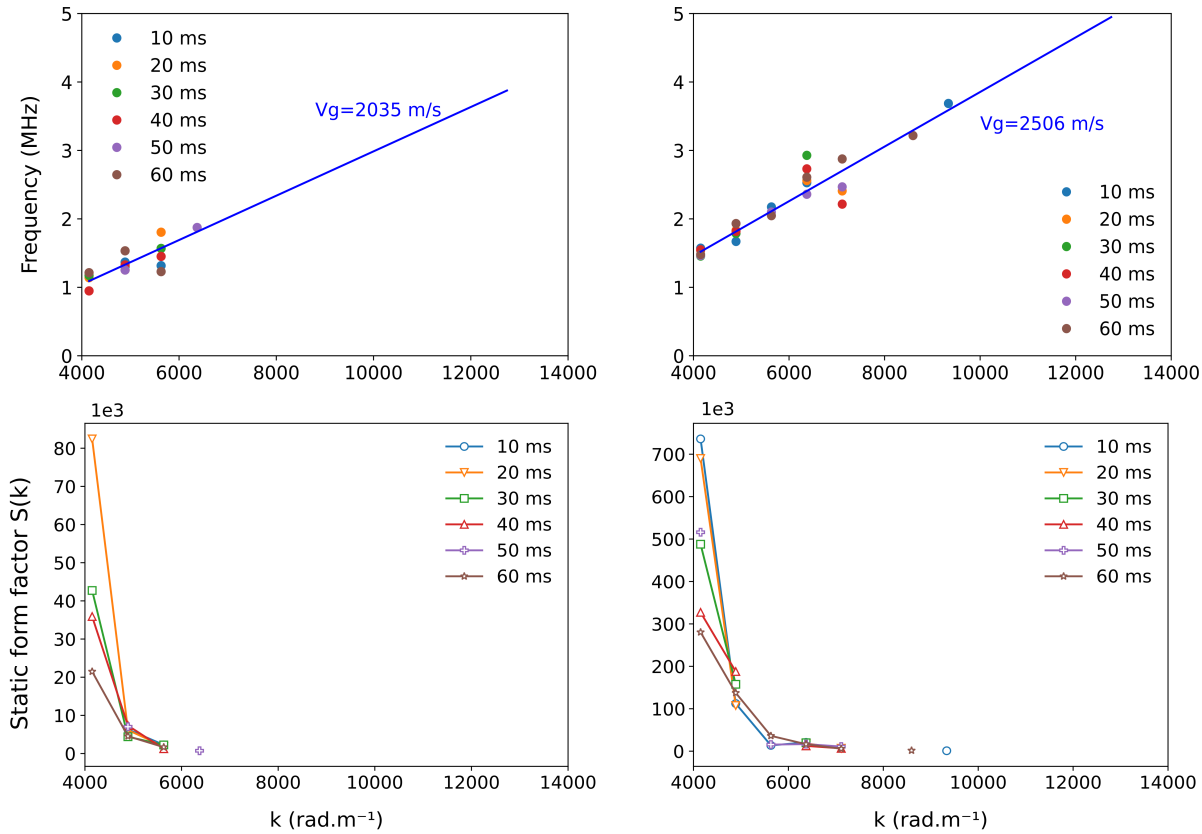

Figure 6.15: *Experimental dispersion relations in the argon discharge, at an axial distance 10 mm from the target and angle* 260°. *Figures on the right correspond to fluctuations parallel to the wave vector; figure on the left to fluctuations antiparallel to the wave vector. The group velocity* v_g *is determined by a linear fit and is shown in blue. The static form factor (integrated signal intensity) is shown as a function of* k *for the respective dispersion relations.*

6.4.2 Dispersion relations in the helium discharge

The behavior of dispersion relation in helium is less easy to interpret. Here again, we have shown in blue the points that have a signal and were used for the fit, and in orange those that were excluded.

The first figure for helium, Fig. 6.13, shows the 305° direction, corresponding to the azimuthal mode, and the observation volume is placed 12 mm from the target. This figure shows a lower signal level than argon in the same direction. A single point stands out on the left, which unfortunately does not allow any conclusions to be drawn about group velocity. However, this first point is aligned with its symmetrical counterpart on the right, around 8 MHz. The group velocity observed on the right is much higher than that observed with argon, of the order of 12 km.s^{-1}, as expected with a lighter gas.

The second figure, Fig. 6.18, corresponds to the observation wave vector oriented in the axial direction, 215°, at 12 mm from the target. The group velocity is half that of the purely azimuthal mode, at about 6 km.s^{-1}. Here as well, fluctuations are only observed propagating away from the target. The rate of amplitude decay as a function of k is close to that of argon, with the signal disappearing at around 8000 rad.m^{-1}, for an initial value of 50×10^3 at 4000 rad.m^{-1}.

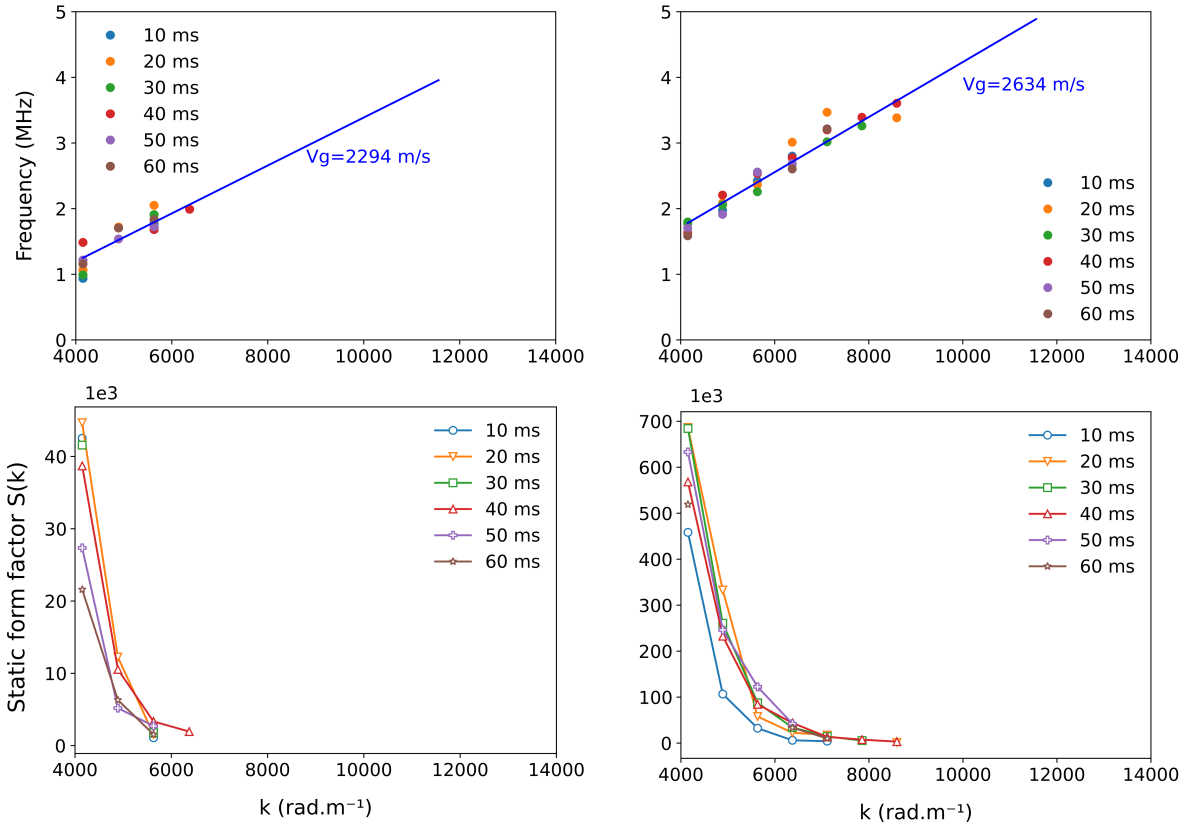

Figure 6.16: *(Repeated experiment in conditions of Fig. 6.15) Experimental dispersion relations in the argon discharge, at an axial distance 10 mm from the target and angle* 260°*. Figures on the right correspond to fluctuations parallel to the wave vector; figure on the left to fluctuations antiparallel to the wave vector. The group velocity v_g is determined by a linear fit and is shown in blue. The static form factor (integrated signal intensity) is shown as a function of k for the respective dispersion relations.*

Finally, for the last figure (Fig. 6.19) at 260°, the dispersion relation is linear, with a group velocity of around 12 km.s^{-1}, very close to that of the azimuthal mode group velocity and much larger than that of the axial mode. The amplitude decay as a function of k is again very rapid, dropping from nearly 10^6 to zero between 4000 and 8000 rad.m^{-1}.

The respective group velocities for each mode, in parallel and antiparallel directions for each direction and each discharge are summarized in Table 6.2.

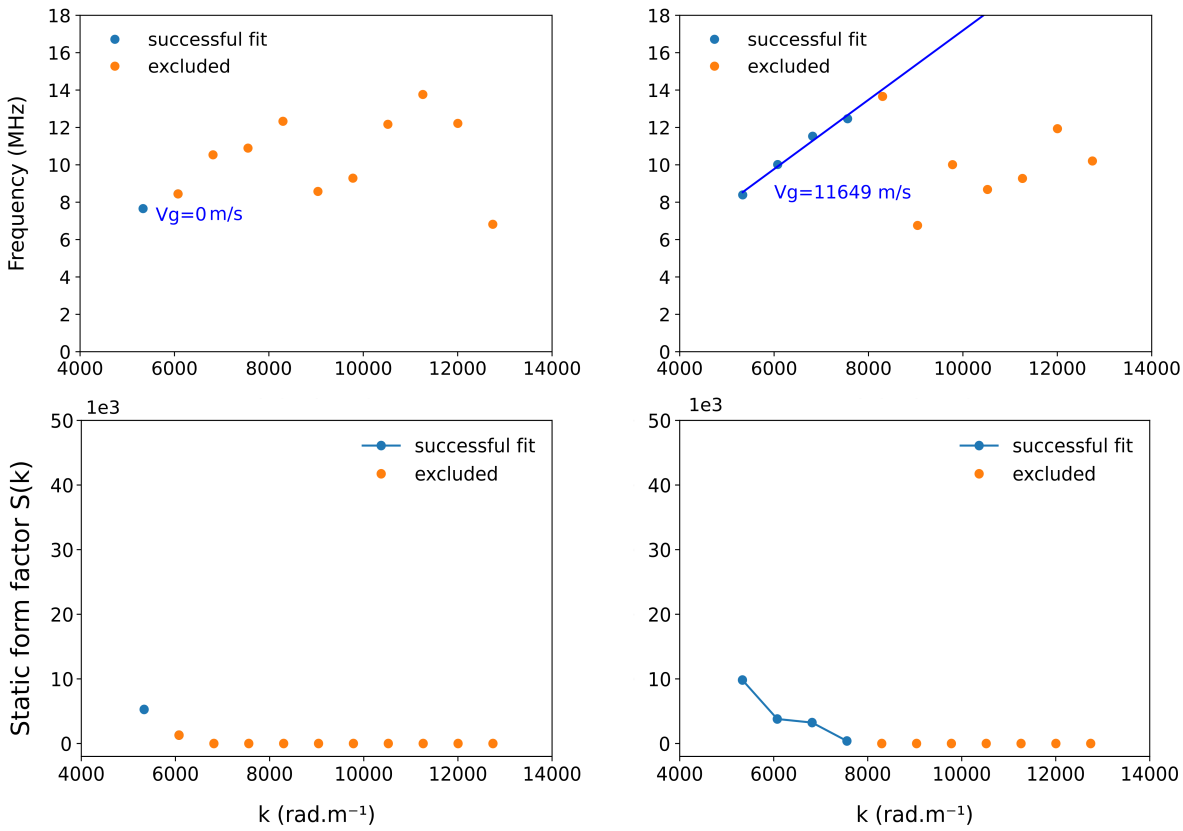

Figure 6.17: *Experimental dispersion relations in the helium discharge, at an axial distance 12 mm from the target and angle* 305°. *Figures on the right correspond to fluctuations parallel to the wave vector; figure on the left to fluctuations antiparallel to the wave vector. The group velocity* v_g *is determined by a linear fit and is shown in blue. The static form factor (integrated signal intensity) is shown as a function of k for the respective dispersion relations.*

6.5 Comparison with theoretical dispersion relations

All the evidence suggests the idea that the mode observed in the 315° direction in this work corresponds to the ECDI, in both discharges. It is detected on either side of the racetrack as an azimuthally-propagating mode at symmetric positive and negative frequencies. The experimental results for this mode can be compared to the previously-developed linear kinetic theory accounting for two ion populations. As we already know the electron properties of these discharges from incoherent Thomson scattering measurements, the only variable left free here is the proportion of the ions populations. The results of this comparison are shown in Fig. 6.20, in (a) for an argon/titanium plasma, and in (b) for a helium/titanium plasma.

Fig. 6.20 shows that the best match between the experimental and linear kinetic theory data is obtained for a titanium ion fraction of 0.3 for the argon discharge and 0.4 for the helium discharge. Experimental points shown correspond to fluctuations measured parallel to the observation wave vector direction.

Initially, it is satisfying to note a good match between the experimental and theoretical results. The range swept by varying the proportion of titanium ions to gas ions is not unlimited. For example, if the slope of the linear fit had been 25% less pronounced in the case of argon (corre-

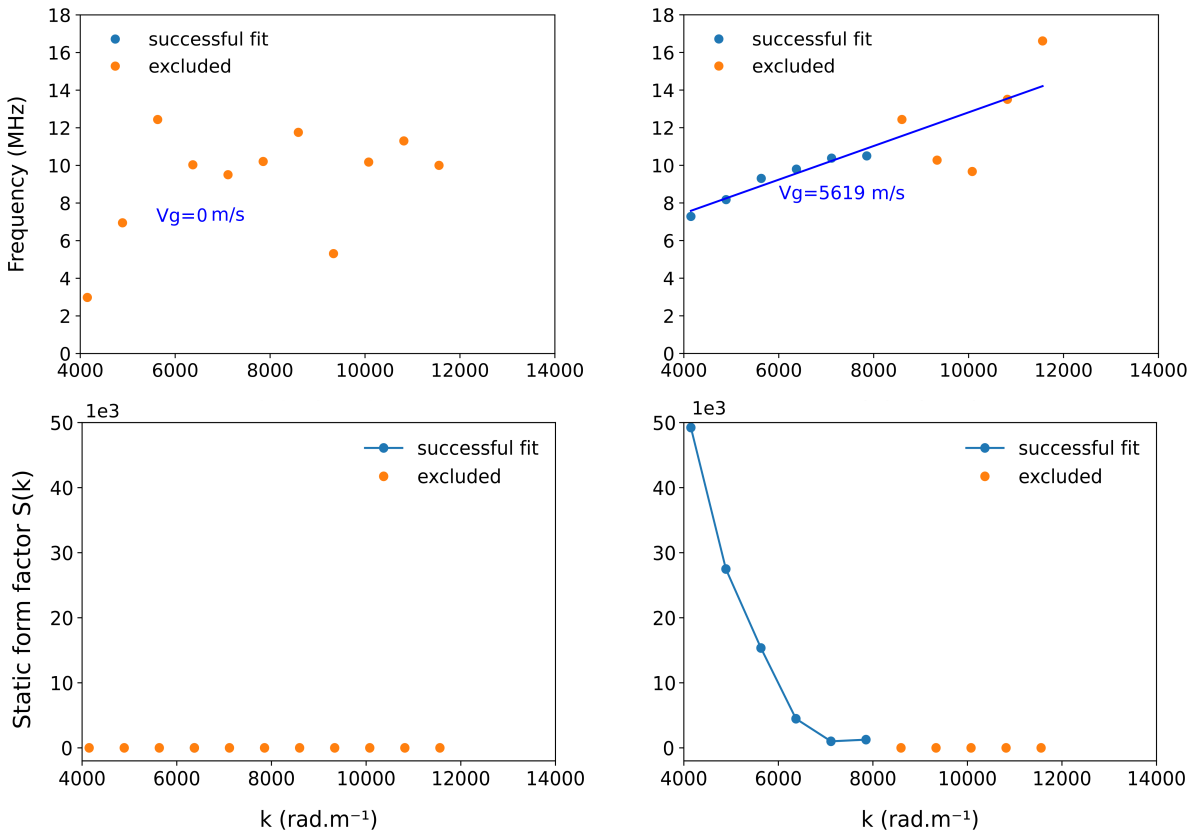

Figure 6.18: *Experimental dispersion relations in the helium discharge, at an axial distance 12 mm from the target and angle* 215°. *Figures on the right correspond to fluctuations parallel to the wave vector; figure on the left to fluctuations antiparallel to the wave vector. The group velocity* v_g *is determined by a linear fit and is shown in blue. The static form factor (integrated signal intensity) is shown as a function of* k *for the respective dispersion relations.*

sponding to a group velocity of 1700 m/s), no proportion of titanium would have made it possible to fit the results. This is also true if the slope had been 10% steeper. The dispersion relation with helium is more permissive, due to the greater mass difference between the gas and metal ions, but the uncertainty is therefore reduced. We remember here that the term ionic fraction is used in accordance with the following definition:

$$F_i = \frac{\text{number of ions of species i}}{\text{number of ions from gas} + \text{number of ion from target}}$$

In the literature, the term is often used to describe the proportion of ions to neutrals in a single species. A precise explanation of the differences between ionized density fraction, ionized flux fraction and the fraction of the sputtered metal atoms that become ionized can be found in Ref. [151].

The observed values for the argon discharge are 70% gaseous ions and 30% metal vapor ions, compared with 60% gaseous ions and 40% metal vapor ions for the helium discharge, 10 mm from the target. It is important to note, however, that this proportion is calculated as an average over the tens of μs of the discharge, and does not take into account variations in this proportion over the course of the pulse.

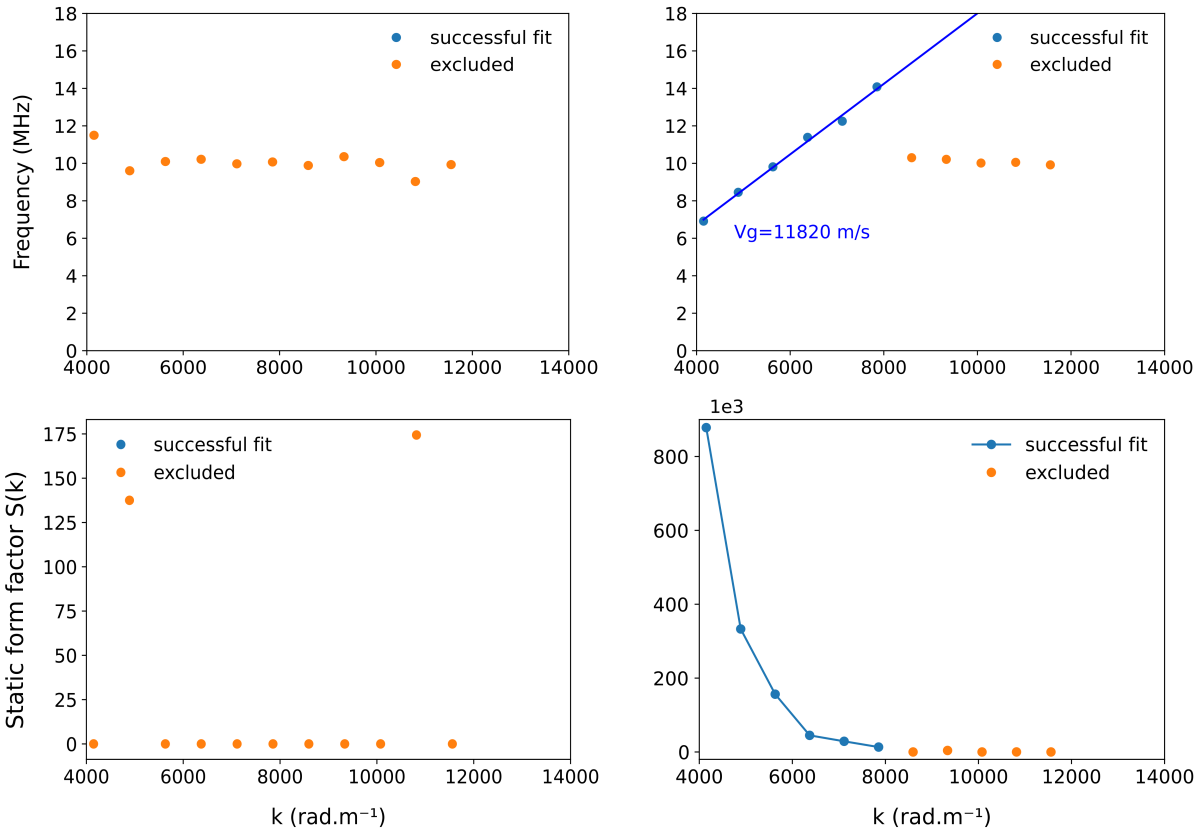

Figure 6.19: *Experimental dispersion relations in the helium discharge, at an axial distance 10 mm from the target and angle* 260°. *Figures on the right correspond to fluctuations parallel to the wave vector; figure on the left to fluctuations antiparallel to the wave vector. The group velocity* v_g *is determined by a linear fit and is shown in blue. The static form factor (integrated signal intensity) is shown as a function of k for the respective dispersion relations.*

Kapran recently carried out [146] measurements on the same planar magnetron used in this manuscript, to verify the influence of magnetic configuration on ionized flux fraction and deposition rate. She also carried out measurements under the conditions corresponding to the argon discharge used in this work, in the C5-E5 magnetic configuration.
Those measurements, combined with the incoherent Thomson scattering investigations obtained using THETIS, can therefore indirectly provide information on the properties of the heavy ion species throughout the discharge, provided that quasi-neutrality is respected at the point of measurement. The ionized flux fraction of titanium (the number of ions relative to the metal neutrals and ions arriving at a microbalance positioned facing the target) is of the order of 12% in the Kapran measurements. This value is an average of values measured between 4 cm and 8 cm from the target (between 8% and 16%).

Using the proportions between the different definitions of ion fractions explained by Butler, one can calculate that in the case presented here, this would correspond to a fraction of titanium ions ($n_{Ti+}/(n_{Ti+} + n_{Ti})$ in the plasma of the order of 58%. This difference is explained by the fact that not all the ions created in the plasma move away from the target, but a large proportion of them return directly to the target to maintain the discharge.

Argon	Mode group velocity in $-\mathbf{k}$ direction (km.s^{-1})	Mode group velocity in $\mathbf{k}$ direction (km.s^{-1})
305°	1.9	2.3
215°	–	2.9
260°	2.0 – 2.3	2.5 - 2.6

Helium	Mode group velocity in $-\mathbf{k}$ direction (km.s^{-1})	Mode group velocity in $\mathbf{k}$ direction (km.s^{-1})
305°	–	11.6
215°	–	5.6
260°	–	11.8

Table 6.2: *Summary of the group velocity of high frequency modes measured at 3 angular wave vector orientations, to observe azimuthal propagation (305°), pure axial propagation (215°), and tilted mode propagation (260°). Results for argon and helium are shown.*

The average electron density at the plateau is of the order of 10^{19} m^{-3} for argon 5.2. Following the previous proportions, the concentration of ion species in the discharge can be established (Table 6.3):

Argon	n_e	n_{Ti+}	n_{Ar+}	n_{Ti}	n_{Ar}
	1×10^{19} m^{-3}	3×10^{18} m^{-3}	7×10^{18} m^{-3}	2.17×10^{18} m^{-3}	$*2.4 \times 10^{20}$ m^{-3}

Table 6.3: *Density of different species present in the HiPIMS discharge. * = obtained from the pressure gauge, assuming uniform gas pressure in the chamber, disregarding gas depletion effects*

The values described in Table 6.3 are slightly lower than those observed by Bohlmark [152]. He carried out spectroscopic measurements of neutral and ionic densities in a HiPIMS argon/titanium configuration, with 100 μs pulses and 50 Hz repetition, and a pressure of 1.3 Pa, very close to our conditions. He observed ionized titanium fractions ranging from 45% to almost 100% by varying the power of each pulse from 0.5 J to 12 J (i.e. from 0.05 kW.cm^{-2} to 1.4 kW.cm^{-2} peak power for his target). In the argon investigations in this work, the individual power of the pulses was 2.2 J, or 0.4 kW.cm^{-2} (average).

Since Bohlmark worked at a range of pulse energies well above and well below our cases, we would therefore expect to find values of the ionized titanium fractionbracketed by those of Bohlmark. The values of ionized titanium fraction found by Bohlmark are consistently slightly higher than ours. Nevertheless, although we do not know his precise magnetic configuration, Bohlmark operated in a slightly unbalanced configuration, and seems to obtain higher peak currents than we do. This is in line with Kapran's measurements, where the ionized flux fraction arriving at the microbalance is higher in the unbalanced case. She attributes this to a reduced Ti+ back-attraction.

Coherent Thomson scattering measurements therefore provide information on the proportion of metal and gas ions in the plasma, via the ECDI form, and on the proportion of singly- and

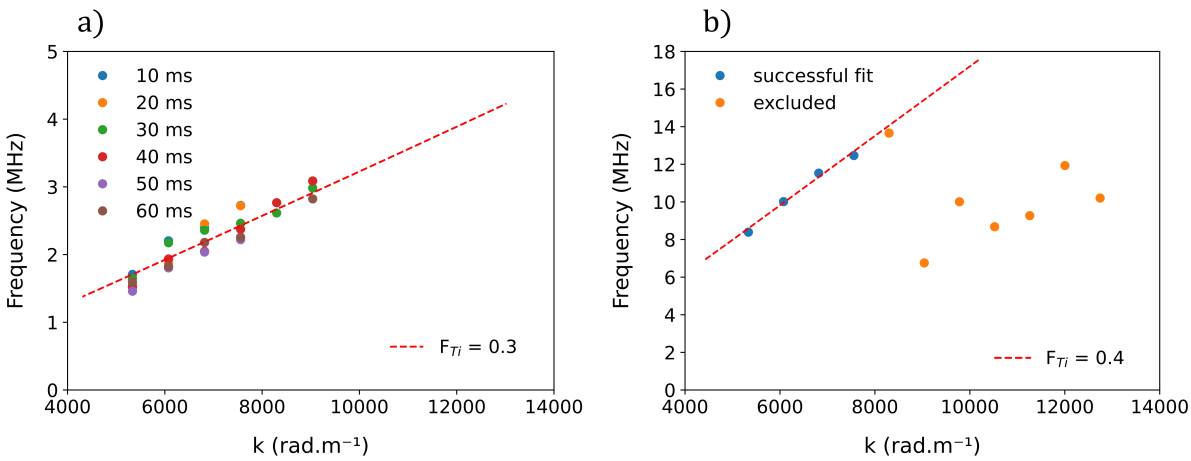

Figure 6.20: *Comparison between the ECDI experimental dispersion relations measured at an angle of* 315°*, for argon (a) and helium (b), and the results of the simple two-ion linear kinetic theory model (argon/titanium and helium/titanium) described in Chapter 5. The best match between the experimental and linear kinetic theory data is obtained for a titanium ion fraction of 0.3 for the argon discharge and 0.4 for the helium discharge. Experimental points shown correspond to fluctuations measured parallel to the observation wave vector direction.*

doubly-charged ions in the flow, via the IITSI. Incoherent Thomson scattering can be used to track the properties of electrons in the plasma, including changes in density over time. However, these diagnostics provide no precise information on neutrals.

This information can be supplemented by more conventional diagnostics, such as optical emission spectroscopy to recover the proportion of ions and neutrals in the plasma, or, as we have seen, by a microbalance to recover the flux of singly-charged ions and neutrals to the anode. Thus, a map of the concentration of species in the discharge can be obtained by the combination of results from multiple diagnostics (Table 6.3).

Due to the low signal level associated with the short duration of the discharge, it was not possible to track the evolution of the density fluctuations within an individual pulse. As DCMS measurements have a much higher average signal level, it would be interesting to reproduce CTS observations on HiPIMS pulses of longer durations. The effect of gas depletion on the fluctuations could be observed in real-time, as we would expect to find only titanium ions after a few tens of μs.

6.6 Influence of the presence of a probe in the plasma on instabilities

6.6.1 Implementation

As mentioned in the introduction, the use of intrusive diagnostics such as Langmuir probes can lead to disturbances in the plasma. This is why we have focused on the use of non-intrusive optical diagnostics, admittedly complex, in this manuscript. The disturbance of the plasma by probes has been documented in numerous references, such as Ref. [153, 154]. We can therefore expect measurements of complex and unstable events, such as instabilities, to be even more prone to probe disturbance. In addition, the conditions (temperature and density) found in some devices in areas such as ionization regions, prohibit the use of probes (which must, at the minimum, be rapidly moved into and out of the plasma during measurements to avoid destruction). This is the case with crossed-field devices like the Hall thruster.

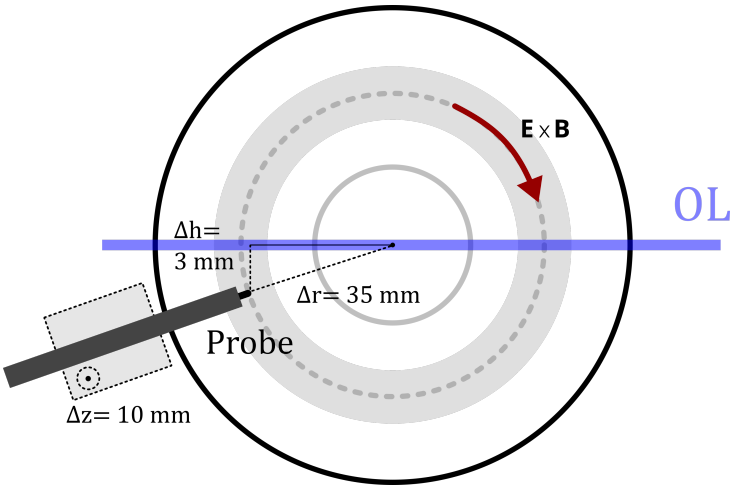

Figure 6.21: *Investigation of probe perturbation effects on instabilities measured. This image shows the position of the probe relative to the planar magnetron surface and the LO laser beam (in blue), seen from the front. z is the axial distance from the surface of the guard ring, r is the radial distance from the center of the target, and h is the vertical separation between the probe and the lateral centerline of the target. The LO beam passes along this lateral centerline.*

Probes in the planar magnetron, although expected to lead to plasma perturbation when used in the ionization region, can still be used without destruction, especially for pulsed operation. In the HiPIMS cases presented in this manuscript, the operating cycle is quite short, with only a few pulses lasting a few tens of μs. This means that a small probe, even a few mm in front of the target, does not have time to heat up. This is all the more the case as the synchronization required for the measurements leaves the plasma on for only a few seconds at most for each measurement point. We therefore took advantage of this configuration to use non-intrusive diagnostics to check the influence of an intrusive probe on the fluctuations (ECDI and axial modes). We also know with certainty that the aforementioned instabilities exist in this plasma, following previous measurements, thus we can perform comparisons of their features with and without the probe.

The probe is placed in the configuration shown in Figure 6.21. This is the most basic Langmuir-type probe possible, consisting of an alumina body from which a tungsten tip of radius 0.6 mm and length 2 mm emerges. It is aligned along a radius of the target, with the end of the tip exactly

35 mm from the center (δr), and at a vertical distance (δh) of 3 mm below the planar magnetron lateral centerline. The aim was to bring the tip as close as possible to the measurement volume, without causing diffraction of the primary laser beam. Finally, the probe is placed along the plane parallel to the target surface, at an axial distance of $z = 10$ mm, i.e. in the same plane as the OL. The probe tip, as seen in Fig. 6.21, is thus placed at the very core of the racetrack, in the zone of highest density. The tip is left at the floating potential, with no power supply of any kind. The plasma conditions for this investigation are identical to those used previously for argon and helium, for comparison purposes.

6.7 Angular exploration

The same method of angular exploration at fixed wavenumber as in the case without a probe is applied. This corresponds to an angular exploration of the mode frequencies and amplitudes between 215° and 305° (Fig. 6.6), for a fixed k value, here $k = 4150$ rad.m^{-1}.
These results are not discussed or presented in this manuscript, since they are remarkably similar in shape and amplitude to what was found for the case without a probe. These are results for a single value of k but we can conclude that on the basis of these tests, that the presence of the given probe does not have a major influence on angular features of the instability present in this plasma.

6.8 Experimental dispersion relations

In contrast to the results obtained with the angular exploration, a difference in the dispersion relations was observed between discharges with and without a probe. The experimental campaigns did not take place in the same chronological order as the manuscript results are presented, and at the time of the probe measurements, the existence of an tilted mode at 260° was not yet known. Thus, only the angles corresponding to 305° (ECDI) and 215° (axial fluctuations) were studied in the probe comparisons. Experimental dispersion relations in this section are thus limited to these two angles.

6.8.1 Dispersion relations in the argon discharge

Figure 6.22 shows the dispersion relation obtained in argon, for the ECDI (angle 305°), measured at an axial distance of 12 mm from the target. The static form factor is of the same order of magnitude as in the case without the probe (Fig. 6.13), and the range of k over which the signal is detectable is more or less the same. A data point can be seen in the top-right figure, around k = 10^4 rad.m^{-1}, confirming the linearity of the fit over a large wavenumber range. **A very remarkable point, which is seen again in subsequent figures, is that this linear fit to the group velocity gives values around 50% higher than without probe.**

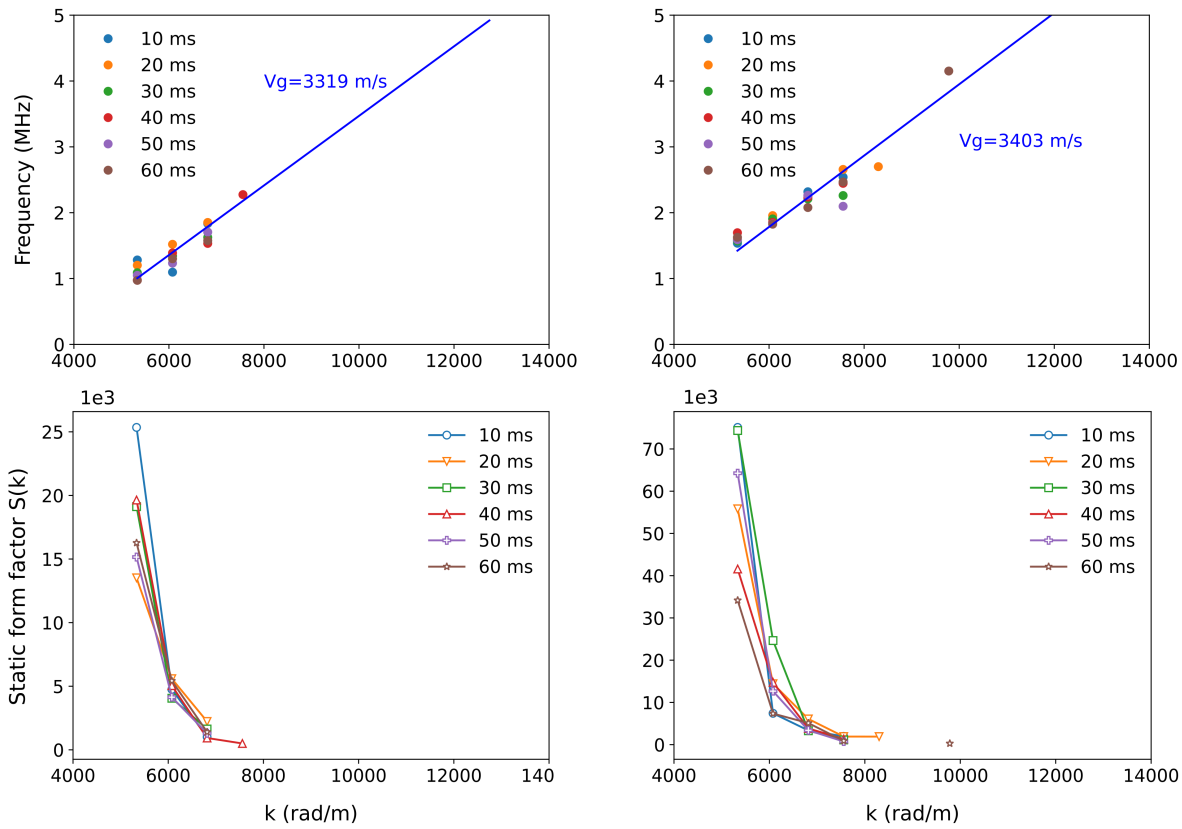

Figure 6.22: *Experimental dispersion relations in the argon discharge, at an axial distance 12 mm from the target and fixed angle* 305°, ***with the presence of a probe in the plasma****. Figures on the right correspond to fluctuations parallel to the wave vector; figures on the left to fluctuations antiparallel to the wave vector. The group velocity v_g is determined by a linear fit and is shown in blue. The static form factor (integrated signal intensity) is shown as a function of k for the respective dispersion relations.*

Fig. 6.23 shows the dispersion relation results for argon at 215° (axial fluctuations). This figure also gives remarkable results. Note that in the case without the probe, the signal level was too low on the left-hand side of the spectrum, corresponding to fluctuations propagating axially towards the target. Here, we obtain a slightly larger signal, enabling us to deduce a group velocity of around 1.1 km/s. However, given the signal level of the majority of points, which is very close to the noise level, we shall refrain from drawing any conclusions for this direction. The figures on the right, corresponding to axial fluctuations propagating away from the target, show much larger signal intensities. Here too, as in the case without a probe, the signal level decreases slowly with increasing k. Two points in particular were excluded from the fit (circled in gray), despite having sufficient signal levels to be taken into account. This point will be discussed later. **The group velocity of the axial mode is around 4 km/s, i.e. 50% higher than for the discharge without a probe (Fig. 6.14), echoing the feature observed with the ECDI.**

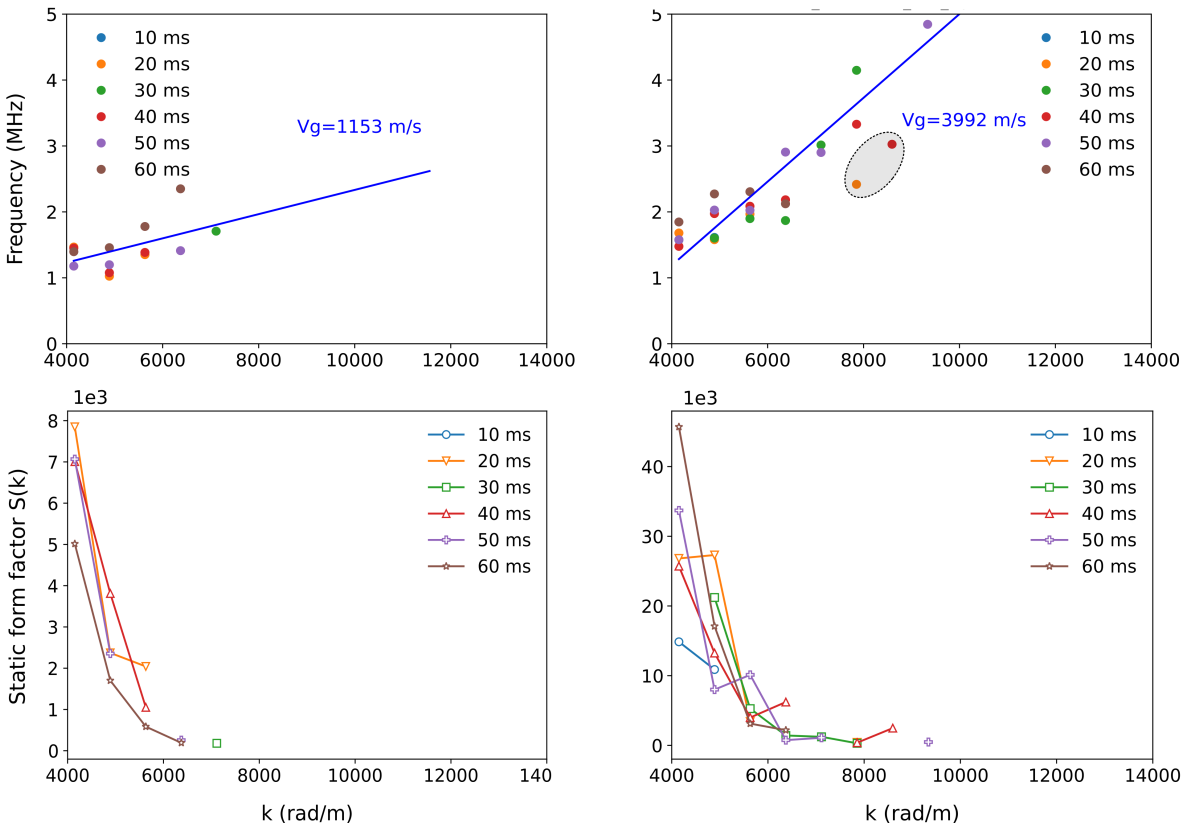

Figure 6.23: *Experimental dispersion relations in the argon discharge, at an axial distance 12 mm from the target and fixed angle 215°,* ***with the presence of a probe in the plasma****. Figures on the right correspond to fluctuations parallel to the wave vector; figures on the left to fluctuations antiparallel to the wave vector. The group velocity v_g is determined by a linear fit and is shown in blue. The static form factor (integrated signal intensity) is shown as a function of k for the respective dispersion relations.*

6.8.2 Dispersion relations in the helium discharge

Dispersion relations in helium with the probe present at the same position as for argon are carried out, again investigating the fixed angular values of 305° (ECDI) and 215° (axial mode fluctuations).

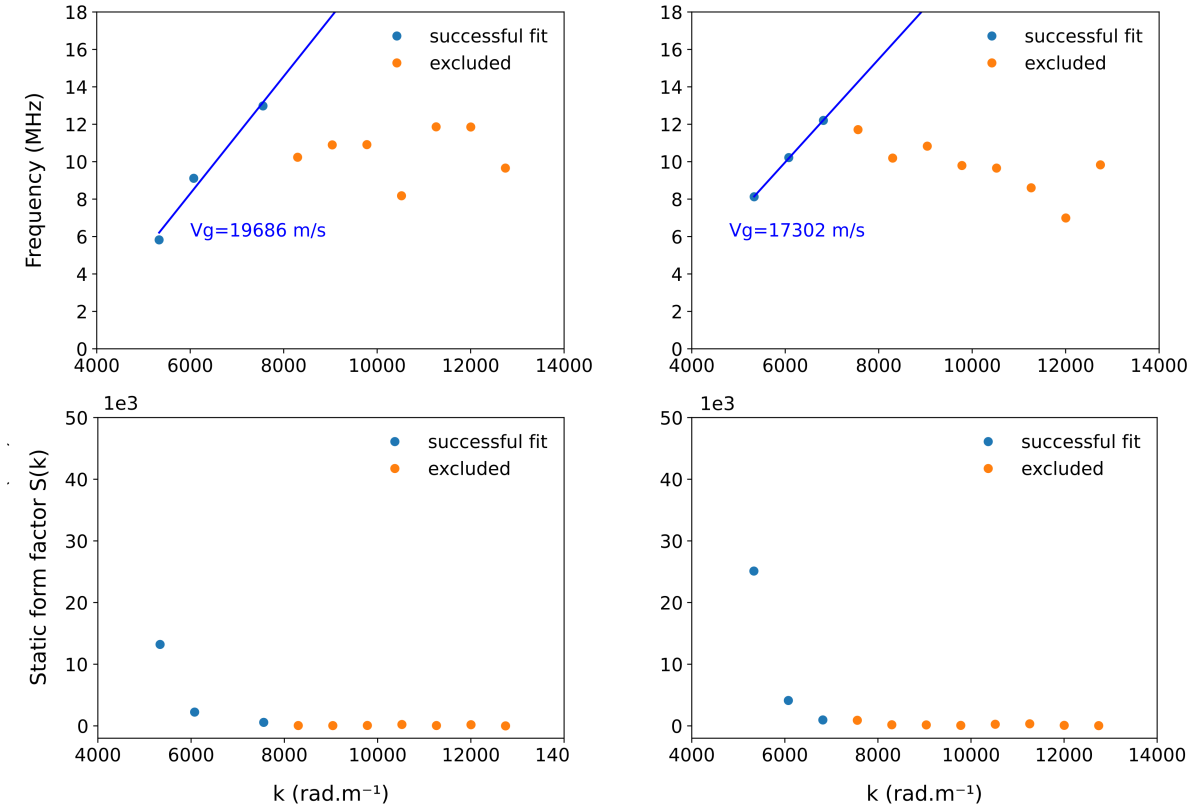

Figure 6.24: *Experimental dispersion relations in the helium discharge, at an axial distance 12 mm from the target and fixed angle 305°,* ***with the presence of a probe in the plasma****. Figures on the right correspond to fluctuations parallel to the wave vector; figures on the left to fluctuations antiparallel to the wave vector. The group velocity v_g is determined by a linear fit and is shown in blue. The static form factor (integrated signal intensity) is shown as a function of k for the respective dispersion relations.*

Figure 6.24 shows the dispersion relation for the helium. In measurements without a probe, it was difficult to draw a conclusion when considering the azimuthal fluctuation propagating antiparallel to k (left figures), as the signal level for those cases were too low to derive a dispersion relation (Fig. 6.17). **In contrast, in the present case with the probe, a signal of the same order of magnitude in intensity is detected for both the antiparallel and parallel fluctuations (right and left), and the group velocities detected are similar, to within 15% in intensity. The fits are very accurate and, once again, group velocities are higher than those observed in the absence of a probe (Fig. 6.17).**

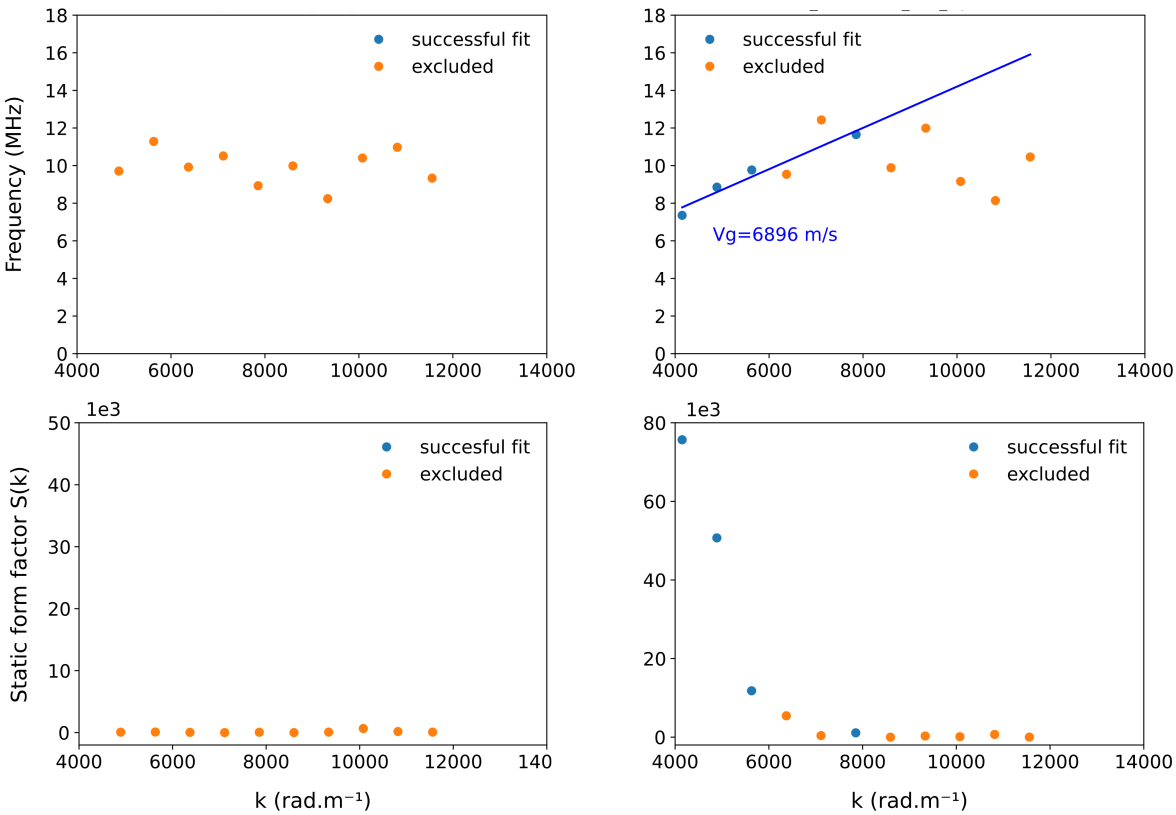

Figure 6.25: *Experimental dispersion relations in the helium discharge, at an axial distance 12 mm from the target and fixed angle 215°,* ***with the presence of a probe in the plasma****. Figures on the right correspond to fluctuations parallel to the wave vector; figures on the left to fluctuations antiparallel to the wave vector. The group velocity v_g is determined by a linear fit and is shown in blue. The static form factor (integrated signal intensity) is shown as a function of k for the respective dispersion relations.*

Finally, Fig. 6.25 shows the dispersion relations correspond to observations in the purely axial direction (215°). **As before, no signal is detected for fluctuations directed axially towards the target, while fluctuations directed axially away from the target are present. Unsurprisingly, the group velocity observed here is also higher than previously (Fig. 6.18)**.

6.9 Discussion

Table 6.4 summarizes the group velocities observed in the two types of discharge, with and without the probe, as well as the percentage variation between these two cases.

Argon	Mode group velocity in $-\mathbf{k}$ direction (km.s^{-1})	Mode group velocity in $+\mathbf{k}$ direction (km.s^{-1})
305°	1.9	2.3
305° with probe	3.3 (+74%)	3.4 (+48%)
215°	–	2.9
215° with probe	–	4 (+38%)

Helium	Mode group velocity in $-\mathbf{k}$ direction (km.s^{-1})	Mode group velocity in $+\mathbf{k}$ direction (km.s^{-1})
305°	–	11.6
305° with probe	20.0	17.3 (+72%)
215°	–	5.6
215° with probe	–	6.9 (+23%)

Table 6.4: *Measured group velocity of high frequency modes (305° ECDI, 215° axial mode), in the antiparallel ($-\mathbf{k}$) and parallel ($+\mathbf{k}$) directions, with and without the probe in the plasma. The percentage velocity difference resulting from probe insertion is shown in parentheses.*

One obvious effect of the presence of the probe is a systematic increase in group velocity, between 25% and 75%. This effect is found in all directions and in both gases. Unfortunately, in the absence of other quantitative measurements of plasma properties, it is very difficult to speculate on the origin of this behavior. One could imagine partial vaporization of the probe tip, producing a population of tungsten ions, which could locally modify the instability properties. As shown in the previous chapter, the presence of different concentrations of ion species, when analyzed using linear kinetic theory, has an effect on the dispersion relation characteristics. However, we do not possess sufficient information on the degree of vaporization of the tungsten tip and the possible effect of the injection of this new (heavy) ion species on the dispersion relation.

The most likely explanation for the increase in the group velocity is a significant rise in the temperature of the electrons in the plasma near the probe. We recall, when considering the ion acoustic wave that contributes to the formation of the ECDI, a dependence of the group velocity on the electron temperature. In these measurements, the mechanism leading to this electron heating in the presence of a probe is not known. It should be noted, however, that these two effects are linked, as an increase in the electron temperature leads to an increase in the electron current extracted from the plasma by the probe, according to Ref. [148], and thus to an increase in the Joule effect in the probe tip, as well as in the Bohm velocity, leading to an increased probability of atom sputtering from the tips.

These results show that the presence of a probe at the core of the plasma itself has a non-negligible

influence on the instabilities. This is a fundamental point, since very recent work has relied on probes to detect ECDI-like fluctuations in Hall thrusters, at larger length scales [149, 131].

A second remark needs to be added concerning the two isolated (circled) points in Figure 6.23. They are very far from the clustering of the other points on this figure (and have not been taken into account in the dispersion relation fit), but they have not been deliberately ignored. For the two values of wavenumber corresponding to the circled points, visual inspection of the spectra revealed not one, but two distinct peaks close together at the observed frequencies. The Gaussian fit automatically generated in the analysis was applied to only one of each peak (producing the circled frequency value shown) at each k. This was not considered representative of other cases shown that were used to determine the dispersion relation. Fig. 6.26 shows the dynamic form factor for the higher amplitude outlier point, showing the presence of two peaks; the automatically-generated Gaussian fit appears on only one.

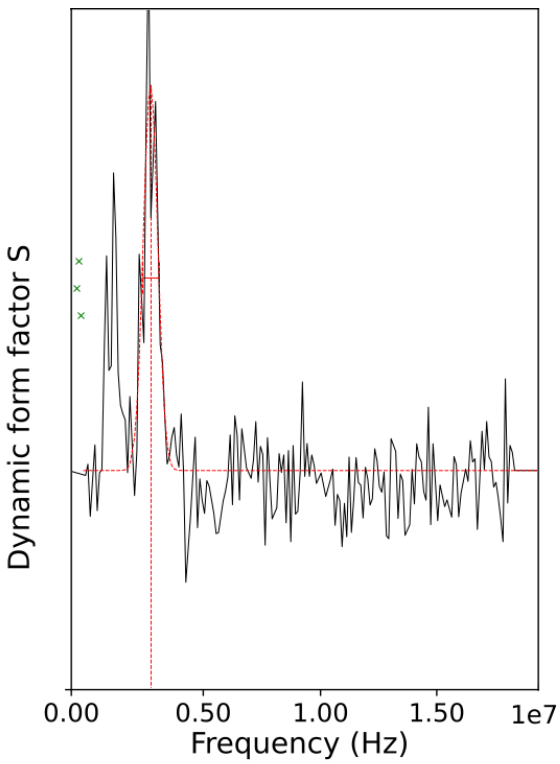

Figure 6.26: *Dynamic form factor for the highest "outlier" point in Figure 6.23. Two peaks close in frequency are present and the Gaussian fit (red) is applied to only one of them.*

This double frequency peak is only found under very specific conditions, i.e. only in the presence of the probe, and only at the highest k values. It does not always occur at all points meeting these conditions. However, the high level of noise visible in Figure 6.26 suggests that these two peaks are sometimes close enough for the FFT to show them as entangled.

The observation of the double peak feature corresponds to an axially-oriented wave vector (i.e., fluctuations measured propagating axially towards or away from the target). In the presence of the probe, it is possible that the propagation of these fluctuations is disrupted, and as a result, distinct axial density fluctuations appear on the spectra at different frequencies. The insertion

of the probe breaks the plasma symmetry, such that axial fluctuations originating from the left side of the racetrack (facing the target) are affected by the presence of the probe, while axial fluctuations originating from the right side of the racetrack (facing the target) are unaffected.

6.10 Discussion (Français)

Le tableau 6.4 résume les vitesses de groupe observées dans les deux types de décharge, avec et sans la sonde, ainsi que la variation en pourcentage entre ces deux cas.

Un effet évident de la présence de la sonde est une augmentation systématique de la vitesse de groupe, entre 25% et 75%. Cet effet est observé dans toutes les directions et dans les deux gaz. Malheureusement, en l'absence d'autres mesures quantitatives des propriétés du plasma, il est très difficile de spéculer sur l'origine de ce comportement. On pourrait imaginer une vaporisation partielle de la pointe de la sonde, produisant une population d'ions de tungstène, qui pourrait modifier localement les propriétés d'instabilité. Comme le montre le chapitre précédent, la présence de différentes concentrations d'espèces ioniques, lorsqu'elle est analysée à l'aide de la théorie cinétique linéaire, a un effet sur les caractéristiques de la relation de dispersion. Cependant, nous ne disposons pas d'informations suffisantes sur le degré de vaporisation de la pointe en tungstène et sur l'effet possible de l'injection de cette nouvelle espèce ionique (lourde) sur la relation de dispersion.
L'explication la plus probable de l'augmentation de la vitesse de groupe est une augmentation significative de la température des électrons dans le plasma près de la sonde. Nous rappelons, en considérant l'onde acoustique ionique contribuant à la formation de l'ECDI, une dépendance de la vitesse de groupe sur la température électronique. Dans ces mesures, le mécanisme conduisant à ce chauffage des électrons en présence d'une sonde n'est pas connu. Il convient cependant de noter que ces deux effets sont liés, car une augmentation de la température électronique entraîne une augmentation du courant électronique extrait du plasma par la sonde, selon la référence [148], et donc une augmentation de l'effet Joule dans la pointe de la sonde, ainsi que de la vitesse de Bohm, entraînant une probabilité accrue d'éclatement d'atomes des pointes.

Ces résultats montrent que la présence d'une sonde au cœur du plasma lui-même a une influence non négligeable sur les instabilités. Il s'agit d'un point fondamental, car des travaux très récents se sont appuyés sur des sondes pour détecter des fluctuations similaires à l'ECDI dans les propulseurs à effet Hall, à des échelles de longueur plus grandes [149, 131].

Une deuxième remarque doit être ajoutée concernant les deux points isolés (cercles) dans la Figure 6.23. Ils sont très éloignés du regroupement des autres points sur cette figure (et n'ont pas été pris en compte dans l'ajustement de la relation de dispersion), mais ils n'ont pas été délibérément ignorés. Pour les deux valeurs de nombre d'onde correspondant aux points encerclés, l'inspection visuelle des spectres a révélé non pas un, mais deux pics distincts proches aux fréquences observées. L'ajustement gaussien automatiquement généré dans l'analyse a été appliqué à un seul de chaque pic (produisant la valeur de fréquence encerclée montrée) à chaque k. Cela n'a pas été considéré comme représentatif des autres cas montrés qui ont été utilisés pour déterminer la relation de dispersion. La figure 6.26 montre le facteur de forme dynamique pour le point aberrant à amplitude plus élevée, montrant la présence de deux pics ; l'ajustement gaussien généré automatiquement apparaît sur un seul.

Ce double pic de fréquence n'est trouvé que dans des conditions très spécifiques, c'est-à-dire uniquement en présence de la sonde, et uniquement aux valeurs de k

les plus élevées. Il ne se produit pas toujours à tous les points répondant à ces conditions. Cependant, le niveau élevé de bruit visible sur la figure 6.26 suggère que ces deux pics sont parfois suffisamment proches pour que la FFT les montre entrelacés.

L'observation de la double caractéristique de pic correspond à un vecteur d'onde orienté axialement (c'est-à-dire, des fluctuations mesurées se propageant axialement vers ou loin de la cible). En présence de la sonde, il est possible que la propagation de ces fluctuations soit perturbée, et par conséquent, des fluctuations de densité axiales distinctes apparaissent sur les spectres à différentes fréquences. L'insertion de la sonde rompt la symétrie du plasma, de sorte que les fluctuations axiales provenant du côté gauche de la piste (face à la cible) sont affectées par la présence de la sonde, tandis que les fluctuations axiales provenant du côté droit de la piste (face à la cible) ne le sont pas.

Chapter 7

Conclusion

Contents

7.1 Summary

The work presented in this manuscript focuses on accurate, non-perturbative, and highly-sensitive measurements of electron properties in crossed-field plasma sources using optical diagnostics. It is divided into six distinct chapters, which can be grouped into four main subsections.

The first of these sections covers the first two chapters. The main instabilities likely to be encountered in cross-field plasma sources are presented, along with a comprehensive description of the two Thomson scattering diagnostics to be used in this work: THETIS (incoherent Thomson scattering), for measuring individual electron properties such as temperature, density and drift velocity. This diagnostic is directional, enabling these properties to be probed along different directions, and thus measuring the potential anisotropy of these properties. PRAXIS (coherent Thomson scattering) is used to measure small-scale fluctuations in electron density (associated with MHz waves). The diagnostic here is also directional, offering the possibility of probing the presence of instability in different directions, and over a wide frequency range.

The second part of this work is concerned with measurements on a planar magnetron in HiPIMS configuration with a titanium target. An exploration of the evolution of electron properties along the axial direction was carried out for a discharge with argon, and it was found that the density followed a bi-exponential decay with distance, very consistent with the existence of the electron confinement zone in front of the cathode. Temperature, on the other hand, follows a simply exponential decay, indicating that the energy exchange process does not vary over the full axial range. Two temporal explorations during the full pulse duration and in the afterglow were then carried out with argon, for two different peak current amplitudes, 40 and 80 A. In addition, in order to study electron dynamics with another gas, measurements with helium were carried out for different pulse lengths. In the first case, for argon, the evolution of the electron density closely follows the shape of the current, but with slight disparities between the azimuthal and radial positions, indicating that ionization is certainly not uniform during the pulse. The

electron temperature starts at several eV at the beginning of the discharge, before decreasing rapidly and reaching a plateau until the afterglow. During the latter, both the temperature and the density decrease with two characteristic times, rapid at the beginning after the voltage cut-off, attributed to the fast depletion of the higher-energy electrons formed by the end of the pulse, followed by a slow diffusion of the lower-energy electrons.
A clear difference is observed for helium. The density, which is high at the start of the discharge, only decreases throughout the pulse, while the electron temperature is inverted, low at the start of the pulse with a constant increase, regardless of pulse duration.
Lastly, the drift velocity measurements are the only ones to show any significant anisotropy. A large drift evolution along the radial direction is observed in all pulses. This has been attributed to an expansion-contraction mechanism for argon pulses. For helium, the observed velocities are even higher than the drift velocity, of the order of 100 km/s. Centrifugal forces could be responsible for creating this significant and sustained radial electron drift. As far as azimuthal drift is concerned, a competitive effect was observed between the $E \times B$ drift and the opposite diamagnetic drift, with one varying with respect to the other as a function of time. A second, less systematic study was carried out on pulses at higher currents, up to 400 A, for titanium and molybdenum targets, with helium as the working gas. In comparison with each other and with measurements carried out at lower currents, several points were highlighted. The nature of the target seems to have an influence on the delay between the application of the voltage and the start of current growth, as well as on the time variation of the electron density and the electron heating mechanism.
The value of the maximum electron density reached during the pulse depends solely on the value of the discharge current, but the latter does not appear to be linked at all to the heating mechanism.

The third part of this work concerns the study of a 1.5 kW Hall-effect thruster using xenon and krypton. Using the high spatial resolution of the THETIS diagnostic, it has been possible to probe the evolution of electron properties along the radial direction at the exit of the discharge channel. This novel measurement indicates that the plasma is strongly inhomogeneous along the radial direction, but more importantly, the electron density, temperature, and the velocity drift are generally increasing towards the outer channel wall. This effect seems to be much more pronounced in the use of krypton. Previous measurements in the literature with Langmuir-type probes tend to support isothermal electrons along the radial direction, although recent PIC simulations find the same results as we do. These simulations attribute this behavior to the difference in sheath behavior at the two walls, attributed to the magnetic mirror effect, as well as to the centrifugal force due to the $E \times B$ drift, consistent with what had been observed in the case of the HiPIMS discharge.
In 2013, Cavalier developed a linear kinetic theory model linking the dispersion relation of the electron cyclotron drift instability (ECDI) to the plasma properties in a Hall thruster. This instability is known to play a role in the anomalous transport of electrons across magnetic field lines, and has been identified in different crossed-field plasma sources. This same analytical approach to the dispersion relation has been applied in this work, with directly-measured electron properties along the discharge channel injected into the model for the first time. It has been shown that the large inhomogeneity in properties along the radial direction plays an important role in smoothing the dispersion relation. The latter is largely compatible and consistent with the actual experimental dispersion relations obtained previously using PRAXIS on a large Hall thruster.

Finally, the last part of this manuscript is devoted to the study of high-frequency instability in

the planar magnetron in the HiPIMS configuration, under the same experimental conditions as those explored previously using incoherent Thomson scattering. The fifth chapter presents the adaptation of the linear kinetic model to the case of the planar magnetron discharge, taking into account in particular the existence of two different atomic species in the discharge, metallic and gaseous. The sixth and final chapter shows the existence of two main high-frequency instabilities in the discharges, under experimental conditions identical to the previous measurements.
One is azimuthal, with a group velocity compatible with a smoothed ECDI, with an inclination of 10° to the cathode plane, as previously observed in a DCMS discharge.
The second is tilted, at an angle of 45° with respect to the axial direction, with group velocities close to those observed for ECDI. This could be the ion-ion two-stream instability recently studied in numerical, experimental and theoretical work. For this mode, the ion velocity vector would not be purely axial, but would have a radial component. This result is consistent with the radial velocity component of the electrons observed in Chapter 3, attributed to an effect of plasma expansion and centrifugal forces. Finally, a third instability is observed in the purely axial direction, but at significantly lower amplitudes. A follow-up experiment was carried out to check the influence on the instabilities of inserting a Langmuir probe into the plasma. No change in the angular features of the instabilities was observed, but a large systematic effect of a group velocity increase was observed for every instability. This result may have some bearing on the interpretation of probe measurements used to detect instabilities of this type, and underlines the importance of using non-intrusive diagnostics wherever possible.

7.2 Perspectives

This thesis focused on the experimental measurement of electron properties using two unique optical diagnostics. Although these diagnostics have already yielded large amounts of information on electron properties and dynamics, several ideas can be implemented in the future.

1. **Diagnostic improvements on THETIS:** In previous work, ideas for increasing the sensitivity of THETIS were described, which included: (i) the use of an advanced emCCD camera for detection, and (ii) the use of double Bragg filters to more effectively eliminate stray light. **It should be noted that this work already involved improvements to the original diagnostic (such as a new fiber bundle with large numerical aperture).**

2. **Diagnostic improvements on PRAXIS:** The PRAXIS diagnostic can be modified in a number of ways, including to allow the exploration of a larger range of wavenumbers, and to allow the measurement of multiple wavenumbers at once (rather than single wavenumber measurements). It can also be noted that the performance of the original acquisition card (in terms of acquisition frequency and vertical resolution) can now be matched or exceeded by high-performance oscilloscopes. **These can be used to significantly augment the signal quality recorded and permit more post-processing, particularly important in the experiments of this work, which address several instability features in pulsed conditions for the first time**.

3. **Diagnostic combination**: This work provides a validation of the approach attempted during this thesis, in which outputs from more than one diagnostic were successfully combined to check the agreement between theory and experiments. This may be taken a step further, via the use of other complementary (preferably non-invasive) diagnostics such as

optical emission spectroscopy or laser-induced fluorescence. The implementation of multiple tools of this type is costly and complex, nevertheless, can offer extremely detailed information on the plasma constituents, which would signficantly aid numerical simulation efforts.

4. **Study of multiscale plasma features**: It would be of great interest to be able to measure the evolution of electron properties and small-scale density fluctuations as large-scale plasma structures such as spokes traverse the measurement volume on PRAXIS. This would require careful synchronization of the plasma and the diagnostics. The key interest such work would be to clarify the mechanisms underlying the formation of spokes, present across a range of crossed-field plasmas, but perhaps more importantly, clarify links between transport arising from small- and large-scale modes. Recent numerical work suggests that while small-scale modes contribute to anomalous electron transport, they may also feed energy into larger scales (inverse cascade).

5. **Numerical simulations**: Finally, it should be mentioned that specific simulation work carried out under the conditions of this work would be a valuable complement to this manuscript. The linear kinetic theory models studied here were applied with strong assumptions about ion populations, which might not reflect the full reality. For example, doubly-charged ions were not taken into account in the linear kinetic modeling of the discharge in this work, even though they are known to exist in non-negligible quantities and influence the modes (IITSI) excited. A complete understanding of the nature of the instabilities observed for the planar magnetron would require a 3D numerical code, describing not only the axial mode and the ECDI, but taking into account the simultaneous existence of several ion species, gaseous and metallic, and with several ionization levels.

7.3 Conclusion (Français)

Le travail présenté dans ce manuscrit se concentre sur des mesures précises, non perturbatives et hautement sensibles des propriétés électroniques dans des sources de plasma en champ croisé à l'aide de diagnostics optiques. Il est divisé en six chapitres distincts, qui peuvent être regroupés en quatre sous-sections principales.

La première de ces sections couvre les deux premiers chapitres. Les principales instabilités susceptibles d'être rencontrées dans les sources de plasma à champ croisé sont présentées, ainsi qu'une description complète des deux diagnostics de diffusion Thomson qui ont été utilisé dans ce travail : THETIS (diffusion Thomson incohérente), pour mesurer les propriétés électroniques individuelles telles que la température, la densité et la vitesse de dérive. Ce diagnostic est directionnel, permettant de sonder ces propriétés le long de différentes directions, et donc de mesurer une anisotropie potentielle de ces propriétés. PRAXIS (diffusion Thomson cohérente) est utilisé pour mesurer les fluctuations à petite échelle de la densité électronique (associées aux ondes MHz). Le diagnostic ici est également directionnel, offrant la possibilité de sonder la présence d'instabilité dans différentes directions, et sur une large plage de fréquences.

La deuxième partie de ce travail concerne les mesures sur un magnétron planaire en configuration HiPIMS avec une cible en titane. Une exploration de l'évolution des propriétés électroniques le long de la direction axiale a été réalisée pour une décharge avec de l'argon, et il a été constaté que la densité suivait une décroissance bi-exponentielle avec la distance, très cohérente avec l'existence de la zone de confinement des électrons devant la cathode. La température, en revanche, suit une décroissance simplement exponentielle, indiquant que le processus d'échange

d'énergie ne varie pas sur toute la plage axiale. Deux explorations temporelles pendant la durée complète de l'impulsion et dans l'afterglow ont ensuite été réalisées avec de l'argon, pour deux amplitudes de courant de crête différentes, 40 et 80 A. De plus, afin d'étudier la dynamique des électrons avec un autre gaz, des mesures avec de l'hélium ont été réalisées pour des impulsion de différentes durées. Dans le premier cas, pour l'argon, l'évolution de la densité électronique suit étroitement la forme du courant, mais avec de légères disparités entre les positions azimutales et radiales, indiquant que l'ionisation n'est certainement pas uniforme pendant l'impulsion. La température électronique commence à plusieurs eV au début de la décharge, avant de diminuer rapidement et d'atteindre un plateau jusqu'à l'afterglow. Pendant ce dernier, à la fois la température et la densité diminuent avec deux temps caractéristiques, rapide au début après la coupure de tension, attribué à l'attrition rapide des électrons de plus haute énergie formés à la fin de l'impulsion, suivi d'une diffusion lente des électrons de plus basse énergie.
Une différence claire est observée pour l'hélium. La densité, qui est élevée au début de la décharge, ne diminue que tout au long de l'impulsion, tandis que la température électronique est inversée, faible au début de l'impulsion avec une augmentation constante, quelle que soit la durée de l'impulsion.

Enfin, les mesures de vitesse de dérive sont les seules à montrer une anisotropie significative. Une grande évolution de la dérive le long de la direction radiale est observée dans toutes les impulsions. Cela a été attribué à un mécanisme d'expansion-contraction pour les impulsions d'argon. Pour l'hélium, les vitesses observées sont encore plus élevées que la vitesse de dérive, de l'ordre de 100 km/s. Les forces centrifuges pourraient être responsables de la création de cette dérive électronique radiale significative et soutenue. En ce qui concerne la dérive azimutale, un effet de compétition a été observé entre la dérive $E \times B$ et la dérive diamagnétique opposée, l'une variant par rapport à l'autre en fonction du temps. Une deuxième étude, moins systématique, a été réalisée sur des impulsions à des courants plus élevés, jusqu'à 400 A, pour des cibles en titane et en molybdène, avec de l'hélium. En les comparant les unes aux autres et aux mesures réalisées à des courants plus faibles, plusieurs points ont été mis en évidence. La nature de la cible semble avoir une influence sur le délai entre l'application de la tension et le début de la croissance du courant, ainsi que sur la variation temporelle de la densité électronique et le mécanisme de chauffage des électrons.
La valeur de la densité électronique maximale atteinte pendant l'impulsion dépend uniquement de la valeur du courant de décharge, mais ce dernier ne semble en aucun cas lié au mécanisme de chauffage.

La troisième partie de ce travail concerne l'étude d'un propulseur à effet Hall de 1,5 kW utilisant du xénon et du krypton. En utilisant la haute résolution spatiale du diagnostic THETIS, il a été possible de sonder l'évolution des propriétés électroniques le long de la direction radiale à la sortie du canal de décharge. Cette nouvelle mesure indique que le plasma est fortement inhomogène le long de la direction radiale, mais plus important encore, la densité électronique, la température et la dérive de vitesse augmentent généralement vers la paroi externe du canal. Cet effet semble être beaucoup plus prononcé dans l'utilisation du krypton. Les mesures précédentes dans la littérature avec des sondes de type Langmuir tendent à confirmer l'isothermie des électrons le long de la direction radiale, bien que des simulations PIC récentes trouvent les mêmes résultats que nous. Ces simulations attribuent ce comportement à la différence de comportement de la gaine aux deux parois, attribuée à l'effet miroir magnétique, ainsi qu'à la force centrifuge due à la dérive $E \times B$, conforme à ce qui avait été observé dans le cas de la décharge HiPIMS.

En 2013, Cavalier a développé un modèle de théorie cinétique linéaire liant la relation de dis-

persion de l'instabilité de dérive cyclotronique électronique (ECDI) aux propriétés du plasma dans un propulseur à effet Hall. Cette instabilité est connue pour jouer un rôle dans le transport anormal des électrons à travers les lignes de champ magnétique, et a été identifiée dans différentes sources de plasma à champ croisé. Cette même approche analytique de la relation de dispersion a été appliquée dans ce travail, avec des propriétés électroniques directement mesurées le long du canal de décharge injectées dans le modèle pour la première fois. Il a été montré que l'inhomogénéité importante des propriétés le long de la direction radiale joue un rôle important dans l'amortissement de la relation de dispersion. Cette dernière est largement compatible et cohérente avec les relations de dispersion expérimentales réelles obtenues précédemment à l'aide de PRAXIS sur un propulseur à effet Hall de grande taille.
Enfin, la dernière partie de ce manuscrit est consacrée à l'étude de l'instabilité haute fréquence dans le magnétron planaire en configuration HiPIMS, dans les mêmes conditions expérimentales que celles explorées précédemment en utilisant la diffusion Thomson incohérente. Le cinquième chapitre présente l'adaptation du modèle cinétique linéaire au cas de la décharge du magnétron planaire, tenant compte en particulier de l'existence de deux espèces atomiques différentes dans la décharge, métallique et gazeuse. Le sixième et dernier chapitre montre l'existence de deux principales instabilités haute fréquence dans les décharges, dans des conditions expérimentales identiques aux mesures précédentes.
L'une est azimutale, avec une vitesse de groupe compatible avec une ECDI lissée, avec une inclinaison de 10° par rapport au plan de la cathode, comme observé précédemment dans une décharge DCMS.
La seconde est inclinée, à un angle de 45° par rapport à la direction axiale, avec des vitesses de groupe proches de celles observées pour l'ECDI. Il pourrait s'agir de l'ion-ion two-stream instability récemment étudiée dans des travaux numériques, expérimentaux et théoriques. Pour ce mode, le vecteur de vitesse ionique ne serait pas purement axial, mais aurait une composante radiale. Ce résultat est cohérent avec la composante de vitesse radiale des électrons observée dans le chapitre 3, attribuée à un effet d'expansion du plasma et de forces centrifuges.
Enfin, une troisième instabilité est observée dans la direction purement axiale, mais à des amplitudes significativement plus faibles. Une expérience de suivi a été réalisée pour vérifier l'influence des instabilités de l'insertion d'une sonde de Langmuir dans le plasma. Aucun changement dans les caractéristiques angulaires des instabilités n'a été observé, mais un effet systématique important d'une augmentation de la vitesse de groupe a été observé pour chaque instabilité. Ce résultat peut avoir une certaine incidence sur l'interprétation des mesures de sonde utilisées pour détecter des instabilités de ce type, et souligne l'importance de l'utilisation de diagnostics non intrusifs chaque fois que possible.

7.4 Perspectives (Français)

Cette thèse s'est concentrée sur la mesure expérimentale des propriétés électroniques à l'aide de deux diagnostics optiques uniques. Bien que ces diagnostics aient déjà fourni de grandes quantités d'informations sur les propriétés et la dynamique des électrons, plusieurs idées peuvent être mises en œuvre dans le futur.

1. **Améliorations du diagnostic THETIS :** Dans des travaux antérieurs, des idées pour accroître la sensibilité de THETIS ont été décrites, notamment : (i) l'utilisation d'une caméra EMCCD avancée pour la détection, et (ii) l'utilisation de doubles filtres de Bragg pour éliminer plus efficacement la lumière parasite. **Il convient de noter que ce travail a déjà impliqué des améliorations du diagnostic original (telles qu'un nouveau faisceau de fibres avec un grand angle d'ouverture).**

2. **Améliorations du diagnostic PRAXIS :** Le diagnostic PRAXIS peut être modifié de plusieurs façons, notamment pour permettre l'exploration d'une plage plus large de nombres d'onde, et pour permettre la mesure de plusieurs nombres d'onde à la fois (plutôt que des mesures de nombre d'onde unique). Il convient également de noter que les performances de la carte d'acquisition originale (en termes de fréquence d'acquisition et de résolution verticale) peuvent maintenant être égalées ou dépassées par des oscilloscopes haute performance. **Ces derniers peuvent être utilisés pour améliorer considérablement la qualité du signal enregistré et permettre plus de post-traitement, particulièrement important dans les expériences de ce travail, qui abordent plusieurs caractéristiques d'instabilité dans des conditions pulsées pour la première fois**.

3. **Combinaison des diagnostics** : Ce travail valide l'approche tentée pendant cette thèse, dans laquelle les resulats de plusieurs diagnostics ont été combinées avec succès pour vérifier l'accord entre la théorie et les expériences. Cela pourrait être poussé plus loin, via l'utilisation d'autres diagnostics complémentaires (de préférence non invasifs) tels que la spectroscopie d'émission optique ou la fluorescence induite par laser. La mise en œuvre de plusieurs outils de ce type est coûteuse et complexe, néanmoins, elle peut offrir des informations extrêmement détaillées sur les constituants du plasma, ce qui aiderait considérablement les efforts de simulation numérique.

4. **Étude des caractéristiques du plasma à plusieurs échelles** : Il serait très intéressant de pouvoir mesurer l'évolution des propriétés électroniques et des fluctuations de densité à petite échelle lorsque des structures plasmatiques à grande échelle telles que les « spokes » traversent le volume de mesure sur PRAXIS. Cela nécessiterait une synchronisation soigneuse du plasma et des diagnostics. L'intérêt principal de ces travaux serait de clarifier les mécanismes sous-jacents à la formation des « spokes », présents dans toute une gamme de plasmas à champ croisé, mais peut-être plus important encore, de clarifier les liens entre le transport résultant des modes à petite et grande échelle. Des travaux numériques récents suggèrent que si les modes à petite échelle contribuent au transport électronique anormal, ils peuvent également fournir de l'énergie à des échelles plus grandes (cascade inverse).

5. **Simulations numériques** : Enfin, il convient de mentionner que des travaux de simulation spécifiques réalisés dans les conditions de ce travail seraient un complément précieux à ce manuscrit. Les modèles de théorie cinétique linéaire étudiés ici ont été appliqués avec des hypothèses fortes sur les populations ioniques, qui pourraient ne pas refléter pleinement la réalité. Par exemple, les ions doublement chargés n'ont pas été pris en compte dans la modélisation cinétique linéaire de la décharge dans ce travail, même s'ils sont connus pour exister en quantités non négligeables et influencer les modes (IITSI) excités. Une compréhension complète de la nature des instabilités observées pour le magnétron plan nécessiterait un code numérique en 3D, décrivant non seulement le mode axial et l'ECDI, mais tenant compte de l'existence simultanée de plusieurs espèces ioniques, gazeuses et métalliques, et avec plusieurs niveaux d'ionisation.

Appendix A

Static form factor dependence on the direction of the probed vector

In Section 6.2.1, the amplitude of the static form factor S(**k**) is plotted as a function of observation angle. For argon discharges, the results have been averaged over successive pulses (5 or 6) during the 65 ms of acquisition, to improve readability. This section shows the unaveraged raw spectra superimposed for reference.

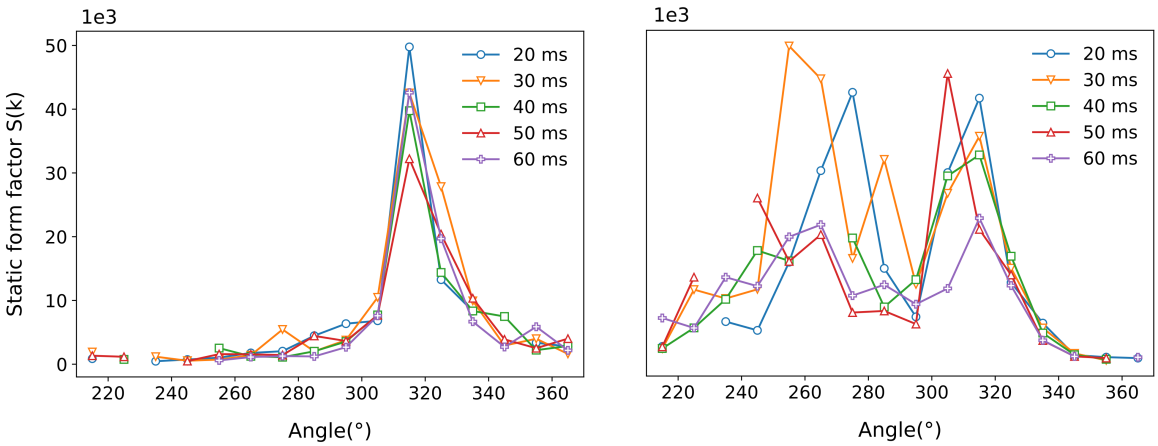

Figure A.1: *Results of an angular exploration in the argon discharge, at an axial distance 12 mm from the target. The corresponding observation wave vector k is 5630 rad.m^{-1}. The static form factor (integrated signal intensity) is shown as a function of angle in the* $(\mathbf{E}, \mathbf{E} \times \mathbf{B})$ *plane. The figure on the left corresponds to the identified negative frequency peak; the figure on the right corresponds to the identified positive frequency peak. The same convention is used for the following figures. Corresponds to the averaged figure 6.7.*

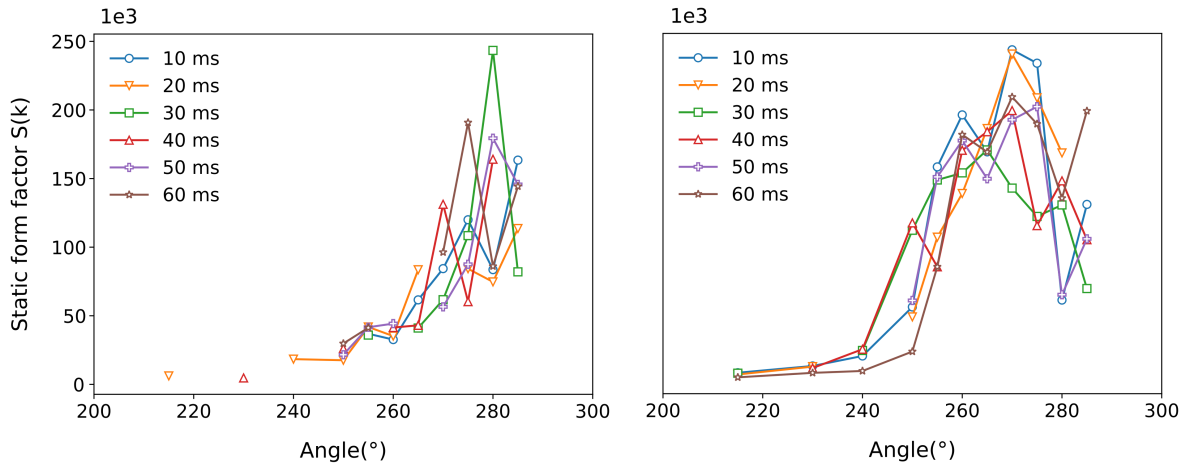

Figure A.2: *Results of an angular exploration in the argon discharge, at an axial distance 10 mm from the target. The corresponding observation wave vector k is 4150 rad.m*$^{-1}$*. The static form factor (integrated signal intensity) is shown as a function of angle in the* $(\mathbf{E}, \mathbf{E} \times \mathbf{B})$ *plane. The figure on the left corresponds to the identified negative frequency peak; the figure on the right corresponds to the identified positive frequency peak. Corresponds to the averaged figure 6.8.*

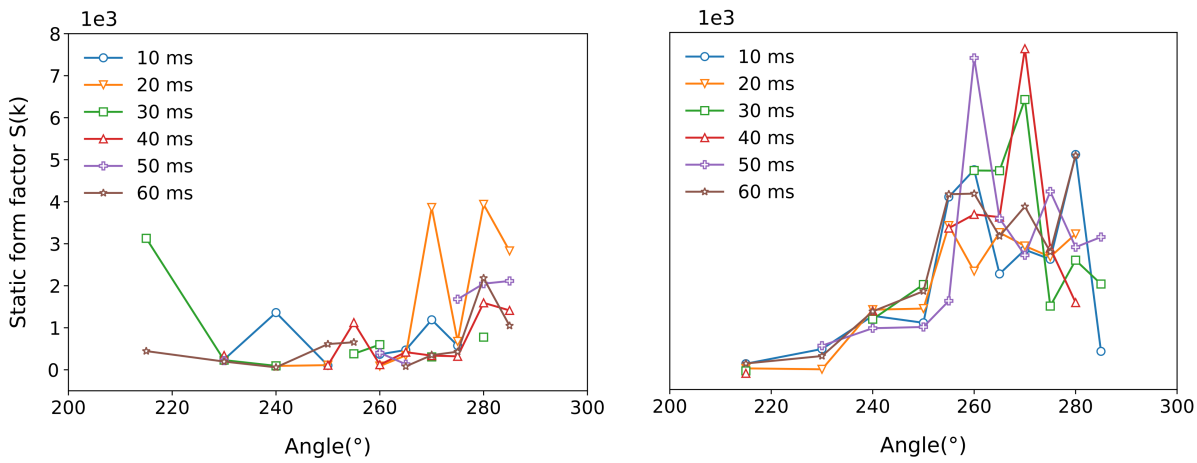

Figure A.3: *Results of an angular exploration in the argon discharge, at an axial distance 20 mm from the target. The corresponding observation wave vector k is 4150 rad.m*$^{-1}$*. The static form factor (integrated signal intensity) is shown as a function of angle in the* $(\mathbf{E}, \mathbf{E} \times \mathbf{B})$ *plane. The figure on the left corresponds to the identified negative frequency peak; the figure on the right corresponds to the identified positive frequency peak. Corresponds to the averaged figure 6.9.*

Appendix B

Frequency dependence on the direction of the probed vector

In Section 6.2.1, an angular exploration of the static form factor has been presented, with the aim of determining the presence of instability. Similarly, the frequency corresponding to the center of the Gaussian fit on the dynamic form factor has been investigated and is presented here as a function of angle. There is a very large difference between the average frequency of argon discharge and that of helium.

B.1 Angular exploration of the frequency in the argon discharge

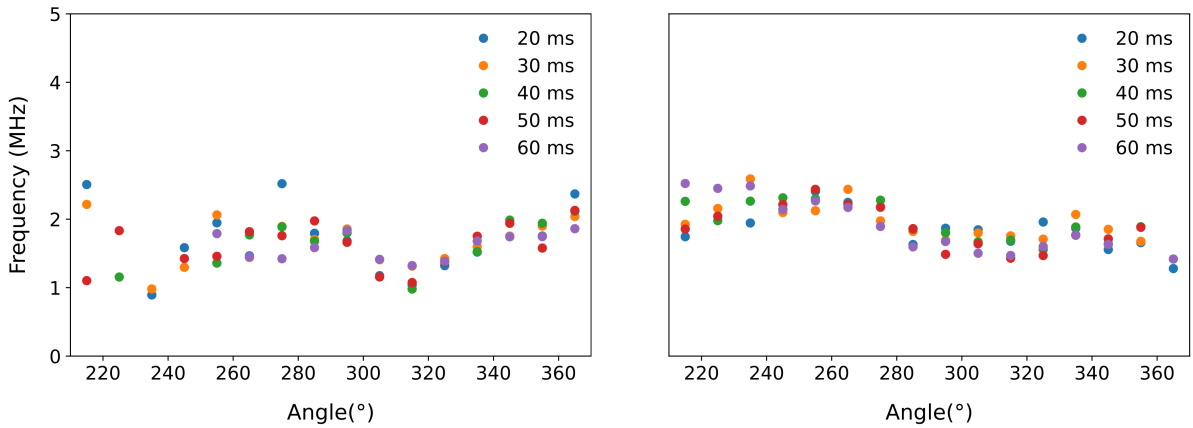

Figure B.1: *Angular exploration of the main frequency of the dynamic form factor in argon discharge, 12 mm from the target, and for a wave number k= 5630 rad.m^{-1}. The figure on the left corresponds to the identified negative frequency peak; the figure on the right corresponds to the identified positive frequency peak. The same convention is used for the following figures.*

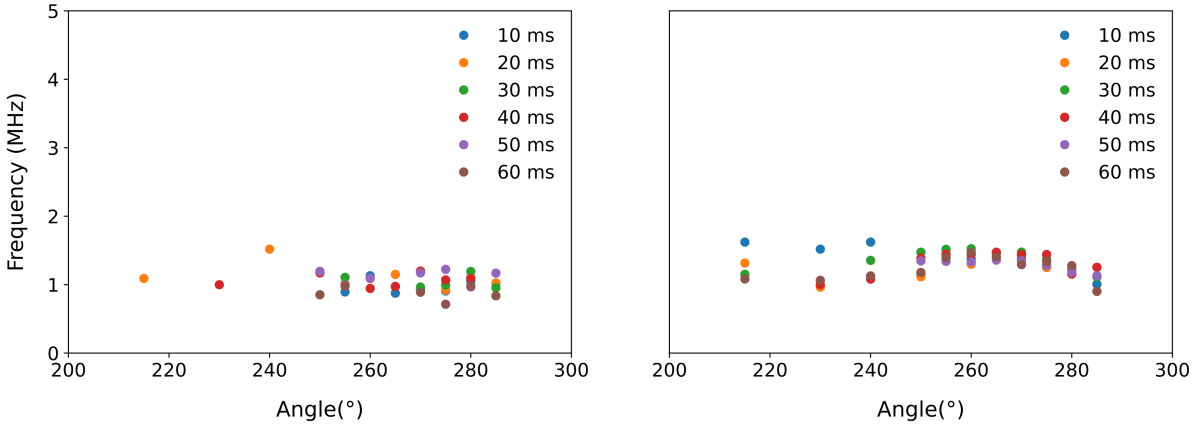

Figure B.2: *Angular exploration of the main frequency of the dynamic form factor in argon discharge, 10 mm from the target, and for a wave number k= 4150 rad.m^{-1}. The figure on the left corresponds to the identified negative frequency peak; the figure on the right corresponds to the identified positive frequency peak.*

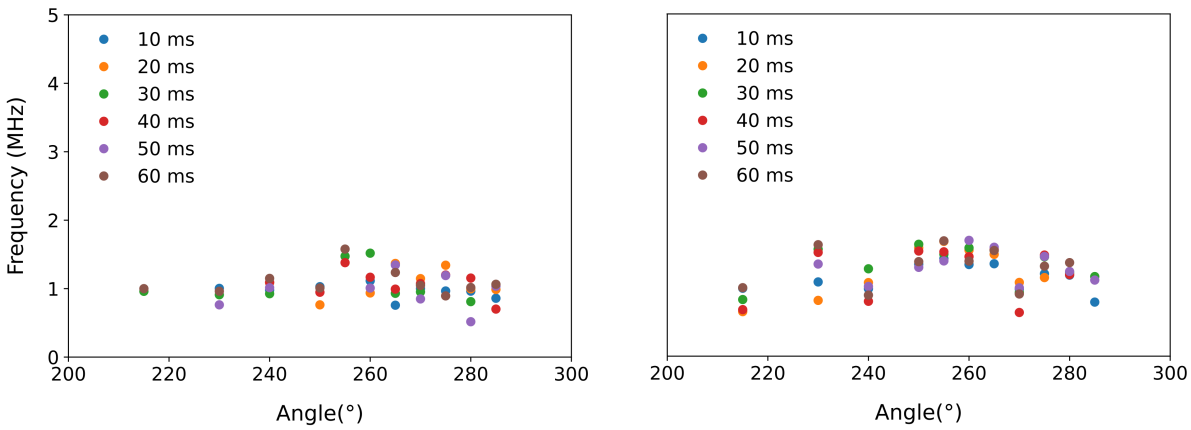

Figure B.3: *Angular exploration of the main frequency of the dynamic form factor in argon discharge, 20 mm from the target, and for a wave number k= 4150 rad.m^{-1}. The figure on the left corresponds to the identified negative frequency peak; the figure on the right corresponds to the identified positive frequency peak.*

B.2 Angular exploration of the frequency in the helium discharge

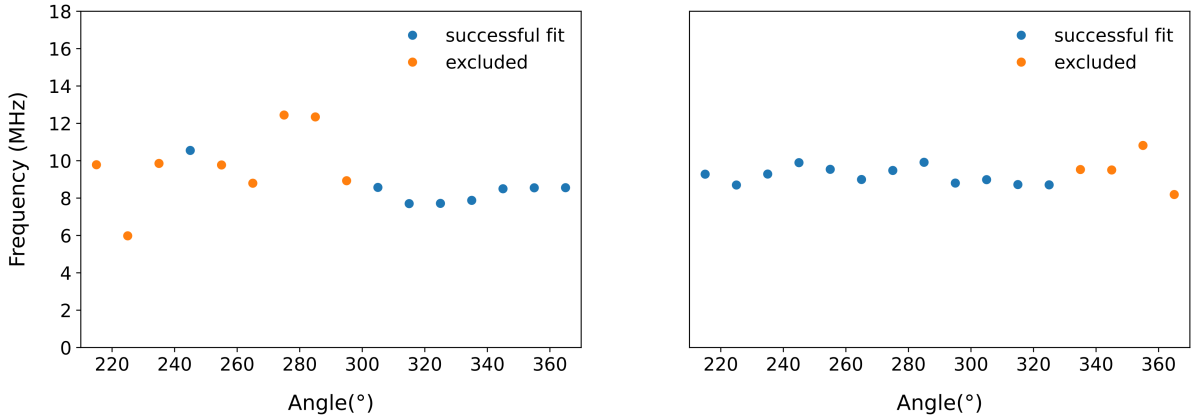

Figure B.4: *Angular exploration of the main frequency of the dynamic form factor in helium discharge, 12 mm from the target, and for a wave number $k = 5630$ rad.m^{-1}. The figure on the left corresponds to the identified negative frequency peak; the figure on the right corresponds to the identified positive frequency peak. The orange dots are the positions where no signal was detected.*

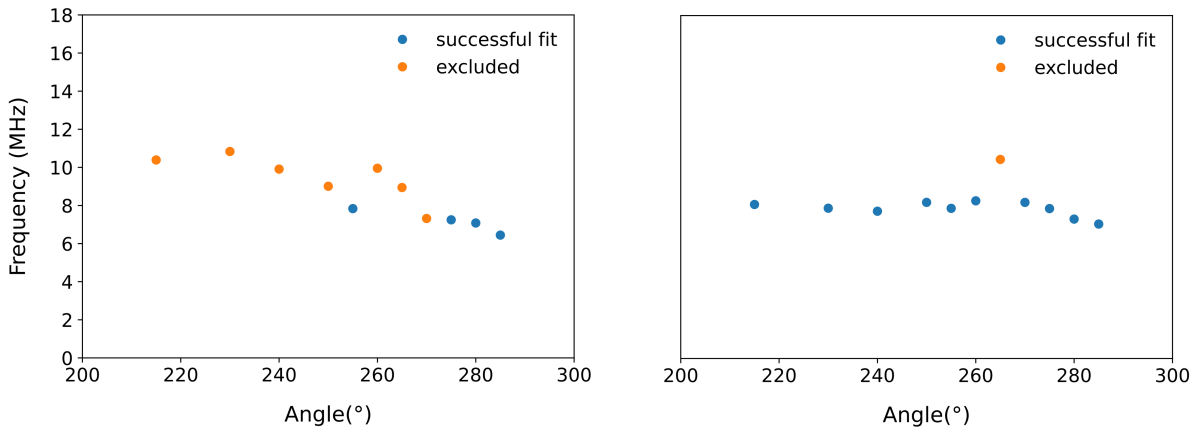

Figure B.5: *Angular exploration of the main frequency of the dynamic form factor in helium discharge, 10 mm from the target, and for a wave number $k = 4150$ rad.m^{-1}. The figure on the left corresponds to the identified negative frequency peak; the figure on the right corresponds to the identified positive frequency peak. The orange dots are the positions where no signal was detected.*

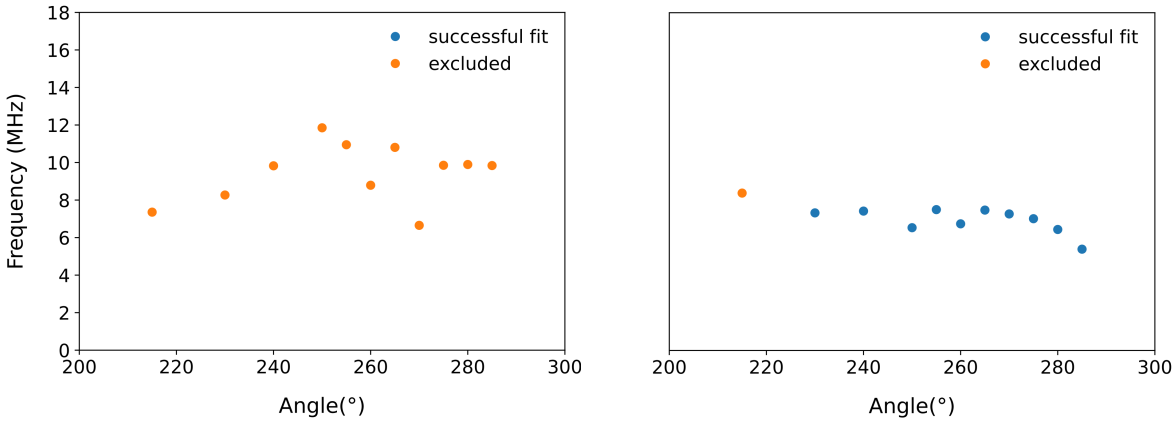

Figure B.6: *Angular exploration of the main frequency of the dynamic form factor in helium discharge, 20 mm from the target, and for a wavenumber $k = 4150$ rad.m^{-1}. The figure on the left corresponds to the identified negative frequency peak; the figure on the right corresponds to the identified positive frequency peak. The orange dots are the positions where no signal was detected.*

Bibliography

[1] J.P. Boeuf and L. Garrigues. Low frequency oscillations in a stationary plasma thruster. *J. Appl. Phys.*, 84(7):3541–3554, 1998. (cited on pages v, 16, 18, and 79)

[2] S. Tsikata. *Small-scale electron density fluctuations in the Hall thruster, investigated by collective light scattering.* PhD thesis, Citeseer, 2009. (cited on pages vi, 20, 31, 32, 35, 80, 93, 97, 98, 100, 103, 106, 109, 120, 127, and 133)

[3] J. Cavalier. *Modèles cinétiques et caractérisation expérimentale des fluctuations électrostatiques dans un propulseur à effet Hall.* PhD thesis, Université de Lorraine, 2013. (cited on pages x, 20, 80, 95, and 96)

[4] Union of concerned scientists. Satellite database. `https://www.ucsusa.org/resources/satellite-database`, 22024. (cited on page 1)

[5] H. A. Arbit, S. D. Clapp, and C. K. Nagai. Lithium-fluorine-hydrogen propellant investigation. Technical report, National Aeronautics and Space Administration, 1970. (cited on page 3)

[6] A.I. Morozov. The conceptual development of stationary plasma thrusters. *Plasma Phys. Rep.*, 29(3):235–250, 2003. (cited on page 5)

[7] A.I. Morozov. Stationary plasma thruster (spt) development steps and future perspectives. In *Proceedings of the 23rd International Electric Propulsion Conference*, pages 13–16, 1993. (cited on page 5)

[8] V. Kim, K.N. Kozubsky, V. M. Murashko, and A.V. Semenkin. History of the hall thrusters development in ussr. In *30th International Electric Propulsion Conference*, pages 17–20, 2007. (cited on page 5)

[9] F.M. Penning. Die glimmentladung bei niedrigem druck zwischen koaxialen zylindern in einem axialen magnetfeld. *Physica*, 3(9):873–894, 1936. (cited on page 9)

[10] J.S. Chapin. The planar magnetron. *Research Development*, 25(1):37–40, 1974. (cited on page 9)

[11] P. Sigurjonsson and J.T. Gudmundsson. Plasma parameters in a planar dc magnetron sputtering discharge of argon and krypton. In *Journal of Physics: Conference Series*, volume 100, page 062018. IOP Publishing, 2008. (cited on page 10)

[12] V. Kouznetsov, K. Macak, J.M. Schneider, U. Helmersson, and I. Petrov. A novel pulsed magnetron sputter technique utilizing very high target power densities. *Surf. Coat. Technol.*, 122(2-3):290–293, 1999. (cited on pages 10 and 21)

[13] J-P. Boeuf. Tutorial: Physics and modeling of hall thrusters. *J. Appl. Phys.*, 121(1):011101, 2017. (cited on page 13)

[14] D.M. Goebel and I. Katz. *Fundamentals of electric propulsion: ion and Hall thrusters.* John Wiley & Sons, 2008. (cited on page 13)

[15] E. Clementi, D.L. Raimondi, and W.P. Reinhardt. Atomic screening constants from scf functions. ii. atoms with 37 to 86 electrons. *J. Chem. Phys.*, 47(4):1300–1307, 1967. (cited on page 14)

[16] J.W. Koo and I.D. Boyd. Modeling of anomalous electron mobility in hall thrusters. *Phys. Plasmas*, 13(3):033501, 2006. (cited on page 15)

[17] J.M. Haas and A.D. Gallimore. Internal plasma potential profiles in a laboratory-model hall thruster. *Phys. Plasmas*, 8(2):652–660, 2001. (cited on page 15)

[18] J. Bohlmark, U. Helmersson, M. VanZeeland, I. Axnäs, J. Alami, and N. Brenning. Measurement of the magnetic field change in a pulsed high current magnetron discharge. *Plasma Sources Sci. Technol.*, 13(4):654, 2004. (cited on page 15)

[19] D. Lundin, S. Al Sahab, N. Brenning, C. Huo, and U. Helmersson. Internal current measurements in high power impulse magnetron sputtering. *Plasma Sources Sci. Technol.*, 20(4):045003, 2011. (cited on page 15)

[20] T.E. Sheridan and J. Goree. Low-frequency turbulent transport in magnetron plasmas. *J. Vac. Sci. Technol. A*, 7(3):1014–1018, 1989. (cited on pages 15 and 21)

[21] V.V. Zhurin, H.R. Kaufman, and R.S. Robinson. Physics of closed drift thrusters. *Plasma Sources Sci. Technol.*, 8(1):R1, 1999. (cited on pages 15 and 80)

[22] A.I. Morozov and V.V. Savel'Ev. Theory of the near-wall conductivity. *Plasma Phys. Rep.*, 27(7):570–575, 2001. (cited on page 15)

[23] A.I. Morozov and V.V. Savelyev. Fundamentals of stationary plasma thruster theory. *Reviews of Plasma Physics*, pages 203–391, 2000. (cited on page 15)

[24] A.I. Morozov. Effect of near-wall conductivity in a strongly magnetized plasma. *Zh. Tekh. Fiz*, 3:19, 1968. (Russian). (cited on page 15)

[25] N.P. Kozlov and A.I. Morozov. Plasma accelerators and ion injectors. *Moscow Izdatel Nauka*, 1984. (Russian). (cited on page 15)

[26] A.I. Bugrova and A.I. Morozov. Near wall conductivity. *Moscow Izdatel Nauka*, page pp 189–200, 1984. (Russian). (cited on page 15)

[27] N.B. Meezan, W.A. Hargus Jr, and M.A. Cappelli. Anomalous electron mobility in a coaxial hall discharge plasma. *Phys. Rev. E*, 63(2):026410, 2001. (cited on page 15)

[28] M. Cappelli, W.A. Hargus, and N. Meezan. Coherent structures in crossed-field closed-drift hall discharges. *IEEE Trans. Plasma Sci.*, 27(1):96–97, 1999. (cited on page 15)

[29] W. Hargus, Jr and M. Cappelli. Development of a linear hall thruster. In *34th AIAA/ASME/SAE/ASEE Joint Propulsion Conference and Exhibit*, page 3336, 1998. (cited on page 15)

[30] G. Guerrini and C. Michaut. Characterization of high frequency oscillations in a small hall-type thruster. *Phys. Plasmas*, 6(1):343–349, 1999. (cited on page 15)

[31] F. Taccogna, S. Longo, M. Capitelli, and R. Schneider. Anomalous transport induced by sheath instability in hall effect thrusters. *Appl. Phys. Lett.*, 94(25):251502, 2009. (cited on page 15)

[32] D. Sydorenko, A. Smolyakov, I. Kaganovich, and Y. Raitses. Plasma-sheath instability in hall thrusters due to periodic modulation of the energy of secondary electrons in cyclotron motion. *Phys. Plasmas*, 15(5):053506, 2008. (cited on page 15)

[33] E.Y. Choueiri. Plasma oscillations in hall thrusters. *Phys. Plasmas*, 8(4):1411–1426, 2001. (cited on page 16)

[34] A.P. Ehiasarian, A. Hecimovic, T. De Los Arcos, R. New, M. Schulz-von der Gathen, V.and Böke, and J. Winter. High power impulse magnetron sputtering discharges: Instabilities and plasma self-organization. *Appl. Phys. Lett.*, 100(11):114101, 2012. (cited on page 16)

[35] J. Fife, M. Martinez-Sanchez, and J. Szabo. A numerical study of low-frequency discharge oscillations in hall thrusters. In *33rd Joint Propulsion Conference and Exhibit*, page 3052, 1997. (cited on page 16)

[36] Y. Yang, X. Zhou, J. X Liu, and A. Anders. Evidence for breathing modes in direct current, pulsed, and high power impulse magnetron sputtering plasmas. *Appl. Phys. Lett.*, 108(3):034101, 2016. (cited on page 16)

[37] K. Hara, M.J. Sekerak, I.D. Boyd, and A.D. Gallimore. Mode transition of a hall thruster discharge plasma. *J. Appl. Phys.*, 115(20):203304, 2014. (cited on page 16)

[38] P. Coche and L. Garrigues. A two-dimensional (azimuthal-axial) particle-in-cell model of a hall thruster. *Phys. Plasmas*, 21(2):023503, 2014. (cited on pages 16 and 20)

[39] E.T. Dale and B.A. Jorns. Non-invasive time-resolved measurements of anomalous collision frequency in a hall thruster. *Phys. Plasmas*, 26(1):013516, 2019. (cited on page 16)

[40] A.R. Mansour and K. Hara. Full fluid moment modeling of rotating spokes in penning-type configuration. *Plasma Sources Sci. Technol.*, 31(5):055012, 2022. (cited on page 17)

[41] A. Anders and Y. Yang. Direct observation of spoke evolution in magnetron sputtering. *Appl. Phys. Lett.*, 111(6):064103, 2017. (cited on page 17)

[42] M. McDonald and A. Gallimore. Rotating spoke instabilities in hall thrusters. *IEEE Trans. Plasma Sci.*, 39(11):2952–2953, 2011. (cited on page 17)

[43] S. Vincent. *Azimuthal waves modification by current injection in a magnetized plasma column.* PhD thesis, Université Lyon 1, 2021. (cited on page 17)

[44] Yang Y., Liu J., Liu L., and A. Anders. Propagation direction reversal of ionization zones in the transition between high and low current magnetron sputtering. *Appl. Phys. Lett.*, 105(25), 2014. (cited on page 17)

[45] J. Held. *Transient transport phenomena in high power impulse magnetron sputtering discharges.* PhD thesis, Ruhr University Bochum, 2021. (cited on page 17)

[46] A. Hecimovic and A. Von Keudell. Spokes in high power impulse magnetron sputtering plasmas. *J. Phys. D: Appl. Phys.*, 51(45):453001, 2018. (cited on page 17)

[47] A. Guglielmi. *Propulseur à courant de Hall double étage à source RF inductive: étude expérimentale du fonctionnement et des instabilités basses fréquences.* PhD thesis, Université Paul Sabatier-Toulouse III, 2020. (cited on page 17)

[48] G.S. Janes and R.S. Lowder. Anomalous electron diffusion and ion acceleration in a low-density plasma. *Phys. Fluids*, 9(6):1115–1123, 1966. (cited on page 17)

[49] A. Schutze, J.Y. Jeong, S.E. Babayan, J. Park, G.S. Selwyn, and R.F. Hicks. The atmospheric-pressure plasma jet: a review and comparison to other plasma sources. *IEEE Trans. Plasma Sci.*, 26(6):1685–1694, 1998. (cited on page 17)

[50] A. Simon. Instability of a partially ionized plasma in crossed electric and magnetic fields. *Phys. Fluids*, 6(3):382–388, 1963. (cited on page 18)

[51] F.C. Hoh. Instability of penning-type discharges. *Phys. Fluids*, 6(8):1184–1191, 1963. (cited on page 18)

[52] Y. Sakawa, C. Joshi, P.K. Kaw, F.F. Chen, and V.K. Jain. Excitation of the modified simon–hoh instability in an electron beam produced plasma. *Phys. Fluids B*, 5(6):1681–1694, 1993. (cited on page 18)

[53] R Kawashima, K Hara, and K Komurasaki. Numerical analysis of azimuthal rotating spokes in a crossed-field discharge plasma. *Plasma Sources Science and Technology*, 27(3):035010, 2018. (cited on page 18)

[54] Jean-Pierre Boeuf and M Takahashi. New insights into the physics of rotating spokes in partially magnetized e× b plasmas. *Physics of Plasmas*, 27(8), 2020. (cited on page 18)

[55] A. Hecimovic. Anomalous cross-b field transport and spokes in hipims plasma. *J. Phys. D: Appl. Phys.*, 49(18):18LT01, 2016. (cited on page 18)

[56] M. McDonald, C. Bellant, B. St. Pierre, and A. Gallimore. Measurement of cross-field electroncurrent in a hall thruster due to rotating spoke instabilities. In *47th AIAA/ASME/SAE/ASEE Joint Propulsion Conference & Exhibit*, page 5810, 2011. (cited on page 18)

[57] C.L. Ellison, Y. Raitses, and N.J. Fisch. Cross-field electron transport induced by a rotating spoke in a cylindrical hall thruster. *Phys. Plasmas*, 19(1):013503, 2012. (cited on page 18)

[58] Ioannis G Mikellides and Alejandro Lopez Ortega. Growth of the modified two-stream instability in the plume of a magnetically shielded hall thruster. *Physics of Plasmas*, 27(10), 2020. (cited on page 19)

[59] Ioannis G Mikellides and Alejandro Lopez Ortega. Growth of the lower hybrid drift instability in the plume of a magnetically shielded hall thruster. *Journal of Applied Physics*, 129(19), 2021. (cited on page 19)

[60] S. Janhunen, A. Smolyakov, D. Sydorenko, M. Jimenez, I. Kaganovich, and Y. Raitses. Evolution of the electron cyclotron drift instability in two-dimensions. *Phys. Plasmas*, 25(8):082308, 2018. (cited on pages 19, 20, and 80)

[61] D.W. Forslund, R.L. Morse, and C.W. Nielson. Electron cyclotron drift instability. *Phys. Rev. Lett.*, 25(18):1266, 1970. (cited on page 19)

[62] S.P. Gary and J.J. Sanderson. Longitudinal waves in a perpendicular collisionless plasma shock. *J. Plasma Phys.*, 4(4):739–751, 1970. (cited on page 19)

[63] I.B. Bernstein. Waves in a plasma in a magnetic field. *Phys. Rev.*, 109(1):10, 1958. (cited on page 19)

[64] B. B. Kadomtsev. *Plasma Turbulence.* Academic Press, 1965. (cited on page 19)

[65] CN Lashmore-Davies. A possible mechanism for instability in a perpendicular collisionless shock wave. *J. Phys. A: General Physics*, 3(5):L40, 1970. (cited on page 19)

[66] H.V. Wong. Electrostatic electron-ion streaming instability. *Phys. Fluids*, 13(3):757–760, 1970. (cited on page 19)

[67] M. Lampe, W. M. Manheimer, J. B. McBride, J. H. Orens, R. Shanny, and R. N. Sudan. Nonlinear development of the beam-cyclotron instability. *Phys. Rev. Lett.*, 26:1221–1225, May 1971. (cited on page 19)

[68] M. Lampe, W. M Manheimer, J.B. McBride, and J.H. Orens. Anomalous resistance due to cross-field electron-ion streaming instabilities. *Phys. Fluids*, 15(12):2356–2362, 1972. (cited on page 19)

[69] J.C. Adam, A. Héron, and G. Laval. Study of stationary plasma thrusters using two-dimensional fully kinetic simulations. *Phys. Plasmas*, 11(1):295–305, 2004. (cited on pages 19, 20, and 80)

[70] A. Ducrocq, J.C. Adam, A. Héron, and G. Laval. High-frequency electron drift instability in the cross-field configuration of hall thrusters. *Phys. Plasmas*, 13(10):102111, 2006. (cited on pages 19, 20, and 80)

[71] S. Tsikata, N. Lemoine, V. Pisarev, and D.M. Gresillon. Dispersion relations of electron density fluctuations in a hall thruster plasma, observed by collective light scattering. *Phys. Plasmas*, 16(3):033506, 2009. (cited on page 20)

[72] S. Tsikata, C. Honore, and D. Gresillon. Collective thomson scattering for studying plasma instabilities in electric thrusters. *J. Instrum.*, 8(10):C10012, 2013. (cited on page 20)

[73] S. Tsikata, C. Honoré, N. Lemoine, and D.M. Grésillon. Three-dimensional structure of electron density fluctuations in the hall thruster plasma: E× b mode. *Phys. Plasmas*, 17(11):112110, 2010. (cited on page 20)

[74] F. Taccogna and P. Minelli. Three-dimensional particle-in-cell model of hall thruster: The discharge channel. *Phys. Plasmas*, 25(6):061208, 2018. (cited on page 20)

[75] A. Tavant, V. Croes, R. Lucken, T. Lafleur, A. Bourdon, and P. Chabert. The effects of secondary electron emission on plasma sheath characteristics and electron transport in an discharge via kinetic simulations. *Plasma Sources Sci. Technol.*, 27(12):124001, 2018. (cited on pages 20 and 80)

[76] K. Hara and S. Tsikata. Cross-field electron diffusion due to the coupling of drift-driven microinstabilities. *Phys. Rev. E*, 102(2):023202, 2020. (cited on pages 20, 80, 120, and 135)

[77] J. Cavalier, N. Lemoine, G. Bonhomme, S. Tsikata, C. Honoré, and D. Grésillon. Hall thruster plasma fluctuations identified as the e× b electron drift instability: Modeling and fitting on experimental data. *Phys. Plasmas*, 20(8):082107, 2013. (cited on pages 20, 80, and 94)

[78] T. Lafleur, S.D. Baalrud, and P. Chabert. Theory for the anomalous electron transport in hall effect thrusters. i. insights from particle-in-cell simulations. *Phys. Plasmas*, 23(5), 2016. (cited on page 20)

[79] W. Villafana, B. Cuenot, and O. Vermorel. 3d particle-in-cell study of the electron drift instability in a hall thruster using unstructured grids. *Physics of Plasmas*, 30(3):033503, 2023. (cited on pages 20 and 80)

[80] S.P. Gary and N. Omidi. The ion-ion acoustic instability. *Journal of plasma physics*, 37(1):45–61, 1987. (cited on page 20)

[81] Yoshiharu Nakamura and Yoshifumi Saitou. Observation of ion-acoustic waves in two-ion-species plasmas. *Plasma physics and controlled fusion*, 45(5):759, 2003. (cited on page 20)

[82] S. P. Gary. Electromagnetic ion/ion instabilities and their consequences in space plasmas: A review. *Space Science Reviews*, 56(3):373–415, 1991. (cited on page 20)

[83] S. Tsikata, J. Cavalier, A. Héron, C. Honoré, N. Lemoine, D. Grésillon, and D. Coulette. An axially propagating two-stream instability in the hall thruster plasma. *Phys. Plasmas*, 21(7), 2014. (cited on pages 20 and 135)

[84] E. Martines, R. Cavazzana, G. Serianni, M. Spolaore, L. Tramontin, M. Zuin, and V. Antoni. Electrostatic fluctuations in a direct current magnetron sputtering plasma. *Phys. Plasmas*, 8(6):3042–3050, 2001. (cited on page 21)

[85] D. Lundin, U. Helmersson, S. Kirkpatrick, S. Rohde, and N. Brenning. Anomalous electron transport in high power impulse magnetron sputtering. *Plasma Sources Sci. Technol.*, 17(2):025007, 2008. (cited on page 21)

[86] P. Kumar, S. Tsikata, and K. Hara. Effects of multiply charged ions on microturbulence-driven electron transport in partially magnetized plasmas. *J. Appl. Phys.*, 130(17), 2021. (cited on pages 21 and 135)

[87] J.D. Jackson. *Classical electrodynamics second edition.* Wiley, 1998. (cited on page 25)

[88] D.J. Griffiths and D.F. Schroeter. *Introduction to quantum mechanics.* Cambridge university press, 2018. (cited on page 27)

[89] D. H. Froula, S. H. Glenzer, Jr. N. C. Luhmann, and J. Sheffield. *Plasma Scattering of Electromagnetic Radiation: Theory and Measurement Techniques.* Elsevier, 2011. (cited on page 31)

[90] B. Vincent, S. Tsikata, S. Mazouffre, T. Minea, and J. Fils. A compact new incoherent Thomson scattering diagnostic for low-temperature plasma studies. *Plasma Sources Sci. Technol.*, 27(5):055002, 2018. (cited on pages 31, 43, and 51)

[91] B. Vincent. *Incoherent Thomson scattering investigations in Hall thruster, planar magnetron and ECR ion source plasmas.* PhD thesis, Université d'Orléans, 2019. (cited on pages 36, 44, 45, and 83)

[92] A. L. Glebov, O. Mokhun, A. Rapaport, S. Vergnole, V. Smirnov, and L. B. Glebov. Volume bragg gratings as ultra-narrow and multiband optical filters. *Proc. SPIE*, 8428:84280C, 2012. (cited on page 37)

[93] Penney C.M., Peters R.L.S., and Lapp M. Absolute rotational raman cross sections for n 2, o 2, and co 2. *J. Opt. Soc. Am.*, 64(5):712–716, 1974. (cited on page 39)

[94] N. Hershkowitz, O. Auciello, and D.L. Flamm. How langmuir probes work. *Plasma diagnostics*, 1:113–183, 1989. (cited on page 42)

[95] K. Muraoka, K. Uchino, and M.D. Bowden. Diagnostics of low-density glow discharge plasmas using thomson scattering. *Plasma Phys. Control. Fusion*, 40(7):1221, 1998. (cited on page 42)

[96] S. M. Meier, A. Hecimovic, T. V. Tsankov, D. Luggenhölscher, and U. Czarnetzki. First measurements of the temporal evolution of the plasma density in HiPIMS discharges using THz time domain spectroscopy. *Plasma Sources Sci. Technol.*, 27(3):035006, 2018. (cited on pages 42 and 51)

[97] S. Tsikata, B. Vincent, T. Minea, A. Revel, and C. Ballage. Time-resolved electron properties of a HiPIMS argon discharge via incoherent thomson scattering. *Plasma Sources Sci. Technol.*, 28(3):03LT02, 2019. (cited on pages 42, 43, and 44)

[98] P.J. Ryan, J.W. Bradley, and M.D. Bowden. Comparison of langmuir probe and laser Thomson scattering for plasma density and electron temperature measurements in HiPIMS plasma. *Phys. Plasmas*, 26(4):040702, 2019. (cited on page 42)

[99] M. A. Law, F. L. Estrin, M. D. Bowden, and J. W. Bradley. Diagnosing asymmetric bipolar HiPIMS discharges using laser Thomson scattering. *Plasma Sources Sci. Technol.*, 30(10):105019, 2021. (cited on page 42)

[100] B. Vincent, S. Tsikata, G.C. Potrivitu, L. Garrigues, G. Sary, and S. Mazouffre. Electron properties of an emissive cathode: Analysis with incoherent thomson scattering, fluid simulations and langmuir probe measurements. *J. Phys. D: Appl. Phys.*, 53(41):415202, 2020. (cited on page 43)

[101] S. Tsikata and T. Minea. Modulated electron cyclotron drift instability in a high-power pulsed magnetron discharge. *Phys. Rev. Lett.*, 114(18):185001, 2015. (cited on pages 43, 113, and 120)

[102] J. Bohlmark, J. T. Gudmundsson, J. Alami, M. Latteman, and U. Helmersson. Spatial electron density distribution in a high-power pulsed magnetron discharge. *IEEE Trans. Plasma Sci.*, 33(2):346–347, 2005. (cited on pages 46 and 55)

[103] A. Anders, P. Ni, and A. Rauch. Drifting localization of ionization runaway: Unraveling the nature of anomalous transport in high power impulse magnetron sputtering. *J. Appl. Phys.*, 111(5):053304, 2012. (cited on page 50)

[104] M. A. Raadu, I. Axnäs, J. T. Gudmundsson, C. Huo, and N. Brenning. An ionization region model for high-power impulse magnetron sputtering discharges. *Plasma Sources Sci. Technol.*, 20(6):065007, 2011. (cited on pages 51 and 68)

[105] A. D. Pajdarová, J. Vlček, P. Kudláček, and J. Lukáš. Electron energy distributions and plasma parameters in high-power pulsed magnetron sputtering discharges. *Plasma Sources Sci. Technol.*, 18(2):025008, 2009. (cited on page 51)

[106] P. Poolcharuansin and J. W. Bradley. Short-and long-term plasma phenomena in a HiPIMS discharge. *Plasma Sources Sci. Technol.*, 19(2):025010, 2010. (cited on page 51)

[107] J. T. Gudmundsson, J. Alami, and U. Helmersson. Evolution of the electron energy distribution and plasma parameters in a pulsed magnetron discharge. *Appl. Phys. Lett.*, 78(22):3427–3429, 2001. (cited on page 51)

[108] A. Revel, T. Minea, and C. Costin. 2d PIC-MCC simulations of magnetron plasma in HiPIMS regime with external circuit. *Plasma Sources Sci. Technol.*, 27:105009, 2018. (cited on pages 52, 54, 69, 70, 77, and 108)

[109] S-H. Seo, J-H. In, and H.-Y. Chang. Temporal evolution of electron energy distribution function and plasma parameters in the afterglow of drifting magnetron plasma. *Plasma Sources Sci. Technol.*, 14(3):576, 2005. (cited on page 52)

[110] G. D. Stancu, N. Brenning, C. Vitelaru, D. Lundin, and T. Minea. Argon metastables in HiPIMS: validation of the ionization region model by direct comparison to time resolved tunable diode-laser diagnostics. *Plasma Sources Sci. Technol.*, 24(4):045011, 2015. (cited on pages 53 and 65)

[111] O. Chapurin and A. Smolyakov. On the electron drift velocity in plasma devices with E $\times$ B drift. *J. Appl. Phys.*, 119(24):243306, 2016. (cited on pages 53 and 54)

[112] G. Yu. Yushkov and A. Anders. Origin of the delayed current onset in high-power impulse magnetron sputtering. *IEEE Trans. Plasma Sci.*, 38(11):3028–3034, 2010. (cited on pages 61 and 73)

[113] A. Hecimovic, M. Böke, and J. Winter. The characteristic shape of emission profiles of plasma spokes in HiPIMS: the role of secondary electrons. *J. Phys. D: Appl. Phys.*, 47(10):102003, 2014. (cited on pages 64 and 66)

[114] A. Mishra, P. J. Kelly, and J. W. Bradley. The 2d plasma potential distribution in a hipims discharge. *J. Phys. D: Appl. Phys.*, 44(42):425201, 2011. (cited on page 68)

[115] Nils Brenning, I Axnäs, Michael A Raadu, Daniel Lundin, and U Helmerson. A bulk plasma model for dc and hipims magnetrons. *Plasma Sources Science and Technology*, 17(4):045009, 2008. (cited on page 68)

[116] S. Muralikrishnan, A. J. Cerfon, M. Frey, L. F. Ricketson, and A. Adelmann. Sparse grid-based adaptive noise reduction strategy for particle-in-cell schemes. *J. Comput. Phys.*, 11:100094, 2021. (cited on page 69)

[117] L. Garrigues, B. Tezenas du Montcel, G. Fubiani, and B. C. G. Reman. Application of sparse grid combination techniques to low temperature plasmas particle-in-cell simulations. II. electron drift instability in a hall thruster. *J. Appl. Phys.*, 129(15):153304, 2021. (cited on page 69)

[118] E. Morel, Y. Rozier, and T. Minea. Hyper power impulse magnetron–hypim–glow discharge. *EPL*, 138(2):24001, 2022. (cited on page 72)

[119] A. El Farsy, E. Morel, Y. Rozier, L. de Poucques, J. Robert, and T. Minea. On the role of helium metastable (23s1) measured by time resolved tunable diode laser spectroscopy in high current magnetron discharge. *Plasma Sources Sci. Technol.*, 31(12):12LT01, 2022. (cited on page 72)

[120] K. Macák, V. Kouznetsov, J. Schneider, U. Helmersson, and I. Petrov. Ionized sputter deposition using an extremely high plasma density pulsed magnetron discharge. *J. Vac. Sci. Technol. A*, 18(4):1533–1537, 2000. (cited on page 75)

[121] G.z Greczynski, J. Lu, J. Jensen, I. Petrov, J. E. Greene, S. Bolz, W. Kölker, C. Schiffers, O. Lemmer, and L. Hultman. Metal versus rare-gas ion irradiation during ti1- xalxn film growth by hybrid high power pulsed magnetron/dc magnetron co-sputtering using synchronized pulsed substrate bias. *J. Vac. Sci. Technol. A*, 30(6), 2012. (cited on page 75)

[122] J. Haas, F.S. Gulczinski, A. Gallimore, G. Spanjers, and R. Spores. Performance characteristics of a 5 kw laboratory hall thruster. In *34th AIAA/ASME/SAE/ASEE Joint Propulsion Conference and Exhibit*, page 3503, 1998. (cited on page 80)

[123] M. Keidar, A. D Gallimore, Y. Raitses, and I. Boyd. On the potential distribution in hall thrusters. *Appl. Phys. Lett.*, 85(13):2481–2483, 2004. (cited on page 80)

[124] F. Taccogna and P. Minelli. Three-dimensional particle-in-cell model of hall thruster: The discharge channel. *Phys. Plasmas*, 25:061208, 2018. (cited on page 80)

[125] P. Coche and L. Garrigues. A two-dimensional (azimuthal-axial) particle-in-cell model of a hall thruster. *Phys. Plasmas*, 21:023503, 2014. (cited on page 80)

[126] J.D. Huba and C.S. Wu. Effects of a magnetic field gradient on the lower hydrid drift instability. *Phys. Fluids*, 19(7):988–994, 1976. (cited on page 80)

[127] L. Muschietti and B. Lembège. Microturbulence in the electron cyclotron frequency range at perpendicular supercritical shocks. *J. Geophys. Res.*, 118(5):2267–2285, 2013. (cited on page 80)

[128] A. Héron and J.C. Adam. Anomalous conductivity in hall thrusters: Effects of the non-linear coupling of the electron-cyclotron drift instability with secondary electron emission of the walls. *Phys. Plasmas*, 20(8):082313, 2013. (cited on pages 80, 90, and 91)

[129] L. Garrigues, B. Tezenas du Montcel, G. Fubiani, and B.C.G. Reman. Application of sparse grid combination techniques to low temperature plasmas particle-in-cell simulations. ii. electron drift instability in a hall thruster. *J. Appl. Phys.*, 129(15):153304, 2021. (cited on page 80)

[130] V.I. Demidov, S.V. Ratynskaia, and K. Rypdal. Electric probes for plasmas: The link between theory and instrument. *Rev. Sci. Instrum.*, 73(10):3409–3439, 2002. (cited on page 80)

[131] Z.A. Brown and B.A Jorns. Spatial evolution of small wavelength fluctuations in a hall thruster. *Phys. Plasmas*, 26(11), 2019. (cited on pages 81, 120, 153, and 154)

[132] Lasgorceix P., Raffin M., Lengrand JC., Dudeck M., Gbkalp I., Bouchoule A., and Cadiou A. A new french facility for ion propulsion research. In *24th International Electric Propulsion Conference, Moscow, Russia*, 1995. (cited on page 82)

[133] B. Vincent, S. Tsikata, and S. Mazouffre. Incoherent thomson scattering measurements of electron properties in a conventional and magnetically-shielded hall thruster. *Plasma Sources Sci. Technol.*, 29(3):035015, 2020. (cited on pages 83, 86, 90, and 91)

[134] J.P. Boeuf. Physics and modeling of hall thrusters. *J.Appl.Phys*, 121:011101, 2017. (cited on page 89)

[135] F. Taccogna, S. Longo, and M. Capitelli. Very-near-field plume simulation of a stationary plasma thruster. *Eur. Phys. J. AP*, 28(1):113–122, 2004. (cited on pages 90 and 91)

[136] A. Domínguez-Vázquez, F. Taccogna, and E. Ahedo. Particle modeling of radial electron dynamics in a controlled discharge of a hall thruster. *Plasma Sources Sci. Technol.*, 27(6):064006, 2018. (cited on pages 90 and 91)

[137] Spektor R., Diamant K.D., Beiting E.J., Raitses Y, and Fisch N.J. Laser induced fluorescence measurements of the cylindrical hall thruster plume. *Phys. Plasmas*, 17(9), 2010. (cited on pages 90 and 91)

[138] M. Chung To Sang, L. Garrigues, T. Dubois, and S. Tsikata. 3d sparse pic modeling of a hall thruster: Comparisons with experimental results. *37th International Electric Propulsion Conference, June 19-23 2022, Cambridge, MA, USA*, (IEPC-2022-316), 2022. (cited on pages 91 and 92)

[139] G.V. Gordeev. *Zh. Eksp. Teor. Fiz*, 23:660, 1952. (cited on page 94)

[140] G. Bourgeois, S. Mazouffre, and N. Sadeghi. Unexpected transverse velocity component of xe+ ions near the exit plane of a hall thruster. *Phys. Plasmas*, 17(11), 2010. (cited on page 94)

[141] Gawron D., Mazouffre S., and Boniface C. A fabry–pérot spectroscopy study on ion flow features in a hall effect thruster. *Plasma Sources Sci. Technol.*, 15(4):757, 2006. (cited on page 95)

[142] Bryan Reid, Rohit Shastry, Alec Gallimore, and Richard Hofer. Angularly-resolved exb probe spectra in the plume of a 6-kw hall thruster. In *44th AIAA/ASME/SAE/ASEE Joint Propulsion Conference & Exhibit*, page 5287, 2008. (cited on page 106)

[143] A.P. Ehiasarian, R. New, W.D. Münz, L. Hultman, U. Helmersson, and V. Kouznetsov. Influence of high power densities on the composition of pulsed magnetron plasmas. *Vacuum*, 65(2):147–154, 2002. (cited on page 114)

[144] P. Poolcharuansin, M. Bowes, T.J. Petty, and J.W. Bradley. Ionized metal flux fraction measurements in hipims discharges. *J. Phys. D: Appl. Phys.*, 45(32):322001, 2012. (cited on pages 114 and 117)

[145] S. Konstantinidis, J.P. Dauchot, M. Ganciu, A. Ricard, and M. Hecq. Influence of pulse duration on the plasma characteristics in high-power pulsed magnetron discharges. *J. Appl. Phys.*, 99(1):013307, 2006. (cited on page 114)

[146] A. Kapran, V. G Antunes, Z. Hubička, C. Ballage, and T. Minea. Investigation of the magnetron balancing effect on the ionized flux fraction and deposition rate of sputtered titanium species for the high-power impulse magnetron sputtering pulses of different lengths. *J. Vac. Sci. Technol. A*, 41(1), 2023. (cited on pages 115 and 143)

[147] J. Bohlmark, M. Lattemann, J.T. Gudmundsson, A.P. Ehiasarian, Y.A. Gonzalvo, N. Brenning, and U. Helmersson. The ion energy distributions and ion flux composition from a high power impulse magnetron sputtering discharge. *Thin Solid Films*, 515(4):1522–1526, 2006. (cited on page 118)

[148] R.B. Lobbia and B.E. Beal. Recommended practice for use of langmuir probes in electric propulsion testing. *J. Propuls. Power*, 33(3):566–581, 2017. (cited on pages 120, 152, and 154)

[149] Z.A. Brown and B.A. Jorns. Growth and saturation of the electron drift instability in a crossed field plasma. *Phys. Rev. Lett.*, 130(11):115101, 2023. (cited on pages 120, 153, and 154)

[150] V. Croes, A. Tavant, R. Lucken, R. Martorelli, T. Lafleur, A. Bourdon, and P. Chabert. The effect of alternative propellants on the electron drift instability in hall-effect thrusters: Insight from 2d particle-in-cell simulations. *Phys. Plasmas*, 25(6), 2018. (cited on page 132)

[151] Butler A., Brenning N., Raadu M.A., Gudmundsson J.T., T. Minea, and D. Lundin. On three different ways to quantify the degree of ionization in sputtering magnetrons. *Plasma Sources Sci. Technol.*, 27(10):105005, 2018. (cited on page 142)

[152] J. Bohlmark, J. Alami, C. Christou, A.P. Ehiasarian, and U. Helmersson. Ionization of sputtered metals in high power pulsed magnetron sputtering. *J. Vac. Sci. Technol. A*, 23(1):18–22, 2005. (cited on page 144)

[153] Waymouth J.F. Perturbation of a plasma by a probe. *Phys. Fluids*, 7(11):1843–1854, 1964. (cited on page 146)

[154] N. Sternberg and V. Godyak. Plasma density perturbation caused by probes at low gas pressure. *Phys. Plasmas*, 24(9), 2017. (cited on page 146)

Thibault Dubois

Dynamique des électrons dans les décharges en champs croisés

Les décharges plasma en champs croisés ont une grande variété d'applications, y compris la propulsion spatiale (les propulseurs de Hall) et le traitement des matériaux (magnétrons planaires). La configuration croisée des champs magnétiques et électriques crée des phénomènes tels que la turbulence plasma et des anisotropies dans les propriétés des particules, dont la compréhension nécessite des informations détaillées sur les électrons. L'étude expérimentale directe de ces caractéristiques contribuerait au développement de simulations numériques de haute fidélité de ces plasmas et à une meilleure compréhension de leur fonctionnement.
Un effort de recherche intense a été consacré ces dernières années à l'étude de phénomènes tels que le transport "anormal" d'électrons à travers les lignes de champ, qui dépasse de plusieurs ordres de grandeur le transport attendu par les collisions. L'incompréhension de ce phénomène limite la capacité de prédiction des codes numériques pour les propulseurs et autres dispositifs. Des travaux récents ont cependant établi un lien entre ce transport et les instabilités à haute fréquence dans le plasma. La complexité de ce comportement (propagation 3D, effets de couplage) nécessite le développement de codes numériques performants à trois dimensions, mais aussi des diagnostics avancés pour sonder pour le comportement et les propriétés des électrons.

La nature de ces décharges (électrons énergétiques et magnétisés, leur architecture) rend les diagnostics invasifs tels que les sondes de Langmuir limités dans leur capacité à sonder les caractéristiques des électrons. Dans ce travail, deux diagnostics basés sur la diffusion Thomson ont été appliqués : THETIS (diffusion Thomson incohérente), pour mesurer les propriétés individuelles des électrons telles que la température (plus largement, les fonctions de distribution de l'énergie des électrons), la densité et la vitesse de dérive, et PRAXIS (diffusion Thomson cohérente), pour mesurer les fluctuations à petite échelle de la densité des électrons (associées aux ondes MHz).

Dans un propulseur à effet Hall de 1,5 kW, l'évolution des propriétés des électrons le long de la direction radiale a été directement mesurée. Une variation radiale, plus marquée pour la température, a été observée. Un modèle de théorie cinétique linéaire a été utilisé pour évaluer la forme de la relation de dispersion correspondant aux conditions de plasma mesurées, et celle-ci a été comparée aux mesures antérieures effectuées avec PRAXIS. Cette analyse a révélé un effet de lissage de la relation de dispersion qui peut être expliqué par la variation des propriétés des électrons le long du volume de mesure. Dans un magnétron planaire HiPIMS, plusieurs conditions de décharge ont été étudiées, avec de l'argon et de l'hélium, pour des courants de pointe allant de 40 A à 600 A. Des caractéristiques résolues en temps, telles que l'anisotropie de la vitesse de dérive, ont été mesurées, et une analyse des contributions aux dérives des particules a été réalisée dans des différentes conditions. La théorie cinétique linéaire a été adaptée pour le magnétron. L'application de PRAXIS aux mesures dans le magnétron planaire a révélé la présence de deux instabilités dans le mode HiPIMS, l'une identifiée comme l'instabilité de dérive cyclotronique électronique (ECDI), étudiée dans des travaux antérieurs, et le second mode se propageant à un angle de 45° par rapport à la surface de la cible. Une analyse préliminaire de la perturbation par une simple sonde de Langmuir dans le plasma a également été effectuée sur le magnétron planaire, et il a été observé qu'une augmentation systématique de la vitesse de groupe de l'instabilité se produisait en présence de la sonde.

L'application de diagnostics avancés dans le cadre de ce travail a permis une meilleure caractérisation (y compris avec une résolution temporelle élevée) des propriétés et de la dynamique des électrons de ces dispositifs en champs croisés.

Mots clés : Décharges magnétisées, champs croisés, instabilités, diffusion Thomson, plasma froid, electrons

Thibault Dubois

Electron dynamics in crossed-field discharges

Crossed-field plasma discharges have a wide variety of applications, including space propulsion (e.g. Hall thrusters) and materials processing (planar magnetrons). The crossed magnetic and electric field configuration creates features such as plasma turbulence and anisotropies in particle properties, the understanding of which require detailed information on electrons. Direct experimental study of these features would contribute to the development of high-fidelity numerical simulations of such plasmas, and to an improved understanding of their operation.

An intense research effort has been devoted in recent years to the study of phenomena such as so-called "anomalous" electron transport across the field lines, which exceeds by several orders of magnitude that expected from collisions. The lack of complete understanding of this phenomenon limits the predictive capability of numerical codes for thrusters and other devices. Recent work has, however, established a link between this transport and high-frequency instabilities within the plasma. The complexity of this behavior (3D propagation, coupling effects) requires not only the development of high-performance, full-dimensional numerical codes, but also advanced diagnostics for electron behavior and properties.
The nature of these discharges (such as high degrees of electron magnetization and energy, architecture) render invasive diagnostics such as Langmuir probes limited in their capacity to probe electron features. In this work, two diagnostics based on Thomson scattering were applied to the study of such features: THETIS (incoherent Thomson scattering), for measurement of individual electron properties such as temperature (more broadly, electron energy distribution functions), density and drift velocity, while PRAXIS (coherent Thomson scattering), for measurement of small-scale electron density fluctuations (associated with MHz-frequency waves).

In a 1.5 kW Hall-effect thruster, the evolution of electron properties along the radial direction was directly measured. A radial variation in the electron properties, most marked for electron temperature, was observed. A linear kinetic theory model was used to evaluate the form of the dispersion relation corresponding to the measured plasma conditions, and this was compared with previous measurements made using PRAXIS. This analysis revealed a smoothing effect of the dispersion relation which could be accounted for due to the variation of electron properties along the characteristic measurement volume dimensions. In a HiPIMS planar magnetron, several discharge conditions were studied, with argon and helium, for peak currents ranging from 40 A to 600 A. Time-resolved features such as anisotropy of the drift velocity were measured, and an analysis of the contributions to the particle drifts was performed under varying conditions. The linear kinetic theory was adapted to the magnetron. The application of PRAXIS to measurements in the planar magnetron revealed the presence of two instabilities in the HiPIMS mode, one identified as the electron cyclotron drift instability (ECDI), studied in previous work, and the second mode propagating at an angle of 45° to the target surface. A preliminary analysis of the perturbative influence of a simple Langmuir probe in the plasma was also carried out on the planar magnetron, and it was observed that a systematic increase in the instability group velocity was occurred in the presence of such a probe.

The application of advanced electron diagnostics to measurements in this work have enabled an improved characterization (including with high temporal resolution) of the electron properties and dynamics of these crossed-field devices.

Keywords : Magnetized discharges, crossed-fields, instabilities, Thomson scattering, cold plasma, electrons

Institut de Combustion Aérothermique, Réactivité et Environnement (ICARE)
1C Avenue de la Recherche Scientifique, 45071 Orléans